

ANALYSIS OF MOISTURE EVAPORATION FROM UNDERWEAR DESIGNED FOR FIRE-FIGHTERS

Elena Onofrei^{*1,2}, Teodor-Cezar Codau³, Stojanka Petrusic³, Gauthier Bedek¹, Daniel Dupont¹, Damien Soulat³

¹GEMTEX, HEI, Université Catholique de Lille, Lille, F-59046, France

²Technical University "Gheorghe Asachi" of Iasi, Iasi, 700050, Romania

³GEMTEX, ENSAIT, Université Lille Nord de France, Roubaix, F-59056, France
eonofrei@yahoo.com, elena.onofrei@hei.fr

Abstract:

In this study we analysed the effect of moisture on the thermal protective performance of fire-fighter clothing in case of routine fire-fighting conditions. In the first stage of this research we investigated simultaneous heat and moisture transfer through a single-layer fabric, used as underwear for fire-fighters, at different moisture conditions. In the second stage of the study, the underwear in dry and wet state was tested together with protective clothing systems for fire-fighter consisting of three or four layers. It was found that during the evaporation of the moisture, a temperature plateau appeared during which temperatures hardly rose. The energy consumption used for the phase change of moisture located in the assembly dominated the heat transfer process as long as there was moisture present. As soon as all water had evaporated, the temperatures approached the temperatures measured for dry samples. The moisture within the clothing assembly did not lead to increased temperatures compared with the measurements with dry samples. This research has confirmed that moisture can positively affect the thermal protection of a clothing system.

Keywords:

heat transfer, moisture transport, protective clothing, thermal comfort

1. Introduction

Thermal comfort is the key factor to be considered in clothing design, and furthermore a crucial factor for protective clothing systems for fire-fighters working in hot environments. Comfort researchers recognise that clothing comfort has two main aspects that combine to create a subjective perception of satisfactory performance. These are thermo-physiological and sensorial comfort. The moisture transmission behaviour of a clothing assembly plays a very important role in influencing its efficiency with respect to both thermo-physiological and sensorial body comfort [1].

Thermo-physiological comfort has two distinct phases. During normal wear, insensible perspiration is continuously generated by the body. Steady-state heat and moisture vapour fluxes are thus created and must be gradually dissipated to maintain thermoregulation and a feeling of thermal comfort. In transient wear conditions, characterised by intermittent pulses of moderate or heavy sweating caused by strenuous activity or climatic conditions, sensible perspiration and liquid sweat occur and must be rapidly managed by the clothing. Therefore, heat and moisture transfer properties under both steady and transient conditions must be considered for prediction of wearer comfort [1, 2].

Studies show that the maximum rate of sweat production by an average man is about 30 g/min (1.8 l/h) [3]. The sweat rate may even reach up to 4 l/m² for shorter duration [4]. Schopper-Jochum *et al.* found that 30–44% of the sweated

amount of moisture is accumulated in the clothing system [5]. Keiser C. and Rossi R.M. found that under usual fire-fighting circumstances, about two-thirds of this moisture may remain in the clothing system [6].

By analysing the moisture distribution in the different combinations of underwear with fire-fighter protective clothing, Mäkinen *et al.* observed that 50–80% of the sweat accumulated in the inner two layers [7]. Rossi R. found that 80% of the moisture remained in the inner two layers after 10 minutes sweating and still more than 60% after 20 minutes. Keiser C. made measurements on the sweating cylinder and discovered that over 90% of the moisture remained in the first three layers [4].

Studies on the influence of moisture in clothing system on the heat transfer suggest that moisture can inhibit or increase heat transfer through thermal protective material depending upon specific conditions. Chen investigated simultaneous heat and moisture transfer through single-layer cotton fabrics at different moisture conditions (dry, conditioned and moist) and for varying heat flux intensities (21–188 kW/m²), for time exposure from 1 to 15 seconds. He found that at high heat exposures and for short test durations, moisture detrimentally affects thermal protection. For longer exposures, moisture can increase thermal protection [8]. Lee and Barker studied heat transfer through single-layered protective fabrics at 20 W/m² and 84 W/m² radiant heat exposures. Three different moisture conditions were used in their study: dry, conditioned and wet, at moisture loads ranging from 60% to 80%. These tests

showed that at high radiant exposure (84 W/m^2), the thermal protective performance of the fabric is reduced by up to 35%. At incident heat flux level of 20 W/m^2 , the thermal protection of wet samples increases [9]. *Mäkinen et al.* studied the effect of moisture content in underwear on thermal protection. The garments (layers moistened with different amounts of water) were exposed to a source of radiant heat of 20 W/m^2 according to the standard ISO 6942. They found that humidity in underwear decreased time to pain and time to burn, with the shortest burn time occurring at a moisture content of 30–40%. These data were obtained on systems without a moisture barrier [7]. *Rossi and Zimmerli* investigated the influence of humidity on the protective clothing during exposure to a radiant heat of 80 W/m^2 and 5 W/m^2 , respectively. They found that at low radiant heat flux exposures, humidity in the inner clothing layers generally decreases the time to pain and the time to burn [10].

These contradictory results can be attributed to the different factors that influence heat transfer in protective clothing: the amount, the location and the transfer of the moisture, the type and conditioning of materials and the duration and intensity of thermal exposure [6].

According to *Mäkinen* [11], thermal environments are divided into three categories: routine, corresponding to a common intervention for firefighters characterised by low radiant heat flux from 0.42 to 1.26 kW/m^2 and air temperatures in the range of 10 – 60°C ; hazardous, representing an intervention in the presence of high radiant heat flux from 1.26 to 8.37 kW/m^2 and air temperatures in the range of 60 – 300°C ; and emergency corresponding to extreme conditions from 8.37 to 125.6 kW/m^2 and air temperatures in the range of 300 – 1000°C .

Data obtained over the years show that most burn injuries sustained by fire-fighters occurred in thermal environments with low radiation level (classified as routine or hazardous conditions), as a result of prolonged exposure [12–14]. So far, almost all the studies on thermal protective performance were conducted for high-level radiant heat flux corresponding to the emergency conditions; only a few studies have been conducted on thermal protective performance with prolonged exposure to hazardous conditions; and no studies have been found for the moisture influence on heat transfer through thermal protective clothing under routine conditions.

Thus, a research was started to study the effect of moisture on the thermal protective performance of fire-fighter clothing in low-level radiant heat environment, the most common conditions in which the fire-fighters work. Understanding mechanisms by which moisture in textiles affects heat transfer through clothing systems could lead to improvements in the design of thermal protective clothing [15].

The problem of vapour diffusion through the layers of the protective clothing is complicated and has to be approached through the integration of the interaction between heat and mass transfer and heat of phase changes [4]. Therefore, in the first stage of this research moisture effect on heat transfer through single-layer fabrics was studied. We investigated

simultaneous heat and moisture transfer through a single-layer fabric, used as underwear for fire-fighters, at different moisture conditions, in the case of routine firefighting operation (radiant heat flux of 1100 W/m^2).

In the second stage of the study, the underwear in dry and wet state was tested together with protective clothing systems for a fire-fighter consisting of three and four layers.

For the wet tests, at the beginning of the experiments, the underwear was wetted only with defined amounts of water, in order to simulate the accumulation of sweat in this layer. The moisture membrane prevents the passage of liquid water from underwear to outer layers, and the water-vapour diffusion will occur only through the layers of protective system.

2. Experimental

2.1. Materials

Protective clothing systems consisting of three and four aramid-based layers which are typical in the underwear designed for fire-fighters:

- Outer layer – which protects against all kinds of thermal hazards and mechanical impact;
- Moisture barrier – which protects against water and other fluids;
- Thermal barrier – which is an insulating layer which protects against heat; and
- Inner layer – which protects the thermal barrier against abrasion.

Two multi-layer fire-fighter jackets were chosen for analysis. The first assembly was composed of outer shell, moisture barrier and thermal barrier, respectively. The moisture barrier is a hydrophilic polyurethane (PU) membrane. The second one contains outer shell, moisture barrier, thermal barrier and inner layer. The moisture barrier is based on the microporous hydrophobic polytetrafluoroethylene (PTFE) membrane.

In firefighting, underwear's principal role is to provide an additional layer of material between the hazard (radiant or direct flame contact) and the person's skin. Cotton is the most commonly used underwear, but wool, silk, aramid or other flame-resistant materials are also used [16]. Fabrics made by synthetic fibres, 100% or blended with natural fibres, resistant to high temperatures as well as to chemical agents are used for underwear for firemen, due to their improved ability to remove moisture, which seemingly could improve fire-fighters' comfort and might increase efficiency. In this study, underwear made of functionalised polyamide base fibres, resistant to high temperatures as well as to chemical agents and with good moisture management capacity, was used.

The physical properties (thickness, surface weight, bulk density) and the thermo-physical properties (water-vapour resistance and thermal resistance) of the fabrics were measured and are displayed in Table 1.

Table 1. Physical and thermo-physical properties of the fabrics

	Material	Surface weight, g/m ²	Thickness, mm	Density, kg/m ³	R _{ct} m ² K/W	Ret m ² Pa/W
Underwear (UW)	Functionalised polyamide base knitted -piqué	283± 4	1.19 ± 0.01	238 ± 4	0.0281±0.0003	4.08±0.03
Fire-fighter Jackets						
Fire-fighter Jacket 1 (FJ1)		540±4	2.40±0.04	224±5	0.0938±0.0048	34.95±0.04
Outer shell	100% aramid woven	242 ± 2	0.5 ± 0.01	489 ± 5	0.0129±0.0006	5.76±0.27
Thermal liner	100% aramid non-woven	98 ± 2	1.46 ± 0.03	67 ± 2	0.0689±0.0034	6.64±0.21
Moisture barrier	polyurethane coated 100% aramid knitted (coated)	195 ± 2	0.47 ± 0.00	418 ± 6	0.0134±0.0034	30.16±0.02
Fire-fighter Jacket 2 (FJ2)		570±4	2.13±0.03	267±4	0.0715±0.0023	25.27±0.91
Outer shell	100% aramid woven	242 ± 2	0.5 ± 0.01	489 ± 5	0.0129±0.0006	5.76±0.27
Thermal liner	100% aramid non-woven	49±2	0.38±0.01	127±3	0.0147±0.0003	1.93±0.00
Moisture barrier	PTFE membrane laminated to 100% aramid non-woven	128±3	0.98±0.03	131±5	0.0263±0.0008	7.27±0.03
Inner layer	100 % aramid woven	150±1	0.37±0.00	403±6	0.0129±0.0003	3.44±0.14

Thickness was measured under the pressure of 1 ± 0.01 kPa, according to the standard ISO 5084:1996. Density was calculated from the values of fabric monolayer thickness and surface weight (which was determined using an analytical balance). The average of ten measurements was calculated.

Measurements of thermal (R_{ct}) and water-vapour resistance (R_{et}) of mono- and multi-layer fabrics were carried out on the sweating-guarded hotplate according to the standard ISO 11092:1993 [17]. Specific environment testing conditions prescribed by this standard were met using a climatic chamber.

It can be noted that the sum of R_{ct} values of individual layers is close to the measured R_{ct} of the assembly composed of the corresponding layers. In contrast with the thermal resistance, the total water-vapour resistance of a combination of textiles is not always equal to the sum of the single resistances. In particular, the inclusion of hydrophilic components imparts the complexity of the phenomenon, as the water-vapour resistance of these materials depends on the relative humidity of the membrane [18].

2.2. Experimental set-up and procedure

2.2.1. The test apparatus

The scheme of the test apparatus for determining heat and moisture transfer under both steady and transient conditions through single-layer or multi-layer fabrics, when exposed to a low-level radiant heat flux, is shown in Figure 1.

An infrared lamp (*SICCA RED 150W 240V HG*) was used as

radiant heat source in order to supply a constant radiant heat flux at the surface of the sample corresponding to the routine condition of the firefighting environment. Figure 2 shows the relative intensity distribution of the lamp [19].

For every Watt electrical power, the radiant intensity is expressed by the equation (1):

$$I = \frac{P}{\Omega} \tag{1}$$

P – the power source, W
I - the radiant intensity, W/Sr
Ω - the solid angle, Sr.

$$\Omega = \frac{S}{r^2} \tag{2}$$

S – the limited area of the spherical zone of solid angle Ω, m²
r - the radius of the sphere, m.

Thus, from equations (1) and (2):

$$I = \frac{P \times r^2}{S} \tag{3}$$

or,

$$\Phi = \frac{I}{r^2} \tag{4}$$

where F is the radiant heat flux density, W/m².

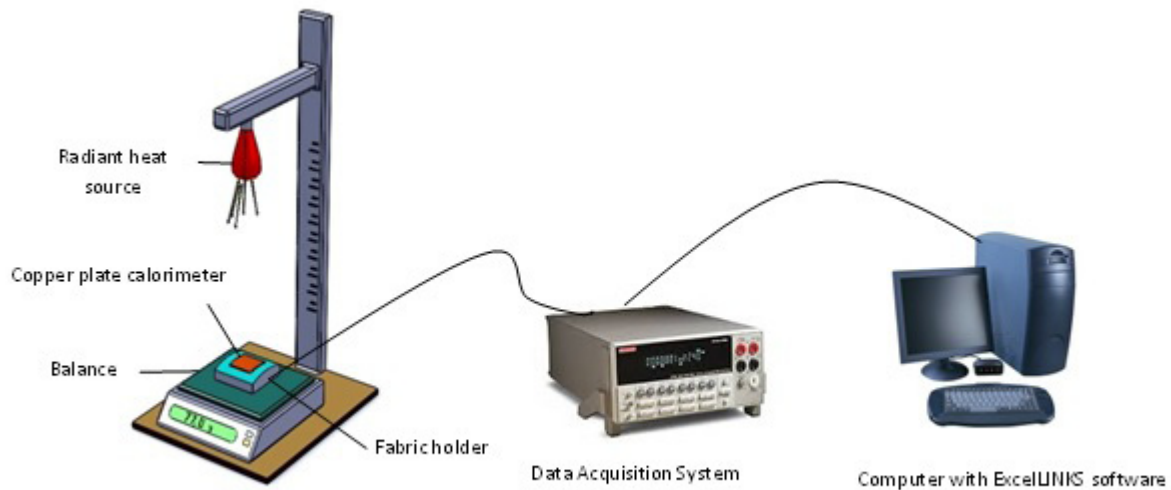


Figure 1. Configuration of the test apparatus for determining heat and moisture transfer through fabrics exposed to a low-level radiant heat flux

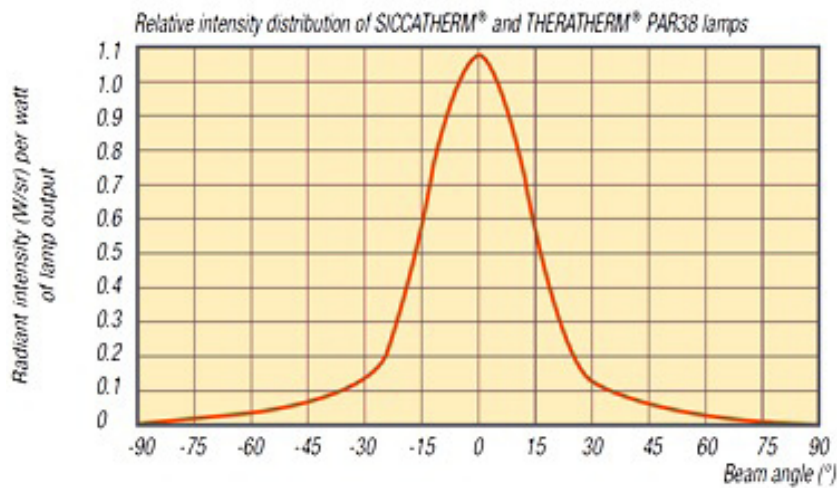


Figure 2. Relative intensity distribution of SICCATHERM® lamp

For small angles, the radius of the sphere can be approximated with the distance “d” between the radiant source and calorimeter. In our arrangement, the maximum distance between the source and the calorimeter is 420 mm. For this distance the beam angle value is between 0 and 3.6 (°) and the average intensity of the lamp is 1.01 [W/Sr]. For a radiant source of 150 [W] the minimum heat flux density is 852 [W/m²].

The fabric holder assembly was fabricated to hold and position a fabric sample rigidly against the hot air impinging flow. The heat transferred across the fabric is measured with a sensor assembly positioned on the fabric holder. The fabric holder consists of 90x90 mm square piece of extruded PVC board of nominal thickness 25 mm and known density and thermal characteristics.

The sensor assembly is composed of a copper plate calorimeter 50 x 50 mm, 1.6 mm thick, an insulating board and a Chromega™ - Constantan thermocouple silver welded on the copper plate. The calorimeter face is painted with a flat black

paint having a coefficient of absorption greater than 0.9, so as to absorb radiant flux. The copper plate is bent into an arc with a radius of 130 mm. The copper plate is accurately weighed before assembly. The curved copper plate is bonded to the mounting block around its edges using an adhesive resistant to high temperature.

The fabric holder assembly is placed on the precise METTLER TOLEDO balance in order to register the evaporation rate. The data are collected and stored with the LabX direct Balance 2.3 system on a PC.

E-type Chromega™-Constantan thermocouples (Omega Engineering LTD, USA) are placed between fabric layers in order to measure the temperature distribution through the multi-layer assembly during experiments.

A Data Acquisition System Keithley 2700 with 20-Channel Differential with Multiplexer module 7700 coupled to a computer with ExcelLINKS software has been used to register the data.

2.2.2. Calibration of the radiant source

In the presented configuration, calibration of the test apparatus is performed as follows:

1. The test frame is positioned at a distance 'd', on the vertical central line of the radiant source.
2. The temperature measuring device is switched on.
3. The radiation source is switched on and allowed to heat the movable screen closed until the radiation is constant. The steady state is reached in about 30 seconds.
4. The movable screen is removed and returned to position after a temperature rise of about 12°C has been reached.
5. The recorded output shows a linear temperature/time relationship. From this linear region, the rate of the rise in temperature R is determined, expressed in °C/s.
6. The incident heat flux density, in kW/m², is then determined from the following equation:

$$Q_0 = \frac{M \cdot c_p \cdot R}{\alpha \cdot A} \tag{5}$$

where:

- M - the mass of copper plate, kg
- c_p – the specific heat of copper, J/kgK
- R – the rate of rise in the calorimeter temperature in the linear region, °C/s
- A – the area of copper plate, m²
- a - the absorption coefficient of the painted surface of the calorimeter.

The incident heat flux density can be adjusted to the required level by varying the distance between the radiant source and the calorimeter.

The calibration of the radiant source is confirmed by measurements using an ultra-thin Heat Flow Meter 50 x 50mm, from CAPTEC with a sensibility of 11.7 mV/(W/m²).

2.2.3. Experiments

2.2.3.1. Single-layer tests

The specimen had the dimension (57.5 x 57.5) mm. The distance between the infrared lamp and the outer surface was defined in order to supply a constant radiant heat flux of 1100 W/m² at the surface of the sample.

The experiment started by first applying the flux on a movable screen which was initially closed for 30 seconds to prevent

premature heating of the fabric prior to testing. When the screen was quickly opened the heat flux reached the front fabric surface. The fabric sample was exposed to the heat flux until the steady state was reached.

Both dry and wet tests were performed. For the wet tests, at the beginning of the experiment the underwear was wetted with a defined amount of water (1.08 g, 1.38 g and 1.74 g). This corresponds to the moisture content of 120%, 160% and 200%, respectively, for the underwear relative to the conditioned weight (20 °C and 40 % RH). To moisten the sample, the following protocol was used: the specimen was first conditioned in the testing room prior to moisture application and testing. The sample was immersed in distilled water and then placed between sheets of rolled-over blotting paper using a metal roller for removing the excess water until the needed amount of water was obtained.

The testing conditions were constant during the experiments: ambient temperature T_{amb} = 20 °C and air relative humidity RH= 40%.

2.2.3.2. Multi-layer fabric system tests

The same protocol was used for multi-layer fabric systems without additional water (dry condition) and with additional water within the underwear. The outer shell, thermal liner and moisture barrier and inner layer specimens have the dimension (70x70) mm and were fastened on the specimen holder using some clamps. A slight tensioning force of 2N was applied in order to avoid the air gaps between layers. The underwear specimen had the dimension (57.5x57.5) mm.

For the wet tests, the underwear was wetted with the same amounts of water (1.08 g, 1.38 g and 1.78 g), corresponding to the moisture content of 120%, 160% and 200%, respectively, for the underwear.

E-type Chromega™-Constantan thermocouples (Omega Engineering LTD, USA) were placed between fabric layers in order to measure the temperature distribution (T1, T2 and T3) through the textile assembly during the experiment. The thermocouple accuracy was 0.3 °C, the response time 0.3 s, wire diameter 0.075 mm and Teflon insulation 0.3 mm.

The locations of thermocouples into the fabric systems are shown in Figure 3.

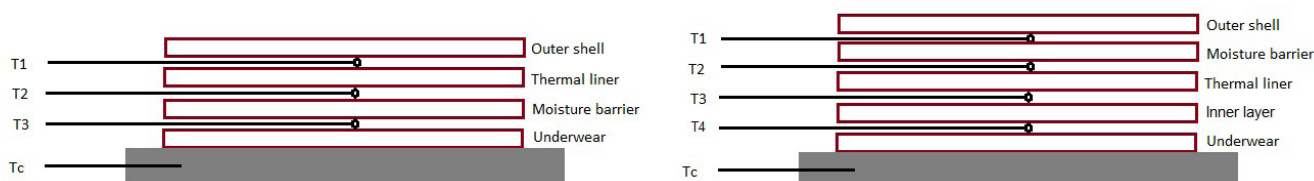


Figure 3. The thermocouples location

3. Results and Discussion

3.1. Single-underwear tests

Figure 4 shows the temperature variation for the constant heat flux of 1100 W/m², for underwear with different moisture content. The temperature pattern for wetted fabrics can be divided into four different phases: an initial rising phase, a stagnation phase, a final rising phase and a final stagnation phase. During the first phase energy was used mainly in heating up the fabric and moisture, and only a small quantity of moisture was evaporated. During the second phase the temperature was constant (43.5 °C) regardless of the initial amount of water contained in the material. On the contrary, the amount of moisture had a significant influence on the second phase duration. Thus, for the 1.08 g moisture content (120%) the temperature plateau was registered for 1398 seconds, for 1.38 g moisture content (160%) for 1608 seconds and for 1.74 g moisture content (200%) for 1956 seconds. Keiser C. [4] found a linear correlation between the amount of water and the duration of the second phase. This linear correlation was confirmed by our results (see Figure 5).

In the third phase the temperature started rising again, and the fourth phase represented the equilibrium.

The temperature was lower during evaporation of the moisture than during the measurement of the dry sample. The higher the initial moisture content the higher the difference during the evaporation. For all experiments, as soon as the moisture had evaporated, the temperature approached the temperatures measured for dry sample, 75°C.

Figure 6 shows the decrease in the moisture contents.

The moisture content stayed constant at the beginning for about 30–60 seconds and then decreased. The moisture decreased linearly with time. From these results the evaporation rates were calculated by dividing the moisture content by the time it took to evaporate the amount of water. The evaporation rates were 0.981 x 10⁻³ g/s for 200% moisture content, 0.927 x 10⁻³ g/s for 160% moisture content and 0.841 x 10⁻³ g/s for 120% moisture content, respectively, that is, 0.297 g/m².s, 0.280 g/m².s and 0.255 g/m².s, respectively. Thus, for the same radiant heat flux, the rate of evaporation rate seemed to increase linearly with the moisture content (Figure 7).

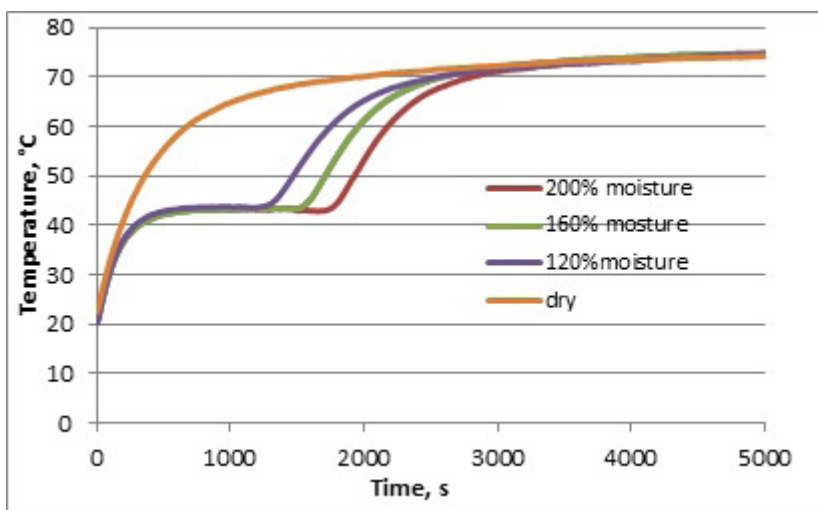


Figure 4. The temperature variation for constant heat flux of 1100 W/m², for underwear with different moisture content

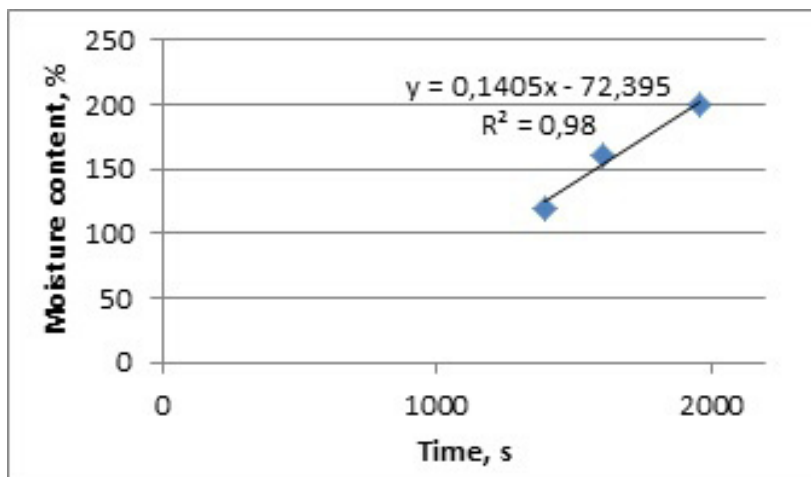


Figure 5. Correlation of the amount of water and the time at the end of phase two

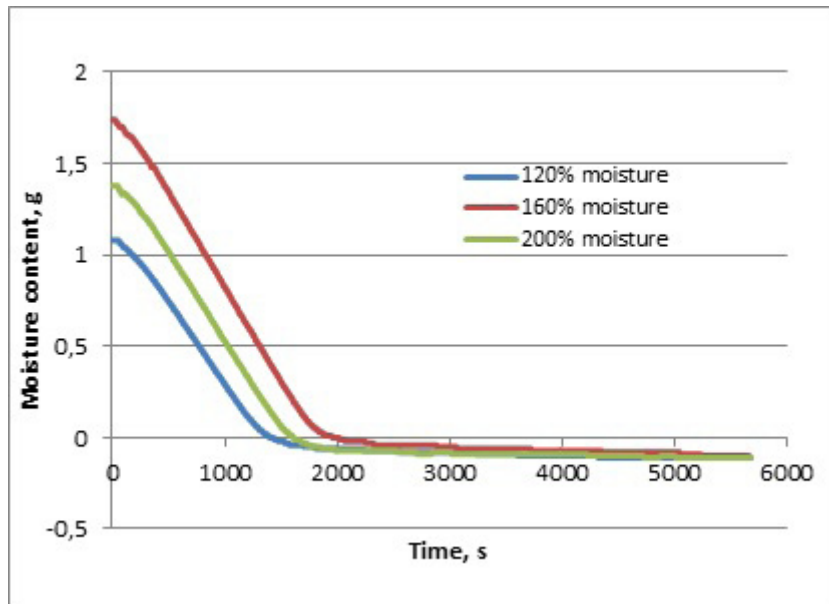


Figure 6. Variation of moisture content

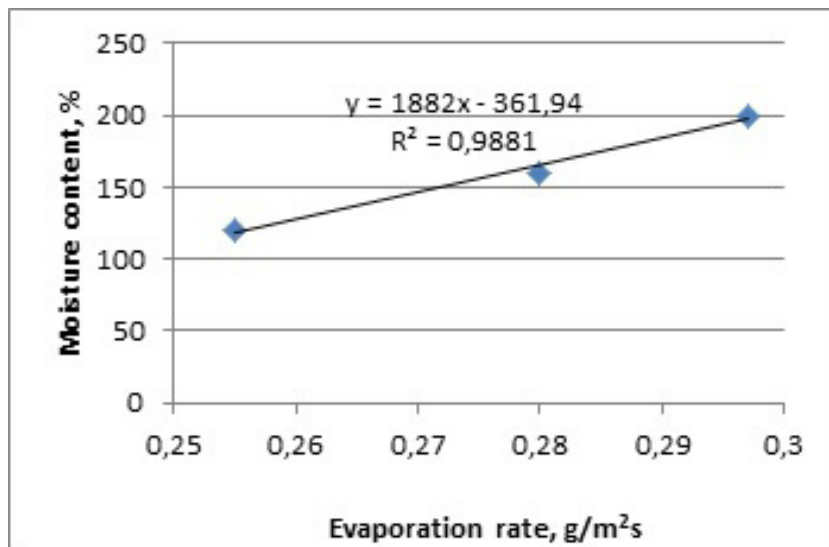


Figure 7. Correlation of the evaporation rate and the amount of moisture

At the end of the experiment, moisture content reached a negative value. As the weight of the whole system was set to zero initially, a negative amount of water at the end of measurement indicates that this amount of water must be present within the textile layer at the beginning of the measurement. The samples were kept at room condition prior to the tests, and therefore an initial amount of water corresponding to their moisture regain was present in the material. After radiation was cut off, the same amount of water was absorbed back into the fabric from the surrounding atmosphere. This amount represents 12.79% of the mass of perfectly dry material and corresponds to the moisture regain of fibres, that is, 12%.

The energy used for evaporation can be calculated from

$$Q_{evap} = \dot{m}_{evap} \cdot \varphi_{evap} \quad (W/m^2) \quad (6)$$

where

\dot{m}_{evap} is the evaporative mass flux, kg/m^2s

φ_{evap} is the latent heat of evaporation, J/kg .

Considering that the temperature of the system remains constant during evaporation, we can calculate the energy used for evaporation:

$$Q_{evap} = Q_{in} - Q_{rad-out} - Q_{conv} \quad (W/m^2) \quad (7)$$

The general inward heat flux Q_{in} (W/m^2) represents a heat flux that enters into domain.

$$Q_{in} = \varepsilon Q \quad (W/m^2) \quad (8)$$

ε is the emissivity of the fabric

Q is the radiant heat flux, W/m^2 .

The emitted thermal radiate heat flow is defined as

$$Q_{rad-out} = \varepsilon \sigma (T_{surf}^4 - T_{amb}^4) \quad (W/m^2) \quad (9)$$

where

ε is the emissivity of the fabric

σ is the Stefan–Boltzmann constant, W/m^2K^4

T_{surf} is the surface temperature, K

T_{amb} is the ambient temperature, K.

Natural convection heat transfer following the temperature gradient between the surface and the environment occurs:

$$Q_{conv} = h_c (T_{surf} - T_{amb}) \quad (W/m^2) \quad (10)$$

where h_c is the natural convection heat transfer coefficient (W/m^2K) calculated using the definition of the Nusselt number:

$$h_c = Nu \frac{k_{air}}{L} \quad (W/m^2K) \quad (W/m^2K) \quad (11)$$

where

Nu is the Nusselt number

k_{air} is the thermal conductivity of the air $W/(m \cdot K)$

L is the characteristic length, m.

According to the empirical correlation of free convection on a horizontal plate for $T_{surf} > T_{amb}$ [20]:

$$Nu = \begin{cases} 0.54 Ra_L^{1/4} & Ra_L \leq 10^7 \\ 0.15 Ra_L^{1/3} & Ra_L > 10^7 \end{cases} \quad (12)$$

$$Ra_L = \frac{g |\partial \rho / \partial T|_p \cdot \rho C_p \cdot \Delta T \cdot L^3}{k \mu} \quad (13)$$

where

g is the acceleration of gravity, m/s^2

ΔT is the temperature difference between the surface and ambient conditions, K

k is the thermal conductivity of the fluid $W/(m \cdot K)$

ρ is the fluid density, kg/m^3

C_p is the heat capacity of the fluid, $J/(kg \cdot K)$

μ is the dynamic viscosity, $Pa \cdot s$

L is the characteristic length, m

Ra_L is the Rayleigh number.

The constants used for the calculation of the energy balance are shown in Table 2.

Table 2. Constants used for the calculation of the energy balance

Constant	Value	Unit
Q_{in}	1100	W/m^2
e	0.95	-
T_{surf}	51	$^{\circ}C$
T_{amb}	20	$^{\circ}C$
h_c	9.8	W/m^2K
m_{evap}	0.280	g/m^2s
j_{evap}	2257	J/g

The heat of evaporation according to equation (6) is $632 W/m^2$ and according to equation (7) is $600 W/m^2$. Thus, a good correlation can be considered between the two values, taking into account the assumptions made.

3.2. Fire-fighter Jackets + Underwear tests

Figure 8 shows the evolution of temperature over time according to measurements at all the four interfaces, for the three-layer protective system with underwear, FJ1 +UW, in dry condition.

Figure 8 shows that the temperature of the thermocouples starts rising sharply from the moment the fabric system is exposed to the radiant flux at $t=0$ and then gradually rises until stabilisation. The highest rate of rise is registered by T1 temperature and the smallest rate in temperature increase is registered by the calorimeter temperature, Tc. The energy is conducted to the copper plate interface, but in a relatively slower process that proves the thermal protective effect of the fabric system. The temperature at the back face stabilises at approximately $72^{\circ}C$, and the temperature T1 at about $95^{\circ}C$.

Figures 9, 10 and 11 show the evolution of temperature over time according to measurements at all the four interfaces,

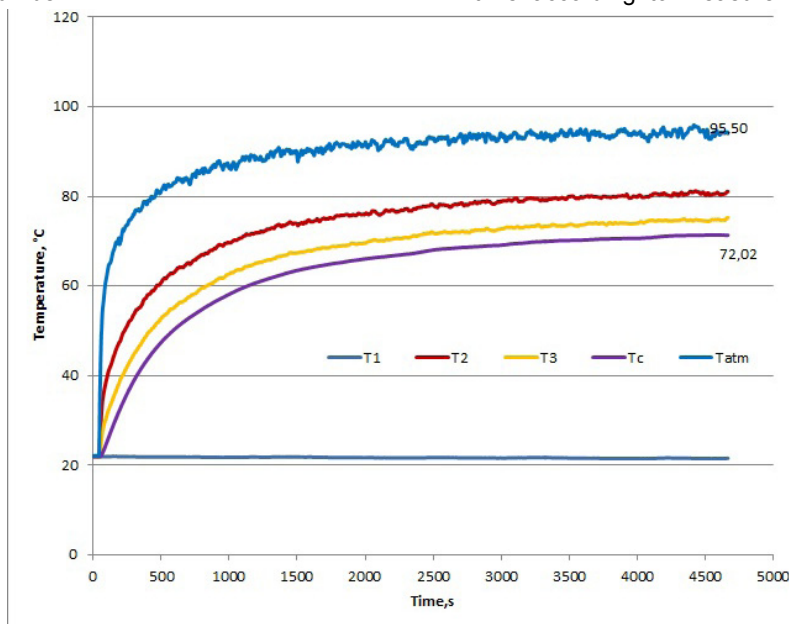


Figure 8. Temperature profiles with dry fabrics (FJ1+UW) when exposed to a radiant heat flux of $1100 W/m^2$

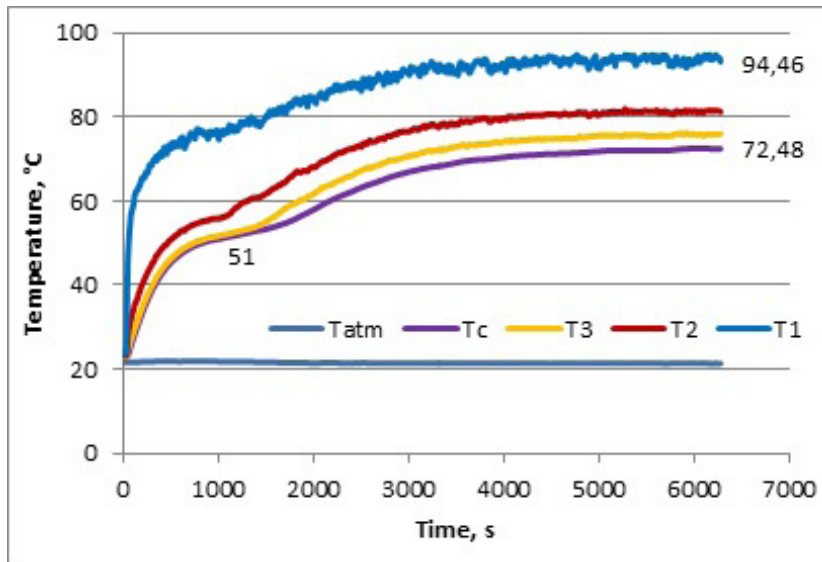


Figure 9. Temperatures between the layers (FJ1+W) Moisture content 120%, located in the underwear; heat flux 1100 W/m²

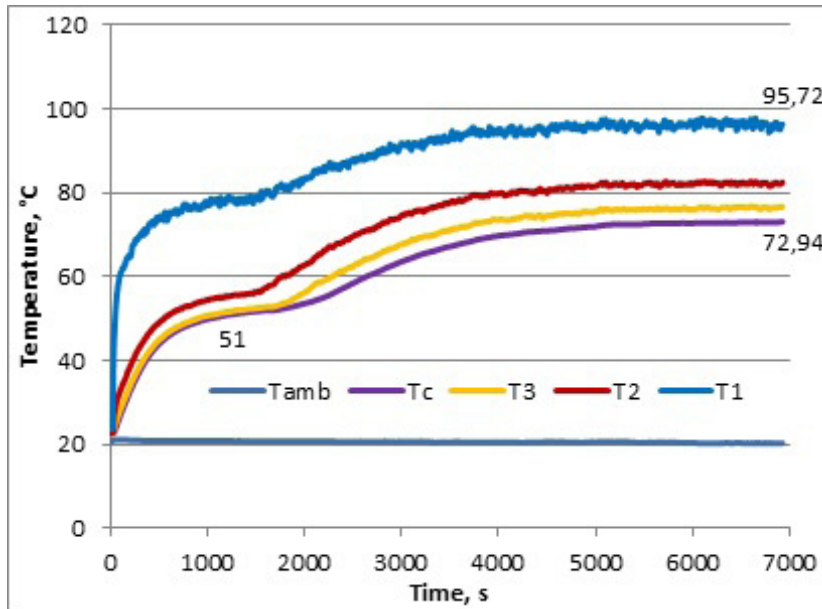


Figure 10. Temperatures between the layers (FJ1+UW); moisture content 160%, located in the underwear; heat flux 1100 W/m²

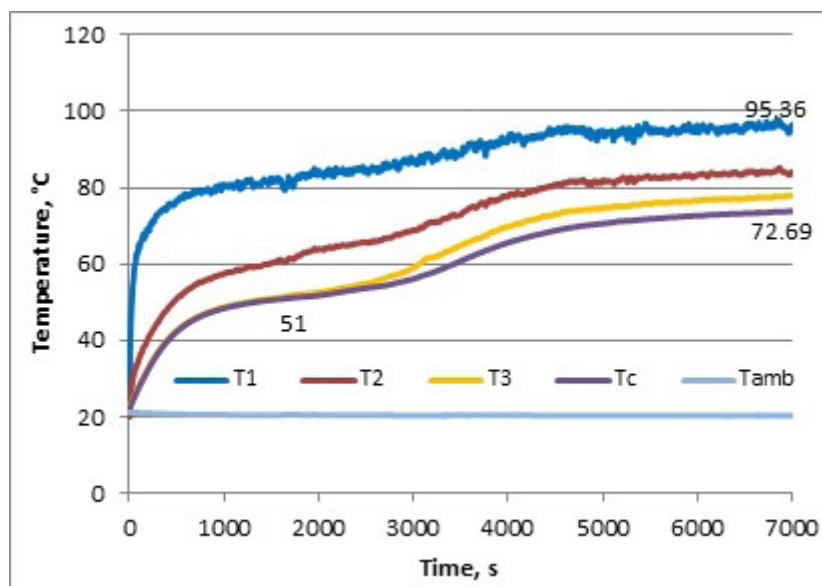


Figure 11. Temperatures between the layers (FJ1+UW); moisture content 200%, located in the underwear; heat flux 1100 W/m²

for a three-layer protective system + underwear, for 120%, 160% and, respectively, 200% initial moisture content in the underwear layer.

Similar to the previous discussion, the temperature pattern can be divided into four different phases: an initial rising phase, a stagnation phase, a final rising phase and a final stagnation phase.

After the first stagnation phase, the temperature starts rising again and a steady-state condition is reached, indicating that the fabric is completely dry. The temperature at the back face stabilises at approximately 72 °C and the temperature T1 at about 95 °C. In fact, as soon as the moisture evaporates, the temperatures approach the temperatures measured for dry samples.

Figure 12 shows the comparison of the temperatures T1 and Tc, respectively, for different amounts of moisture content in underwear under a radiant heat flux of 1100 W/m². The moisture within the clothing assembly did not lead to increased temperatures compared with the measurements with dry samples. On the contrary, lower temperatures were reached during the evaporation process. This research demonstrates

that moisture can positively affect the thermal protection of a clothing system.

The evaporation rates were 0.195 g/m²s for 200% moisture content, 0.183 g/m²s for 160% moisture content and 0.145 g/m²s for 120% moisture content, respectively. The time of evaporation was 1645 seconds for 120% moisture content, 2120 seconds for 160% moisture content and 2355 seconds for 200% moisture content. Thus, linear correlations were again confirmed between the moisture content and both the evaporation time and the evaporation rate.

For multi-layer clothing system the water-vapour resistance of the upper layers leads to a lower evaporation rate and consequently lower energy absorbed by evaporation. Thus, for the FJ1 + UW tests, the temperature plateau is recorded at a higher value (51 °C) than for single underwear (43.5 °C).

The underwear containing 160% moisture was tested in combination with fire-fighter protective clothing consisting of four layers (FJ2) for three different heat flux densities: 1700 W/m², 1100 W/m² and 875 W/m². Figures 13, 14 and 15 show the temperature variations.

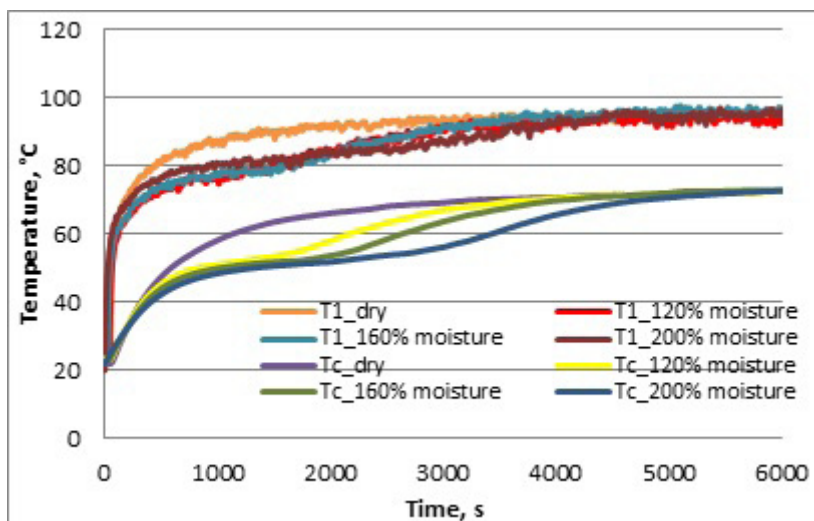


Figure 12. Comparison of the temperatures T1 and Tc, respectively, for different amounts of moisture content in underwear (FJ1+UW); heat flux 1100 W/m²

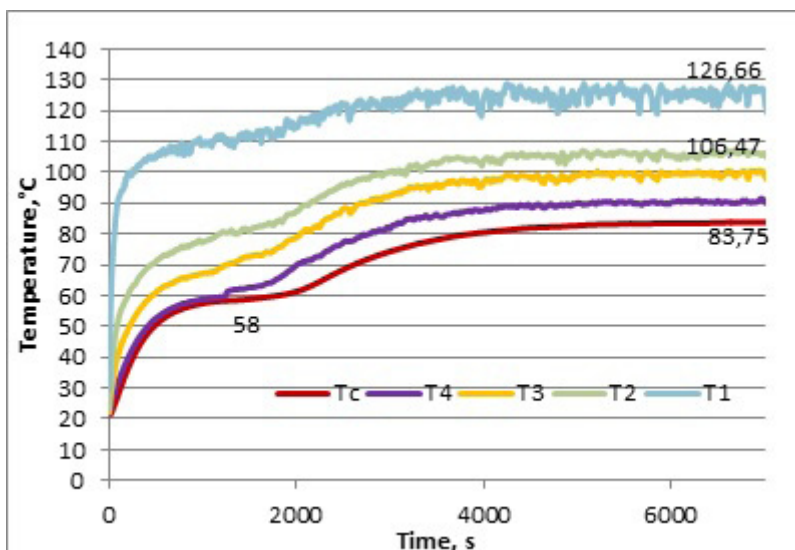


Figure 13. Temperatures between the layers (FJ2+UW); moisture content 160%, located in the underwear; heat flux 1700 W/m²

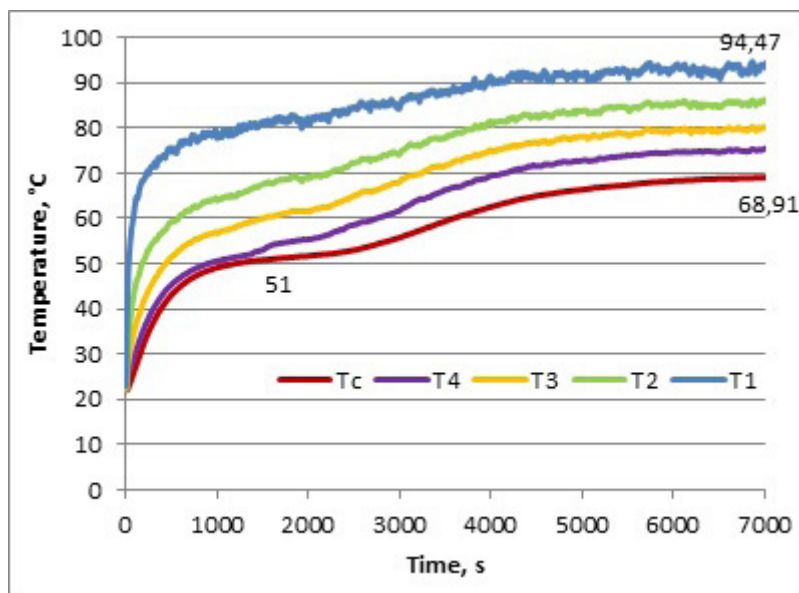


Figure 14. Temperatures between the layers (FJ2+UW); moisture content 160%, located in the underwear; heat flux 1100 W/m²

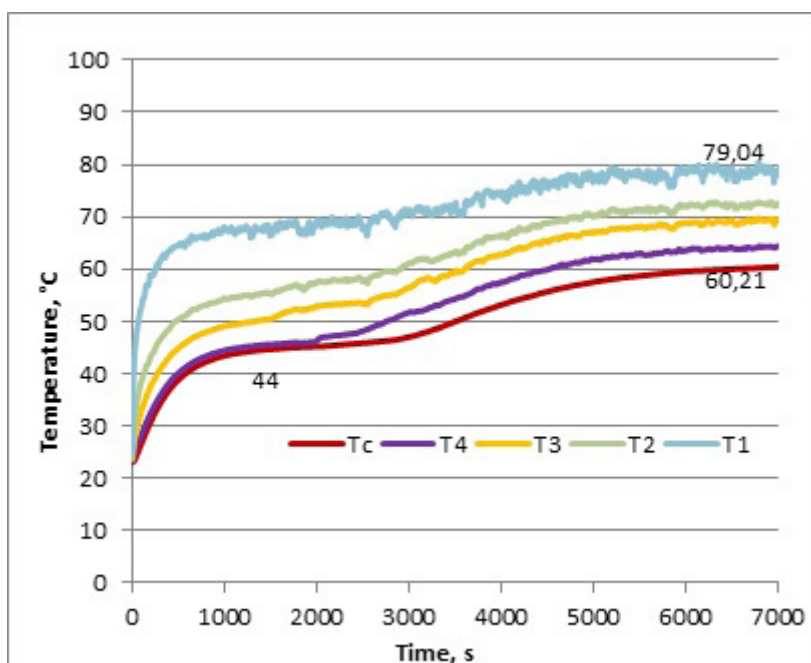


Figure 15. Temperatures between the layers (FJ2+UW); moisture content 160%, located in the underwear; heat flux 875 W/m²

In combination with FJ2 the evaporation rates were 0.223 g/m²s for the heat flux of 1700 W/m², 0.170 g/m²s for the heat flux of 1100 W/m² and 0.150 g/m²s for the heat flux of 875 W/m², respectively. The time of evaporation was 2000 s for the heat flux of 1700 W/m², 2610 s for the heat flux of 1100 W/m² and 3078 s for the heat flux of 875 W/m², respectively. Thus, linear correlations were confirmed between the heat flux density and both the second phase duration and the evaporation rate.

The evaporation temperature depends on the heat flux density: the higher the heat flux the higher the temperature at which the constant plateau is registered.

Even if the thermal resistance of FJ2 is lower than the thermal resistance of FJ1, comparable temperatures have been registered at steady state. This can be because of the fact that FJ2 has four layers, that is, one supplementary air gap

between the textile layers compared with FJ1. This air gap can determine an increase of FJ2 thermal resistance.

On the contrary, for FJ1 with 34.9 m²Pa/W water-vapour resistance, the evaporation rate is 0.183 g/m²s and the evaporation time 2120 seconds. For FJ2 with 25.27 m²Pa/W water-vapour resistance, the evaporation rate is 0.170 g/m²s and the evaporation time 2660 seconds. This means that for the FJ1, with higher R_{et}, the evaporation rate is higher and the time of evaporation is shorter. This is a contradiction that can be explained by the fact that barrier properties of hydrophilic membrane (component of FJ1) do depend on the applied water-vapour pressure because of membrane swelling effect. Thus, the water-vapour resistance of hydrophilic membrane is reduced by increasing the water-vapour pressure applied to the sample, or, expressed in more simple terms, hydrophilic membrane responds to increasing water-vapour pressure by becoming

more breathable [21, 22]. Following the presence of liquid water in the textile layers beneath the hydrophilic membrane, the vapour pressure under membrane gets close to the saturation pressure which results in an increase in the relative humidity and consequently a decrease in the water-vapour resistance.

4. Conclusions

We investigated simultaneous heat and moisture transfer through a single-layer fabric, used as underwear for fire-fighters, at different moisture conditions, when exposed to a low level of radiant heat. In the absence of a standardised method for testing the heat and moisture transfer through protective equipment for fire-fighters under routine conditions, a measuring device was developed, which was calibrated to deliver a constant radiant flux corresponding to these conditions of the fire-fighting environment.

The energy used for water evaporation was calculated from the evaporation rate and the energy balance equation, and a good correlation was found.

The underwear without additional water (dry condition) and with additional water was also tested together with two multi-layer fire-fighter jackets. In this experiment, moisture was applied before exposure to radiant heat.

During the evaporation of the moisture, a temperature plateau appeared during which temperatures were hardly rising. The energy consumption used for the phase change of moisture located in the assembly dominated the heat transfer process as long as there was moisture present. As soon as all water had evaporated, the temperatures approached the temperatures measured for dry samples.

Water has higher thermal conductivity relative to air and it has been assumed that heavily wet condition within the fire-fighter clothing makes faster temperature increase. But this research has confirmed that moisture can positively affect the thermal protection of a clothing system in case of routine fire-fighting operation. The moisture within the clothing assembly did not lead to increased temperatures compared with the measurements with dry samples. The effect of the higher heat capacity and energy absorption through vaporising overtook the effect of higher heat conductivity of the wet material.

Linear correlations were confirmed between the moisture content and both the evaporation time and the evaporation rate as well as between the heat flux density and both the evaporation time and the evaporation rate.

The evaporation temperature depends on the heat flux density: the higher the heat flux the higher the temperature at which the constant plateau is registered.

This study contributes to a better understanding of the impact of moisture retained in the underwear on the protective behaviour of overall fire-fighter clothing system, under the conditions of low-level radiant heat flux.

Acknowledgements

The authors gratefully acknowledge the region Nord-Pas-de-Calais and the European Regional Development Fund for their financial support in the context of the research program FLUTEX.

References

- [1] Song, G. (2011). *Improving comfort in clothing*. Woodhead Publishing Limited, Cambridge.
- [2] Yoo, S., Barker, R.I. (2005). *Comfort Properties of Heat-Resistant Protective Workwear in Varying Conditions of Physical Activity and Environment. Part I: Thermophysical and Sensorial Properties of Fabrics*, *Textile Research Journal*, 75, 523.
- [3] Durney, C.H., Massoudi, H., Iskander, M. F. (1986). *Radiofrequency radiation dosimetry handbook*. The University of Utah. Retrieved 30.05.2013 from Web site: <http://www.radhaz.com/docs/RF%20Dosimetry%20Handbook%20ver%204.pdf>.
- [4] Keiser, C. (2007). *Steam burns. Moisture management in firefighter protective clothing*. PhD Thesis, Swiss Federal Institute of Technology Zurich, Swiss.
- [5] Schopper-Jochum, S., Schubert, W. and Hocke, M. (1997) *Vergleichende Bewertung des Trageverhaltens von Feuerwehreinsatzjacken (Phase 1)*. *Arbeitsmedizin, Sozialmedizin und Umweltmedizin*, 32(4).
- [6] Keiser, C. and Rossi, R.M. (2008). *Temperature analysis for the prediction of steam formation and transfer in multilayer thermal protective clothing at low level thermal radiation*. *Textile Research Journal*, 78 (11), 1025-1035.
- [7] Mäkinen, H., Smolander, J., Vuorinen, H. (1988). *Simulation of the effect of moisture content in underwear and on the skin surface on steam burns of firefighters*. In: Mansdorf, S.Z., Sager, R., Nielsen, A.P., (eds). *Performance of Protective Clothing: Issues and Priorities for the 21st Century, Second Symposium (ASTM STP 989)*. Philadelphia, PA, USA: American Society for Testing and Materials (ASTM), 415–421.
- [8] Chen, N.Y. (1959). *Transient Heat and Moisture Transfer to Skin through Thermally Irradiated Cloth*. Doctoral Dissertation, Massachusetts Institute of Technology, Boston.
- [9] Lee, Y.M., Barker, R.L. (1986). *Effect of Moisture on the Thermal Properties of Heat-Resistant Fabrics*. *Journal of Fire Sciences*, 4, 315–331.
- [10] Rossi, R.M., Zimmerli, T. (1996). *Influence of Humidity on the Radiant, Convective and Contact Heat Transmission through Protective Clothing Materials*. In: *Performance of Protective Clothing: Fifth Volume*, ASTM STP 1237, James S. Johnson, J.S., Mansdorf, S. Z. (eds.) American Society for Testing and Materials, (ASTM), 269–280.
- [11] Mäkinen, H. (2005) *Firefighter's protective clothing*. In: Scott RA (ed.) *Textiles for Protection*. Cambridge, Woodhead, UK, 622-647
- [12] Song, G., Paskaluk, S., Sati, R. et al. (2011). *Thermal protective performance of protective clothing used for low radiant heat protection*, *Textile Research Journal*, 81(3), 311–323.
- [13] Song, G., Gholamreza, F., Cao, W. (2011). *Analyzing thermal stored energy and effect on protective performance*, *Textile Research Journal*, 81(11), 1124–1138.

- [14] Fu, M., Wenguo Weng, W., Yuan, H. (2013) *Effects of multiple air gaps on the thermal performance of firefighter protective clothing under low-level heat exposure*, *Textile Research Journal* published online 12 December 2013. DOI: 10.1177/0040517513512403.
- [15] Lawson, L.K., Crown, E.M., Ackerman, M.Y., Dale, J.D. (2004). *Moisture Effects in Heat Transfer Through Clothing Systems for Wildland Firefighters*. *International Journal of Occupational Safety and Ergonomics (JOSE)*, 10(3), 227–238.
- [16] Petrilli, T., Ackerman, M. (2008). *Tests of Undergarments Exposed to Fire*. *Fire tech Tips*. Retrieved 30.05.2013 from Web site <http://www.fs.fed.us/t-d/pubs/pdfpubs/pdf08512348/pdf08512348dpi72.pdf>
- [17] ISO 11092:1993 - *Textiles - Physiological effects - Measurement of thermal and water-vapour resistance under steady-state conditions (sweating guarded-hotplate test)*. ISO: Geneva, Switzerland
- [18] Petrusic, S., Onofrei, E., Bedek, G., Dupont, D., Soulat, D. (2013). *Investigation of Thermal Comfort Properties of Firefighter Protective Clothing*. 4th ITMC Lille Metropole 2013 International Conference, ENSAIT, Roubaix, France.
- [19] http://www.osram.fr/media/resource/hires/333561/theratherm_siccattherm_infrared-en.pdf
- [20] Kothandaraman, CP. (2006). *Fundamental of heat and mass transfer*. 3rd ed. New Delhi: New Age International (P) Limited, 608.
- [21] Bartels, V. T. (2005). *Physiological comfort of sportswear*. In *Textiles in Sports*, Woodhead Publishing Limited, Cambridge.
- [22] Nomax, G.R. (1990). *Hydrophilic polyurethane coatings*. *Journal of Industrial Textiles*, 20:88. DOI: 10.1177/152808379002000205

Heat transfer simulation through textile porous media

Elena Codau, Teodor-Cezar Codau, Iuliana-Gabriela Lupu, Aliona Raru & Daniela Farima

To cite this article: Elena Codau, Teodor-Cezar Codau, Iuliana-Gabriela Lupu, Aliona Raru & Daniela Farima (2023) Heat transfer simulation through textile porous media, The Journal of The Textile Institute, 114:2, 257-264, DOI: [10.1080/00405000.2022.2027608](https://doi.org/10.1080/00405000.2022.2027608)

To link to this article: <https://doi.org/10.1080/00405000.2022.2027608>



Published online: 17 Jan 2022.



Submit your article to this journal [↗](#)



Article views: 675



View related articles [↗](#)



View Crossmark data [↗](#)



Citing articles: 8 View citing articles [↗](#)

Heat transfer simulation through textile porous media

Elena Codau, Teodor-Cezar Codau, Iuliana-Gabriela Lupu, Aliona Raru and Daniela Farima

Faculty of Industrial Design and Business Management, Technical University “Gheorghe Asachi” of Iasi, Iasi, Romania

ABSTRACT

Over the last decade, modelling of heat and mass transfer through textile materials has become a constant focus of researchers, the research being directly influenced by the development of computer systems. The importance of the heat transfer properties of clothing is particularly crucial in high-risk professions, such as firefighters and military, or in sportswear and healthcare. While some analytical and numerical models have been developed regarding these materials, most approaches are at the macroscopic level, where microscopic details are filtered out to reduce numerical and physical complexity. When the unsteady transfer occurs, the results can have significant errors. On the other hand, simulation is a cheaper method to obtain the static or dynamic characteristics of porous materials. This paper aims to model a simple textile structure and to perform a heat transfer simulation using Comsol Multiphysics®. Comsol Multiphysics® is a software that allows the simulation of physical phenomena using geometric models. By applying the standard boundary conditions, a comparison between the simulated and experimental values was made. To have a significant result for the entire system, the dimension of the sample was chosen so that it becomes a Representative Elementary Volume. Starting from the characteristics of the yarns and a geometric model of the textile structure, by simulation has been achieved the global characteristics of the material such as thermal resistance, porosity, heat flux and relative times for which the transfer becomes stationary. Global values were obtained by the volumetric average method using predefined functions in Comsol Multiphysics®.

ARTICLE HISTORY

Received 8 September 2021
Accepted 5 January 2022

KEYWORDS

Simulation; textiles; heat transfer; temperature; thermal resistance; heat flux

1. Introduction

The first significant model for textile heat transfer was developed and validated by Torvi (Łapka et al., 2016) for testing fabrics at high temperatures and open flame. The physical model is one-dimensional, the textile material is considered homogeneous and the mathematical equations refer to heat transfer through conduction and radiation. Mell and Lawson (Onofrei et al., 2015) take over the Torvi model but use multilayer textile structures used in protective clothing for firefighters.

Gibson (Song et al., 2008) proposes a model in which the textile material is considered a hygroscopic porous medium, coupling mass and heat transfer according to Whitaker's theory. The proposed mathematical model takes into account the conservation of momentum and energy and the continuity equation.

Prasad (Onofrei et al., 2015) developed a detailed mathematical model for studying non-stationary heat and moisture transfer through multilayer fabric assemblies with or without air gaps between the layers. The model shows the variation of the thermodynamic and transport properties of the fabric, due to the presence of water. The second-order differential equations are solved by the Runge-Kutta approximation method, and the results obtained proved to be comparable with the experimental measurements.

Recently, Łapka (Łapka et al., 2016) presents a more complex mathematical model of heat and moisture transfer through protective clothing for firefighters, taking into account the interaction with human skin. Heat transfer takes place through conduction and radiation being coupled with the diffusion of water vapour through porous media.

Currently, two approaches are highlighted in the simulation of heat and mass through porous materials, depending on the model scale: microscopic and macroscopic. Each of these two types of models comes with its working assumptions that directly influence the accuracy of the results and the costs of simulation.

Due to the large data storage and processing capacity involved in the microscopic model, in most cases, the macroscopic scale is preferred in simulations. However, the comparisons between the values from the macroscopic scale simulation and the results from the experiment revealed substantial differences in the transitory area (dynamic regime) for temperature, heat flow, etc.) (Onofrei et al., 2014). These differences are of particular importance in critical applications such as firefighting interventions, for steelworkers exposed to fire and very high temperatures, etc.

Over the last decade, due to the advances in computer science, the microscopic approach in simulating has become much more accessible.

In this study, a Direct Numerical Simulation (DNS) has been performed of heat flow over a three-dimensional textile

model at a microscopic scale and the results were compared with the results from a macroscopic approach simulation of the heat flow through textile.

To simulate heat transfer through textiles, Comsol Multiphysics® was used, which is a cross-platform software that allows modelling and simulation of physical processes based on Finite Element Method (FEM) (Comsol Inc, 2015). Comsol Multiphysics® has a large number of modules that allow solving engineering or scientific problems, with the possibility of coupling these modules. Due to the predefined models, the simulation is much easier. The emphasis is on the physical quantities and there is no need to define new equations.

To validate the model, the thermal resistance, R_{ct} , of a textile material obtained by simulation and experimentally determined according to ISO 11092-2014 were compared. Thus, the applied boundary conditions are similar to those corresponding to this standard method.

2. Theoretical consideration

Heat transfer through porous materials takes place in two ways: through the solid matrix and through the fluid in the voids. Through solid, heat is transferred by conduction mechanism and through the fluid by conduction, convection and radiation.

2.1. Conduction heat transfer

Thermal conduction is a mechanism of heat transfer that takes place within a thermodynamic system or between systems with thermal contact. Conduction is due to direct molecular interactions and does not involve a mass transfer. The equations of conduction heat transfer were deduced by Fourier in 1882, based on experimental results. Thus, it was established that the heat flux, ϕ , in any direction, is proportional to the temperature gradient in that direction. The coefficient of proportionality is called thermal conductivity, k , and is a tensor type. For homogeneous and isotropic materials, the thermal conductivity becomes a scalar with a constant value, and the Fourier law can be written as (Rathore, 2015):

$$\frac{\partial T}{\partial t} = \frac{1}{C_p \cdot \rho} \cdot k \cdot \nabla^2 T \quad (1)$$

where: k is thermal conductivity, ρ - density, C_p - thermal capacity, T - temperature, t - time variable and $\nabla^2 T$ - divergence of gradient temperature (Laplace operator).

It is also possible to define a thermal diffusion coefficient, a_t , which expresses the thermal inertia of the material:

$$a_t = \frac{k}{C_p \cdot \rho} \quad (2)$$

The equation (1) has an infinite number of solutions that define a curves family. To find a unique solution it is necessary to apply border conditions such as Dirichlet, Neumann or Fourier conditions.

2.2. Radiation heat transfer

The radiation heat transfer mechanism is based on electromagnetic waves. A thermodynamic system that has a temperature above absolute zero emits thermal radiation. The range of wavelengths that produce thermal effects starts from 0.1 μm (ultraviolet) to 100 μm (infrared). The relationship between emitted energy and temperature was deduced experimentally by Jozef Stefan and theoretically by Ludwig Boltzmann, using the virtual concept of the black body (Cengel & Ghajar, 2015):

$$E_b = \varepsilon \cdot \sigma \cdot T^4 \quad (3)$$

where: E_b is the emitted energy in unit time, per unit area, T is the temperature, σ - Stefan-Boltzmann constant and ε - the emissivity coefficient.

Heat exchange by radiation is a surface propriety and depends on temperature, optical properties and surfaces orientation. To define the influence of surface orientation the *shape factor* was introduced. The relationship between two shape factors of two opposite surfaces that emit and respectively receive thermal energy by electromagnetic waves is called the reciprocity theorem (F. M, 2013):

$$A_1 F_{1,2} = A_2 F_{2,1} \quad (4)$$

The $F_{1,2}$ shape factor by definition is (Cengel & Ghajar, 2015):

$$F_{1,2} = \frac{1}{A_1} \int_{A_1} \int_{A_2} \frac{\cos \theta_1 \cdot \cos \theta_2}{\pi \cdot \Delta x} \cdot dA_2 dA_1 \quad (5)$$

where: A_1 and A_2 are the emitting and respectively receiving surfaces of thermal radiation, θ_1 and θ_2 - the angles between the perpendicular direction to the surface and the direction of propagation and Δx - the distance. The $F_{2,1}$ shape factor has a similar expression.

For natural porous materials the shape factors are impossible to be calculated inside of the voids, but Song (Song, 2002) concluded that in the case of textiles, the heat transfer by radiation can be neglected due to very small voids dimension between the structural components (yarns/fibres).

2.3. Convection heat transfer

Convection is the mechanism of heat transfer associated with fluid mass transport. Depending on the factor that generates the movement, the convection type can be:

- free convection, when the flow is a result of temperature gradient;
- forced convection, due to a pressure gradient.

When the flow lines are parallel there is a laminar flow, otherwise, it is turbulent flow. The law of thermal convection was deduced by Newton and has the following form:

$$\frac{\dot{Q}}{S} = h_t \cdot (T_s - T_\infty) \quad (6)$$

where: \dot{Q}/S is the heat flow, h_t - the thermal convection coefficient, T_∞ - the fluid temperature and T_s - the temperature on the border.

The convection coefficient includes all factors on which the heat transfer depends: the fluid properties, surface geometry, flow type (Bejan, 2013). For most porous materials this coefficient is impossible to be calculated or experimental determined. For that reason, the similarity and boundary layer theory are necessary. Thus, at the border between solid and fluid, it is considered that the heat transfer takes place by conduction on a very thin boundary layer characterized by thermal resistance and a certain thickness. According to Yunus Cengel (Cengel & Ghajar, 2015), free or natural convection is associated with Rayleigh number (Ra) that characterizes the fluid's flow regime:

$$Ra = Pr \cdot Gr \quad (7)$$

where Gr is the *Grashof number* and Pr is the *Prandtl number*.

The *Grashof number* is a dimensionless number definite by (Cengel & Ghajar, 2015):

$$Gr = \frac{g \cdot \beta_v \cdot \Delta T}{\nu^2} L_{ch}^3 \quad (8)$$

where: g is the gravitational acceleration, β_v - the coefficient of thermal expansion, ΔT - the difference between surface temperature T_s and bulk temperature T_∞ , L_{ch} - the characteristic length and ν - the kinematic viscosity.

For ideal gases the β_v can be approximated with:

$$\beta_v \approx \frac{1}{T} \quad (9)$$

On the other hand (Cengel & Ghajar, 2015):

$$Pr = \frac{C_{p,a} \cdot \mu_a}{k_a} \quad (10)$$

where: μ_a is the dynamic viscosity of air, $C_{p,a}$ - the specific heat capacity and k_a - the thermal conductivity.

Dynamic or absolute viscosity (μ_a) is a measure of the viscosity of a fluid and is directly proportional to the shear stress, while kinematic viscosity (ν) is defined as the absolute viscosity of a liquid divided by its density at the same temperature, $\nu = \mu_a/\rho$.

Thus, the *Rayleigh number* becomes:

$$Ra = \frac{\rho^2 \cdot g \cdot \beta_v \cdot C_{p,a}}{\mu_a \cdot k_a} \cdot L_{ch}^3 \cdot \Delta T \quad (11)$$

The *Rayleigh number* (Ra) characterizes the fluid's flow regime:

- $Ra > 10^9$ denotes a turbulent flow;
- $10^3 < Ra < 10^9$ denotes a laminar flow;
- $Ra < 10^3$ denotes that convection can be neglected.

Thus, to determine if there is a convection phenomenon, it is important to calculate the Rayleigh number, Ra .

For the woven textile structure shown in Figure 1, the characteristic length L_{ch} is difficult to be calculated, but the hypothesis of forces acting on a channel (tube) tangentially limited by the warp and weft yarns was considered. Thus, the characteristic length can be replaced with the equivalent hydraulic diameter, d_h (Incropera et al., 2011):

$$d_h = \frac{4 \cdot A}{C_s} \quad (12)$$

where A is the area of the channel section and C_s is the perimeter of the section.

The section of this channel is obtained by projecting in a horizontal plane the gap between the yarns of the textile structure. The area and the perimeter of the section were calculated by the integrals provided by Comsol Multiphysics®. An area of 0.193 mm² and a perimeter of 1,762 mm were thus obtained. By replacing the numerical values in equation (12), an equivalent diameter $d_h = 0.44$ mm resulted.

According to the tables with the properties of air in the literature (Engineering-ToolBox, 2022), the following values were also used in equation (11):

- $\mu_a = 1.85 \cdot 10^{-5}$ [kg/ms] - the dynamic viscosity of air;
- $C_{p,a} = 1049$ [J/kgK] - the specific heat capacity;
- $k_a = 0.026$ [W/mk] - the thermal conductivity;
- $\rho = 1.2$ [kg/m³] - the air density;
- $\beta_v = 0.003$ [K⁻¹] - the coefficient of thermal expansion.

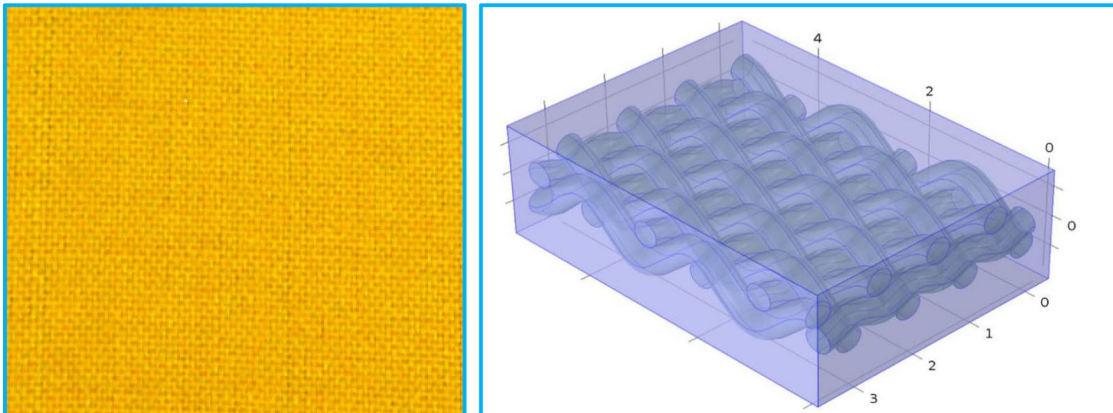


Figure 1. Woven fabric structure and 3D geometrical model.

and the *Rayleigh number* $Ra = 0.131$ was obtained. Since this value is very small, the thermal convection can be neglected, thus the conduction heat transfer is predominantly through textiles.

2.4. Method description

In this paper, a Direct Numerical Simulation (DNS) has been performed of heat flow over a three-dimensional textile model at a microscopic scale and the results were compared with the results from a macroscopic approach simulation of the heat flow through textile.

DNS is based on the theory of Richard Courant, who proposed a new approach to the phenomena that take place in physical systems: the finite element method (FEM) (Courant, 1943). The method consists in dividing the system into small domains (discretization), linked together by nodes. Unlike the Rayleigh-Ritz method that seeks a system-wide function that satisfies boundary conditions, by FEM these functions are defined on simple geometric elements and are approximated by values at each node of the discretization network. The evaluation of such functions requires a large volume of algebraic computation and, for this reason, the importance of the FEM was highlighted only after 1973, being linked to the evolution of electronic computers (Strang & Fix, 2008).

DNS is the most accurate method of simulating mass and heat transfer. However, the accuracy of the method involves high costs in terms of resource allocation (Antonia et al., 2017). The porous materials, being complex systems in which the geometry of the solid matrix is not fully known, require the use of DNS simultaneously with other methods such as volume-averaged Navier–Stokes (VANS) equations, Reynolds-averaged equations or statistical methods.

Even if the geometric model of the solid matrix is very close to the porous material structure its size has generated major problems related to the allocated software resources and the accuracy of the results. To reduce the costs of simulation without influencing the accuracy of the results, Whitaker proposes the use of a Representative Elementary Volume (REV) (Sbutega et al., 2015).

The Representative Elementary Volume is the smallest volume of a material that can be measured, provided that the values must be representative of the entire system. The dimensions of the elementary volume must be much larger than the geometric characteristics of voids, but at the same time considerably smaller than the entire studied area (Groşan, 2012).

Whitaker defines the average volumetric operator, $\langle \Psi \rangle$, for any scalar, vector, tensor Ψ (Whitaker, 1999):

$$\langle \Psi \rangle = \frac{1}{V} \int_V \Psi \cdot dV \quad (13)$$

The average volumetric operator is a smooth function for dimensions larger than REV and obeys the relationship:

$$\langle \langle \Psi \rangle \rangle = \langle \Psi \rangle \quad (14)$$

3. Geometric model of the textile structure

For the microscopic three-dimensional model, a simple woven fabric structure was chosen (Figure 1).

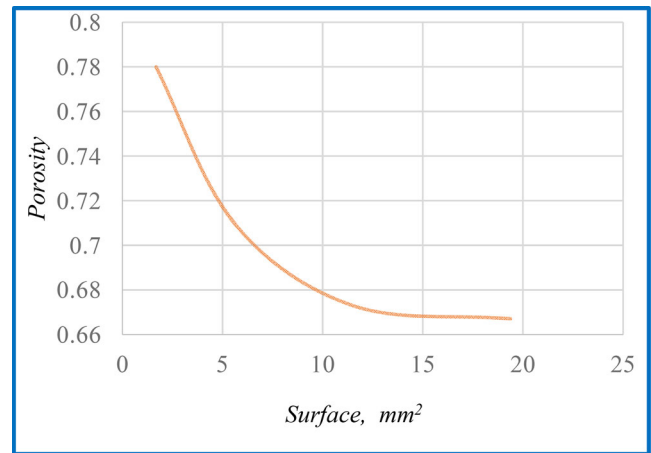


Figure 2. Variation of local porosity depending on the textile material surface.

The woven fabric is made from aramid yarns containing: 93% Nomex[®], 5% Kevlar[®] and 2% PA (antistatic). The water vapour resistance of the textile structure, determined in standard condition (ISO 11092-2014) is $R_{et} = 5.76$ (m²·Pa/W). The yarn diameters are d_u for warp and d_b for weft. To determine the density of the fabric, the distance between yarns, numbers of yarns and the wave's relative amplitude were taken into account.

Due to the complex phenomena that occur during the heat transfer through the porous materials a very fine meshing is recommended that involves additional costs with the simulation. According to Whitaker's theory (Whitaker, 1999), one can choose an "elementary volume" that characterizes the porous material. By definition, the dimensions of this elementary volume are chosen so that the properties of the material become relatively constant. The most important property that influences all characteristics of the porous media is the porosity and it is taken into account when determining the size of the sample.

Thus, using the porosity definition and the volumetric integration functions the porosity variation depending on the surface area of the textile material was determined. The results are shown in Figure 2. It can be seen that for a surface area larger than 15 mm², the porosity becomes relatively constant. To avoid the problems regarding meshing on the borders, an integer number of yarns have been chosen.

4. Results and discussions

4.1. Simulation of heat transfer in stationary conditions

Taking into account the analysis presented above, the material properties and the boundary conditions from ISO 11092-2014, a Comsol Multiphysics[®] simulation of heat transfer was performed through the textile sample from Figure 1, under steady-state conditions.

The temperature fields for outer borders are shown in Figures 3 and 4, respectively. The heat flux under the same conditions is shown in Figure 5.

In this case, according to the ISO 11092-2014 standard, there is no additional pressure on the surface of the textile material, which is placed on the metal plate maintained at a

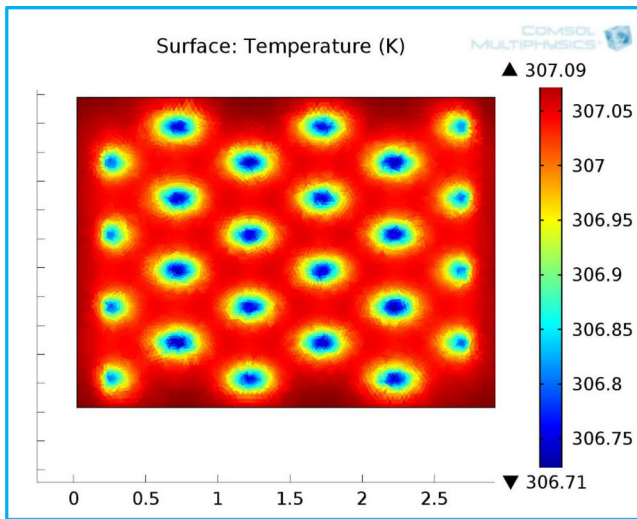


Figure 3. Local temperature under steady-state condition on the lower border.

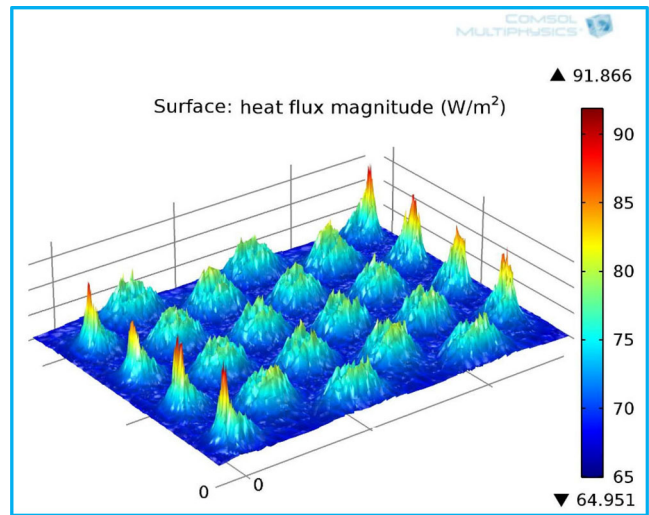


Figure 5. Heat flux under steady-state condition.

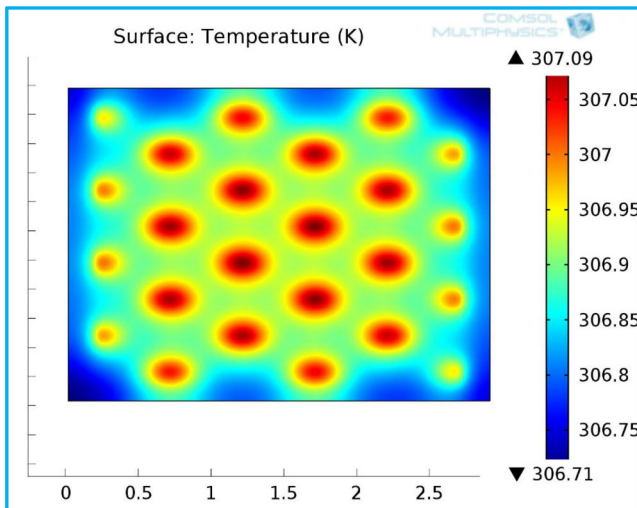


Figure 4. Local temperature under steady-state condition on the upper border.

constant temperature. The contact between the textile material and the plate is made in "contact areas". Analyzing the graphical results, it can be seen that the areas where the heat transfer has maximum intensity take the shape of "contact spots" for the temperature field, corresponding to the "contact areas". In these areas, heat flux values increase by more than 50% (Figure 5).

The "contact areas" surface increase if pressure is applied to the boundary surfaces of the textile. The pressure applied to the surface of the fabrics differs from one standard device to another and this explains why the thermal properties of textiles vary depending on the standard used.

The temperature fields and the heat flow provide information on the maximum and minimum values as well as the distribution mode. Usually, in calculations, global values are used. In Comsol simulation these values can result by mediation on a certain field.

Using the volume averaging method the following values were obtained:

- $T_{in} = 307.8797$ K, the average temperature on the lower border;
- $T_{out} = 306.9641$ K, the average temperature on the upper border;
- $\Phi_{med} = 67.998$ W/m², the average heat flow.

To calculate the effective thermal resistance of the textile material, R_{ct} , the following equation was used:

$$R_{ct} = \frac{\Delta T}{\Phi_{med}} \quad (15)$$

where $\Delta T = T_{in} - T_{out}$ is the difference between the average boundary temperatures and ϕ_{med} is the average heat flow.

By replacing the numerical values in equation (15), the thermal resistance of $R_{ct} = 0.0135$ W/mK was found. Comparing this value with the standard thermal resistance $R_{ct} = 0.0128$ W/mK (ISO 11092-2014) an error of 5.2% results.

These differences are acceptable taking into account the working assumptions:

- The 3D model used is an ideal representation of the textile structure, in which the yarns of the fabric are considered to have a uniform section. In reality, the section of the yarns is not uniform, and the contact between yarns take place on larger surfaces, depending on the yarn twist, tensions of the yarns etc.
- The heat transfer by thermal radiation as well as the mass convection through voids was neglected.

4.2. Simulation of heat transfer in dynamic conditions

For unsteady regime (dynamic), two simulations of heat transfer through textile material were performed, under the conditions of ISO 11092-1014. The first simulation takes into account the microscopic structure (a three-dimensional model) and the second one (macroscopic scale) considers the homogeneous and isotropic textile material, with the

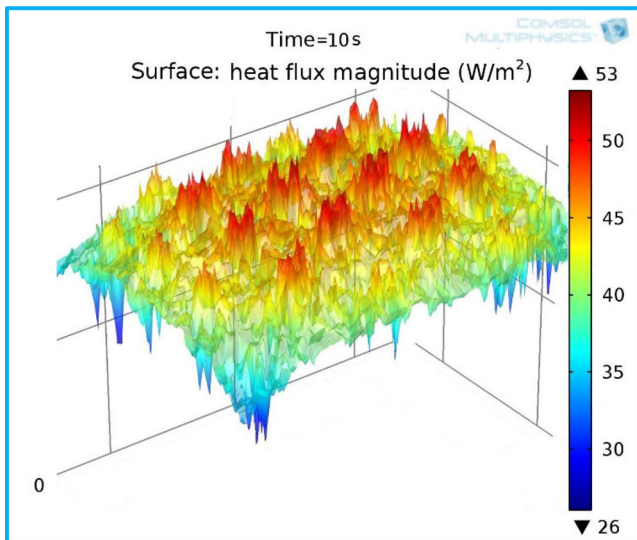


Figure 6. Variation of heat flux through the textile material, in dynamic regime at time $t = 10$ s, on the upper border.

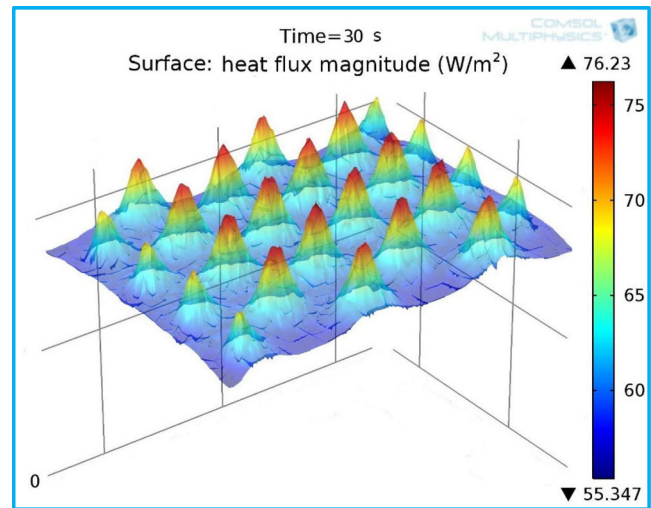


Figure 7. Variation of heat flux through the textile material, in dynamic regime at time $t = 30$ s, on the upper border.

global properties obtained by standard determinations. For the microscopic simulation, the local values of the heat flux at different simulation times (10 s and 30 s) on the upper border are shown in Figures 6 and 7, respectively. The average heat flux variation for both microscopic and macroscopic simulations are shown in Figure 8.

From Figure 8 it is found that, for the two simulation models, the heat flow has a relatively similar evolution over time, but there are differences in the transition area. Even if the differences between the absolute values are not very large, the percentage differences at a certain time are significant, reaching 9% in the first part of the transfer process and gradually reducing to 0.1% towards the end of the process when the steady-state is reached (Figure 9).

Textiles are porous materials made of air gaps (fluid) and fibres (solid medium) and the heat transfer phenomenon takes place through and between two totally different environments. Therefore, the internal geometry of the system plays an important role in the dynamic of heat transfer, in addition to its thermal properties and external conditions. The macroscopic approach considers the textile material homogeneous, while the microscopic approach takes into account the existence and the interaction between these two media (fluid and solid). For this reason, in the transient regime, there are differences in terms of heat transfer between the two models: macroscopic and microscopic. These differences are important for applications such as protection against burns.

Stoll and Chianta (Stoll & Chianta, 1969) have quantified the reaction of human skin based on the time of exposure to a certain amount of heat flux. Thus, an important parameter to be considered is the time after which a heat flux reaches a certain value. This time estimated by the two simulation methods differs, depending on the approached scale (microscopic or macroscopic). The differences between the microscopic and macroscopic simulations for the estimated time after which a heat flux reaches a certain value are shown in Figure 10.

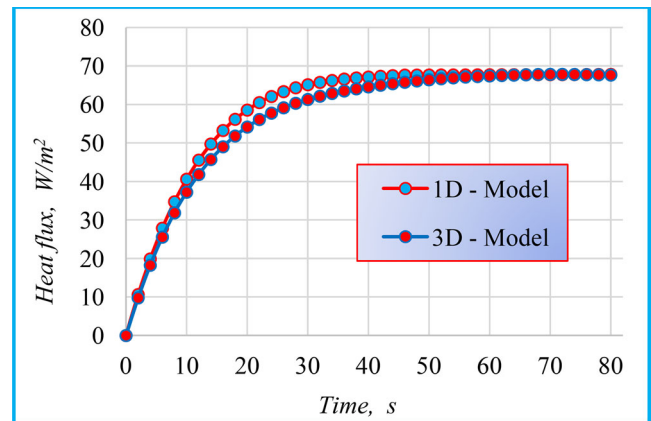


Figure 8. Heat flux through the textile material in the dynamic regime.

The difference increases with the increase of heat flow and the maximum value exceed 30%. This result demonstrates that the “thermal inertia” of the system has a different value depending on the microscopic or macroscopic approach, influencing the prediction of the thermal protective performance (TPP) and the estimated time of onset of the second-degree skin burn.

5. Conclusions

Simulation is a fast and less expensive method to obtain the heat transfer characteristics through porous materials. The simulation results have higher accuracy in the case of microscopic scale but in the textile field, this approach has not been used so far due to the very large resources required. By using Whitaker’s theory and averaging on Representative Elementary Volume, the software resources required has been greatly reduced.

Using the Comsol Multiphysics® application, the heat transfer simulation was performed through a woven fabric for both microscopic and macroscopic scales.

At steady-state, the average heat flow through the textile has a constant value and it was used to determine the

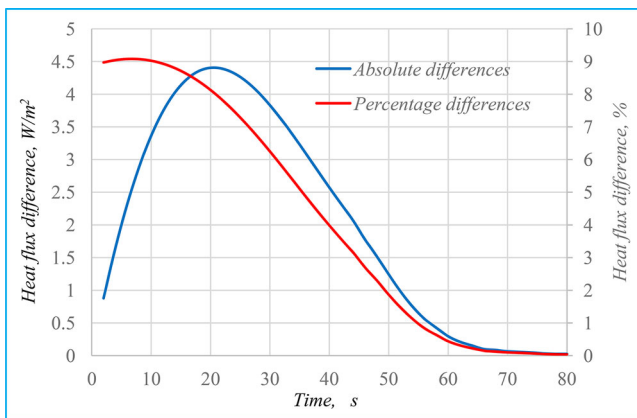


Figure 9. Differences in heat flux through the textile material between the microscopic model and the macroscopic model.

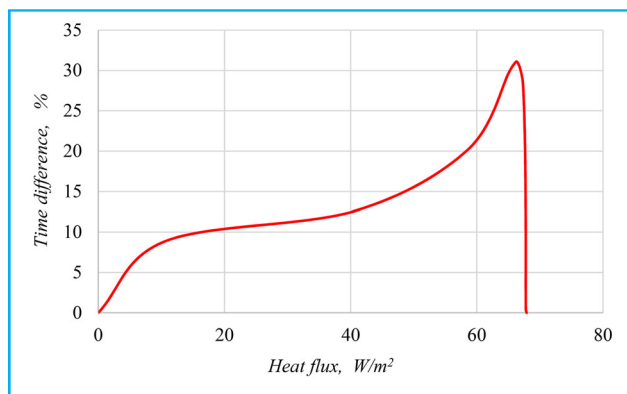


Figure 10. The differences between the estimated time after which the heat flux reaches a certain value.

thermal resistance of the textile material. The value obtained has a deviation of 5.2% from the thermal resistance determined according to ISO 11092-1014.

The heat transfer simulation in dynamic conditions confirms that the scale at which the modelling is conducted influences the value of heat transfer characteristics. Thus, the average heat flux in the transition zone under the conditions of ISO 11092-2014, can register a difference of up to 9%, for the two simulation methods - microscopic and macroscopic scale.

Moreover, the estimated time after which the heat flux reaches a certain value depends on the approach scale, the maximum difference being over 30%. That has a particular interest in the case of protective clothing for firefighters exposed to radiative heat sources. The estimated thermal protective performance (TPP) and the predicted time after which second-degree skin burn occurs depend on the approached modelling scale.

6. Future work and perspectives

The future research will focus mainly on:

- Extending the simulation to complex textiles structures using different types of yarn section models. Because Comsol Multiphysics® has only basic geometric tools,

new software modules like LiveLink™ for SOLIDWORKS® are required. This interface includes functionality to import/export and even link CAD files with Comsol Multiphysics® models.

- Performing the mass transfer simulation through textiles and coupling the mass transfer with heat transfer that occurs simultaneously.
- Parameterization of geometric models to optimize textile structures in terms of heat and mass transfer.

Acknowledgements

Thanks to HEI for the resources provided under the Erasmus + program, especially for Comsol Multiphysics®.

Disclosure statement

No potential conflict of interest was reported by the authors.

Funding

This work was supported by a publication grant of the TUIASI, project number GI/P 24/2021.

References

- Antonia, R. A., Djenidi, L., Danaila, L., & Tang, S. L. (2017). Small scale turbulence and the finite Reynolds number effect. *Physics of Fluids*, 29(2), 020715. <https://doi.org/10.1063/1.4974323>
- Bejan, A. (2013). *Convection heat transfer* (4th ed., Vol. 1). John Wiley & Sons.
- Cengel, Y., & Ghajar, A. (2015). *Heat and mass transfer: Fundamentals and applications* (5th ed., Vol. 1). McGraw-Hill.
- Comsol Inc. (2015). *Introduction to COMSOL Multiphysics®*. [Online]. <https://www.comsol.com/documentation>.
- Courant, R. (1943). Variational methods for the solution of problems of equilibrium and vibrations. *Bulletin of the American Mathematical Society*, 49(1), 1–23. <https://doi.org/10.1090/S0002-9904-1943-07818-4>
- Engineering-ToolBox. (2022). *engineeringtoolbox.com*. https://www.engineeringtoolbox.com/dry-air-properties-d_973.html.
- F. M, M. (2013). *Radiative heat transfer*. Elsevier.
- Groșan, T. (2012). *Modelarea matematică a fenomenelor convective în mediile poroase* (Vol. 1), Ed. C. C. D. Știință. Casa cărții de știință.
- Incropera, P. F., Dewitt, P. D., Bergman, L. T., & Lvine, S. A. (2011). *Fundamentals of heat and mass transfer* (7th ed.). John Wiley & Sons.
- Łapka, P., Furmański, P., & Wisniewski, T. S. (2016). Numerical modelling of transient heat and moisture transport in protective clothing. *Journal of Physics: Conference Series*, 676, 012014. <https://doi.org/10.1088/1742-6596/676/1/012014>
- Łapka, P., Furmański, P., & Wiśniewski, T. S. (2016). Analysis of influence of different heat transfer modes on temperature distribution in the protective clothing and skin. *Procedia Engineering*, 157, 72–81. <https://doi.org/10.1016/j.proeng.2016.08.340>
- Onofrei, E., Codau, T. C., Petrusic, S., Bedek, G., Dupont, D., & Soulat, D. (2014). Simulation and modeling of heat and mass transfer through fabrics exposed at low-level thermal radiation. " In *7th International Textile, Clothing & Design Conference – Magic World of Textiles* (pp. 418–423). Croatia.
- Onofrei, E., Petrusic, S., Gauthier, B., Dupont, D., Soulat, D., & Codau, T. C. (2015). Study of heat transfer through multilayer protective clothing at low-level thermal radiation. *Journal of Industrial Textiles*, 45(2), 222–238. <https://doi.org/10.1177/1528083714529805>

- Rathore, M. (2015). *Engineering heat and mass transfer* (3rd ed.). Laxmi Publications.
- Sbutega, K., Geb, D., & Cotton, I. (2015). *Advances in heat transfer*. Eds. E. Sparrow, J. Abraham, and J. Gorman. Academic Press Publications-Elsevier.
- Song, G., Chitrphimsri, P., & Ding, D. (2008). Numerical simulations of heat and moisture transport in thermal protective clothing under flash fire conditions. *International Journal of Occupational Safety and Ergonomics: Jose*, 14(1), 89–106. <https://doi.org/10.1080/10803548.2008.11076752>
- Song, G. (2002). *Modeling thermal protection outfits for fire exposures* [PhD thesis]. North Carolina State University. <https://repository.lib.ncsu.edu/handle/1840.16/5766>.
- Stoll, A., & Chianta, M. (1969). Method and rating system for evaluation of thermal protection. *Aerospace Medicine*, 40(3).
- Strang, G., & Fix, G. (2008). *An analysis of the finite element method, new edition* (2nd ed., p. 400). Wellesley-Cambridge Press.
- Whitaker, S. (1999). *The method of volume averaging*. Kluwer Academic Publishers.

RESEARCH ARTICLE



Research on monitoring the transfer of water vapors through textile materials using humidity sensors

Elena Codau^a, Teodor-Cezar Codau^{a,b}, Aliona Raru^a and Daniela Farima^a

^aFaculty of Industrial Design and Business Management, Technical University “Gheorghe Asachi” of Iasi, Iasi, Romania; ^bFibrenamics, University of Minho, Guimaraes, Portugal

ABSTRACT

The ability of textile materials to transfer water vapor greatly influences the protective and comfort functions of clothing. In order to appreciate the water vapor transfer capacity, standard methods have been defined, but these standardized methods have also some drawbacks. One of these drawbacks is the fact that the environmental conditions for determining the standard characteristics greatly differ from the real operating conditions, which are mostly dynamic. This paper proposes a method for dynamic monitoring of water vapor transfer through multilayer textile assemblies using relative humidity sensors. In addition, the method offers the possibility to determine the water vapor resistance of the textile materials with good accuracy and at a much lower price than using the standard ISO 11092 – 2014. These humidity sensors can be an important component of smart wearable electronic textiles and have potential applications in healthcare in the management of wounds, bed-wetting, and skin pathologies or for microclimate control in clothing for military, firemen, athletes, etc.

ARTICLE HISTORY

Received 6 September 2021
Accepted 12 January 2023

KEYWORDS

Protective textiles;
multilayer textile structures;
relative humidity sensors;
water vapor flow; water
vapor resistance

1. Introduction

In recent years, new functional textiles have been developed, called “smart textiles”, and the market growth rates of these products are climbing over 35%. In this category of products, those that emerge from the combination of textiles and electronics are called “electronic textiles” and have a very wide range of applications, such as technical textiles for the automotive industry, houses and industry, healthcare, military, firefighters, and sport (Kinkeldei et al., 2011). Such electronic textiles can be used to measure the body’s microclimate, that is, temperature and humidity.

To be able to compare textiles in terms of the ability of vapors transfer, standards have been created over time and physical characteristics have been defined, between which certain correlations can be established (Codau et al., 2015). These methods are essentially static laboratory methods, conducted in very well-established environmental conditions (Midha, 2016). In reality, clothing is used in a constantly changing environment and balance is rarely achieved. Moreover, due to the anatomical shape of the human body, additional layers of air are formed between the textile material and the body and between the textile layers that modify the clothing structure and consequently the water vapor transfer conditions.

The first studies on the transfer of moisture through textiles were carried out on firefighters’ clothing in the context of its influence on the degree of protection, but the results obtained were contradictory (Chen, 1959; Lee & Barker, 1984; Mäkinen et al., 1988). These studies are based on mathematical models

and some researchers consider that these diverse results are due to the fact that many other influencing factors were not taken into account (Rossi & Zimerli, 1996; Keiser et al., 2008).

The advent of low-cost microcontrollers and the miniaturization of electronic devices have given new impetus to research into mass and heat transfer in textiles, leading to the creation of smart textiles capable of providing real-time values that characterize moisture or heat transfer (Koncar, 2016).

Currently, there are two directions of the development of moisture wearable sensors: the use of general-purpose sensors attached to the textile material and the development of textile-based humidity sensors using printing and coating (Martínez-Estrada et al., 2019).

Jerzy Weremczuk et al. in (Weremczuk et al., 2012) presented a humidity sensor that was directly printed on a textile using ink-jet printing technology. These sensors were tested in a controlled environment at 25 °C and 5%–95% of RH. The measured impedance shows a non-linear distribution over the range from 40% to 95% of RH and low long-term stability.

A stretchable and printable humidity sensing micro composite was developed by Yusuke Komazaki and Sei Umemura (Komazaki & Uemura, 2019). Sakandar Rauf et al. (Sakandar et al., 2020) used the Langmuir-Blodgett technique for the deposition of a thin film directly onto the fabrics containing interdigitated textile electrodes for the fabrication of a highly selective humidity sensor. The humidity sensors were made from two different types of textiles, namely, linen and cotton, but after 3 weeks of storage, the sensors showed a moderate decrease in response.

Remarkable results in terms of the integration of wearable humidity sensors were obtained by Bi Siyi et al. (Siyi et al., 2021), Pi-Guey Su and Chun-Fu Chang (Su & Chang, 2018). Michal Frydrysiak (Frydrysiak, 2020) made a comparison study of textile-based humidity sensors made by sputtering, printing, and embroidery techniques.

Although textile-based humidity sensors have gained a great advantage in the last time, the scale of measurements does not cover the entire range of humidity, from 0 to 100%. On the other hand, these sensors cannot be used to determine the humidity gradient. Other drawbacks of these sensors are their long-term stability, low resistance for bending, stretching, and “laundryability” (washing resistance).

For these reasons, general-purpose sensors with small dimensions (SMDs) that have a measurement scale between 0% and 100% are equally used for electronic textiles.

The research reported so far, in which relative humidity sensors have been used, is limited to the simple detection of humidity and not to the real-time monitoring of the water vapor flow through textile materials.

In this article, small-scale capacitive humidity sensors were used to determine the water vapor resistance of textile materials and for monitoring the water vapor flow through multilayer textile assemblies.

2. Theoretical considerations

Assuming that the textile material can be considered a homogeneous structure, the diffusion coefficient can be considered a constant of the material, depending only on the temperature. According to Fick’s law, the diffusion flux at equilibrium, $\Phi(T)$, at temperature T , is

$$\Phi(T) = D(T) \cdot M \cdot \frac{\Delta c_i}{\Delta x}, \quad (1)$$

where

- $D(T)$ is the diffusion coefficient, temperature-dependent;
- Δc_i is the variation in concentration on the distance Δx ; and
- M is the molar mass.

According to the equation of the state of a gas, it can be written:

$$c_i = \frac{p_i}{R \cdot T}, \quad (2)$$

where

- p_i is the partial pressure of constituent i ;
- R is the universal gas constant; and
- T is the temperature.

Substituting (2) in Equation (1) results in

$$\Phi(T) = D(T) \cdot M \cdot \frac{\Delta p_i}{\Delta x} \cdot \frac{1}{R \cdot T}, \quad (3)$$

where Δp_i represents the partial pressure variation in the constituent i and Δx represents the distance of variation.

For water vapor passing through a textile material of thickness L_f , Equation (3) can also be written in the following form:

$$\Phi(T) = \frac{D(T)}{L_f} \cdot \frac{\Delta p}{R_{H_2O} \cdot T}. \quad (4)$$

The effective diffusion of water vapor through a textile material, $D_{ef}(T)$, depends on the diffusion coefficient of water vapor in the air, $D_a(T)$, the effective porosity, φ , and the tortuosity, τ . According to T.C. Codau et al. (Codau et al., 2015) for a given temperature value T_{35} , for the effective diffusion the following equation was found:

$$D_{ef}(T_{35}) = D(T_{35}) \cdot \frac{\varphi}{\tau} \quad (5)$$

from where it can be deduced:

$$D_{ef}(T) = D_{ef}(T_{35}) \cdot \frac{D_a(T)}{D_a(T_{35})} \quad (6)$$

The effective diffusion of water vapor at 35 °C can be written as (Codau et al., 2015):

$$D_{ef}(T_{35}) = \frac{L_f}{R_{et}} \cdot \frac{R_{H_2O} \cdot T_{35}}{\lambda_{H_2O}(T)}, \quad (7)$$

where R_{et} represents the water vapor resistance of the textile material determined according to ISO 11092 – 2014.

From the Equations (6) and (7) it results

$$D_{ef}(T) = \frac{D_a(T)}{D_a(T_{35})} \cdot \frac{L_f}{R_{et}} \cdot \frac{R_{H_2O} \cdot T_{35}}{\lambda_{H_2O}(T)}. \quad (8)$$

In these conditions, the Equation (4) becomes

$$\Phi(T) = \Delta p \cdot \frac{1}{R_{et} \cdot \lambda_{H_2O}(T)} \cdot \frac{D_a(T)}{D_a(T_{35})} \cdot \frac{T_{35}}{T}. \quad (9)$$

According to the definition of relative humidity

$$RH\% = \frac{p_v}{p_{sat}(T)} \cdot 100\%, \quad (10)$$

and the Equation (9) can also be written as

$$\Phi(T) = \Delta RH \cdot p_{sat}(T) \cdot \frac{1}{R_{et} \cdot \lambda_{H_2O}(T_{35})} \cdot \frac{D_a(T)}{D_a(T_{35})} \cdot \frac{T_{35}}{T}, \quad (11)$$

where

- $\Phi(T)$ is the water vapor flow at temperature T ;
- ΔRH is the unit variation of the relative humidity between the two surfaces of the textile material;
- $p_{sat}(T)$ is the saturation pressure of water vapor at temperature T ;
- R_{et} is the water vapor resistance;
- $\lambda_{H_2O}(T_{35})$ is the latent heat of evaporation of water at 35 °C;
- $D_a(T)$, $D_a(T_{35})$ is the the coefficients of water vapor diffusion in the air, at the temperature T , respectively, T_{35} ;
- T_{35} is the the temperature in K, corresponding to the temperature of 35 °C.

Equation (11) represents the relationship between the water vapor flow, $\Phi_f(T)$, and the water vapor resistance, R_{et} . The

humidity gradient is a boundary condition and can be measured using specialized sensors. As can be seen, the saturation pressure and the diffusion coefficient of water vapor in the air are temperature-dependent, and the temperature can be monitored using thermal sensors (thermocouples). These values are known from the literature (tables) or can be approximated by empirical functions (Wagner & Pruß, 2002). For not very large temperature variations, these parameters do not change significantly.

In conclusion, by measuring the relative humidity with two sensors and knowing the environmental conditions, the rate of water vapor transfer can be determined using Equation (11). Equation (11) can be also used to determine the evaporation resistance R_{ev} , as a function of the state parameters: temperature and humidity. This is of particular importance in the case of hydrophilic membranes, which have a variable water vapor resistance depending on the relative humidity. The existing standardized methods cannot determine the law of variation of water vapor resistance depending on the humidity gradient due to the strict conditions for performing the experiments.

An important observation must be made regarding Equation (11), namely, the relative humidity taken into account is that on the boundary of the textile material considered as a homogeneous porous medium. If convection phenomena occur at one of these boundaries, the external humidity sensor will provide values closer to the relative humidity of the environment, and Equation (11) will have a more complex form that takes into account the convective phenomenon (Codau et al., 2015).

The application of Fick's law is possible as long as there are no external pressure and the mass transfer can be considered only by diffusion (inertial components or shear forces are negligible).

3. Experiments

3.1. Calibration of humidity sensors

Capacitive humidity sensors were used to monitor the water vapor transfer through textile materials and for water vapor

resistance determination. The operating principle of a capacitive sensor is that it changes its electrical capacity depending on the humidity of the environment. Two moisture sensors CV1 and CV2 of the KFS 140-M SMD type were selected for the following reasons (Reichelt Elektronik):

- large humidity measuring range (between 0% and 100%);
- high thermal stability;
- high resistance to chemical vapors;
- reduced reaction time;
- complete recovery after condensation;
- very small overall dimensions ($4 \times 2 \times 0.38$ mm)

The drawback of this type of sensor is that they must be calibrated individually and the measurement of very small electrical capacities (of the order pF) is not easy. It is difficult to directly measure the value of the electrical capacity of these sensors and for this reason an analog C/V-converter CAV444 can be used, combined with the IC AM411 (Analog Microelectronics). The sensor systems built with this combination are protected against short circuit and has an output voltage between 0 and 10 V (Figure 1).

To calibrate the humidity sensors, it is necessary to have a strictly controlled humidity environment. Using saturated solutions is the most accurate method but it is difficult to perform a large number of determinations evenly distributed over the range of 0%–100% RH. However, it is often more practical to use calibrated instruments. A device using such an instrument (TESTO 435 probe) was made for this purpose and is shown in Figure 2.

The TESTO 435 probe (Testo SE & Co. KGaA) and an assembly of three enclosures were used. The first chamber contains a sufficient amount of silica gel to reduce the relative humidity to 0%, in the second chamber are placed the Testo 435 probe and the humidity sensor and the third chamber contains distilled water. By manipulating the two valves, in the middle enclosure humidity between 0% and 100% was obtained. The relative humidity values were provided by the probe of the TESTO 435 apparatus and the corresponding voltage values were provided by two electronic C/V-converter circuits CAV444 (Figure 1).

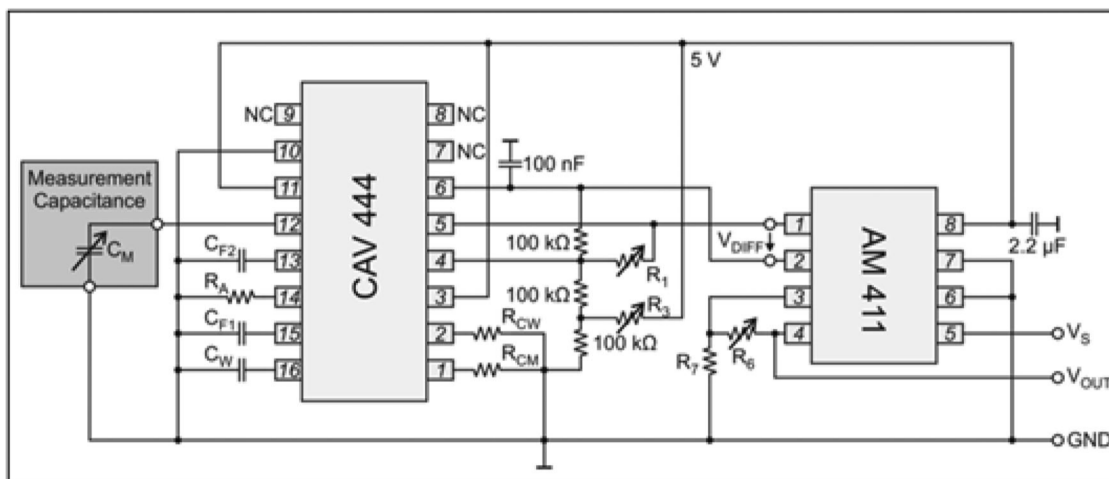


Figure 1. CAV444 with single input capacitance and adjustable (Analog Microelectronics), analog voltage output.

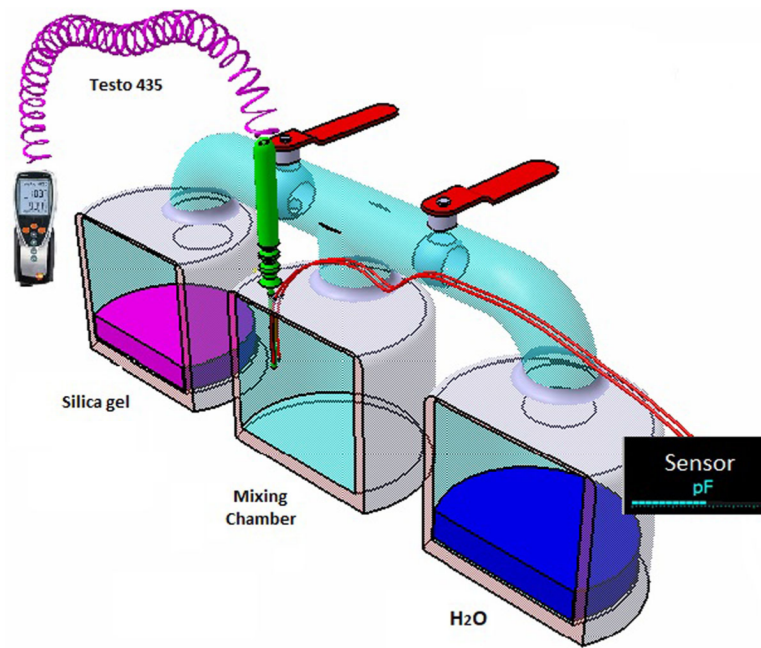


Figure 2. Device for humidity sensor calibration using TESTO 435 probe.

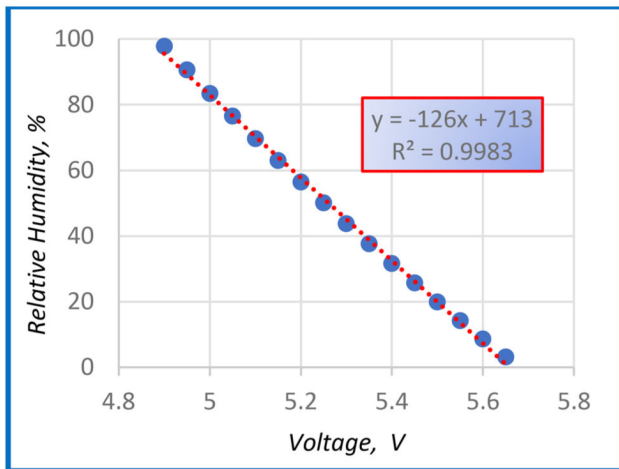


Figure 3. CV1 sensor calibration.

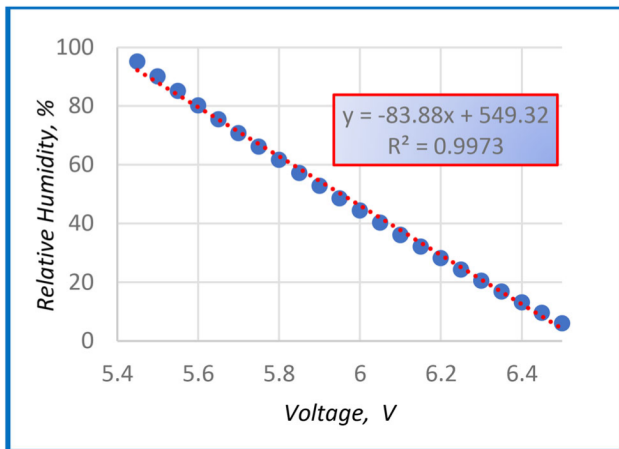


Figure 4. CV2 sensor calibration.

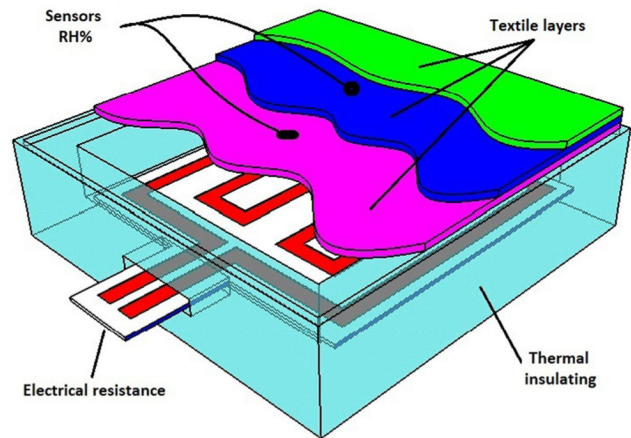


Figure 5. Device for measuring the transfer of water vapors through textile materials.

The results from the experiments are shown in the following calibration graphs (Figures 3 and 4).

The measured voltage versus humidity for both sensors show a linear distribution over the range from 0 to 100% RH, but individual calibration of the sensors is required.

3.2. Description of method and device

In order to perform the experiments, the device from Figure 5 was built. It consists of

- copper chamber, having the dimensions of $92 \times 92 \times 10$ mm;
- thermal insulation (extruded polystyrene);
- flat electrical resistance;
- type E temperature sensors (Omega Engineering);
- relative humidity sensors CV1 and CV2 attached to the outside of the inner textile layer.

The experimental system also contains the following components:

- Mettler Toledo ML 1602 precision electronic balance;
- two electronic modules (Figure 1);
- LabX Direct Balance 2.4 and Excel 2010;
- Data Acquisition System (DAQ-NI USB 6009);
- computer.

Two textile assemblies AsT1 and AsT2 were used for the experiments. These textile assemblies are used in firefighter clothing and consist of three textile layers, where the inner layer is S1 and S2, respectively. S1 is a woven fabric made of 93% m-aramid (Nomex®) + 5% p-aramid (Kevlar®) + 2% Polyamide, characterized by a value of evaporation resistance $R_{et} = 5.8$ [$\text{m}^2\text{Pa}/\text{W}$] while S2 is a nonwoven structure made of 35% p-Aramid + 65% m-Aramid coated with a polytetrafluoroethylene (PTFE) membrane, with $R_{et} = 12.42$ [$\text{m}^2\text{Pa}/\text{W}$]. The water vapor resistance of these fabrics was determined according to the standard ISO 11092 – 2014.

The multilayer textile structure was glued to the circumference of the copper chamber using a neoprene-type adhesive. The whole assembly is placed on an electronic balance. The water from the copper chamber evaporates creating in the space between the water surface and the multilayer textile material a microclimate characterized by high relative humidity, close to 100% RH. This fact leads to the appearance of a moisture gradient and a water vapor flow through the textile material. According to Fick's law, the stationary diffusion flux has the same value in each layer of the textile assembly and can be determined using Equation (11) applied to the inner layer (S1/S2). According to this equation, the diffusion rate can be calculated by measuring the difference in relative humidity and temperature at the boundaries of the inner layer (S1/S2) and knowing the R_{et} value for this layer. The humidity gradient was measured with capacitive sensors, while the temperature is measured with E-type thermocouples placed on the two surfaces of this inner layer, and the evaporated water mass was measured using the electronic balance. The experiments were performed under normal laboratory conditions in which the temperature variation was below 5% and the humidity variation below 3%.

4. Results and discussions

4.1. Determination of water vapor flow using relative humidity sensors

The determination of the evaporation rate is based on the data provided by the electronic balance and for both textile assemblies and the results are shown in Figures 6 and 7.

The average effective evaporation flow obtained with the electronic balance is for AsT1: $\Phi_{med1} = 1.124$ [mg/s]/ 0.008464 [m^2] = 132.79 [$\text{mg}/(\text{m}^2\text{s})$] and for AsT2: $\Phi_{med2} = 0.7253$ [mg/s]/ 0.008464 [m^2] = 85.69 [$\text{mg}/(\text{m}^2\text{s})$].

To determine the water vapor flow through the multilayer textile materials AsT1 and AsT2, the Equation (11) and the device from Figure 5 were used. The relative humidity

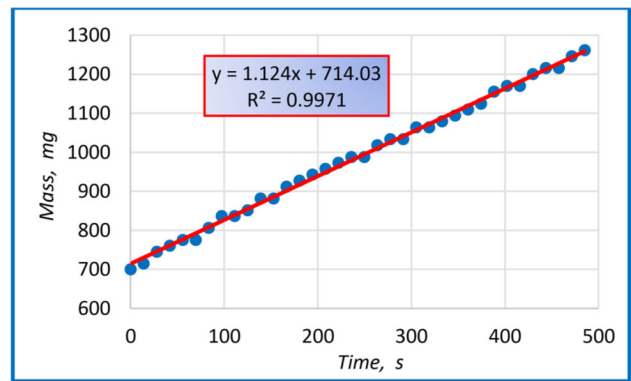


Figure 6. Mass of water evaporated through AsT1 assembly determined with the electronic balance.

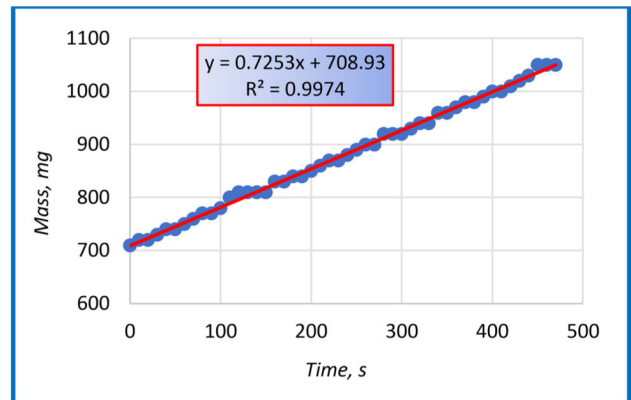


Figure 7. Mass of water evaporated through AsT2 assembly determined with the electronic balance.

gradient was measured by the humidity sensors CV1 and CV2 and the device from Figure 1. The results are shown in Figures 8 and 9.

The average value of the determined water vapor flow has the following value for AsT1: $\Phi_{s_med1} = 136.93$ [$\text{mg}/(\text{m}^2\text{s})$] and for AsT2: $\Phi_{s_med2} = 85.99$ [$\text{mg}/(\text{m}^2\text{s})$].

For AsT1 the average value of the water vapor flow is 136.93 [$\text{mg}/(\text{m}^2\text{s})$] compared to the measured electronic balance value of 132.79 [$\text{mg}/(\text{m}^2\text{s})$], which represents a deviation of 3.11%. The values measured by the two sensors vary between $\pm 6\%$ at the beginning of the experiment and fall between $\pm 4.5\%$ in the second part of the interval.

For AsT2 the determined average value of the water vapor flow 85.99 [$\text{mg}/(\text{m}^2\text{s})$] shows a variation of less than 1% compared to the effective value measured with the electronic balance. The instantaneous values fall between $\pm 5\%$ in the first part of the interval, the dispersion of the values being reduced to $\pm 3.5\%$ on the second part of the interval.

These results validate the proposed method for monitoring the flow of water vapor through textile materials and clothing.

The proposed method for measuring vapor flow through textile materials can be applied in the form presented above for multilayer textile assemblies containing hydrophilic or hydrophobic layers, provided that the inner layer (S1/S2), through which the measurement is performed, is hydrophobic, having so a constant value of R_{et} (water vapor resistance). In general, the protective equipment for firefighters, soldiers, etc. has these characteristics.

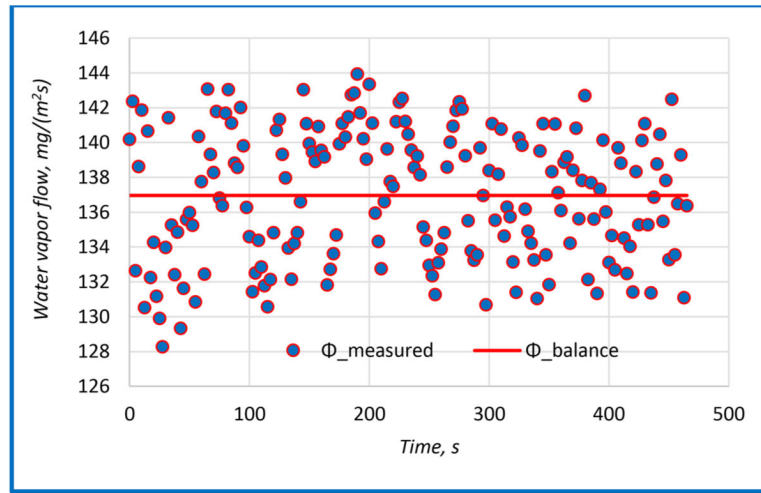


Figure 8. The value of the water vapor flow for AsT1 determined with humidity sensors.

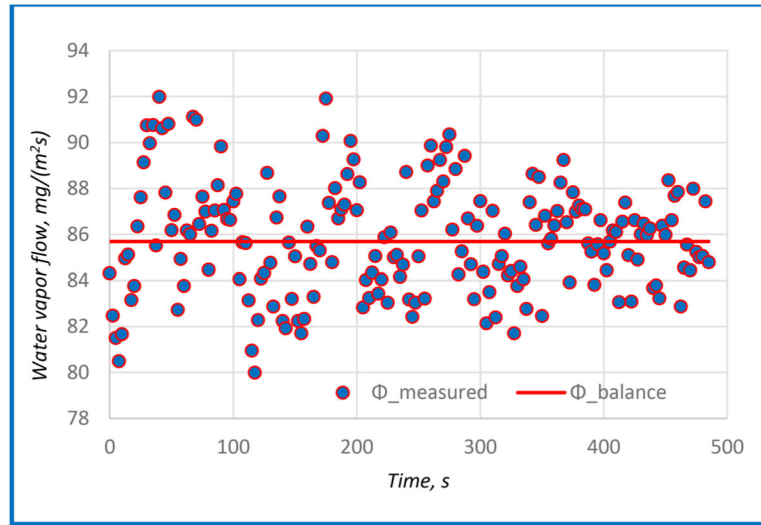


Figure 9. The value of the water vapor flow for AsT2 determined with humidity sensors.

The temperature can influence the transfer rate of vapor flow through the inner layer, through the saturation pressure $p_{\text{sat}}(T)$ as well as through the diffusion coefficient $D_a(T)$ of water vapor in the air. This dependence has been taken into account by measuring the temperature using E-type thermocouples. $D_a(T)$ and $p_{\text{sat}}(T)$ values are tabulated in the literature, and the appropriate values are determined by interpolation depending on the temperature measured by the E-type thermocouples and then transferred to the Excel file that uses Equation (11) for the calculation of the transfer rate.

The different relative humidity of the environment results in different relative humidity values at the boundary of the inner layer (S1/S2). In addition, the relative humidity of the environment can change the porosity of the other textile layers if they are hydrophilic, resulting in different relative humidity values at the boundary of the inner layer, but these values are permanently measured by the humidity sensors.

Thus, the temperature and humidity values are automatically provided by the sensors used and therefore the method is applicable for any humidity and temperature conditions.

If the inner layer (S1/S2) is not hydrophobic, it is necessary to know the law of variation of the R_{et} of this layer,

based on the average relative humidity provided by the sensors, and to enter this law of variation into the Equation (11). But determining R_{et} for the entire humidity range (between 0 and 100%) is a very difficult process, especially for very low or very high values. A very small humidity gradient generates an electrical signal at the noise level produced by electronic components (e.g. Figures 1 and 11).

Thus, the proposed method is an original method for measuring vapor transfer through textile materials under dynamic conditions and has wide applicability for hydrophobic and hydrophilic multilayer structures containing an inner layer with a known R_{et} .

4.2. Determination of water vapor resistance, R_{ev} using relative humidity sensors

In order to determine the water vapor resistance, R_{et} , the Equation (11) was used, written in the following form:

$$R_{\text{et}} = \Delta RH \cdot p_{\text{sat}}(T) \cdot \frac{1}{\Phi(T) \cdot \lambda_{\text{H}_2\text{O}} \cdot (T)} \cdot \frac{D_a(T)}{D_a(T_{35})} \cdot \frac{T_{35}}{T} \quad (12)$$

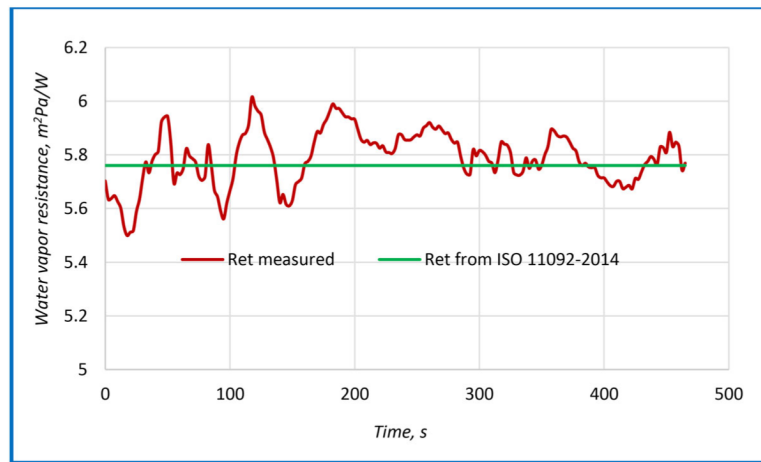


Figure 10. Water vapor resistance, R_{et} , for S1 textile material.

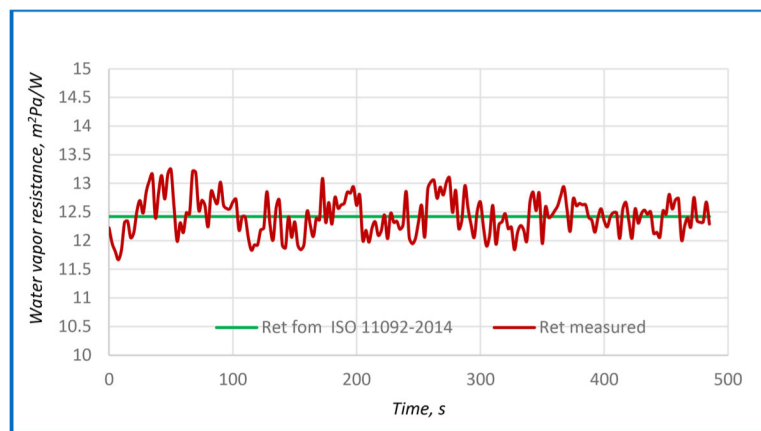


Figure 11. Water vapor resistance, R_{et} , for S2 textile material.

The mass flow of water vapors through the textile material, $\Phi(T)$, is measured with the electronic balance, and the humidity gradient is measured with the two sensors, CV1 and CV2, and the electronic devices from Figure 1. Temperature monitoring is performed by an E-type thermocouple (Omega Engineering). The other parameters are taken from tables (Bolz & Tuve, 1976).

Experiments were made for the two textile materials, S1 and S2, that are part of the AsT1 and AsT2 multilayer textile assemblies, and the results are shown in Figures 10 and 11.

As can be seen, for the S1 textile material the average value of the water vapor resistance determined for the whole period of time is $R_{et} = 5.75$ [m^2Pa/W], which represents a deviation of less than 1% compared to the standard value (ISO 11092 – 2014) $R_{et} = 5.8$ [m^2Pa/W]. The differences between the individual values and the standard value fall within the limits of $\pm 4.5\%$.

Regarding the S2 textile material, the determined average value of the water vapor resistance is $R_{et} = 12.463$ [m^2Pa/W], and it has a deviation of 0.34% compared to the standard value of 12.42 [m^2Pa/W]. Instantaneous values fall within $\pm 5\%$ of the standard value.

In conclusion, the method proposed can also be used to determine the water vapor resistance of textile materials

with good precision. The method is simpler and cheaper than the very expensive one of ISO 11092 – 2014 (skin model) widely used in textiles.

5. Conclusions

In this study, small-scale capacitive humidity sensors were used for monitoring the flow of water vapor through multilayer textile assemblies and to determine the water vapor resistance, R_{et} , of textile materials.

These results validate the proposed method for monitoring the flow of water vapor through textile materials and clothing. Using this method, it is possible to monitor the transfer of vapors in a dynamic regime, the method being more appropriate to the actual wearing conditions of the clothing.

The method is original and has wide applicability for hydrophobic and hydrophilic multilayer structures containing an inner layer with a known R_{et} , regardless of the humidity and temperature conditions.

The method proposed can also be used to determine the water vapor resistance of textile materials with good accuracy. The water vapor resistance of textile materials obtained with the proposed method was compared with the water vapor resistance determined according to ISO 11092 – 2014 and a good correlation was found. This method is simpler

and cheaper than the very expensive one used by the ISO 11092 – 2014 (skin model) widely used in textiles.

Proper individual calibration is required for the capacitive humidity sensor.

The capacitive humidity sensors integrated into a fire-fighter jacket could be used for monitoring of human-environment interface, by monitoring the water vapor flow. Similarly, the sensors could be integrated into sportswear to assess the local energy expenditure of the wearer. Another area of application could be in the field of healthcare.

6. Future research and perspectives

The future research will focus mainly on

- Improving the working method by extending the range of tested textiles. In this regard, for the hydrophilic inner layer, R_{et} will be determined depending on the average humidity. It is well known that the humidity of a textile can change the properties of the textile layer, modifying the water vapor permeability. By standard methods, the water vapor resistance can be determined only at certain concrete values of relative humidity, and not in a dynamic regime.
- Connecting the electronic device with an ESP 32 Dual Core system with Wi-Fi and Bluetooth to transmit data via Wireless in order to remotely monitor the transfer of vapors for situations of special interest (monitoring fire-fighters, hospitalized patients, babies, athletes during training, etc.).

Disclosure statement

No potential conflict of interest was reported by the authors.

Funding

This work was supported by a publication grant of the TUIASI, project number GI/P 24/2021.

References

Analog Microelectronics, "analog-micro.com," Analog Microelectronics [Online]. Available: <https://www.analog-micro.com/en/products/ics/cuconverter/cav444/> [Accessed 16 July 2021].

Bolz, R., & Tuve, G. L. (1976). *Handbook of tables for applied engineering science* (2nd Ed.). CRC Press.

Chen, Y. N. (1959). Dry cloth over skin simulant system. In *Transient heat and moisture transfer to skin through thermally-irradiated cloth*. Massachusetts Institute of Technology, Dept. of Chemical Engineering.

Codau, T. C., Onofrei, E., Petrusic, S., Bedek, G., Dupont, D., & Soulat, D. (2015). Mathematical correlation of test methods for measuring water-vapor transmission through fabrics. *Journal of Porous Media*, 18(3), 245–255. <https://doi.org/10.1615/JPorMedia.v18.i3.50>

Frydrysiak, M. (2020). Comparison of textile resistive humidity sensors made by sputtering, printing and embroidery techniques. *Fibres and Textiles in Eastern Europe*, 28(5(143)), 91–96. <https://doi.org/10.5604/01.3001.0014.2391>

Keiser, C., Becker, C., & Rossi, R. (2008). Moisture transport and absorption in multilayer protective clothing fabrics. *Textile Research Journal*, 78(7), 604–613. <https://doi.org/10.1177/0040517507081309>

Kinkeldei, T., Zysset, C., Cherenack, K. H., & Tröste, G. (2011). A textile integrated sensor system for monitoring humidity and temperature. In 16th International Solid-State Sensors, Actuators and Microsystems Conference.

Komazaki, Y., & Uemura, S. (2019). Stretchable, printable, and tunable PDMS-CaCl₂ microcomposite for capacitive humidity sensors on textiles. *Sensors and Actuators B: Chemical*, 297, 126711. <https://doi.org/10.1016/j.snb.2019.126711>

Koncar, V. (2016). Introduction to smart textiles and their applications. In *Smart Textiles and their Applications* (1st ed., pp. 1–8). Woodhead Publishing.

Lee, Y. M., & Barker, R. (1984). Effect of moisture on the thermal protective performance of heat-resistant fabrics. *Journal of Fire Sciences*, 4(5), 315–331.

Mäkinen, H., Smolander, J., & Hille, H. (1988). Simulation of the effect of moisture content in underwear and on the skin surface on steam burns of fire fighters. In *Performance of Protective Clothing: ASTM STP 989* (pp. 415–421). West Conshohocken, American Society for Testing and Materials.

Martínez-Estrada, M., Moradi, B., Fernandez-Garcia, R., & Ignacio, G. (2019). Impact of conductive yarns on an embroidery textile moisture sensor. *Sensors*, 19(5), 1004. <https://doi.org/10.3390/s19051004>

Midha, V. (2016). Waterproof breathable fabrics. In *Handbook of Technical Textile* (2nd ed., Vol. 2). Woodhead Publishing.

Reichelt Elektronik. "reichelt.com." Accessed (14 July 2021). Reichelt Elektronik [Online]. Available: <https://www.reichelt.com/de/en/moisture-sensor-kfs-140-m-smd-kfs-140-m-smd-p82305.html>.

Rossi, R. M., & Zimerlli, T. (1996). Influence of humidity on the radiant, convective and contact heat transmission through protective clothing materials. In J. Johnson and J. S. Mansdorf (Eds.), *Performance of Protective Clothing Materials: ASTM STP 1237* (Vol. 5, pp. 269–280). American Society for Testing and Materials.

Sakandar, R., Vijjapu, M. T., Andres, M., Gascon, I., Roubeau, O., Eddaudi, M., & Salma, K. (2020). Highly selective metal – organic framework textile humidity sensor. *ACS Applied Materials & Interfaces*, 12, 29999–30006.

Siyi, B., Hou, L., & Yinxiang, L. (2021). An integrated wearable strain, temperature and humidity sensor for multifunctional monitoring. *Composites Part A, Applied Science and Manufacturing*, 149(5), 106504. <https://doi.org/10.1016/j.compositesa.2021.106504>

Su, P.-G., & Chang, C.-F. (2018). Fabrication and electrical and humidity-sensing properties of a flexible and stretchable textile humidity sensor. *Journal of the Taiwan Institute of Chemical Engineers*, 87, 36–43. <https://doi.org/10.1016/j.jtice.2018.03.050>

Testo SE & Co. KGaA. "Testo.com," Testo SE & Co. KGaA [Online]. Available: <https://www.testo.com/en-TH/testo-435-1/p/0560-4351> [Accessed 15 July 2021].

Wagner, W., & Pruß, A. (2002). The IAPWS formulation 1995 for the thermodynamic properties of ordinary water substance for general and scientific use. *Journal of Physical and Chemical Reference Data*, 31(2), 387–535. <https://doi.org/10.1063/1.1461829>

Weremczuk, J., Tarapata, G., & Jachowicz, R. (2012). Humidity sensor printed on textile with use of ink-jet technology. *Procedia Engineering*, 47, 1366–1369. <https://doi.org/10.1016/j.proeng.2012.09.410>

The Influence of Knitted Fabrics' Structure on the Thermal and Moisture Management Properties

Elena Onofrei, Ana Maria Rocha, André Catarino

University of Minho, Guimaraes Braga PORTUGAL

Correspondence to:

Elena Onofrei email: eonofrei@det.uminho.pt

ABSTRACT

This paper studies the influence of fabric's structure on the thermal and moisture management properties of knitted fabrics made of two types of yarns with thermo-regulating effect: Coolmax[®] and Outlast[®]. The main purpose of this study was the selection of the most adequate fabric, to be used in summer and winter sportswear. The results demonstrated that some properties, such as, thermal properties, diffusion ability, air and water vapor permeability are influenced by both raw material type and knitted structure parameters. Wicking ability is influenced to a greater extent by the knitted structure, while the drying ability is primarily determined by raw material and to a lesser extent by the knitted structure parameters. Outlast[®] fabrics are preferred candidates for warmer climate sportswear, particularly due to their lower thermal resistance, higher thermal conductivity and absorptivity, air and water vapor permeability. When considering sportswear for colder weather, Coolmax[®] based structures seem to be the best choice. These findings are an important tool in the design of a sportswear product tailored to the different body areas thermal and moisture management requirements.

Keywords: knitted structure, thermal properties, moisture management, sportswear

INTRODUCTION

The most important feature of functional clothing is to create a stable microclimate next to the skin in order to support body's thermoregulatory system, even if the external environment and physical activity change completely [1].

The thermal comfort of a garment depends on several factors: heat and vapor transport, sweat absorption and drying ability. Total heat loss from skin results from the heat loss promoted by evaporation and the heat loss conveyed by conduction, convection and radiation. Under mild environmental conditions the loss of heat by evaporation takes place in the form of insensible perspiration which accounts for approximately 15% of the heat loss through the skin.

In the case of hard physical exercise or in tropical climates, the heat loss by evaporation is accompanied by sweating and the skin becomes covered with a film of water [2].

For wearer comfort, this sweat should be transported away from the skin surface, in the form of liquid or vapor, so that the fabric touching the skin feels dry. The transport of both moisture vapor and liquid away from the body is called moisture management [3].

Moisture management has the following functions [4]:

Regulation of body temperature – when the human body core temperature exceeds 37 °C, sweat is produced. Transporting the sweat away from the skin and evaporating it to the atmosphere, reduces body temperature.

Control of cloth weight increase – absorbing the moist generated by the body increases cloth weight, making it uncomfortable and with a negative effect on performance. Moisture management avoids this effect.

Natural fibers such as cotton are hydrophilic, meaning that their surface has bonding sites for water molecules. Therefore, water tends to be retained in the hydrophilic fibers, which have poor moisture transportation and release. On the other hand, synthetic fibers such as polyester are hydrophobic, meaning that their surface has few bonding sites for water molecules. Hence, they tend to remain dry and have good moisture transportation and release. Moisture absorption and release properties do not coexist in common fibers. To achieve those, specialty fibers, obtained by a finishing (microencapsulation) process using thermally active materials, such as Outlast[®], or by fiber design, such as Coolmax[®], must be used [5, 6, 7, 8].

When a textile product incorporates thermally active materials or specially designed fibers, it can provide enhanced thermal and moisture management

performance in addition to the existing passive characteristics of the structure to keep the body in the comfort state [1].

The Outlast[®] yarn incorporates PCM (Phase Change Materials) microcapsules within a viscose fibre structure (*Figure 1*). The thermo-regulating effect, resulting either from the heat absorption or heat emission of the PCM, is used to keep the temperature of a surrounding substrate nearly constant [9].



FIGURE 1. Outlast[®] Thermocules[®] in viscose fiber [9](with © Outlast Technologies, Inc. permission).

The Coolmax[®] yarn does not rely on thermally active additives such as Outlast[®], but its thermo-regulating effect relies on fibre's morphology (greater surface area and multi-channel cross section - *Figure 2* and *Figure 3*), which draws sweat way from the body to the outside for easy evaporation. It applies the capillary theory to rapidly remove sweat and moisture from the skin's surface, transport it to the fabric surface, and then evaporate it [10, 6].

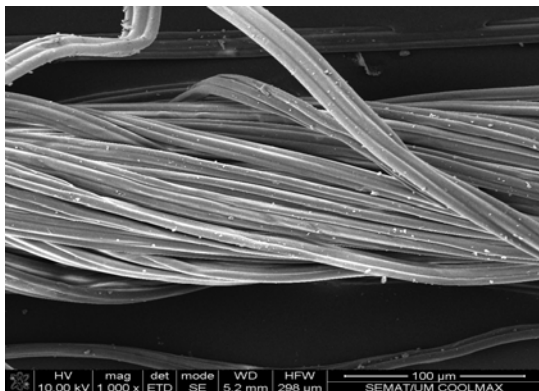


FIGURE 2. SEM image of Coolmax[®] yarn.

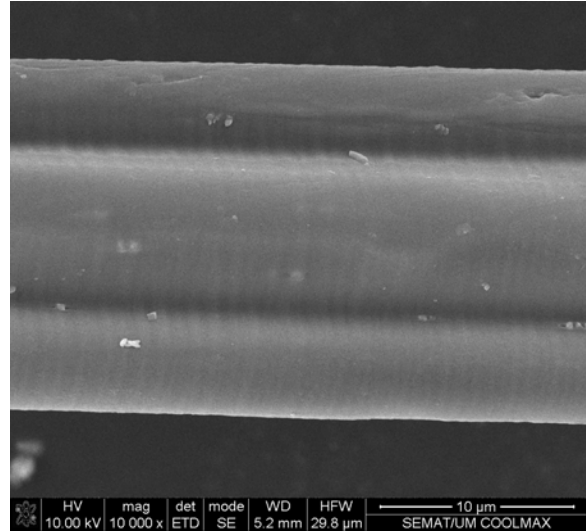


FIGURE 3. SEM image of the Coolmax[®] fibre.

Nowadays, for the majority of sportswear, underwear and outerwear products include elastane. Plating (the simultaneous formation of the loop from two yarns) is a common technique to produce such knitted products [11]. To improve fabric elasticity and shape retention, 2% of elastane is enough; for high-performance garments, such as swimwear and active sportswear, the elastane content can increase up to 30% [8].

In this study, the effect of fabric structure on the thermal and moisture management properties of knitted fabrics incorporating yarns with different thermo-regulating effect were investigated. The yarns used were a 30% Outlast[®]Viscose / 70% Cotton, 14.75 tex and a Dacron 702 WSD 1.7/38, 14.30 tex (Coolmax[®]). The plating yarn was a 44 dtex bare elastane from Creora, plated at every feeder.

EVALUATED PROPERTIES AND EQUIPMENT USED

Air permeability is described as the rate of air flow passing perpendicularly through a known area, under a prescribed air pressure differential between the two surfaces of a material.

Tests were performed according to standard ISO 9237 using a Textest FX-3300 air permeability tester. The air pressure differential between the two surfaces of the material was 100 Pa.

Thermal properties were evaluated using the ALAMBETA instrument [12] and tests performed according to standard ISO EN 31092-1994. In all cases, the measuring head temperature was,

approximately, 32°C and the contact pressure 200 Pa. Thermal comfort was characterized by three properties: Thermal conductivity; Thermal resistance and Thermal absorptivity.

Thermal Conductivity

Thermal conductivity is fundamental to determine the heat transfer through fabrics. For textile materials, still air in the fabric structure is the most important factor for conductivity value, as still air has the lowest thermal conductivity value when compared to all fibers ($\lambda_{\text{air}} = 0.025$). Therefore, air transports a low quantity of energy by conduction and thermal conductivity decreases as well [13].

Thermal Resistance

Thermal resistance expresses the thermal insulation of fabrics and is inversely proportional to thermal conductivity. In a dry fabric or containing very small amounts of water it depends essentially on fabric thickness and, to a lesser extent, on fabric construction and fiber conductivity [2].

Thermal Absorptivity

Thermal absorptivity is the objective measurement of the warm-cool feeling of fabrics and is a surface-related characteristic. If the thermal absorptivity is high, it gives a cooler feeling at first contact with the skin. The surface character of the fabric greatly influences this sensation [12, 14].

Moisture Management

For liquid transport within fabrics, two phenomena must be accounted for – wettability and wickability [15]. The term ‘wetting’ is usually used to describe the change from a solid–air interface to a solid–liquid interface. Wicking is the spontaneous flow of a liquid in a porous substrate, driven by capillary forces. As capillary forces are caused by wetting, wicking is a result of spontaneous wetting in a capillary system [16, 17].

Many test methods have been developed to measure liquid water absorbency and water vapor transport in fabrics [3, 15]. These methods measure different aspects of moisture management characteristics of fabrics.

Diffusion Ability

Expresses the rate of water diffusing in the fabric surface and represents fabric’s instantaneous water (perspiration) absorbency and transferring ability. The fabric samples were placed flat on a hydrophobic board with the outer surface facing down. The diffusion area (mm^2) was measured 30 seconds after dripping 0.2 ml of water, using a precise dropper

whose tip was 10 mm above the fabric surface. The measurement was repeated at five different points and the average of the diffusion area (mm^2) was taken to indicate the diffusion ability of the fabrics.

Wicking - Transverse ‘Plate’ Test Or In-Plane Wicking Test

Expresses fabric’s ability to move sweat away from the skin to the outer surface of the fabric, where it evaporates. The apparatus used to determine the transverse wicking consists of a horizontal glass plate fed from below with water through a capillary tube coming from a reservoir placed on an electronic balance. The sample was placed on the glass plate and was held in contact with it (and with water) applying another glass plate on top of it. The changing weight of the reservoir is measured by an electronic balance to determine the rate of liquid uptake by the textile material. Similar apparatus have been used by Buras, McConnell, among others [18].

Water Vapor Permeability

When vapor passes through a textile layer two processes are involved: diffusion and sorption-desorption. Water vapor diffuses through a textile structure in two ways, simple diffusion through the air spaces between fibers and yarns and along the fiber itself. At a specific concentration gradient, the diffusion rate along the textile material depends on the porosity of the material and also on the water vapor diffusivity of the fiber. Diffusivity of the material increases with the increase in moisture regain. In the same way, moisture transport through sorption-desorption process will increase with the hygroscopicity of the material [19].

The factors associated with knitted fabric’s thickness and construction determine moisture vapor transport properties, especially in low density open textile structures. Fiber-related factors, such as cross-sectional shape and moisture absorbing properties, do not play a significant role [20].

The water vapor permeability was determined on SDL Shirley Water Vapor Permeability Tester M-261, according to standard BS 7209-1990. The cup method is a very common method for testing the moisture transfer ability of fabrics [21].

Drying Time

The drying time is mainly dependent on how much water is absorbed by the fabric and therefore by fabric thickness [20].

In this test, fabrics were cut into circular samples of 100 cm^2 , placed on a horizontal surface and wetted

with 1 ml of distilled water dropped onto it using a precise dropper whose tip was 10 mm above the fabric surface. The remaining water ratio (RWR) and the drying time of fabrics were assessed. In order to determine the drying rate (evaporating curve), the fabrics were weighted in the dry state (dry weight- W_f) and immediately after wetting (wet weight at the initial stage - W_0). The change in weight (W_i) was measured at 10-minute intervals and the remaining water ratio (%) was then calculated, for each interval, using the following equation:

$$RWR = \frac{(W_i - W_f)}{(W_0 - W_f)} \cdot 100 \quad (\%) \quad (1)$$

The remaining water ratios were used to express the drying ability of the fabrics as wetted by sweat.

EXPERIMENT PLANNING

Nine knitted structures were produced combining plain, tuck and float stitches, using an 8-feed Single-Jersey Circular Knitting Seamless Machine MERZ-MBS. Machine details were as follows: gauge – 28 E, diameter – 13”, number of needles – 1152. The yarn input tension for elastane was 4 cN and for the other yarns 2 cN. The machine setting for the loop length was 100, and maintained constant for all fabrics. *Table I* shows the structures selected for this experiment and *Table II* the knitted fabrics’ characteristics.

TABLE I. Knitted fabrics’ structures.

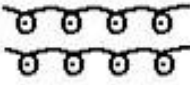
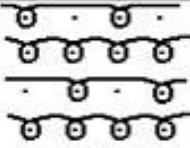
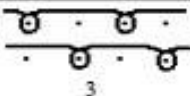






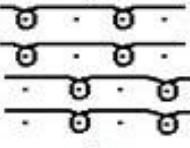
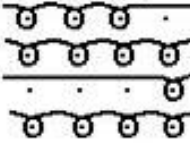
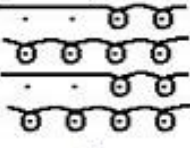






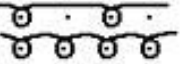
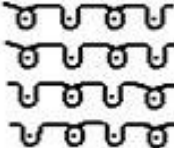
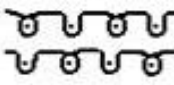






 <p>1</p>		 <p>2</p>		 <p>3</p>	
					
<i>technical face</i>	<i>technical back</i>	<i>technical face</i>	<i>technical back</i>	<i>technical face</i>	<i>technical back</i>
 <p>4</p>		 <p>5</p>		 <p>6</p>	
					
<i>technical face</i>	<i>technical back</i>	<i>technical face</i>	<i>technical back</i>	<i>technical face</i>	<i>technical back</i>
 <p>7</p>		 <p>8</p>		 <p>9</p>	
					
<i>technical face</i>	<i>technical back</i>	<i>technical face</i>	<i>technical back</i>	<i>technical face</i>	<i>technical back</i>

TABLE II. Knitted fabrics' characteristics.

Structure code	Loop length, mm		Fabric density, stitches/cm ²		Mass per unit area, g/m ²		Thickness, mm		Bulk density, g/cm ³	
	Coolmax [®] +Creora	Outlast [®] +Creora	Coolmax [®] +Creora	Outlast [®] +Creora	Coolmax [®] +Creora	Outlast [®] +Creora	Coolmax [®] +Creora	Outlast [®] +Creora	Coolmax [®] +Creora	Outlast [®] +Creora
1	2.90	2.95	578	578	253.78	253.2	1.22	1.08	0.208	0.234
2	1.93/3.0	1.85/2.99	779	774	303.40	288.26	1.36	1.22	0.223	0.236
3	1.84	1.89	1280	1254	380.02	370.07	1.49	1.41	0.255	0.262
4	1.85	1.86	1080	1064	363.04	355.73	1.48	1.38	0.245	0.258
5	1.84/2.95	1.82/2.95	820	836	308.43	296.18	1.89	1.57	0.163	0.189
6	1.87/3.06	1.85/2.96	861	836	334.5	304.58	1.77	1.58	0.189	0.193
7	1.88/2.98	1.89/2.96	860	836	314.60	308.94	1.46	1.30	0.215	0.237
8	2.88	2.92	704	660	334.21	330.3	1.50	1.40	0.222	0.235
9	2.88	2.93	630	645	282.95	278.09	1.33	1.25	0.212	0.222

All tests were carried out after the samples were conditioned under standard atmospheric conditions (temperature $20 \pm 2^\circ\text{C}$, $65 \pm 2\%$ relative humidity), according to standard ISO 139:1973.

An exploratory data analysis containing central tendency and dispersion statistics was performed with the purpose of identifying outliers, normal behavior of the measured properties and also the homogeneity of variances. Then, univariate analysis of variance was made using PASW 17.0 by means of ANOVA procedure, followed by Post Hoc tests.

RESULTS AND DISCUSSION

Air Permeability

As it can be observed in *Figure 4* and was confirmed by ANOVA analysis, there is a significant influence of the fabric structure on air permeability. Both for Outlast[®] and Coolmax[®] fabrics, the lower air permeability values were obtained with structures 3 and 4 (with one-needle floats - known as locknit and double locknit), characterized by higher fabric density. Structures 6 and 7 (with a ribbed surface), as well as, structure 1 (single jersey) presented the higher air permeability values. In the single jersey structure this behavior is mainly due to fabric density; in the ribbed structures to their surface characteristic.

The air permeability is generally higher for Outlast[®] fabrics; this is most probably due to the lower thickness of Outlast[®] fabrics and to fibers' geometry.

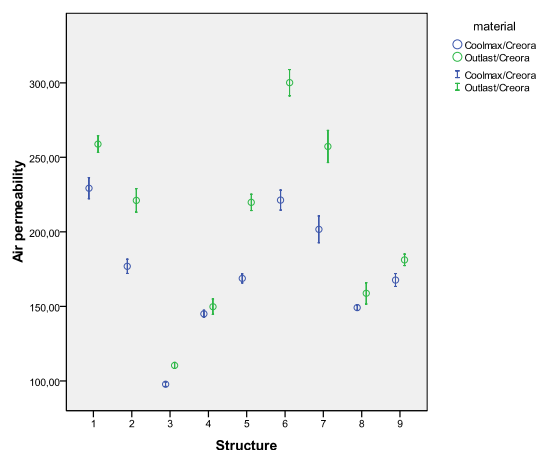


FIGURE 4. Air permeability, l/m²/s.

The higher surface area of the Coolmax[®] fibre increases the resistance to air flow, which results in lower air permeability.

Thermal Properties

Thermal Conductivity:

All Outlast[®] fabrics have higher thermal conductivity than Coolmax[®] fabrics and the difference between them is almost constant for all structures (*Figure 5*). This behavior is in a great extent influenced by the yarn characteristics, but also by the fabric structure. Both for Coolmax[®] and Outlast[®] fabrics, structure 5 (with 3-needle floats) has the lowest thermal conductivity and structures 3 and 4 (one-needle floats – locknit and double locknit) the highest thermal conductivity. These structures have respectively, the lowest and the highest bulk densities.

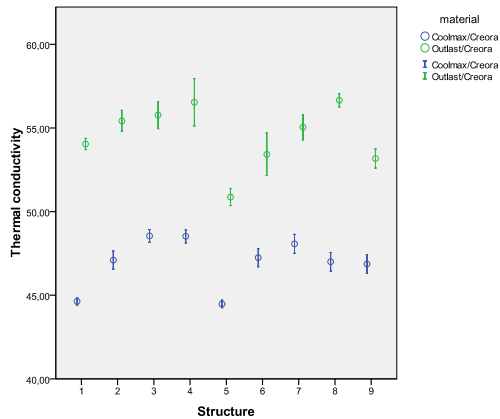


FIGURE 5 Thermal conductivity - λ ($\times 10^{-3}$), W/mK.

Thermal Resistance:

As expected due to the previous behaviour, all Coolmax[®] fabrics have higher thermal resistance (Figure 6). The fabrics with the higher thickness (structures 5 and 6) have the higher thermal resistance for both Coolmax[®] and Outlast[®]. Moreover, the thermal resistance of structures 5 and 6 made of Outlast[®] is similar to the Coolmax[®] ones (except for structures 5 and 6). This is most probably due not only to thickness, but also to fiber conductivity.

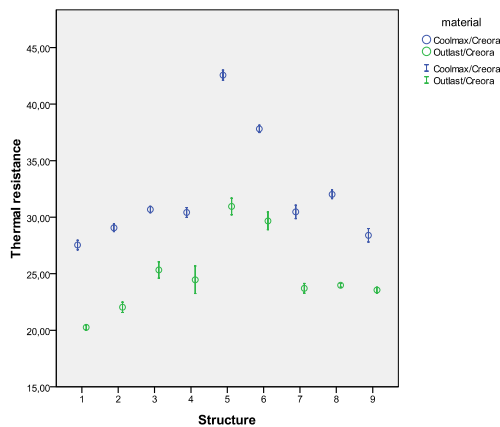


FIGURE 6. Thermal resistance - R ($\times 10^{-3}$), m^2K/W .

Thermal Absorptivity:

Yarn characteristics play a significant role on thermal absorptivity.

As it is observed in Figure 7, the thermal absorptivity of Coolmax[®] fabrics is lower than the Outlast[®] ones,

which provides a warmer sensation when in contact with the skin.

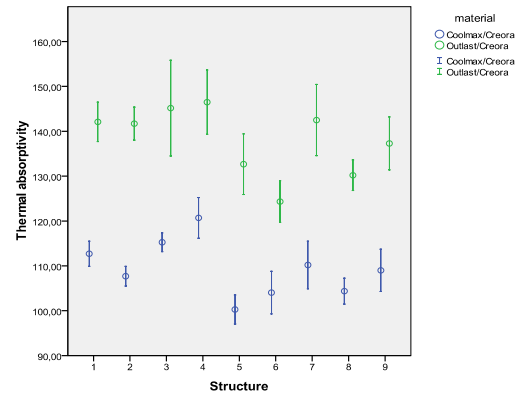


FIGURE 7. Thermal absorptivity - b , $W s^{1/2} / m^2 K$.

Moreover, the ANOVA results revealed that the surface characteristics of the fabric also have a great influence on the warm/cool feeling. Coolmax[®] and Outlast[®] structures 5 and 6 (with 3- and 2-needle floats) and 8 (with tuck stitches – double piqué) showed the lower thermal absorptivity values. The highest thermal absorptivity was obtained with structures 3 and 4 (one-needle floats - locknits).

Moisture management

Diffusion ability

As expected, the diffusion ability of Coolmax[®] fabrics is higher than the Outlast[®] fabrics - Figure 8 - (diffusion area 1.13 – 1.80 times larger).

This behavior is essentially related with yarn characteristics, in particular fiber morphology and nature (hydrophilic or hydrophobic character), and to a certain extent, with the fabric characteristics and structure.

In the Outlast[®] fabrics the hydrophilic character of the cellulose-based fibers is the most influencing factor of diffusion ability. Characterized for absorbing and retaining water, these fibers impair water diffusion through the fabric structure and lead to non significant differences between structures. These differences, however, are probably due to fabric thickness and cover: thinner and less dense fabrics have improved diffusion ability (jersey structure - 1).

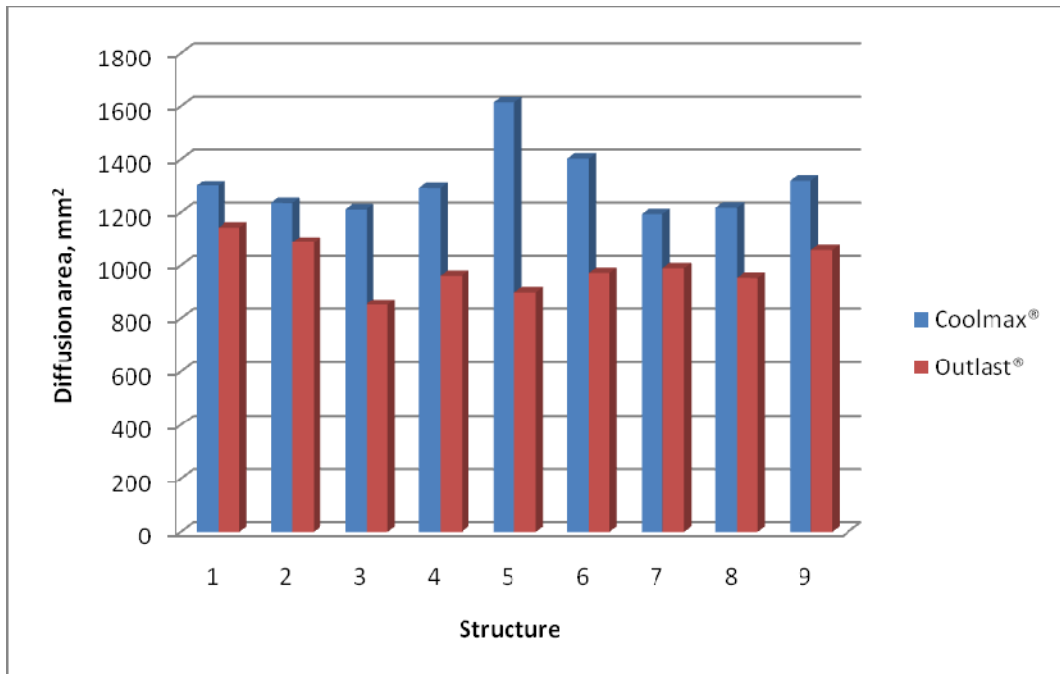


FIGURE 8. Diffusion area after 30 seconds.

In the Coolmax® fabrics, the hygroscopic character and special morphology of the fiber are the main factors promoting water diffusion, but fabric characteristics and structure can significantly contribute to further improve diffusion ability. Structures 5 and 6 characterized by ribbed surfaces clearly demonstrate this.

Wicking - Transverse 'plate' test or in-plane wicking test

The amount of water (ml) taken by the fabrics at fixed intervals was measured and from that, polynomial curves were fitted for all the fabrics (with r^2 values higher than 0.99). *Figure 9* and *Figure 10* present the curves obtained for Outlast® and Coolmax® fabrics, respectively. The rate of water up-take was calculated from the curves.

The initial rate of water up-take in in-plane wicking is generally higher for Coolmax® fabrics than for the Outlast® ones. However, when comparing similar structures produced from the different raw materials, no correlation was found between the yarn hygroscopic character and the amount of water up-take. Fabric characteristics and structure are

determining factors of the amount of water up-take both for Coolmax® and Outlast® fabrics.

For both Coolmax® and Outlast® fabrics, the initial wicking rate is higher for ribbed structures (6 and 7), single jersey (1) and structure 5 (with alternating 3-needle floats).

Outlast® fabrics with a ribbed surface (structures 6 and 7) demonstrated the highest water up-take capacity and very high initial wicking rate. This behavior is most probably due to the structures' ability to behave like a capillary system, removing and transporting water through the structure. Structures 8 (double piqué) and 4 (double locknit), with high bulk density and high thickness showed the worse in-plane wicking ability.

Similar behaviour was observed in Coolmax® fabrics. Structures 5 and 6 (with 3- and 2-needle floats) with the lowest bulk density and the highest thickness have the best wicking ability.

Structures 3 and 4 (locknits) with the highest bulk density and relatively high thickness have the worse wicking ability.

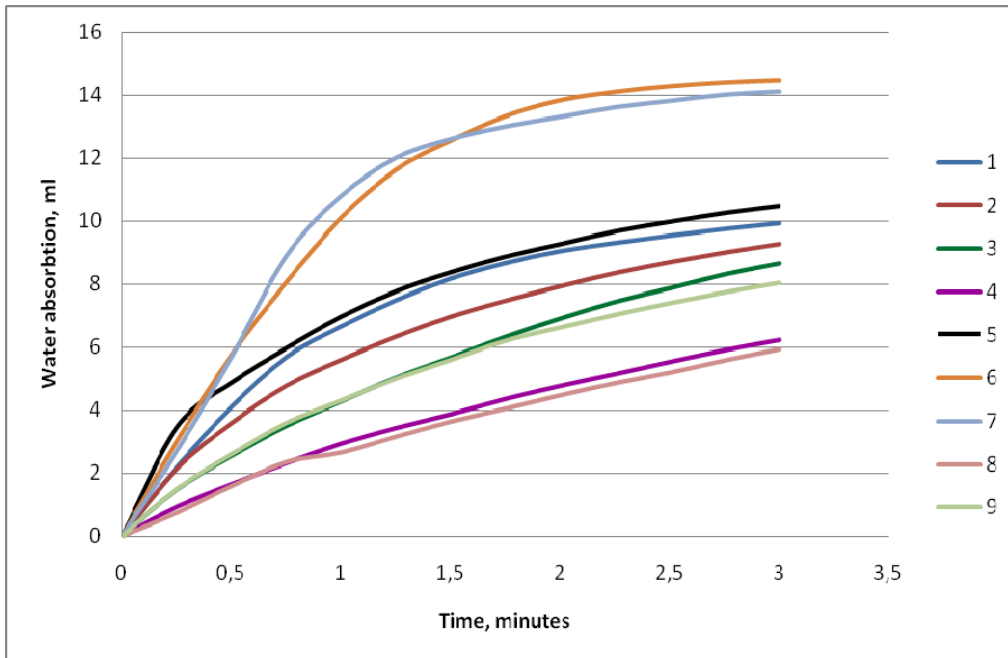


FIGURE 9. Rate of water up-take for Outlast® fabrics.

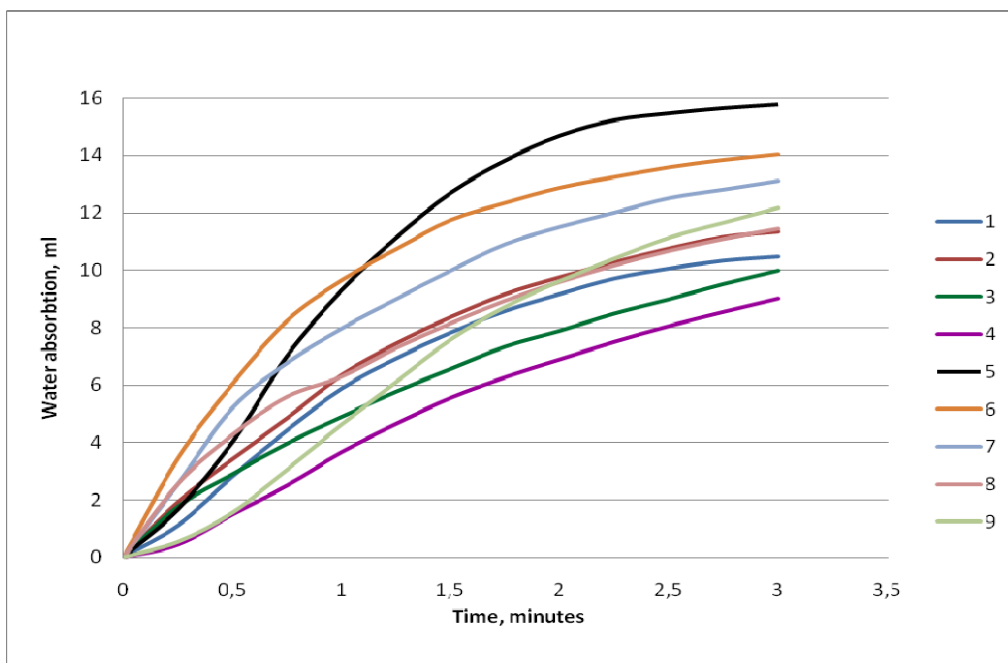


FIGURE 10. Rate of water up-take for Coolmax® fabrics.

Water Vapor Permeability

As illustrated in Figure 11, Outlast® fabrics have higher water vapor permeability than Coolmax® fabrics. This is mainly due to the hygroscopic character of Outlast® fabric which has higher vapor diffusivity.

Moreover, the cross-sectional shape of Coolmax® fibre increases the resistance to vapor flow through the fibre surface, which reduces water vapor permeability.

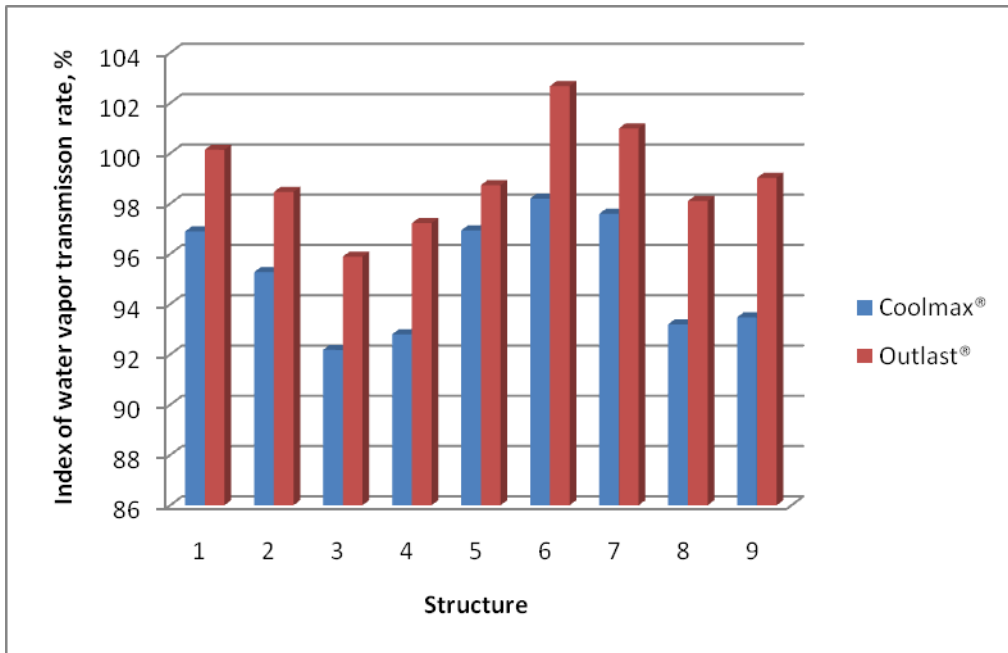


FIGURE 11. Water vapor permeability

These results are in accordance with Brojeswari Das et al. findings [1]. However, fabric characteristics and structure play a significant role on water vapor permeability. When comparing fabrics made of the same yarn, the water vapor transmission rate is primarily a function of fabric thickness and density, as well as, fabric bulk density. For both Coolmax® and Outlast® fabrics, structures 3 and 4 (locknits) with the highest fabric and bulk densities showed the lowest indexes of water vapor transmission rate.

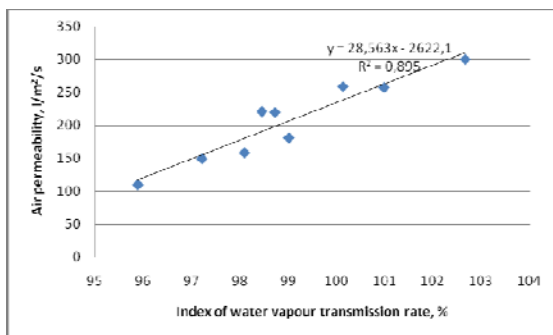


FIGURE 12. Correlation between air permeability and water vapor permeability of Outlast® fabrics

Structures 6 and 7 (with 2- and one-needle floats and a ribbed surface) obtained the highest indexes of water vapor transmission rate.

The results of the present study demonstrated that there is a good correlation between air permeability

and water vapor permeability of the fabrics, the relationship being quite well defined by a linear curve (Figure 12 and Figure 13), as suggested by Stuart et. al [22].

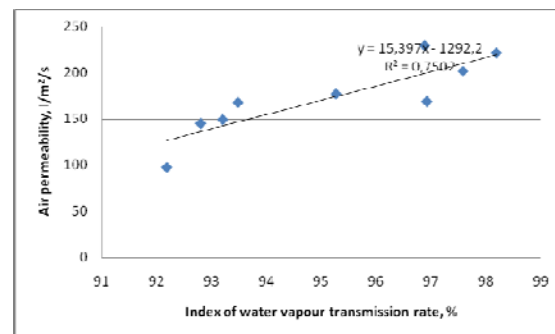


FIGURE 13. Correlation between air permeability and water vapor permeability of Coolmax® fabrics

Drying time

The evaporation curves presented in Figure 14 and Figure 15 demonstrate that the drying rates of Coolmax® fabrics are higher and the drying times lower than the Outlast® ones. As in diffusion ability, this is primarily attributed to fibre geometry and low moisture regain (which increase the rate of capillary migration, enhancing the water transmission to the fabric surface and release from it).

All the curves, around 10-20 % of the remaining water ratio, show an inversion point after which the drying rate begins to decrease. The first part of the curve (with higher slope) corresponds to moisture release from the void spaces between yarns; the second part (with lower slope) corresponds, in the case of Coolmax® fabrics, to the release of moisture retained in the inter-fibre capillaries and, in the case of Outlast® fabrics, also to the release of moisture within the fiber.

The drying time (0% remaining water ratio) for Coolmax® fabric structures lies between 180-210 minutes (respectively for structure 1 - single jersey and 6 - with 2-needle floats) and for all Outlast® fabric structures was about 270 minutes.

Knitted structure parameters affect drying ability but are secondary factors. In Outlast® fabrics, structure 1 (single jersey) demonstrated the highest drying rate

(and also the largest water diffusion area). This is probably due to fabric characteristics, namely, low thickness and mass per unit area. Structures 3 and 4 (the locknits) and structure 8 (the double piqué) showed the lowest drying rates. These structures have the highest thickness and mass per unit area.

In the Coolmax® fabrics, structures 1 (single jersey), 2 (double one-needle floats) and 9 (single piqué) demonstrated the higher drying rates and ribbed structure 6 (with 2-needle floats) and 5 (with 3-needle floats) the lower ones. Once again fabric characteristics, namely thickness and mass per unit area, seem to have affected the drying ability of fabrics (higher drying ability corresponds to structures with the lowest thickness and mass per unit area and lower drying ability to structures with the highest thickness).

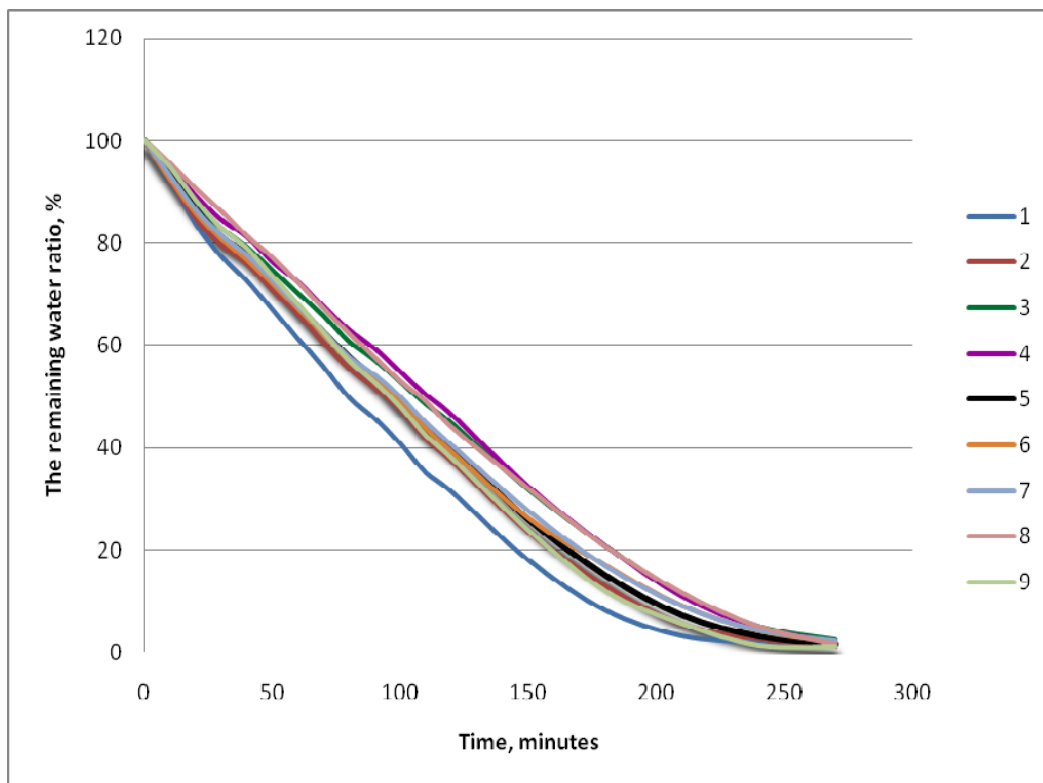


FIGURE 14. Drying time for Outlast® fabrics.

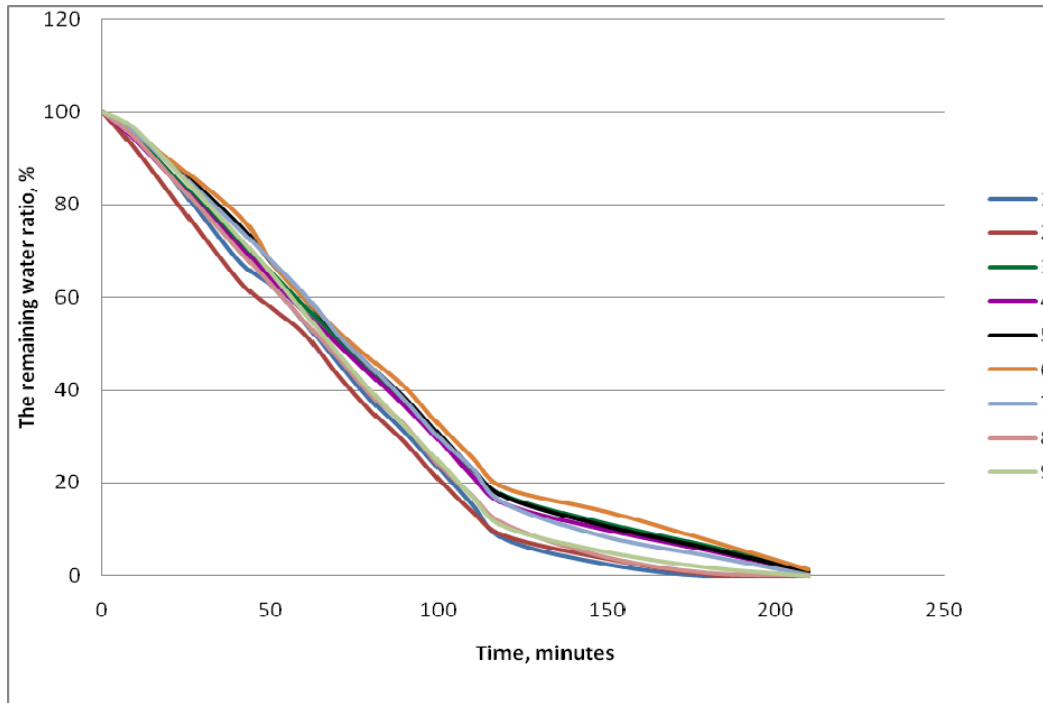


FIGURE 15. Drying time for Coolmax® fabrics.

CONCLUSIONS

This paper presents a quantitative study of various comfort related properties (thermal and moisture management properties) carried out on different knitted fabric structures containing Outlast® and Coolmax® yarns, and aiming at the selection the most adequate fabric for sportswear applications. From the results obtained it can be concluded that the thermal and moisture management performance of the studied fabrics is greatly affected by raw material properties, which significantly increased or decreased the values of the different comfort related properties evaluated. Moreover, the properties of Outlast® and Coolmax® fabrics are significantly influenced by fabric characteristics and structure, particularly in what concerns thermal properties, diffusion ability, air and water vapor permeability. Wicking ability is mainly determined by fabric structure and the drying ability by raw material properties.

Based on the thermal and moisture management behavior demonstrated, Outlast® fabrics are considered preferred candidates for warmer climate sportswear, particularly due to their lower thermal resistance, higher thermal conductivity and absorptivity and higher water vapor permeability.

However, as they demonstrated fair drying ability, fabrics can become wet and damped, creating

discomfort to the user (heavy, sag, feel cold when activity ends). Therefore, different solutions must be proposed, according to the activity level. If the wearer performs mild activities, skin wetness is very low and thermal comfort is managed by skin temperature. In this case, fabrics' air permeability and thermal resistance are determining properties for thermal comfort. Fabrics must have high air permeability and low thermal resistance. Fabrics with structures 1 (single jersey), 2 (alternate double one-needle floats) and 7 (one-needle floats with ribbed surface) fulfill these requirements.

If the wearer performs more intense activities, skin temperature and wetness increase rapidly. Under these conditions, besides high air permeability and low thermal resistance, fabrics must provide higher water vapor transfer, high diffusion and wicking ability, as well as fast drying rate. Fabrics with structures 1, 7 and 2 meet these requirements, but depending on the level of intensity and on ambient temperature, one fits better than the other. Fabric with structure 1 (single jersey) seems the most adequate for higher intensity activities, where the user tends to sweat more. On one hand because it promotes heat and water vapor transfer (it has high air permeability, the lowest thermal resistance, very good water vapor permeability) and on the other hand because it adequately manages sweat absorption and

transfer through evaporation (it has the highest diffusion and drying ability, although average wicking ability).

As regards Coolmax® fabrics, the results pointed to a preferential use on sportswear applications for colder ambient conditions, particularly due to their high thermal resistance together with high wicking and diffusion ability. Fabrics with ribbed structure 6 (with 2-needle floats) and 5 (with 3-needle floats) have the higher thermal resistance and the better overall liquid moisture management capacity (high diffusion and wicking ability) which makes them the best choice for cold weather sport activities.

The previous findings are an important tool in the design of a sportswear product tailored to the different body areas thermal and moisture management requirements.

ACKNOWLEDGEMENT

This work was conducted under support of the FCT - Fundação para a Ciência e a Tecnologia and the 2C2T – O Centro de Ciência e Tecnologia Têxtil, Universidade do Minho, Portugal, within the framework of “Ciência 2008” Program.

REFERENCES

- [1] Das B, Das A, Kothari V K, Fanguiero R, Araújo M “Effect of Fibre Diameter and Cross-sectional Shape on Moisture Transmission through Fabrics”, *Fibers and Polymers* Vol.9 (2), 2008, pp. 225-231.
- [2] Haghi AK “Moisture permeation of clothing, a factor governing thermal equilibrium and comfort”, *Journal of Thermal Analysis and Calorimetry* Vol.76, 2004, pp. 1035–1055.
- [3] Cotton Incorporated - 100% “Cotton Moisture Management”, http://www.tx.ncsu.edu/jtatm/volume2issue3/articles/cottoninc/cottoninc_fulldocument.pdf Accessed at 04.06.2010.
- [4] Salgado C “Moisture management in fabrics” <http://www.tecnitex.es/> Accessed at 13.05.2009.
- [5] Su CI, Fang JX, Chen XH, Wu WY “Moisture Absorption and Release of Profiled Polyester and Cotton Composite Knitted Fabrics”, *Textile Research Journal* Vol. 77, 2007, DOI: 10.1177/0040517507080696.
- [6] <http://www.coolmax.invista.com/> Accessed at 17.12.2009.

- [7] Fanguiero R, Gonçalves P, Soutinho F, Freitas C “Moisture management performance of functional yarns based on wool fibres”, *Indian Journal of Fibres and Textile Researcher*, Vol. 34, 2009, pp. 315-320.
- [8] Voyce J, Dafniotis P, Towlson S “Elastic textile”. In: Shishoo R (ed) *Textiles in sport*, Woodhead Publishing Limited and CRC Press LLC©, 2005, Cambridge England.
- [9] <http://www.outlast.com/> Accessed at 17.12.2009.
- [10] <http://advansa.com> Accessed at 17.12.2009
- [11] Abdessalem SB, Abdelkader YB, Mokhtar S, Elmarzougui S “Influence of Elastane Consumption on Plated Plain Knitted Fabric Characteristics”, *Journal of Engineered Fibers and Fabrics* Vol 4, 2009, pp. 30-35.
- [12] Hes L “Thermal Properties of Nonwovens”, *Proceedings of Congress Index 87*, Geneva, 1987.
- [13] Oglakcioglu N, Celik P, Ute TB, Marmarali A, Kadoglu H “Thermal Comfort Properties of Angora Rabbit/Cotton Fiber Blended Knitted Fabrics”, *Textile Research Journal* Vol.79, 2009, pp. 888-893.
- [14] Hes L, Offermann P, Dvorakova I „The effect of underwear on thermal contact feeling caused by dressing up and wearing of garments”, <http://centrum.tul.cz/centrum/publikace/pristojje/%5b21%5dhesofferdvor.doc> Accessed at 21.05.2009.
- [15] Ghali K, Jones B, Tracy J “Experimental Techniques for Measuring Parameters Describing Wetting and Wicking in Fabrics”, *Textile Res. J.* Vol. 64(2), 1994, pp. 106–111.
- [16] Çil MG, Nergis UB, Candan C “An Experimental Study of Some Comfort-related Properties of CottonAcrylic Knitted Fabrics”, *Textile Research Journal*, 2009, DOI: 0.1177/0040517508099919.
- [17] Pan N, Zhong W “Fluid Transport Phenomena in Fibrous Materials *Textile Progress*”, Vol 35 (4), 2006.
- [18] Sarkar M, Fan J, Qian X “Transplanar water transport tester for fabrics”, *Measurement Science And Technology* Vol.18, 2000, pp. 1465–1471.
- [19] Das B, Das A, Kothari V, Fanguiero R, Araújo M “Moisture Flow through Blended Fabrics - Effect of Hydrophilicity”, *Journal of Engineered Fibers and Fabrics* Vol. 4(4), 2009, pp. 20-28.

- [20] Prahsarn C, Barker RL, Gupta BS “Moisture - Vapor Transport Behavior of Polyester Knit Fabrics” *Textile Research Journal*, 2005, DOI: 10.1177/0040517505053811.
- [21] Scott RA (ed) “Textiles for protection” The Textile Institute, Woodhead Publishing Limited, 2005, Cambridge England.
- [22] Stuart IM, Denby EF “Wind induced transfer of water vapor and heat through clothing”, *Textile Research Journal* Vol. 53(11), 1983, pp. 655-660.

AUTHORS' ADDRESSES

Elena Onofrei

Ana Maria Rocha

André Catarino

University of Minho

Centre for Textile Science and Technology Campus

de Azurém Guimaraes Braga 4800 - 058

PORTUGAL

Investigating the effect of moisture on the thermal comfort properties of functional elastic fabrics

Elena Onofrei, Ana Maria Rocha and André Catarino

Journal of Industrial Textiles published online 20 October 2011

DOI: 10.1177/1528083711425840

The online version of this article can be found at:

<http://jit.sagepub.com/content/early/2011/10/20/1528083711425840>

A more recent version of this article was published on - Jun 20, 2012

Published by:



<http://www.sagepublications.com>

Additional services and information for *Journal of Industrial Textiles* can be found at:

Email Alerts: <http://jit.sagepub.com/cgi/alerts>

Subscriptions: <http://jit.sagepub.com/subscriptions>

Reprints: <http://www.sagepub.com/journalsReprints.nav>

Permissions: <http://www.sagepub.com/journalsPermissions.nav>

Version of Record - Jun 20, 2012

>> [OnlineFirst Version of Record](#) - Oct 20, 2011

[What is This?](#)

Investigating the effect of moisture on the thermal comfort properties of functional elastic fabrics

0(00) 1–18

© The Author(s) 2011

Reprints and permissions:

sagepub.co.uk/journalsPermissions.nav

DOI: 10.1177/1528083711425840

jit.sagepub.com



Elena Onofrei^{1,2}, Ana Maria Rocha¹ and André Catarino¹

Abstract

Thermo-physiological wear comfort is mainly determined by the thermal and moisture performance of clothing. Moreover, moisture is widely recognized as one of the most important factors contributing to discomfort sensations. Functional yarns with a thermo-regulating effect improve thermal and moisture performance of fabrics, but the integration of elastic yarns into the fabric structure can impair thermo-physiological wear comfort. The goal of this research was to compare, in dry and wet states, the thermal comfort properties of elastic knitted fabrics with thermo-regulating yarns, namely Viscose Outlast[®] and Polyester Coolmax[®] to better understand thermal behavioral changes due to moisture content of the fabrics. Surface moisture transfer between the fabrics and a wet skin was also assessed and enabled to evaluate the level of the unpleasant contact feeling. Air permeability that is related to the thermal behavior was also investigated. The results obtained showed that at 22% moisture content, which simulates a sweating sensation, the change in thermal properties is similar for both fabrics. Above the 'sweating sensation' moisture, significant differences on the thermal properties with the moisture content were registered between fabrics, Outlast[®] fabric being more prone to thermal properties changes due to moisture uptake than the Coolmax[®] one. When worn in conditions of wet skin, the unpleasant cool feeling increased for both fabrics, but the effect is more pronounced for Outlast[®] fabric.

Keywords

elastic fabrics, functional clothing, thermo-physiological comfort, moisture management

¹Centre for Textile Science and Technology, University of Minho, Campus de Azurém, 4800-058 Guimarães, Portugal

²Faculty of Textile Leather and Industrial Management, Technical University "Gh. Asachi" Iasi, Blvd. Dimitrie Mangeron, no. 29, 700050 Iasi, Romania

Corresponding author:

Elena Onofrei, Centre for Textile Science and Technology, University of Minho, Campus de Azurém, 4800-058 Guimarães, Portugal

Email: eonofrei@yahoo.com, eonofrei@tex.tuiasi.ro, eonofrei@det.uminho.pt

Introduction

Comfort sensations are classified into three main groups: thermal and moisture sensations, tactile sensations and pressure sensations. During normal wear, i.e., under steady-state conditions, comfort sensations are mostly related to tactile and pressure sensations. These are mainly determined by fabric surface structure, primarily associated with skin contact descriptors (such as smoothness or prickliness) and by clothing fit and stretch, which are related to and influence tactile sensations but also affect the ability of fabrics to dissipate heat and moisture (in vapour and liquid forms) [1]. Under transient wear conditions, caused by physical activity or weather conditions, comfort sensations are mainly related to the thermal properties, the moisture vapor resistance of clothing and the percentage of moisture accumulated inside the clothing [2]. Thus, if the clothes worn next to skin get wet, the final thermo-physiological comfort is dependent on two main factors: the thermal resistance in wet state and the active cooling resulting from the moisture evaporation from skin through the clothing and from the direct evaporation of sweat from the fabric surface [3,4]. The use of functional yarns with a thermo-regulating effect improve the thermal and moisture performance of fabrics made from the yarns, but the integration of elastic yarns into the fabric structure can impair the thermo-physiological wear comfort [5]. Therefore, the study of thermal behavioral changes due to moisture content in functional elastic fabrics, is of importance to design and predict wear comfort, particularly for sportswear applications.

There is limited literature on properties of knits from new generation fibers with elastane yarn, and most studies refer to changes in physical and dimensional characteristics of the fabrics. Knitting with elastomeric yarns usually results in a compact structure because of the yarn extension in the knitting zone, fabric relaxation after taking-off and yarn compression, which leads to changes in the loop geometry. The elastomeric yarn allows the fabric to stretch more than traditional fabrics, creates a more resilient fabric, which is resistant to snagging, fiber fatigue, pin holing and which increase the useful life of fabric [6].

Examination of inter-reliance of geometrical attributes of elastomeric knitted fabrics, particularly loop length and type of structure, and the aerodynamic and comfort properties was the subject of a previous study [7]. The results indicated that the loop length significantly influences especially the air and water vapor permeability of the fabrics, and the structure type influences the thermo-physiological comfort properties.

In this paper, the thermal comfort properties of elastic knitted fabrics produced with functional yarns with thermo-regulating effect are compared in dry and wet states, and the moisture transfer between the fabrics and a wet skin is assessed, using the indirect measuring method derived by Hes [8] for evaluating surface moisture absorptivity of the fabrics. Three parameters were used in the evaluation: thermal conductivity, thermal resistance, and thermal absorptivity. Besides the thermal properties of the fabrics, air permeability that is related to the thermal behavior was also investigated.

Materials and methods

Two functional yarns were used in this study, namely, a 30% Viscose (Outlast[®])/70% Cotton yarn, 14.7 tex, and a 100% Polyester (Dacron) Coolmax[®] yarn, 14.3 tex. These yarns were selected due to the different approach of achieving the thermo-regulating effect. Outlast[®] yarn incorporates thermally active material, i.e., paraffinic phase change material (PCM) microcapsules, within the viscose fiber structure, according to the Outlast[®] Technology, and the thermo-regulating effect results either from heat absorption or heat emission of the PCM [9, 10]. The thermoregulation effect of Coolmax[®] relies on the moisture management due to the shape of the fibers, namely multi-channel cross section (Figures 1 and 2), which applies the capillary theory and absorb sweat and moisture from the surface of the skin, transport it to the fabric surface and then evaporate [11,12].

Single Jersey fabrics incorporating the selected functional yarns, plated with elastane (Creora[®]) 77 dtex, were produced on an 8-feed Single-Jersey Circular Knitting Machine MERZ–MBS with the following characteristics: gage – E28, diameter – 13", speed – up to 1.0 m/s, number of needles – 1152. The machine setting for the loop length was the same for all fabrics.

Plating is a common technique to produce elastic knitted products, and refers to the simultaneous formation of the loop from two yarns so that one yarn will lie on the face of the fabric while the other one is fed to the needles in such a way that it forms the reverse of the fabric [13]. In this case, the elastomeric yarn was fed by using electronic feeder BTR KTF 100 HP. The plaiting yarn (elastane) appears in the back side and the ground yarn in the front side of the plain knitted fabric.

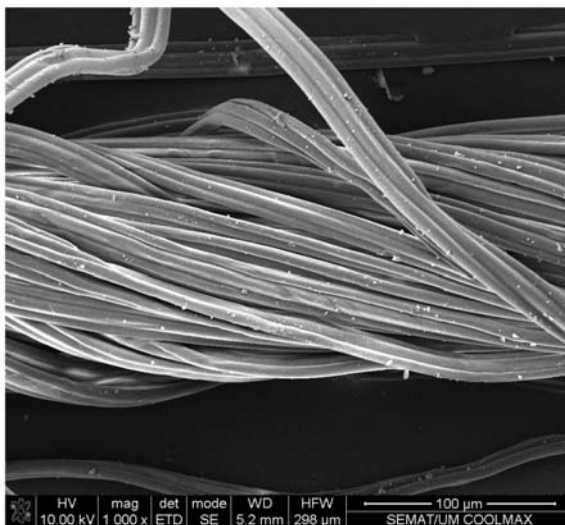


Figure 1. SEM image of Coolmax[®] yarn longitudinal view.

The characteristics of the elastic knitted fabrics produced are presented in Table 1. Maillemètre was used to determine the loop length in accordance with BS EN 14970:2006. Courses and wales densities were measured using the counting glass. Fabric weight per unit area was determined according to ISO 3801:1977 standard using an electronic balance KERN-770.

The thickness of the fabrics was determined using the SDL – Digital Thickness Gage M034A according to the standard NP EN ISO 5084:1996 and was confirmed by Alambeta results. Bulk density of the fabrics was calculated by dividing their mass per unit areas by thickness.

The bulk density is 0.238 g/cm^3 for Viscose Outlast[®] fabric, and respectively 0.279 g/cm^3 for Polyester Coolmax[®] fabric.

The thermal regulation performance of the fabric containing phase change material (PCM) microcapsules – Outlast[®] – was assessed using a DSC- Differential

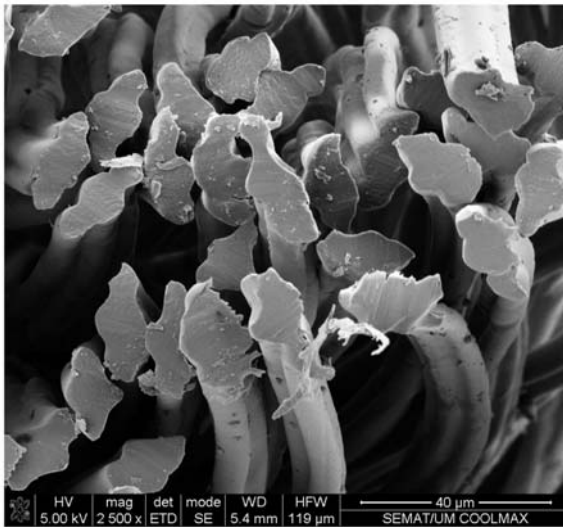


Figure 2. SEM image of Coolmax[®] yarn cross-sectional view.

Table 1. Characteristics of Viscose Outlast[®] and Polyester Coolmax[®] fabrics

	Polyester (Coolmax [®])/ Elastane (Creora [®])	Viscose (Outlast [®])/ Cotton/Elastane (Creora [®])
Loop length (mm)	2.80	2.86
Wales/cm	17.5	17.5
Courses/cm	40	40
Thickness (mm)	1.246	1.121
Mass per unit area (g/m^2)	297.08	313.20

Scanning Calorimeter (Mettler Toledo 822). Table 2 and Figures 3 and 4 present the results obtained.

When the fabric is heated in the PCM temperature transition interval (20–33°C), it absorbs heat energy (2.02 J/g) as the PCM moves from a solid state to a liquid state. This phase change produces a temporary cooling effect in the clothing layers. Once the PCM completely melted the heat accumulation stops, the cooling effect ceases and the textile material behaves as plain fabric that has a certain capacity of thermal insulation. If the PCM garment is worn in a cold environment where the fabric temperature drops below the transition temperature, the microencapsulated liquid PCM will change back to a solid state, generating heat energy (2.38 J/g) and a temporary warming effect.

Air permeability was evaluated according to standard ISO 9237:1995 using a Textest FX-3300 air permeability tester. The air pressure differential between the two surfaces of the material was 100 Pa.

The thermal properties in dry and wet states were evaluated using the Alambeta instrument according to standard ISO 11092:1993. The measuring head temperature of the Alambeta was approximately 32°C and the contact pressure 200 Pa in all cases.

Measuring the thermal properties of wet fabrics requires a rapid technique, especially with specimens containing higher amounts of water, to prevent moisture redistribution during the test [14]. As test duration in the Alambeta instrument is below 180 seconds, a reliable measurement of fabric thermal properties in wet state can be obtained. In this test, the fabrics were cut into circular samples of 100 cm² and the dry weight was recorded. Then, the samples placed on a horizontal surface were wetted with distilled water. The water weight added to the fabric was equal to 115% of the dry sample weight (considered for dripping wet). To get different percentages of moisture in the fabrics, samples were left to dry on the plate of the balance in standard ambient conditions. Before each test, sample weight was recorded and the moisture content relative to initial weight was calculated.

Table 2. Outlast[®] fabric thermal regulation characteristics

	Peak temperature (°C)	Onset temperature (°C)	Endset temperature (°C)	Temperature transition interval	Total heat (J/g)
Heating in the interval 0–50°C, temperature rate 5°C/min	24.79	21.86	26.67	20-33	2.02
Cooling in the interval 50–0°C, temperature rate 5°C/min	22.52	26.50	15.20	33-15	2.38

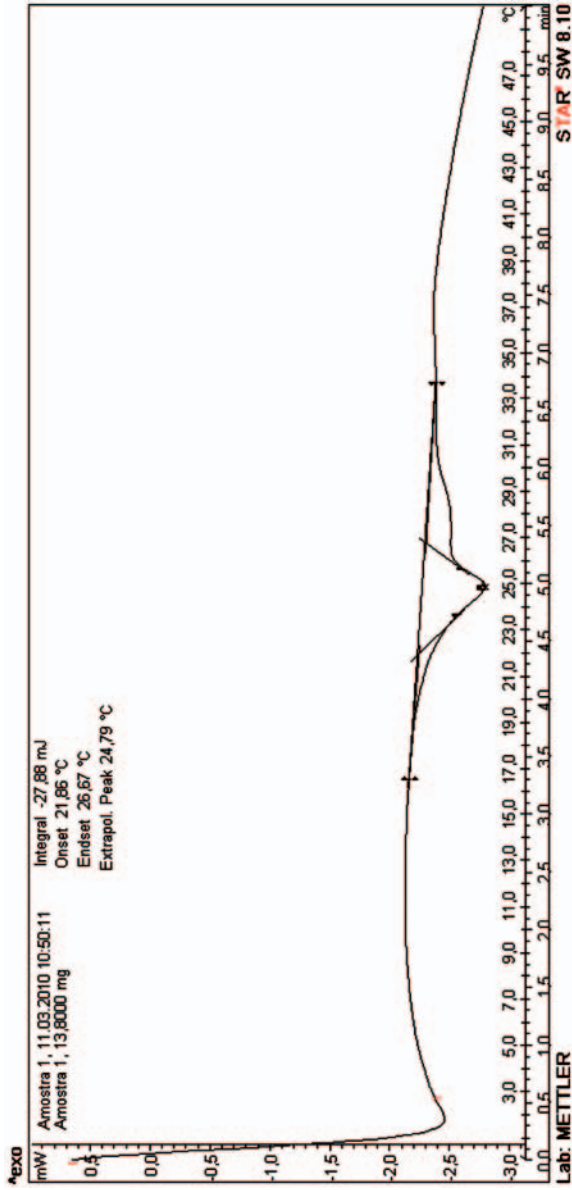


Figure 3. DSC heating curve.

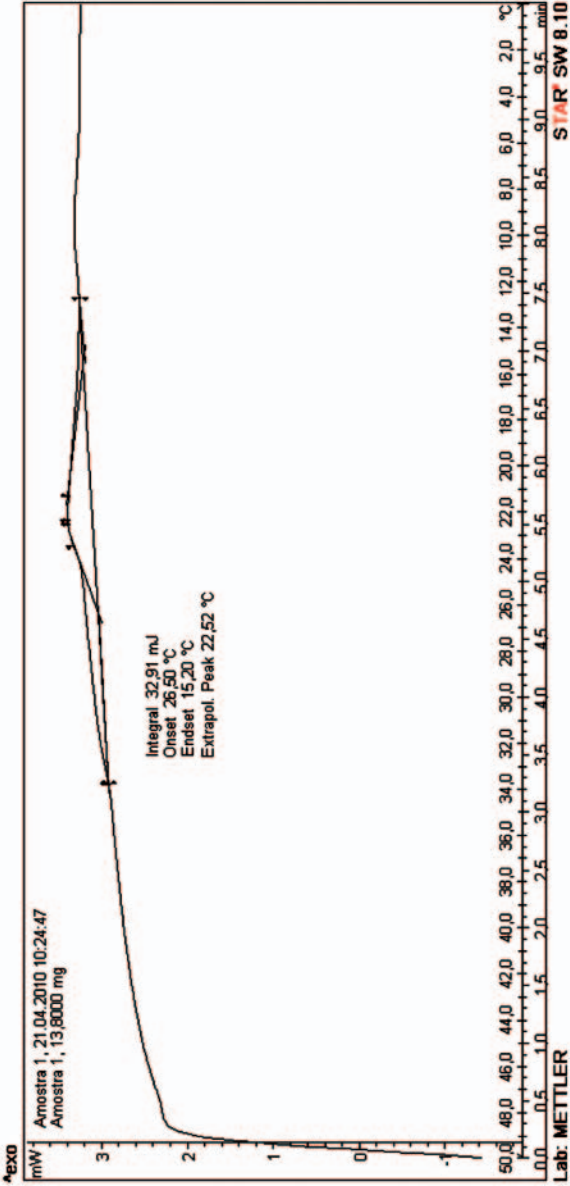


Figure 4. DSC cooling curve.

The surface moisture absorptivity of the fabrics was determined using the indirect method proposed by Hes [8]. To simulate the effect of a sudden sweat discharge onto the skin, a 0.06 mm thick 100% polyester woven fabric, was used as interface and a volume of 0.4 ml of water was placed on the center of the surface of this interface fabric. Within less than 1 minute the liquid distributed uniformly within a circle of approximately 50 mm (to cover the area of $25 \times 25 \text{ mm}^2$ of the heat flux sensors of Alambeta instrument).

All tests were performed under standard ambient conditions ($20 \pm 2^\circ\text{C}$ and $65 \pm 2\%$ R.H).

The statistical evaluation of the data obtained was performed using PASW Statistics 17 software package.

Results and discussion

Knitted fabric properties in dry state

Air permeability: The air permeability of Coolmax[®] fabric is lower than that of Outlast[®] fabric (Figure 5). This is most probably due to the higher thickness of the fabric and to the geometry of fibers. The higher surface area of the Coolmax[®] fiber increases the resistance to air flow, which results in lower air permeability.

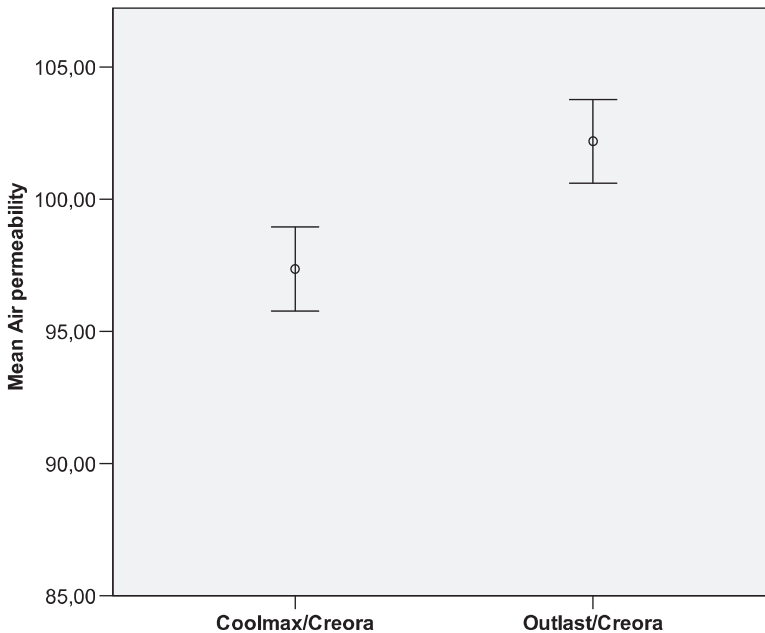


Figure 5. Air permeability in dry state – l/m²/s.

Thermal properties: ANOVA analysis showed that there are statistically significant differences between thermal conductivity, thermal resistance and thermal absorptivity of Coolmax® and Outlast® fabrics in dry state, with a significance level of 95%. Figures 6, 7, and 8 illustrate the differences between the two fabrics.

Thermal conductivity of a fabric represents the ability of the fabric to transport heat and results from the combination of fibers conductivity and structural characteristics of the fabric [15,16].

As it can be observed in Figure 6, the thermal conductivity of Coolmax® fabrics is lower than the Outlast® ones and the ‘spread’ of the data, as measured by the interquartile range (IQR), is approximately the same for both fabrics. Due to the high homogeneity of structural parameters of the fabrics (Table 1), the intrinsic fiber properties such as composition (inclusive the PCM presence), porosity, density and structure are the relevant factors responsible for the difference observed between both fabrics.

As expected due to the previous behavior, Coolmax® fabrics have higher thermal resistance than the Outlast® ones (Figure 7). Moreover, the magnitude of variation in thermal conductivity and thermal resistance values between both fabrics is similar (respectively, a decrease or an increase of approximately 130%). Fiber intrinsic properties, namely fiber conductivity and yarns/fabrics structural characteristics, particularly thickness of the fabric, are the main factors determining, respectively, thermal conductivity and resistance in dry state.

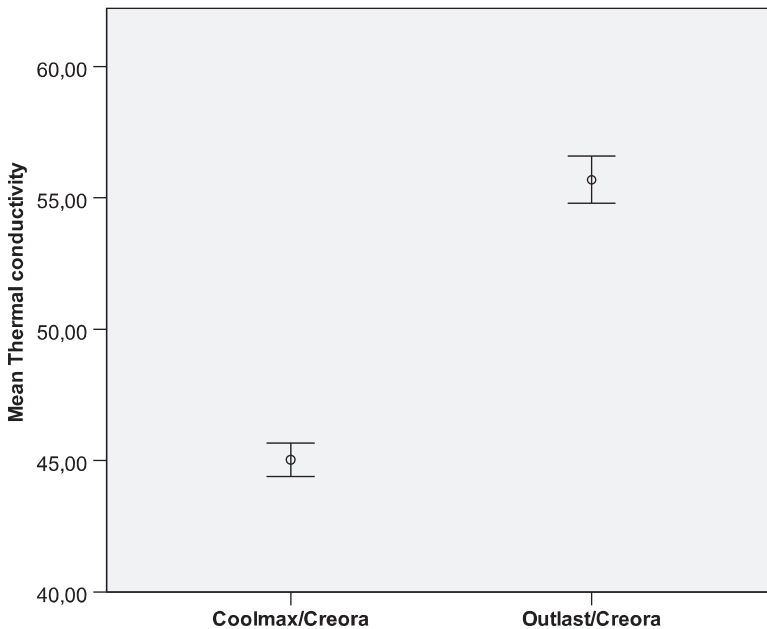


Figure 6. Thermal conductivity in dry state λ ($\times 10^{-3}$), W/mK.

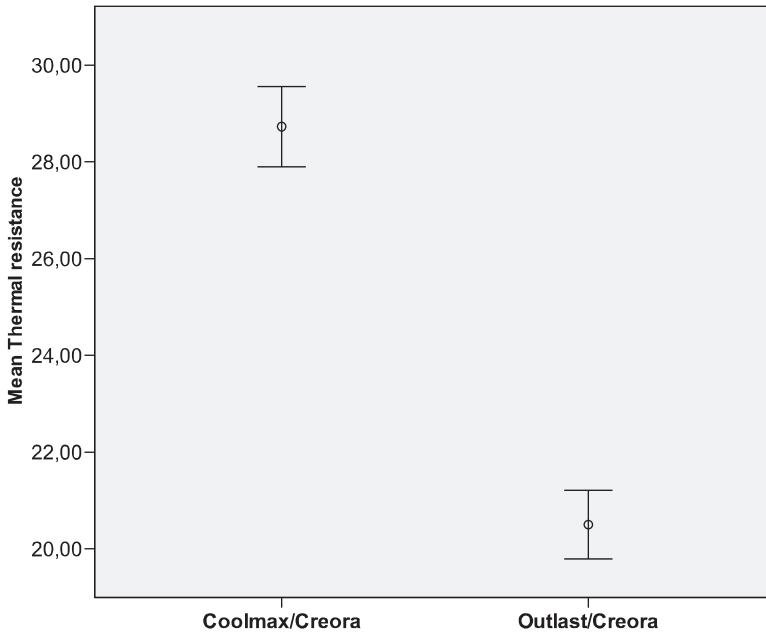


Figure 7. Thermal resistance in dry state R ($\times 10^{-3}$), m^2K/W .

Thermal absorptivity is directly related with heat flux and is a surface-related parameter. It represents the objective measurement of the warm-cool feeling of fabrics. When an individual touches a fabric whose temperature is different from that of the skin, heat exchange occurs between the two surfaces [16]. Experiments demonstrated that, in dry state, thermal absorptivity of the fabrics varies between 20 and 300 $Ws^{1/2}/m^2K$ and these values increase to 330–750 $Ws^{1/2}/m^2K$ when they get superficially wet. For some woven and knitted fabrics in wet state the thermal absorptivity can be higher even than 1000 $Ws^{1/2}/m^2K$. The higher this value is, the cooler the feeling at first contact. In general, fibers with higher moisture regain promote a cooler feeling [17–19].

From Figure 8, it is apparent that the knitted fabrics made of yarns integrating Outlast[®] exhibit higher thermal absorptivity values, thus giving a cooler feeling at first contact with the skin. Once again the magnitude of the variation observed on thermal absorptivity between both fabrics is approximately 130%.

Knitted fabric properties in wet state

Air permeability, thermal conductivity, resistance and absorptivity were measured in both fabrics for different amounts of water added, expressed as percent excess moisture, i.e., the water content above equilibrium regain (throughout this article called, moisture content) ranging from 5% to 115%.

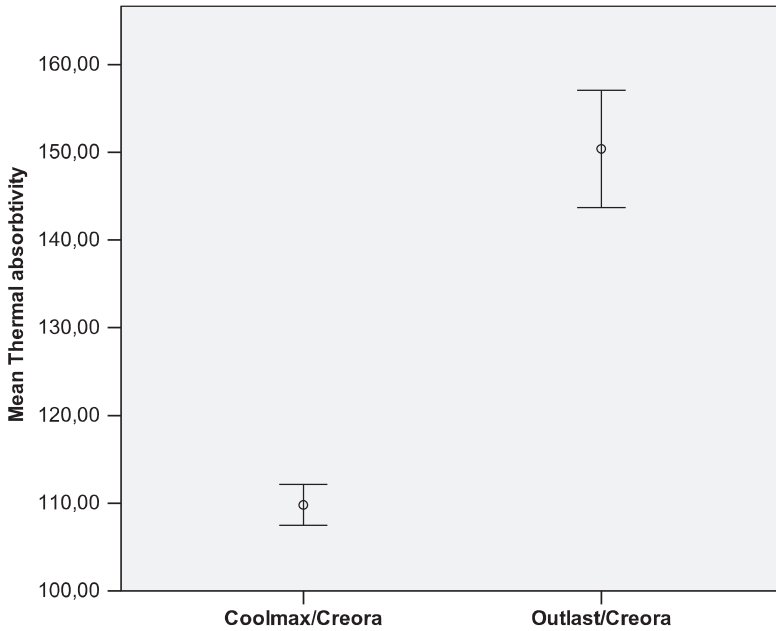


Figure 8. Thermal absorptivity in dry state b, $W s^{1/2}/m^2 K$.

According to Hollies et al. [20], the sweating sensation could be artificially generated by adding approximately 20% of water to the fabrics. Thus, this limit will be considered in this study as a starting point to provide the ‘sweating sensation.’

Air permeability: The results of measurement of air flow through wet fabrics show that with increasing fabric moisture the air flow decreases (Figure 9). The reduction in fabric porosity due to fiber swelling for Outlast® fabric, and the replace of air in the void spaces with water are responsible for this behavior. The relationship between fabric moisture and air permeability was linear up to 80–90% of fabric humidity. At higher moisture level water creates continuous film and the transfer of air through fabric is limited.

Thermal properties: The relationship between the thermal conductivity and the moisture content on both fabrics is illustrated in Figure 10.

As can be seen from the graph in Figure 10, both fabrics in wet state have higher values of thermal conductivity than in dry state. This is an expected result as the thermal conductivity and thermal capacity of water is much higher than those of the fibres and air entrapped within the fabric, which leads to a higher heat conduction. However, the thermal conductivity behavior of the studied fabrics with moisture content is markedly different.

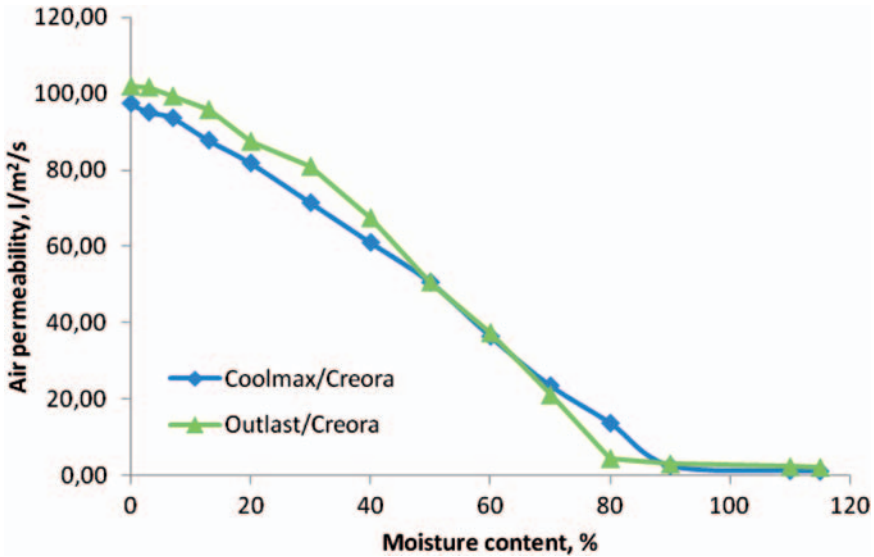
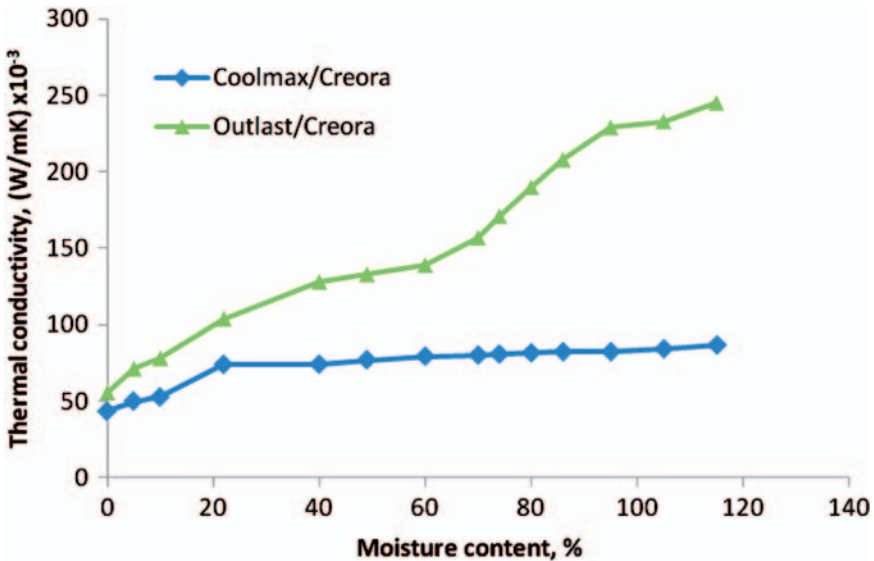


Figure 9. Air permeability of fabrics in wet state.



In the Outlast[®] fabric, the thermal conductivity significantly increases with moisture content of the fabric with a high nonlinear behavior. In the Coolmax[®] one, the increase in thermal conductivity with moisture content is rapidly for a small quantity of water in the structure and is not significant for moisture content

higher than 22%. These disparate behaviors can be explained in terms of different amount of water retained and different types of water held within the fibers and fabrics. The water can be absorbed into the fiber structure (in the case of Outlast[®] material), retained as water vapors (saturated air) in the pores or as free water between fibers and yarns.

The thermal conductivity behavior of Outlast[®] fabric seems to follow a four-step process: the first one taking place between 0% and 40% moisture contents, the second one from 40% to 60%, the third one until 95% moisture content and another from this value on. At lower moisture content the water is mostly absorbed within the fibers structure and the thermal conductivity of the fabric increases linearly with the moisture content increase. Between 40% and 60% moisture content is observed a stabilization of thermal conductivity. At higher moisture contents (from 60%) a steep increase on thermal conductivity values is observed until 95% (which most probably corresponds to fabric saturation) followed by a smooth slope up above this point. Moisture sorption and diffusion until saturation as well as additional moisture in liquid form (free water) onto the surface, seem to trigger and steer this behavior.

The change of thermal properties of Outlast[®] fabric due to increased moisture content will influence also the thermo-regulating effect. With increase moisture content increases the thermal conductivity (i.e., the rate of temperature change of PCM during the transition) and reduces the actuation time of PCM.

For Coolmax[®] fabric (nonabsorbent fibers) a small quantity of water in the structure at the initial stage, 0–22%, will cause the heat flux through the fabric to increase rapidly due to water on the fiber surfaces. The thermal conductivity behavior of Coolmax[®] fabric with moisture content above 22% is fairly linear and constant. This can be explained by the hydrophobic character and the special design of the constituent fibers. Moisture diffusion seems to be assured by the capillary effect of the fibers and the void spaces of fiber and fabric structures, which lead to nonsignificant changes in the thermal conductivity with the moisture content of the fabric.

The amount of internal energy stored per unit volume at different moisture contents was calculated according to Hes et al. [17] for both fabrics, and is illustrated in Figure 11.

Thermal capacity of Outlast[®] fabric increases until 70%, remaining almost constant until 115%. As it can be seen between 40% and 60% moisture contents the rate of increase of the thermal capacity of Outlast[®] fabric is reduced. Accessibility of the fabric to moisture is most likely reduced due to fiber swelling, leading to a higher accumulation of moisture onto the fabric surface and heat transfer takes place mainly on fabric surface, which reduces the rate of increase of thermal capacity.

Thermal capacity of Coolmax[®] fabric increases linear with the moisture content.

The relationship between the thermal resistance and the moisture content of both fabrics is shown in Figure 12.

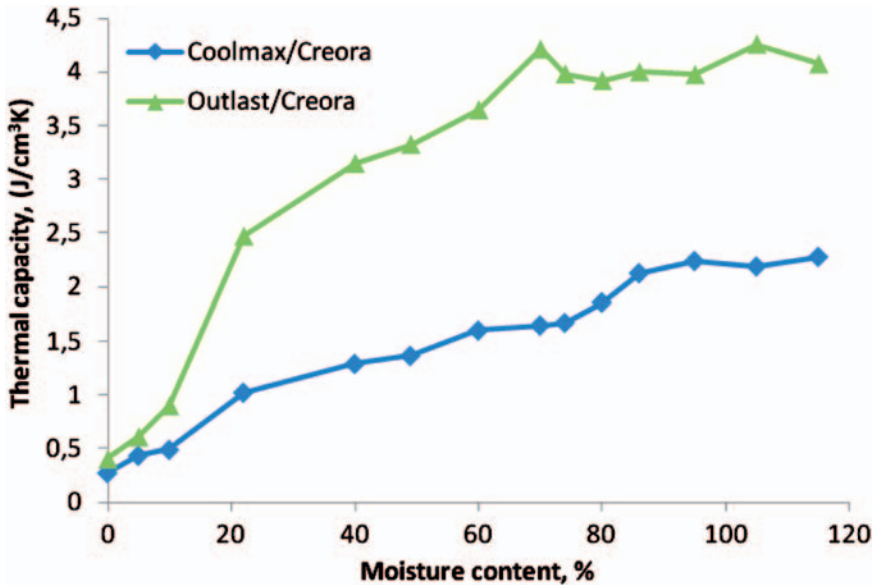


Figure 11. Thermal capacity of fabrics in wet state.

As it can be seen from the graphs, the thermal resistance for both fabrics is lower in wet state than in the dry state. Once again the behavior with moisture content is different for both fabrics. In the Outlast[®] fabric a significant decrease on thermal resistance is observed up to about 40% moisture content, which stabilizes between 40% and 60% and gradually decreases after this moisture content. The thermal resistance of the Coolmax[®] fabric with moisture content follows a similar trend to the one observed with thermal conductivity: thermal resistance variation with moisture content is not significant above 22% moisture content.

The influence of moisture content on the thermal absorptivity of fabrics is illustrated in Figure 13. As it can be depicted from the graphs, an increase in moisture content leads to an increase of the thermal absorptivity for both fabrics. This parameter is greatly influenced by the surface character of the fabric and by the fibre/yarn ability to absorb and diffuse water. In the Coolmax[®] fabric a gradual slope up increase is observed with moisture content. The thermal absorptivity behavior of Outlast[®] fabric follows a trend line similar to the one observed in thermal conductivity. As thermal absorptivity is directly related with thermal conductivity and thermal capacity of the fabric, this is an expected result.

Surface moisture absorptivity: The surface moisture absorptivity of the fabric under test was assessed measuring the thermal absorptivity of the set 'fabric under test-interface fabric.' The resulting thermal absorptivity is related to the amount of liquid kept in the interface fabric due to the poor moisture absorption of the fabric under test.

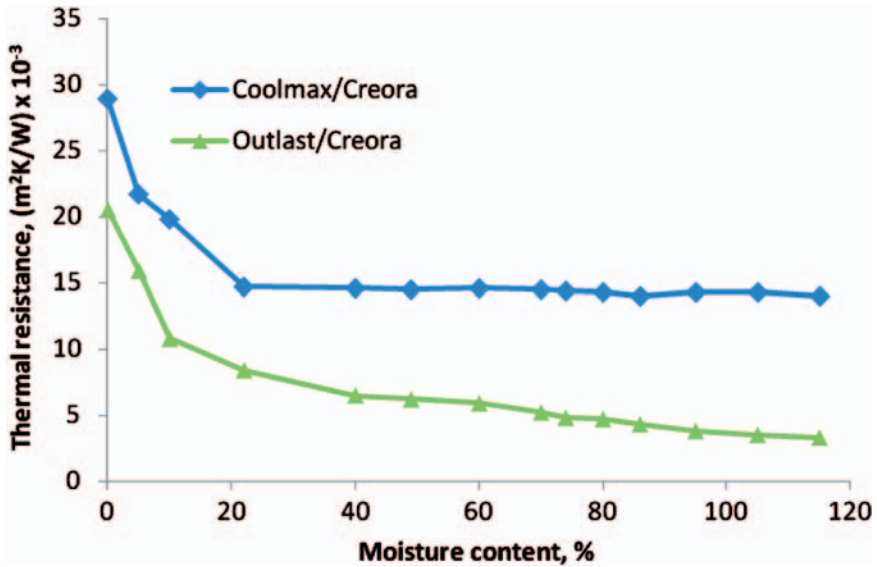


Figure 12. Thermal resistance of fabrics in wet state.

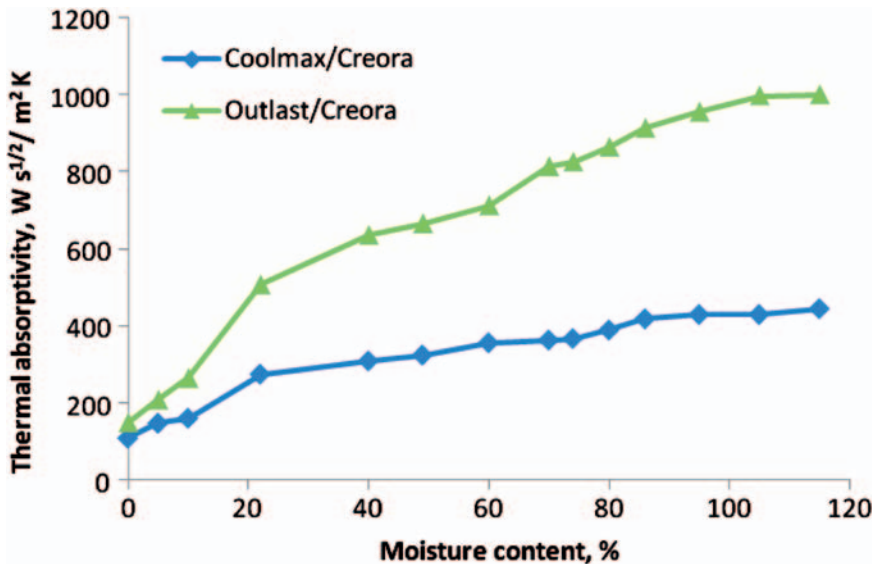


Figure 13. Thermal absorptivity of fabrics in wet state.

Figure 14 compares the thermal absorptivity of Outlast[®] and Coolmax[®] fabrics obtained in dry state and by simulating a sudden sweat discharge (with interface fabric). The results obtained indicate that, in a sudden contact with a wetted surface, the Coolmax[®] fabric has lower thermal absorptivity than the Outlast[®] one

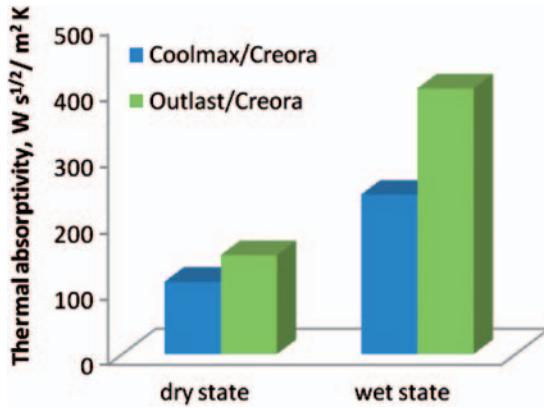


Figure 14. Comparison between the thermal absorptivity of fabrics in dry state and after sudden contact with a wet skin (simulated).

and thus poor surface moisture absorptivity. As most of the liquid is kept in the interface fabric a warmer feeling is given by the Coolmax[®] fabric.

Conclusions

The thermal comfort properties of functional elastic knitted fabrics produced from Coolmax[®] and Outlast[®] yarns have been studied and analyzed. The knitted fabrics were produced with identical constructional parameters and the tests were performed in dry and in wet states.

In dry state, the Coolmax[®] fabric exhibited higher thermal resistance, lower thermal conductivity and lower thermal absorptivity when compared with the Outlast[®] one. Due to the high homogeneity of structural parameters of fabrics, it is apparent that thermal conductivity and hygroscopicity of the constituent fibers determined different thermal properties. The air permeability of Coolmax[®] fabric is lower due to the higher thickness of the fabric and to geometry of fibers.

The air permeability of wet fabrics decreases with increasing fabric moisture. The reduction in fabric porosity due to fiber swelling for Outlast[®] fabric, and the replace of air in the void spaces with water are responsible for this behavior.

In wet state, higher thermal conductivity and absorptivity and lower thermal resistance were registered for both fabrics, when compared to the dry state. For the Coolmax[®] fabric, the effect of increasing moisture content above the 'sweating sensation' was not significant on thermal conductivity and resistance. In the Outlast[®] one, moisture content increase significantly raised thermal conductivity, and to a lesser extent, decreased the thermal resistance. The thermal absorptivity increase with moisture content was steeper on the Outlast[®] fabric.

From the results obtained it is apparent that Outlast[®] fabrics are more prone to significant thermal properties changes due to moisture uptake than the Coolmax[®]

ones. In addition, 60% moisture content seems to be the threshold to major changes on Outlast[®] fabrics thermal properties.

These findings help in designing a product with the most suitable material or combination of materials for sportswear applications, where wear comfort is an important issue. Different solutions can be devised depending on weather or ambient conditions, on the intensity level of the activity to be performed and on the body areas that will be covered by the clothing.

Acknowledgement

This work was conducted under support of FCT – *Fundação para a Ciência e a Tecnologia* and 2C2T – *O Centro de Ciência e Tecnologia Têxtil*, Universidade do Minho, Portugal, within the framework of ‘*Ciência 2008*’ Program.

References

- [1] Li Y. The science of clothing comfort. *Textile Progress* 2001; 31(1/2), ISBN: 1870372247.
- [2] Fan J and Tsang HWK. Effect of clothing thermal properties on the thermal comfort sensation during active sports. *Text Res J* 2008; 78(2): 111–118.
- [3] Hes L. Non-destructive determination of comfort parameters during marketing of functional garments and clothing. *Ind J Fibers Text Res* 2008; 33(3): 239–245.
- [4] Haghi AK. Moisture permeation of clothing - A factor governing thermal equilibrium and comfort. *J Therm Anal Calorim* 2004; 76(3): 1035–1055.
- [5] Shishoo R. *Textiles in sports*. Cambridge: Woodhead Publishing Limited, 2005.
- [6] Pavko-Cuden A and Angelova Y. The thickness measurement of weft knitted structures made with elastomeric yarns. Scientific Bulletin of “Gheorghe Asachi” Technical University of Iasi, Textile Section, 2010, Vol. LVI, pp. 23–28.
- [7] Onofrei E, Rocha AM and Catarino A. Thermal comfort properties of knitted fabrics made of elastane and bioactive yarns. In: *Proceedings of the Fiber Society Spring 2010 International Conference on Fibrous Materials*, Bursa, Turkey, 12–14 May, 2010, pp. 145–146.
- [8] Hes L. Fast determination of surface moisture absorptivity of smart underwear knits. In: *International Textile Conference*, Terrassa, 2001.
- [9] Erkan G. Enhancing the thermal properties of textiles with phase change materials. *Res J Text Apparel* 2004; 8(2): 57–64.
- [10] <http://www.outlast.com> (accessed on 17 February 2009).
- [11] <http://coolmax.invista.com> (accessed on 17 February 2009).
- [12] Li D and Ni M. Moisture properties of Coolmax[®] fiber blended with regenerated cellulose fibers. In: *Second International Conference on Information and Computing Science*, 2009, Vol. 2, pp. 129–131, <http://doi.ieeecomputersociety.org/10.1109/ICIC.2009.141>.
- [13] Ben Abdesslem S, Ben Abdelkader Y, Mokhtar S and Elmarzougui S. Influence of elastane consumption on plated plain knitted fabric characteristics. *J Eng Fibers Fabrics* 2009; 4(4): 30–35.
- [14] Haghi AK. Mechanism of heat and mass transfer in moist porous materials. *Jurnal Teknologi* 2002; 36(F): 1–14.

- [15] Holcombe BV and Hoschke BN. Dry heat transfer characteristics of underwear fabrics. *Text Res J* 1983; 53: 368–374.
- [16] Frydrych I, Dziworska G and Bilska J. Comparative analysis of the thermal insulation properties of fabrics made of natural and man-made cellulose fibres. *Fibres Text East Eur* 2002; 10(4/39): 40–44.
- [17] Hes L, Offerman P and Dvorakova I. The effect of underwear on thermal contact feeling caused by dressing up and wearing of garments. In: *Proceedings of Tecnitex 2001 Autex Conference*, 2001, pp. 236–245.
- [18] Hes L. An indirect method for the fast evaluation of surface moisture absorptiveness of shirt and underwear fabrics. *Vlaknaa Textil* 2000; 7(2): 91–96.
- [19] Hes L. Optimisation of shirt fabrics composition from the point of view of their appearance and thermal comfort. *Int J Cloth Sci Technol* 1999; 11(2/3): 105–115.
- [20] Li Y and Wong ASW. *Clothing biosensory engineering*. Cambridge: Woodhead Publishing Limited, 2006.

Journal of Industrial Textiles

<http://jit.sagepub.com/>

Study of heat transfer through multilayer protective clothing at low-level thermal radiation

Elena Onofrei, Stojanka Petrusic, Gauthier Bedek, Daniel Dupont, Damien Soulat and Teodor-Cezar Codau

Journal of Industrial Textiles published online 7 April 2014

DOI: 10.1177/1528083714529805

The online version of this article can be found at:

<http://jit.sagepub.com/content/early/2014/04/07/1528083714529805>

Published by:



<http://www.sagepublications.com>

Additional services and information for *Journal of Industrial Textiles* can be found at:

Email Alerts: <http://jit.sagepub.com/cgi/alerts>

Subscriptions: <http://jit.sagepub.com/subscriptions>

Reprints: <http://www.sagepub.com/journalsReprints.nav>

Permissions: <http://www.sagepub.com/journalsPermissions.nav>

Citations: <http://jit.sagepub.com/content/early/2014/04/07/1528083714529805.refs.html>

>> [OnlineFirst Version of Record](#) - Apr 7, 2014

[What is This?](#)

Study of heat transfer through multilayer protective clothing at low-level thermal radiation

0(00) 1–17

© The Author(s) 2014

Reprints and permissions:

sagepub.co.uk/journalsPermissions.nav

DOI: 10.1177/1528083714529805

jit.sagepub.com



Elena Onofrei^{1,2}, Stojanka Petrusic^{3,4}, Gauthier Bedek¹, Daniel Dupont¹, Damien Soulat^{3,4} and Teodor-Cezar Codau^{3,4}

Abstract

The goal of this research is to develop a mathematical model of heat transfer in protective garments exposed to routine fire environment (low level of radiant heat flux) in order to establish systematic basis for engineering materials and garments for optimum thermal protective performance and comfort. In the first stage, this paper focuses on the formulation of heat transfer model suitable for predicting temperature and heat flux in firefighter protective clothing, using COMSOL Multiphysics[®] package based on the finite element method. Computational results show the time variation of the temperature at the inner face of the protective clothing system during the exposure to a low-radiant heat flux as well as during the cooling-down period. Model predictions of the temperature agreed very well with the experimental temperature. In the second stage of this study, in order to predict the first and second-degree burns, the model of heat transfer through multilayer protective system was coupled with the heat transfer model in the skin. The Pennes model was used to model heat transfer in the living tissue. The duration of exposure during which the garment protects the firefighter from getting first and second-degree burns is numerically predicted using Henriques equation. The results demonstrated that even for a low-level thermal radiant heat flux, a typical three-layer thermal protective clothing system is required to protect the wearer from skin burn injury.

¹Lille Catholic University, HEI, GEMTEX, Lille, France

²Technical University “Gheorghe Asachi” of Iasi, Iasi, Romania

³University of Lille Nord de France, Lille, France

⁴ENSAIT, GEMTEX, Roubaix, France

Corresponding author:

Elena Onofrei, Université Catholique de Lille, 13 Rue de Toul Lille, 59046 France.

Email: eonofrei@yahoo.com

Keywords

Heat transfer, firefighter protective clothing, numerical model, skin burn injury

Introduction

Thermal comfort of the protective clothing is a topic of active research. According to generally accepted definition given by American Society of Heating, Refrigerating, and Air Conditioning Engineers, thermal comfort is “the condition of mind that expresses satisfaction with the thermal environment” [1]. Nonetheless, the concept of thermal comfort is not solely in a subjective domain since it depends on physiological processes in the body to a certain extent. It is in direct relation with a heat balance of the human body, i.e. the processes that lead to heat production and heat loss. The summary of the heat balance of the human body can be described using the following equation [1,2]:

$$S = M - W - C - R - K - E - RES \quad (1)$$

where S (W/m^2) is the heat storage in the body, M (W/m^2) the metabolic heat production, W (W/m^2) the external mechanical work, C (W/m^2) the heat loss by convection, R (W/m^2) the heat loss by radiation, K (W/m^2) the heat loss by conduction, E (W/m^2) the evaporative heat loss from skin, and RES (W/m^2) the heat loss from respiration.

The terms used in the heat balance depend on a number of factors that could be classified into environmental, physiological, and clothing factors. Therefore, the role of protective clothing in high-risk profession as firefighting is of crucial significance for the thermal comfort of a wearer and its performance.

When firefighters are exposed to a heat source, their body reacts by activating sweat glands, i.e. through evaporative cooling mechanism. The protective clothing protects the firefighters from environmental heat and moisture but simultaneously prevents their flow in opposite direction, away from the body to the environment. Consequently, risks of heat stress and steam burn injuries strongly increase. In hot environments, heat and moisture transfer properties of the protective clothing have a prevailing impact on firefighters' performances and their safety. Optimization of these coupled transfer phenomena from the skin through the garment could improve comfort of the wearers and hence their performance. Effective protective clothing should minimize heat stress while providing protection [3].

The physical model of a firefighter in a firefighting environment consists of three parts that are linked by heat and mass transfer: the human body that produces heat (metabolic heat) and water (sweat), the heat source from the environment, and the protection system (Figure 1).

During the last decade, numerous studies have been carried out regarding the design and the mathematical modeling of different aspects of the physical behavior of the protective clothing [4–7]. Two types of mathematical models have been developed: those that only consider heat transfer [7–13] and those that consider

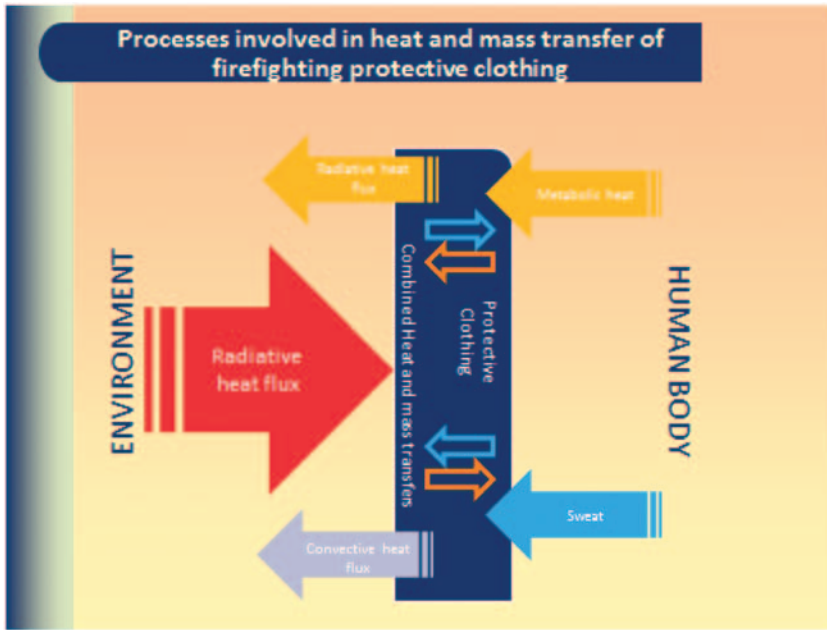


Figure 1. Processes involved in heat and mass transfer of firefighting protective clothing.

heat and moisture transfer [4,5,14–18]. All these studies refer to emergency conditions, which, according to Mäkinen [19], imply extreme heat fluxes in the range from 8.37 to 125.6 kW/m² and air temperatures in the range from 300 to 1000°C. Emergency conditions are quite rare, and firefighters are most frequently exposed to routine and hazardous conditions [3]. Routine corresponds to a common intervention environment for fire fighters with low-radiant heat flux from 0.42 to 1.26 kW/m² and air temperatures in the range from 10 to 60°C. Hazardous represents an intervention environment with high-radiant heat flux from 1.26 to 8.37 kW/m² and air temperatures in the range from 60 to 300°C [19]. Data obtained over the years show that most burn injuries sustained by firefighters occurred in thermal environments with low-radiation level (classified as routine or hazardous conditions), as a result of prolonged exposure. Only a few studies have been conducted on thermal protective performance with prolonged exposure to these conditions. The goal of this research is to develop a mathematical model of heat transfer in protective garments exposed to routine fire environment, the most common conditions in the firefighters work. In such conditions, the most important phenomenon, which significantly affects the thermal comfort, is the heat transfer (often the phenomenon of sweating may be missing). In this study, only heat transfer is taken into account whereas the influence of moisture is not considered. The COMSOL Multiphysics[®] package that uses the finite element method (FEM) was used to simulate heat transfer in protective clothing during low-radiant flux exposure.

Table 1. Physical and thermal properties of monolayers.

Property	Outer shell	Thermal liner	Moisture barrier
Fabric type	Woven	Nonwoven	Knitted (coated)
Composition	100% Aramid	100% Aramid	Polyurethane coated 100% Aramid
Thickness (mm)	0.5 ± 0.01	1.46 ± 0.03	0.47 ± 0.00
Surface weight (g/m^2)	242 ± 2	98 ± 2	195 ± 2
Density (kg/m^3)	489 ± 5	67 ± 2	418 ± 6
Thermal conductivity ($\text{W}/\text{m K}$)	0.1154 ± 0.0018	0.0633 ± 0.0015	0.0900 ± 0.0001
Thermal diffusivity (mm^2/s)	0.248 ± 0.013	0.449 ± 0.001	0.213 ± 0.000
Specific heat capacity ($\text{J}/\text{kg K}$)	951 ± 44	2113 ± 89	1011 ± 3

Approach and methodology

Materials

The fabrics selected for experiments are commonly used as high-performance fabrics in the thermal protective clothing field. The multilayer system consists of three fabric layers: outer shell, thermal liner, and moisture barrier.

General physical and thermal properties of monolayers are displayed in Table 1.

Thickness of the monolayers was measured under the pressure of 1 ± 0.01 kPa, according to the standard ISO 5084:1996. Density was calculated from the values of fabric monolayer thickness and surface weight (determined using an analytical balance). The average of 10 measurements was calculated.

The thermal properties of the fabric samples were measured with the Hot Disk TPS 2500 S instrument in agreement with the standard ISO 22007-2:2008 [20]. For each monolayer, three measurements were performed, and then the average of the measured parameters was calculated.

To simplify the formulation, the textile layers were considered homogeneous.

Numerical model of heat transfer

The first part of this study focuses on the formulation of the heat transfer model suitable for predicting temperature and heat flux in firefighter protective clothing. In order to validate the model by comparing the predicted values with the experimental results, the experimental setup of ISO 6942-2002 was used (Figure 2).

Due to the length scales of clothing thickness compared to their surface, a one-dimensional model is adopted as a valid assumption (the direction normal to the clothing surface).

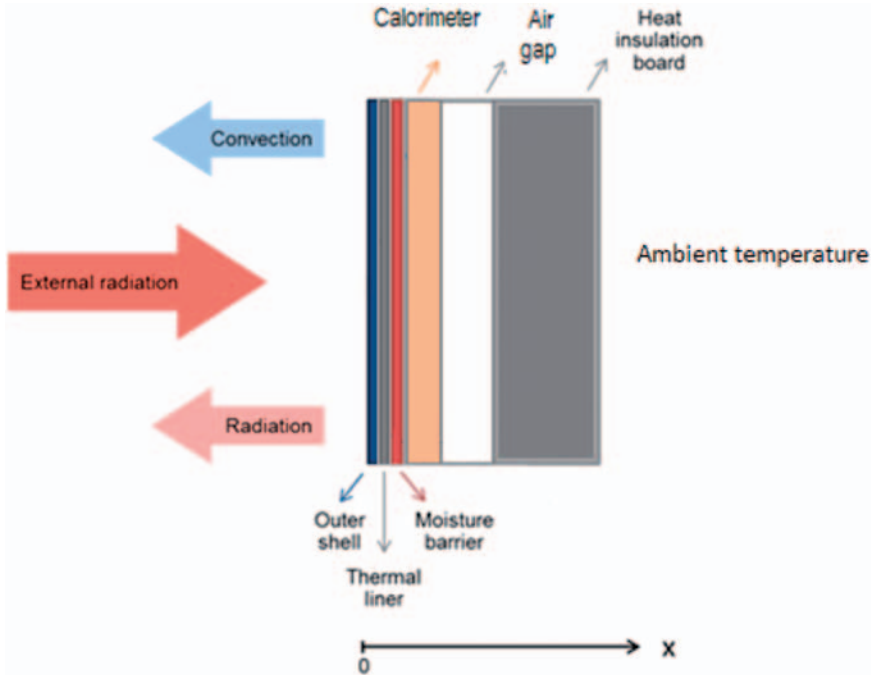


Figure 2. Scheme of the experimental setup used for evaluation of the material assemblies when exposed to a source of low-radiant heat flux.

For the development of the numerical model, it was supposed that the temperature depends only on time and position, $T(t, x)$. Heat conduction and penetrating radiation through solid phase are considered for heat transfer within the fabric. Radiative heat transfer in the fabric is accounted for by introducing in the energy equation a source term similar to that in Torvi's model [8]. It is assumed that radiation penetrates through the outer layer of the fabric only. The conductive and radiation heat transfer mechanisms are considered through the air gap. Heat conduction was considered through the copper plate and insulation board. No external air flow was considered in the model. The evaporative heat was not considered in the present model because the influence of sweating has been not taken into account. All textile structures used are aramid fabrics, so the amount of water regain in the fibers is small (maximum 3–4%), and consequently, the heat of evaporation can be neglected. The evaporation rate of water retained in the fiber was measured experimentally, and a value of $0.0025 \text{ g/m}^2\text{s}$ was obtained. This evaporation rate multiplied by the latent heat of evaporation of water gives the total energy used to evaporate this amount of water. The value obtained is 5.6 W/m^2 , a value which can be neglected in comparison with the value of the incident flux.

The energy balance in the infinitesimal element of the fabric, for one-dimensional heat transfer, can be described in the form of differential equation

$$\rho c_p \frac{\partial T}{\partial t} = -\frac{\partial}{\partial x} \cdot \left(-k \frac{\partial T}{\partial x} \right) + \gamma q_{\text{rad}} e^{-\gamma x} \quad \text{for } 0 < t \leq t_{\text{exp}} \quad (2)$$

$$\rho c_p \frac{\partial T}{\partial t} = -\frac{\partial}{\partial x} \cdot \left(-k \frac{\partial T}{\partial x} \right) \quad \text{for } t > t_{\text{exp}}$$

where ρ is the density (kg/m^3), c_p the heat capacity at constant pressure (J/kg K), k the thermal conductivity (W/m K), γ the extinction coefficient of the fabric ($1/\text{m}$), q_{rad} the incident radiation heat flux (W/m^2), t_{exp} the time of exposure, and x the linear horizontal coordinate.

The extinction coefficient that characterizes the decrease of thermal radiation as it penetrates into the fabric is given as

$$\gamma = \frac{-\ln(\tau)}{l_{\text{fab}}} \quad (3)$$

where τ is the transmissivity of the fabric and l_{fab} is the fabric thickness.

The boundary conditions: A constant inward heat flux, convective, and radiant heat transfers are assumed on the left external boundary and constant temperature (ambient temperature) on the right side.

The general inward heat flux Q (W/m^2) represents a heat flux that enters into domain.

The emitted thermal radiate heat flow is defined as

$$Q_{\text{rad-out}} = \varepsilon \sigma (T_{\text{amb}}^4 - T_{\text{surf}}^4) \quad (\text{W/m}^2) \quad (4)$$

where ε is the emissivity of the fabric, σ the Stefan–Boltzmann constant ($\text{W/m}^2\text{K}^4$), T_{surf} the surface temperature (K), and T_{amb} the ambient temperature (K).

Natural convection heat transfer due to the temperature gradient between the surface and the environment occurs

$$Q_{\text{conv}} = h_c (T_{\text{amb}} - T_{\text{surf}}) \quad (\text{W/m}^2) \quad (5)$$

where h_c is natural convection heat transfer coefficient ($\text{W/m}^2\text{K}$) that is calculated using the definition of the Nusselt number:

$$h_c = \text{Nu} \frac{k_{\text{air}}}{L} \quad (\text{W/m}^2\text{K}) \quad (6)$$

where Nu is the Nusselt number, k_{air} is the thermal conductivity of the air ($W/(mK)$), and L is the characteristic length (m).

According to the empirical correlation of free convection on a vertical plate [21]

$$h_c = \begin{cases} \frac{k}{L} \left[0.68 + \frac{0.67Ra_L^{1/4}}{\left(1 + \left(\frac{0.492k}{\mu C_p}\right)^{9/16}\right)^{4/9}} \right] & Ra_L \leq 10^9 \\ \frac{k}{L} \left[0.825 + \frac{0.387Ra_L^{1/6}}{\left(1 + \left(\frac{0.492k}{\mu C_p}\right)^{9/16}\right)^{8/27}} \right]^2 & Ra_L \geq 10^9 \end{cases} \quad (7)$$

$$Ra_L = \frac{g|\partial\rho/\partial T|_p \cdot \rho C_p \cdot \Delta T \cdot L^3}{k\mu} \quad (8)$$

where g is the acceleration of gravity (m/s^2), ΔT the temperature difference between surface and ambient (K), k the thermal conductivity of the fluid, ($W/(mK)$), ρ the fluid density (kg/m^3), C_p the heat capacity of the fluid ($J/(kgK)$), μ the dynamic viscosity (Pa s), L the characteristic length, height of the wall (m), and Ra_L the Rayleigh number.

The heat flux by radiation across the air gap is the radiation heat exchange between two gray parallel surfaces [22]

$$Q_{rad-air} = \frac{\sigma(T_{surf1}^4 - T_{surf2}^4)}{\left(\frac{1}{\varepsilon_1} + \frac{1}{\varepsilon_2} - 1\right)} \quad (9)$$

where ε_1 is the emissivity of the inner surface of the calorimeter, ε_2 the emissivity of the insulation board, σ the Stefan–Boltzmann constant (W/m^2K^4), T_{surf1} the temperature of the inside surface of the calorimeter (K), and T_{surf2} the temperature of the insulation board surface (K).

Initial conditions: The fabric initial temperature is considered equal to the ambient temperature

$$T_{fab}(x,t = 0) = T_{amb} \quad (10)$$

Based on data in the literature, an emissivity of 0.9 and a transmissivity of 0.01 were assumed for the fabric [6]. Emissivity of the inner surface of the calorimeter was considered 0.78 and the emissivity of the insulation board 0.96 [23].

In the second stage of this study, in order to predict time to the first and second-degree burns, the model of heat transfer through multilayer protective system was

coupled with the heat transfer model in the skin. For this, the calorimeter and the insulation board were replaced by the skin that consists of three layers: epidermis, dermis, and subcutaneous (Figure 3). The Pennes model was used to model heat transfer in the living tissue.

An air gap of 1 mm width is assumed between the fabric and the human skin, and the conductive and radiation heat transfer mechanisms through the air gap are considered according to [16,24].

The heat flux by radiation from the fabric to the skin across the air gap is

$$Q_{\text{rad-air}} = \frac{\sigma(T_{\text{fab}}^4 - T_{\text{skin}}^4)}{\left(\frac{1}{\varepsilon_f} + \frac{1}{\varepsilon_{\text{skin}}} - 1\right)} \quad (11)$$

where ε_f is the emissivity of the inside surface of the fabric, $\varepsilon_{\text{skin}}$ the emissivity of the skin (0.96), σ the Stefan–Boltzmann constant ($\text{W/m}^2\text{K}^4$), T_{fab} the temperature of the inside surface of the fabric (K), and T_{skin} the temperature of the human skin (K).

The skin initial condition is expressed as a linear temperature distribution between 33°C at the epidermis surface and 37°C at the subcutaneous base

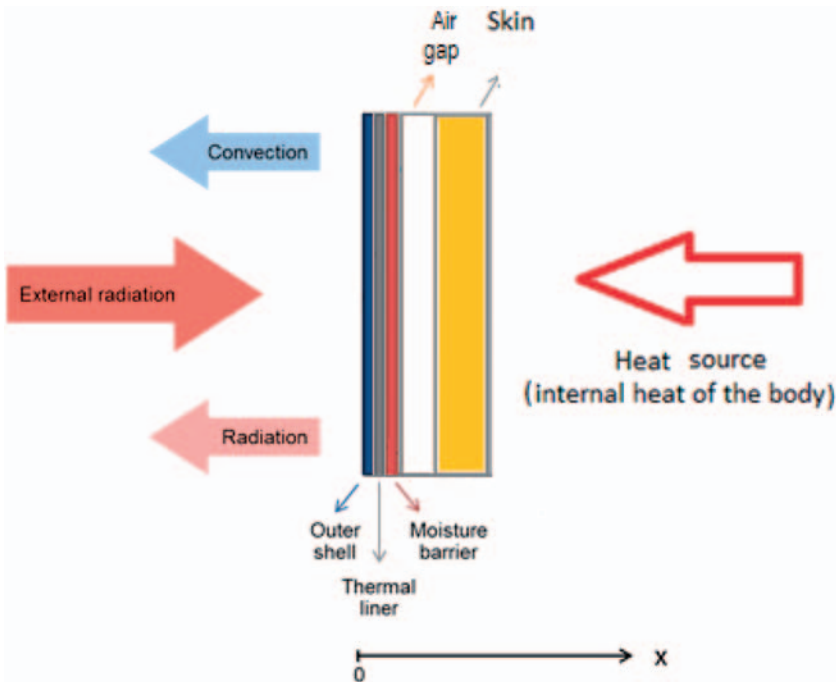


Figure 3. Schematic cross section for one dimensional heat transfer models.

(core body temperature). The boundary condition at the base of subcutaneous layer is set at a constant temperature of 37°C. The ambient temperature was considered at 20°C. Metabolic heat was considered 4343 W/m³. The temperature at the interface between the epidermis and dermis in the human skin was denoted as “T” in Henriques equation (equation (13)). The equation was integrated in MATLAB[®] over the time interval that the temperature at the basal layer is above 44°C, in order to obtain the minimum exposure time for the first and second-degree skin burn.

Bioheat transfer model

In quantitatively estimating fabrics and garments thermal performance under heat conditions, the time to damage the skin beneath the fabric is applied using different skin bioheat transfer models [7,8,11,25].

The Pennes model is used by many authors to model heat transfer in the living tissue [7,8,11]. According to this model, the skin is divided in three layers—epidermis, dermis, and subcutaneous—and the total heat transfer by the flowing blood is proportional to its volumetric flow rate and the temperature difference between the blood and the tissue.

Pennes proposed a transfer equation to describe heat transfer in human tissues. For one-dimensional heat transfer, the equation is

$$\rho c_p \frac{\partial T}{\partial t} + \frac{\partial}{\partial x} \cdot \left(-k \frac{\partial T}{\partial x} \right) = \rho_b c_b \omega_b (T_b - T) + Q_{\text{met}} \quad (12)$$

where the density ρ (kg/m³), heat capacity c_p (J/kg K), and thermal conductivity k (W/m K) are the thermal properties of the tissue, ρ_b (kg/m³) is the blood density, which is the mass per volume of blood, c_b (J/kg K) is blood specific heat, which describes the amount of heat energy required to produce a unit temperature change in a unit mass of blood, ω_b (1/s) is the blood perfusion rate, which, in this case, means (m³/s)/m³) and describes the volume of blood per second that flows through a unit volume of tissue, T_b (K) is the arterial blood temperature, which is the temperature at which blood leaves the arterial blood veins and enters the capillaries; T (K) is the temperature in the tissue, which is the dependent variable that is solved for and not a material property; Q_{met} (W/m³) is the metabolic heat source, which describes heat generation from metabolism [8].

Pennes’ model assumes that skin tissue above an isothermal core is maintained at a constant body temperature. The resulting simplified bioheat equation is based on following specific assumptions: heat is linearly conducted within tissues; tissue thermal properties are constant in each layer, but may vary from layer to layer; blood temperature is constant and equal to body core temperature; negligible exchange between the large blood vessels (arteries and veins) and the tissue; the local blood flow rate is constant. In long duration, low-intensity heat exposure, the rate of metabolic energy production is included in the above equation [8].

Thermophysical/geometrical properties of the human skin are shown in Table 2.

Table 2. Skin and blood properties used in a three-layer skin model.

	Property	Value
Epidermis	Thermal conductivity (W/m K)	0.255
	Density (kg/m ³)	1200
	Specific heat (J/kg K)	3598
	Thickness (m)	8×10^{-5}
Dermis	Thermal conductivity (W/m K)	0.523
	Density (kg/m ³)	1200
	Specific heat (J/kg K)	3222
	Thickness (m)	2×10^{-3}
Subcutaneous	Thermal conductivity (W/m K)	0.167
	Density (kg/m ³)	1000
	Specific heat (J/kg K)	2760
	Thickness (m)	1×10^{-2}
Blood	Density (kg/m ³)	1060
	Specific heat (J/kg K)	3770
	Blood perfusion rate (s ⁻¹)	1.25×10^{-3}

Skin burn model

Henriques and Moritz [7,11,18] were among the first to publish a skin burn injury model. They claimed that skin burn damage can be represented as a chemical rate process, so that a first-order Arrhenius rate equation can be used to estimate the rate of tissue damage as

$$\frac{d\Omega}{dt} = P \exp\left(-\frac{\Delta E}{RT}\right) \quad (13)$$

where Ω refers to a quantitative measure of burn damage at the basal layer or at any depth in the dermis, P the frequency factor (s⁻¹), E the activation energy for skin (J/mol), R the universal gas constant (J/kmol K), T the absolute temperature at the basal layer or at any depth in the dermis (K), t the total time for which T is above 317.15 K.

Integrating this equation yields

$$\Omega = \int_0^t P \exp\left(-\frac{\Delta E}{RT}\right) dt \quad (14)$$

Integration is performed for a time when the temperature of basal layer (the interface between the epidermis and dermis in human skin), T , exceeds or equals to 44°C , because damage to the skin commences when the temperature in the basal layer rises above 44°C .

Henriques found that if $\Omega \leq 0.5$, no damage will occur at the basal layer.

First-degree burn occurs if Ω is 0.5–1.0, and a second-degree burn is indicated when $\Omega > 1.0$.

These tissue burn damage criteria can be applied with providing the appropriate values of P and ΔE . These values were suggested by Weaver and Stoll [6] for the basal layer

$$\text{for } T < 50^{\circ}\text{C}, P = 2.185 \times 10^{124} \text{ s}^{-1}$$

$$\Delta E/R = 93534.9 \text{ K}$$

$$\text{for } T \geq 50^{\circ}\text{C}, P = 1.823 \times 10^{51} \text{ s}^{-1}$$

$$\Delta E/R = 39109.8 \text{ K} \quad (15)$$

The advantage of using the Henriques integral is that time to first and second-degree burn can be estimated.

Use of COMSOL Multiphysics[®]

The numerical model was programmed with Comsol Multiphysics[®] version 4.3 and the equations, together with the already described set of initial and boundary conditions have been solved by FEM. Heat transfer interface and heat transfer in solids module were used for modeling heat transfer. The biological tissue feature was used to provide the source terms that represent blood perfusion and metabolism for modeling heat transfer in biological tissue using the bioheat equation.

Experimental setup

To perform the laboratory simulation of low-level radiant thermal hazards, six silicon carbide heating rods were employed as the radiant heat source as specified in NF EN ISO 6942-2002, for measuring radiant heat resistance. According to this standard, the levels of incident heat flux density should be chosen from the following levels: low level 5 and 10 kW/m^2 , medium level 20 and 40 kW/m^2 and high level 80 kW/m^2 . However, other levels of incident heat flux density may be chosen as well [26]. A copper plate calorimeter is used to record the temperature, and a data acquisition system connected to a computer with TESTPOINT software was used for registering the results. The copper plate calorimeter is constructed of a rectangle copper sheet ($50 \text{ mm} \times 50.3 \text{ mm}$), 1.6 mm thick, bent in the longer direction into an arc with a radius of 130 mm. The copper plate has a mass of 36 g. A copper constantan thermocouple is mounted on the back of the copper plate. An air gap with

the width of 9 mm and an insulation board of 14-mm asbestos-free non-combustible are placed behind the calorimeter.

The specimens have the dimension (230 × 80) mm, and the composite specimen reproduces the arrangement in which the layers are used in practice. The specimen is fastened on the specimen holder using some clamps. The tensioning force of 2 N is applied to the assembly of all layers.

The radiation source was positioned to deliver 1000 W/m² inward heat flux. The calibration followed the standard, and the heat flux value was confirmed by measurements conducted using an ultrathin heat flow meter 50 × 50 mm, from CAPTEC. For the experiments, the specimens were exposed to radiant heat flux for 40 min. A protective shutter positioned between the radiant energy source and the specimen was used to block the radiant energy prior to the exposure of the specimen and to control the exposure time. At the end of exposure period, the specimen was isolated from the heat source by closing the protective shutter and a cooling-down time followed.

Thus, we used only the apparatus and only the procedure described by the standard NF EN ISO 6942 for the source calibration. Furthermore, in our experiment, in order to validate the model, only the temperature recorded by the calorimeter was used. For the temperature record, the calorimeter does not introduce significant errors. The measurements were done for both transient conditions and equilibrium. Three specimens have been tested, and the average temperature registered by calorimeter was determined.

Results and discussion

Figure 4 shows the evolution of temperature over time according to measurements and numerical simulation, respectively. The temperature of the calorimeter starts rising sharply as the fabric system is exposed to the radiant flux at $t = 0$ and then gradually rises until the stabilization. After stopping the radiant flux ($t \geq 2400$), the temperature decreases until it reaches again the initial value of the environment.

The numerically predicted profiles follow the experimental data. During the heating period, the difference between the experimental and the numerical values can be explained by the fact that the heat accumulates in front of the shutter and when the shutter opens this extra heat is added to the radiative flux. As result, there is a steeper temperature gradient compared with the predicted values. The differences between experimental and predicted values during cooling-down period are due the cooling system of the shutter that speeds up the cooling effect and was not considered in the numerical model.

In the second stage of this study, in order to predict time to the first and second-degree burns, the model of heat transfer through multilayer protective system was coupled with the heat transfer model in the skin. For this, the calorimeter and the insulation board were replaced by the skin that consists of three layers—epidermis, dermis, and subcutaneous—and the Pennes model was used to model heat transfer in the living tissue.

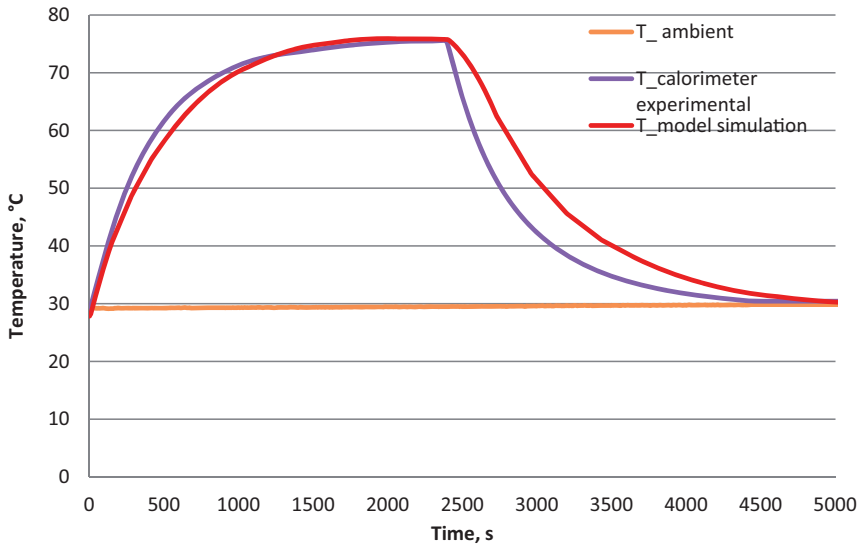


Figure 4. Comparison of computational and experimental results of calorimeter temperature for a three-layer system and 1000 W/m^2 inward heat flux.

An air gap of 1 mm width is assumed between the fabric and the human skin, and the conductive and radiation heat transfer mechanisms through the air gap are considered according to [16,24].

Figure 5 shows the temperature of the basal layer versus time for the heat flux between 400 and 1200 W/m^2 . The temperature of the basal layer increases above 44°C only for heat flux intensity of 1000 and 1200 W/m^2 .

For a radiant heat flux of 1200 W/m^2 , the first-degree burn occurs after $32'20''$, and the second-degree burn occurs after $38'10''$ of exposure.

The thickness of the air gap between the garment and the body depends on the particular location on the human body. According to Song [7,27], the maximum air gaps occur for the leg ($15\text{--}22 \text{ mm}$), and the minimum air gap occurs for the shoulders (1.6 mm).

Figure 6 shows the temperature of the basal layer versus time for the heat flux of 1200 W/m^2 and air gap thickness between the garment and the skin from 1 to 6 mm.

An increase by 5 mm of the air gap thickness causes a decrease of the basal layer temperature by 2.7°C . As air is a good insulator, increasing the size of the air gap will increase the degree of insulation and slow down heat transfer to the skin.

When the air gap between the fabric and the skin was increased to 3 mm for the heat flux of 1200 W/m^2 , the minimum exposure time for skin damage was doubled ($65'40''$ for the first-degree burn and $91'20''$ for the second-degree burn) compared with the time obtained with 1-mm air gap.

The results obtained demonstrate that even for a low-level thermal radiant heat flux, a typical three-layer thermal protective clothing system is required to protect

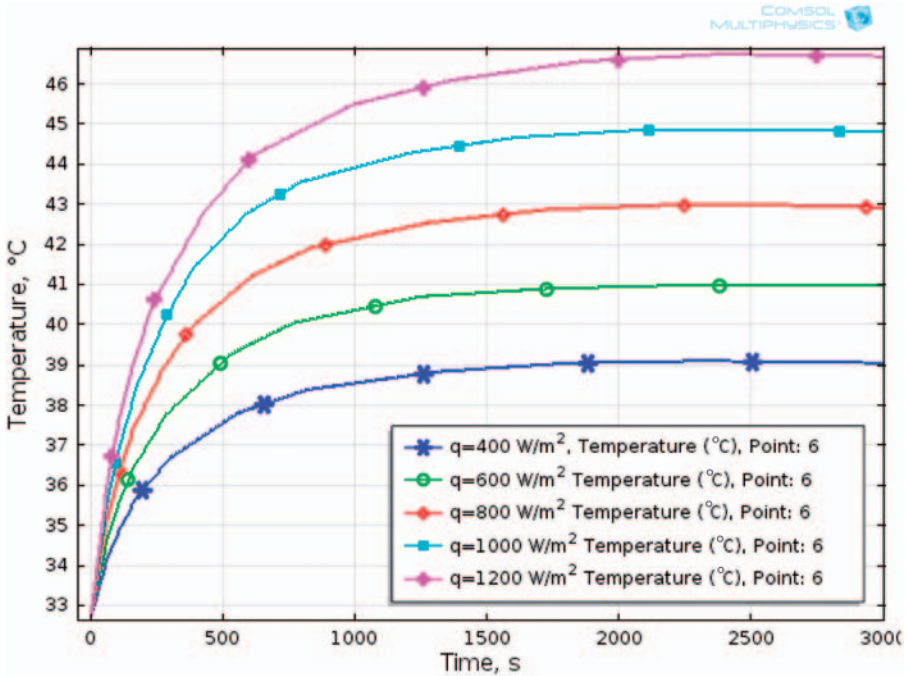


Figure 5. Influence of the heat flux on the temperature of the basal layer for a three-layer system and 1-mm air gap between the fabric and the skin.

the wearer from skin burn injury. A remark should also be done: since the tests are carried out at room temperature (and for simulation, we also considered the ambient temperature of 20°C), the results do not necessarily correspond to the behavior of the materials at higher ambient temperature and therefore are only to a limited extent suitable for predicting the performance of the protective clothing made from the materials under test.

This model could be used as an aid in the design of candidate protective clothing systems, evaluating the performance of current protective clothing systems in various thermal environments. Also, the developed model can serve as a tool for study of potential issues related to the causes of fire fighter burn injuries. Thus, the model can be used to determine the effect of change of different parameters such as fabric thickness and density, thermal properties such as thermal conductivity and specific heat capacity, optical properties, and air gap width, or even environmental conditions such as radiant heat flux density and ambient temperature on the protective performance of clothing.

In addition to studying the physical characteristics of the fabrics utilized in protective clothing, the model can also be used to predict the performance of a thermal protective fabric system in terms of skin burn. In this respect, the minimum

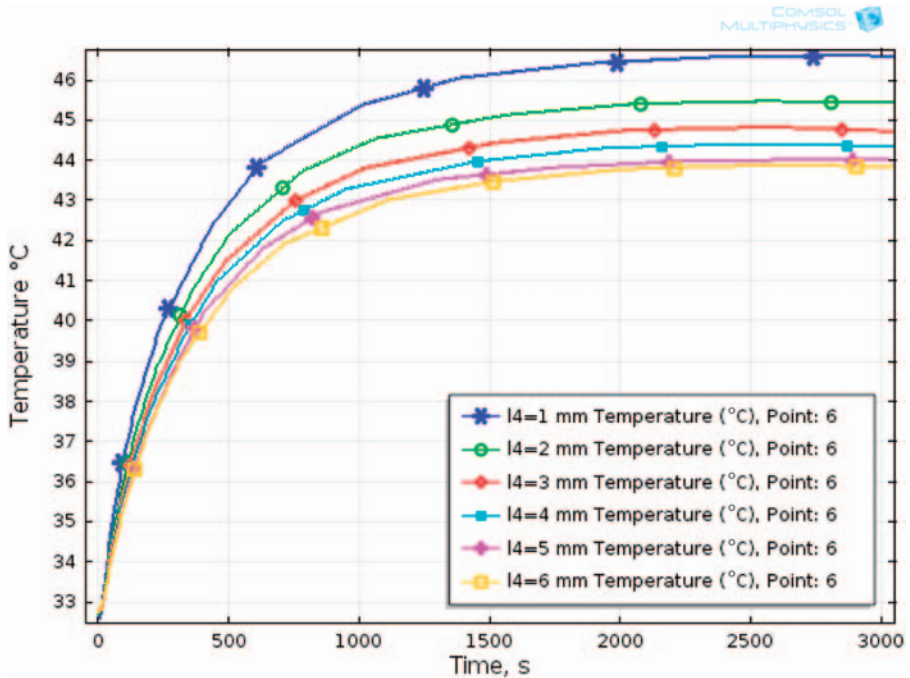


Figure 6. Influence of the air gap width on the temperature of the basal layer for a three-layer system and 1200 W/m^2 inward heat flux.

exposure time required to generate a second-degree burn can be predicted, using a three-layer skin model.

Conclusions

A numerical model of heat transfer in protective clothing during exposure to low-level radiant heat flux was investigated using the software Comsol Multiphysics®.

The goal of this study is to improve firefighter comfort through better understanding of heat transfer in the protective garments they wear. Both experimental and modeling approaches were used. The model results were compared to experimental case, typical of routine conditions with a commonly used three-layer protective clothing assembly. Model predictions of the temperature agreed very well with experimental temperature.

The numerical model incorporates separate layers of a composite fabric so as to evaluate the response of both the individual materials and the entire assembly.

The numerical model of heat transfer in protective clothing was coupled to the three-layer skin model to predict the performance of thermal protective system in terms of skin burn. The time to first and second-degree burn was estimated during exposure to low-level radiant heat flux. The influence of air gap width between the

fabric and the skin was analyzed. Increasing the air gap width an extra insulation is provided, and the heat transfer to the skin is slow down.

At this stage, the model is restricted to dry fabrics but further developments should include moisture effects. Estimations of burn injury risk would then be more accurate.

Funding

The authors gratefully acknowledge the region Nord-Pas-de-Calais and the European Regional Development Fund for their financial support.

References

- [1] ASHRAE Standard 55:2010. Thermal environmental conditions for human occupancy.
- [2] Holmer I. Protection against cold. In: Shishoo R (ed.) *Textiles in sports*. Cambridge, UK: Woodhead Publishing Limited, 2005, p.266.
- [3] Song G, Paskaluk S, Sati R, et al. Thermal protective performance of protective clothing used for low radiant heat protection. *Text Res J* 2011; 81: 311–323.
- [4] Keise C. *Steam burns. Moisture management in firefighter protective clothing*. PhD Thesis, Swiss Federal Institute of Technology Zurich, Swiss, 2007.
- [5] Korycki R. Method of thickness optimization of textile structures during coupled heat and mass transport. *Fibres Text East Eur* 2009; 17: 33–38.
- [6] Loghin C. *Imbracaminte functională—modelarea și simularea funcțiilor de protective*. Iasi: PIM, 2008.
- [7] Song G. *Modeling thermal protection outfits for fire exposures*. PhD Thesis, North Carolina State University, USA, 2002.
- [8] Torvi, D. *Heat transfer in thin fibrous materials under high heat flux conditions*. PhD Thesis, University of Alberta, USA, 1997.
- [9] Das A, Alagirusamy R and Kumar P. Study of heat transfer through multilayer clothing assemblies: A theoretical prediction. *AUTEX Res J* 2011; 11: 54–60.
- [10] Ghazy A and Bergstrom DJ. Influence of the air gap between protective clothing and skin on clothing performance during flash fire exposure. *Heat Mass Transfer* 2011; 47: 1275–1288.
- [11] Mercer GN and Sidhu SH. Mathematical modeling of the effect of fire exposure on a new type of protective clothing. *ANZIAM* 2008; 49: C289–C305.
- [12] Mell WE and Lawson R. A heat transfer model for firefighters' protective clothings. *Fire Technol* 2000; 36: 39–68.
- [13] Lee S and Park C. Experiment-based thermal model for permeable clothing systems under hot air jet impingement conditions. *Int J Therm Sci* 2012; 51: 102–111.
- [14] Sybilska W and Korycki R. Analysis of coupled heat and water vapour transfer in textile laminates with a membrane. *Fibres Text East Eur* 2010; 18: 65–69.
- [15] Li Y and Zhu Q. Simultaneous heat and moisture transfer with moisture sorption, condensation, and capillary liquid diffusion in porous textiles. *Tex Res J* 2003; 73: 515–524.
- [16] Song G, Chitraphiromsri P and Ding D. Numerical simulations of heat and moisture transport in thermal protective clothing under flash fire conditions. *Int J Occup Saf Ergo* 2008; 14: 89–106.

- [17] Chitrphiromsri P. *Modeling of thermal performance of firefighter protective clothing during the intense heat exposure*. PhD Thesis, North Carolina State University, USA, 2004.
- [18] Chitrphiromsri P and Kuznetsov AV. Modeling heat and moisture transport in firefighter protective clothing during flash fire exposure. *Heat Mass Transfer* 2004; 41: 206–215.
- [19] Mäkinen H. Firefighter's protective clothing. In: Scott RA (ed.) *Textiles for protection*. Cambridge, UK: Woodhead, 2005, pp.622–647.
- [20] ISO 22007-2:2008. Plastics—determination of thermal conductivity and thermal diffusivity, part 2: transient plane heat source (hot disc) method.
- [21] Comsol Multiphysics® package.
- [22] Kothandaraman CP. *Fundamental of heat and mass transfer*, 3rd edn. New Delhi: New Age International (P) Limited, 2006, p.608.
- [23] Tools and basic information for design, engineering and construction of technical applications, www.engineeringtoolbox.com/emissivity-coefficients-d_447.html (accessed 21 October 2013).
- [24] Prasad K, Twilley W and Lawson JR. Thermal performance of fire fighters' protective clothing. Numerical study of transient heat and water vapor transfer. Report no. 6881, NISTIR, USA, August 2002.
- [25] Zhu F, Cheng XP and Zhang W. Estimation of thermal performance of flame resistant clothing fabrics sheathing a cylinder with new skin model. *Tex Res J* 2003; 79: 205–212.
- [26] ISO 6942:2002. Protective clothing—Protection against heat and fire—evaluation of materials and material assemblies when exposed to a source of radiant heat.
- [27] Song GW, et al. Modeling the thermal protective performance of heat resistant garments in flash fire exposures. *Tex Res J* 2004; 74: 1033–1040.

MATHEMATICAL CORRELATION OF TEST METHODS FOR MEASURING WATER-VAPOR TRANSMISSION THROUGH FABRICS

Teodor-Cezar Codau,¹ Elena Onofrei,^{1,2,*} Stojanka Petrusic,³ Gauthier Bedek,¹ Daniel Dupont,¹ & Damien Soulat³

¹Université Catholique de Lille, HEI, GEMTEX, 13 Rue de Toul, Lille, F-59046, France

²Technical University “Gheorghe Asachi” of Iasi, Iasi, 700050, Romania

³Université Lille Nord de France, ENSAIT, GEMTEX, Roubaix, F-59056, France

* Address all correspondence to Elena Onofrei E-mail: elena.onofrei@hei.fr

Original Manuscript Submitted: 6/19/2014; Final Draft Received: 11/11/2014

The purpose of this study was to investigate the relationship between resistance to evaporated heat loss from the sweating guarded hot plate (ISO 11092) and water-vapor permeability of fabrics measured using the evaporative dish method (BS 7209). Experimental correlation was studied for air-permeable fabrics that follow Fick's Law, hybrid membrane containing microporous and hydrophilic components and multilayer systems consisting of their combinations, with the intention to cover as wide a range of breathability as possible. A mathematical correlation was established between the two methods. Thus, one can easily determine the resistance to evaporated heat loss (R_{et}) based on the water-vapor transmission rate of fabrics (WVTR) measured by the evaporative dish method, and using a simple numerical method (bisection method, tangent method, etc.). WVTR may be determined knowing R_{et} measured by the sweating guarded hot plate (skin model), with a good accuracy.

KEY WORDS: water-vapor permeability, gravimetric method, “sweating hot plate” method, mathematical correlation

1. INTRODUCTION

Textile fabrics are flat porous materials which are produced by different textile manufacturing techniques using different fibrous forms of input material (or structural elements), consequently having different porous structures:

- woven fabrics are made by interlacing vertical warp and horizontal weft yarns at right angles to each other [Fig. 1(a)];
- knitted fabrics are made by interlacing the yarn loops [Fig. 1(b)];
- non-woven fabrics are produced from the staple fibers or filaments by different web-forming, bonding, and finishing techniques [Fig. 1(c)];

- membranes which are thin, soft material made from a polymer that contains a lot of pores with diameter smaller than the water molecule and larger than water-vapor molecules, which is laminated to the fabric to provide properties such as strength, water-proofing or windproofing to enhance the fabric's performance [Fig. 1(d)];

The water-vapor transfer properties of a fabric, garment, or clothing assembly play a very important role in determining thermal comfort properties, influencing their efficiency in respect to both thermo-physiological and sensorial body comfort. There are a great number of methods available for measuring the ability of fabrics to transport water vapor (i.e., the fabric breathability) and these methods can be divided into two groups (Arabuli et al., 2010):

NOMENCLATURE

A	area of the measuring unit (m^2)	Pr	Prandtl number
c	water-vapor molar concentration (mol/m^3)	R_{et}	water-vapor resistance of the fabric ($m^2 \cdot Pa/W$)
$D_{0,35}$	diffusion coefficient of water-vapor through the cellophane membrane at $35^\circ C$ (m^2/s)	R_{et0}	water-vapor resistance of the cellophane membrane ($m^2 \cdot Pa/W$)
$D_{t,35}$	total diffusion coefficient at $35^\circ C$ (m^2/s)	R	universal gas constant ($J/kmol \cdot K$)
$D_{f,35}$	diffusion coefficient of water vapor through the fabric at $35^\circ C$ (m^2/s)	R_{H_2O}	universal constant of water vapor ($J/kg \cdot K$)
$D_{air,20}$	diffusion coefficient of water vapor through the air at $20^\circ C$ (m^2/s)	Re	Reynolds number
$D_{a,b}$	diffusivity of "a" element in "b" element (m^2/s)	\dot{Q}/A	heat flux provided by hot plate (W/m^2)
$D_{f,20}$	diffusion coefficient of water vapor through the fabric at $20^\circ C$ (m^2/s)	Sc	Schmidt number
Gr	Grashof number	Sh	Sherwood number
g	gravitational acceleration (m/s^2)	T_{35}	temperature in Kelvin corresponding to $35^\circ C$
h_m	mass convection coefficient (m/s)	T_{20}	temperature in Kelvin corresponding to $20^\circ C$
H	heating power supplied to the measuring unit (W)	x	space coordinate for the c water-vapor molar concentration (m)
L_0	thickness of the water-vapor permeable membrane (m)	Greek Symbols	
L_f	thickness of the fabric (m)	ϵ	fabric porosity
L_{air}	thickness of the air gap between the water and sample (m)	ϕ_{65}	relative humidity of 65%
L_{ch}	geometrical characteristic of the surface (m)	Φ_{m0}	mass flux of the water vapor through water-vapor-permeable membrane, at steady state ($kg/m^2 \cdot s$)
M_{H_2O}	molar mass of water (kg/mol)	Φ_{m2}	mass flux of the water vapor, at steady state ($kg/m^2 \cdot s$)
Nu	Nusselt number	λ_{H_2O}	latent heat of vaporization of water (J/kg)
$p_{sat,35}$	saturation water-vapor partial pressure (Pa) at $35^\circ C$	τ	fabric tortuosity
$p_{sat,20}$	saturation water-vapor partial pressure (Pa) at $20^\circ C$	ν	kinematic viscosity (m^2/s)
p_v	partial water-vapor pressure (Pa)	ν_{20}	kinematic viscosity at $20^\circ C$ (m^2/s)
$p_{v,65}$	partial pressure of the water vapor at $20^\circ C$ and 65% RH (Pa)	μ	dynamic viscosity (Pa·s)
p_1	partial pressure of the water vapor at the lower surface of the textile sample (Pa)	ρ	air density (kg/m^3)
p_2	partial pressure of the water vapor at the upper surface of the textile sample (Pa)	ρ_v	partial density of water vapor (kg/m^3)
		$\Delta\rho_v$	difference of water-vapor partial density (kg/m^3)
		Δc	difference of water-vapor concentration (mol/m^3)
		Δp_v	difference of water-vapor partial pressure (Pa)
		ΔH	correction term for heating power (W)

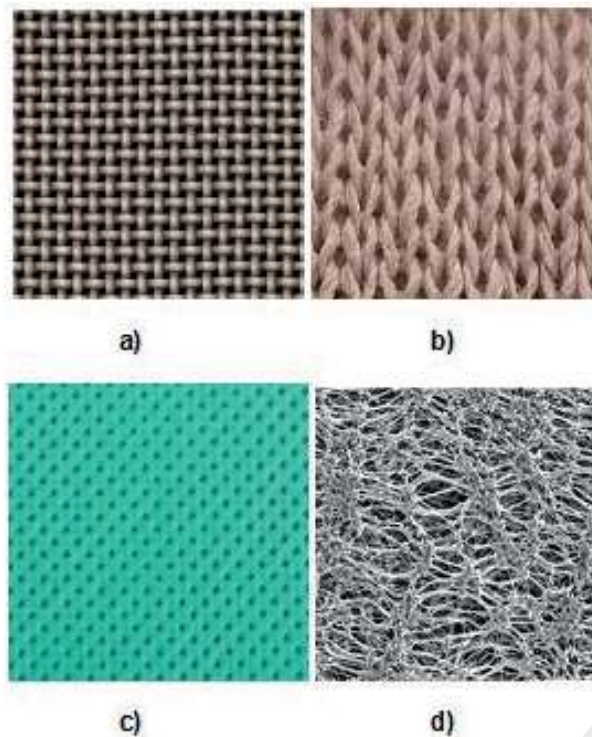


FIG. 1: Fabrics morphology (a) woven fabric; (b) knitted fabric; (c) non-woven fabric; (d) PTFE membrane

- Gravimetric methods
- Sweating hot plate methods

These methods differ in the construction mechanism, test conditions, measurement parameters, and units.

Much controversy exists concerning which test method gives the most meaningful results in relation with the actual performance in the field. Also, direct comparisons between these methods are not possible because a wide range of units are used to express the results (Gretton et al., 1996).

The breathability of a textile can be expressed in different ways. The most common are *The water-vapor transmission rate (WVTR)* is defined as the water-vapor flow in unit time through unit area of the fabric under specific conditions of temperature and relative humidity. The WVTR obtained under steady-state conditions has an SI quantity of $\text{kg/m}^2/\text{s}$ but $\text{g/m}^2/\text{day}$ unit is most widely accepted. The reciprocal quantity of water-vapor transmission rate is *the water-vapor resistance*.

The water-vapor transmission rate is determined using gravimetric methods, and there are two basic types

of tests: evaporation methods and desiccant methods [5]. Even when the transmission rates from two different methods are expressed in the same units, the results cannot be compared because the varying water-vapor pressure gradients produce large variation in the transmission rate (Gretton et al., 1996; Lomax, 1990).

The resistance to evaporated heat flow (R_{et}) of a textile layer is defined as the quantity which determines the latent evaporative heat flux across a given area, in response to a steady applied water-vapor pressure gradient perpendicular to the fabrics. The R_{et} values that can be derived from skin model measurements are, in essence, another way of expressing the resistance of the fabric to water-vapor flow. The usual units are $\text{m}^2 \cdot \text{Pa}/\text{W}$.

Several investigations have been undertaken to compare the different test methods for measuring water-vapor permeability of the fabrics.

Gretton et al. (1996) studied experimentally the correlations between the resistance to evaporated heat loss value (R_{et}) and the percentage water-vapor permeability index. It was found that a direct relationship exists between all fabrics that transmit water vapor according to Fick's law of diffusion. Materials containing hydrophilic polymers do not provide an overall correlation because their inherent resistance changes depending upon the test method used.

Lomax (2007) examined the correlation between methods testing a variety of nylon and polyester fabrics coated with Witcoflex hydrophilic polyurethane. A linear relationship between ISO 11092 and the Turl dish method as well as BS 7209 (which is derived from the Turl dish method) was observed. On the contrary, a nonlinear correlation was found between the Turl dish and Gore cup methods.

Gibson (1993) undertook a detailed correlation concerning the ASTM E 96-80 procedure B upright cup method and a sweating guarded hot plate method. He found out that the two methods correlate for permeable materials, and hydrophobic membranes show certain correlation, but hydrophilic membranes show poor agreement between the two test types.

Huang and Qian (2008) used a new method to determine the water-vapor permeability of fabrics and compared their results with other standard test methods: sweating guarded hot plate, desiccant inverted cup method, the dynamic moisture penetration cell, inverted cup method, and upright cup method. Most of the correlations between any two of the methods are strong, except the upright cup method.

McCullough et al. (2003) measured the water-vapor permeability and evaporative resistance of 26 different waterproof, windproof, and breathable shell fabrics using five standard test methods. The water-vapor transmission rate (WVTR) was measured using the ASTM E 96 upright and inverted cup tests with water, the JIS L 1099 desiccant inverted cup test, and the ASTM F 2298 standard using the dynamic moisture permeation cell (DMPC). The evaporative resistance was measured using the ISO 11092 sweating hot plate test. The WVTRs were consistently highest when measured with the desiccant inverted cup, followed by the inverted cup, DMPC, and upright cup. The upright cup was significantly correlated with the DMPC (0.97), and the desiccant inverted cup was correlated to the sweating hot plate (-0.91).

Investigations undertaken at the Hohenstein Institute indicated a relationship occurring between the Gore cup method results and the R_{et} values obtained by the sweating guarded hot plate. Both the experimental and theoretical results indicate an inverse relationship occurring from which an equation has been derived allowing R_{et} values to be calculated from Gore cup results (Gretton et al., 1996).

The sweating guarded hot plate is a complex piece of equipment; it is expensive and has a high running cost, but is becoming an increasingly important test method for the European market (Lomax, 1990). Therefore, it would be advantageous to establish correlation between the resistance to evaporated heat loss values and the results obtained using other less expensive and more widely available methods. One such method is the evaporative dish method described by the standard BS 7209.

The purpose of this study was to investigate the relationship between the resistance to evaporated heat loss determined using the sweating guarded hot plate (ISO 11092) and water-vapor transmission rate of fabrics measured using the evaporative dish method according to the standard BS 7209. Both methods have been proposed for the European Committee for Standardization (CEN) for the breathable fabrics used in personal protective equipment (PPE) (Lomax, 1990).

2. EXPERIMENTS AND MATHEMATICAL CORRELATION

2.1 Materials

Monolayers and clothing assemblies (multilayers) have been used with the intention to cover as wide a range of breathability as possible. Woven and knitted air-

permeable fabrics were selected for experiments. The air permeable fabrics include knitted fabrics made of cotton or viscose/aramid fibers (S1, S3, S4, S5) as well as medium open and tightly woven fabrics constructed from aramid fibers (S2 and S6). A hybrid sample (HS) consisting of nonwoven aramid laminated with a PTFE membrane to which a thin hydrophilic coating had been applied was also tested. The multilayer fabrics were obtained by overlapping the monolayers one over the top of the other. Thus, three bilayers (S3-S2, S4-S2, and S5-S2), a three-layer assembly (Ass1) without membrane, and two four-layer clothing assemblies (Ass2 and Ass3) consisting of different combinations of the above-mentioned monolayers and the hybrid sample were also included in experiments. These materials are under development for the fire protection applications and are not commercially available.

2.2 Mathematical Approach

2.2.1 Sweating Guarded Hot Plate Tests—ISO 11092-1993

The measuring unit of the sweating guarded hot plate possesses both temperature and water supply control. According to the standard, the procedure for determination of the thermal resistance of material implies the placement of the specimen on an electrically heated porous sintered stainless steel plate with conditioned air ducted to flow across and parallel to its upper surface. For the measurement of water-vapor resistance, an electrically heated porous plate is covered by a water-vapor permeable but liquid-water impermeable membrane (Fig. 2). Water supplied by channels beneath the hot plate (measuring unit), can evaporate through the numerous pores of the plate, just like sweat from the pores of the skin. The hot plate

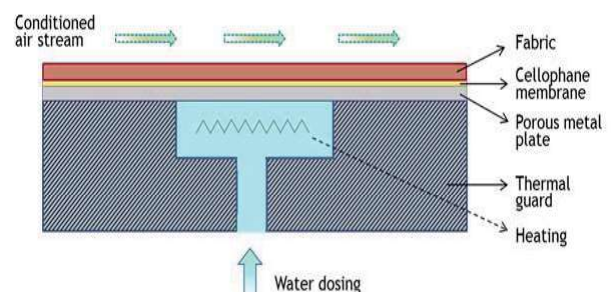


FIG. 2: Scheme of the skin model system for determination of the fabric water-vapor resistance

is kept at a temperature of 35°C. Thus, heat and moisture transport are comparable to those of the human skin. The standard conditions for measurement of water-vapor resistance implied 35 ± 0.1°C and 40 ± 3% RH.

After steady state was reached the total water-vapor resistance of the fabric R_{et} (m² · Pa/W) is calculated using Eq. (1):

$$R_{et} = \frac{(p_{sat,35} - p_v) \cdot A}{H - \Delta H} - R_{et0} \quad (1)$$

where $p_{sat,35}$ is the saturation water-vapor partial pressure (Pa) at 35°C and p_v is the partial water-vapor pressure (Pa) of the air in the test enclosure, A is the area of the measuring unit (m²), and H is the heating power supplied to the measuring unit (W), while ΔH is the correction term for heating power (W) for the measurement of water-vapor resistance R_{et} . R_{et0} (m² · Pa/W) is the corresponding apparatus constant, determined with a smooth water-vapor permeable but liquid-water impermeable cellophane membrane over the porous plate. R_{et0} can be calculated as

$$R_{et0} = \frac{(p_{sat,35} - p_v) \cdot A}{H_0 - \Delta H_0} \quad (2)$$

If \dot{Q}/A is the heat flux provided by the hot plate (W/m²), then

$$\frac{\dot{Q}}{A} = \frac{H - \Delta H}{A} \quad (3)$$

On the other hand,

$$\frac{\dot{Q}}{A} = \lambda_{H_2O} \cdot \Phi_{m0} \quad (4)$$

where Φ_{m0} represents the mass flux of the water vapor at steady state (kg/m² · s) and λ_{H_2O} is the latent heat of vaporization of water (J/kg).

From Eqs. (2) and (4) it results that

$$R_{et0} = \frac{p_{sat,35} - p_v}{\lambda_{H_2O} \cdot \Phi_{m0}} \quad (5)$$

According to the Fick's first law of diffusion, at steady state (one-dimensional case), the mass flux of the water vapor through water-vapor permeable membrane is Φ_{m0} :

$$\Phi_{m0} = D_{0,35} \cdot M_{H_2O} \cdot \frac{\Delta c}{\Delta x} \quad (6)$$

where $D_{0,35}$ is the diffusion coefficient of water vapor through the permeable membrane at 35°C (m²/s), M_{H_2O} is the molar mass of water (kg/mol), c is the water-vapor molar concentration (mol/m³), and x is the space coordinate for the c water-vapor molar concentration (m).

Furthermore, if we assume the water vapor behaves as an ideal gas, Δc can be expressed as

$$\Delta c = \frac{\Delta p_v}{R \cdot T_{35}} \quad (7)$$

where p_v is the water-vapor partial pressure (Pa), R is universal gas constant (8.315 × 10³ J/kmol · K), and T_{35} is the temperature in Kelvin corresponding to 35°C.

The mass flux of the water vapor can be expressed by Eq. (8):

$$\Phi_{m0} = \frac{D_{0,35}}{L_0} \cdot \frac{p_{sat,35} - p_v}{R_{H_2O} T_{35}} \quad (8)$$

R_{H_2O} is the universal constant of water vapor (461.915 J/kg · K) and L_0 is the thickness of the water-vapor permeable membrane (m).

Replacing Φ_{m0} from Eq. (8) to Eq. (5),

$$R_{et0} = \frac{L_0}{D_{0,35}} \cdot \frac{R_{H_2O} \cdot T_{35}}{\lambda_{H_2O}} \quad (9)$$

Similarly,

$$R_{et} = \frac{L_0 + L_f}{D_{t,35}} \cdot \frac{R_{H_2O} \cdot T_{35}}{\lambda_{H_2O}} - R_{et0} \quad (10)$$

but,

$$\frac{L_0 + L_f}{D_{t,35}} = \frac{L_f}{D_{f,35}} + \frac{L_0}{D_{0,35}} \quad (11)$$

where L_f is the thickness of the fabric (m), $D_{t,35}$ is the total diffusion coefficient at 35°C (m²/s), and $D_{f,35}$ is the diffusion coefficient of water vapor through the fabric at 35°C (m²/s).

Thus, Eq. (10) can be represented as

$$R_{et} = \frac{L_f}{D_{f,35}} \cdot \frac{R_{H_2O} \cdot T_{35}}{\lambda_{H_2O}} \quad (12)$$

or else,

$$\frac{L_f}{D_{f,35}} = \frac{\lambda_{H_2O}}{R_{H_2O} \cdot T_{35}} \cdot R_{et} \quad (13)$$

For a textile material with porosity ϵ and tortuosity τ , the effective diffusivity of the water vapor in the fabric is defined by Chittriphomsri and Kuznetsov (2004) as

$$D_{f,35} = D_{air,35} \cdot \frac{\epsilon}{\tau} \quad (14)$$

where $D_{air,35}$ is the diffusion coefficient of water vapor through the air at 35°C (m²/s).

From Eqs. (13) and (14) it follows that

$$\frac{L_f \cdot \tau}{\epsilon} = D_{air,35} \cdot \frac{\lambda_{H_2O}}{R_{H_2O} T_{35}} \cdot R_{et} \quad (15)$$

2.2.2 Dish method test—BS 7209-1990 (ASTME 96)

The cup method is a very common method for testing the moisture transfer ability of fabrics (Fig. 3). It is used to measure the rate of water-vapor transmission perpendicularly through a known area of a fabric in a controlled atmosphere (Gretton, 1996; Huang and Qian, 2008; Onofrei, 2009).

In this method, a sample covers a cup containing distilled water and is placed in a controlled environment of 20° ° and 65% relative humidity. By adjusting the initial weight of water in the cup to 46 mL, a constant air gap is set between the water surface and the sample. The test lasts for 16 h and the weight of each cup is recorded initially and after a conditioning period. The water-vapor transmission rate $WVTR$ ($\text{g}/\text{m}^2/\text{day}$) is calculated by the following equation:

$$WVTR = \frac{G \times 24}{A \times t} \quad (16)$$

where G is the weight change of the cup with fabric sample (g), t is the time during which G occurred (h), and A is the testing area (0.0054113) (m^2).

The water-vapor permeability index I (%) is calculated by expressing the water-vapor permeability of the fabric as a percentage of the water-vapor permeability of a reference woven fabric which is tested in a similar manner, concurrently and along with the test specimen. The reference fabric is tightly woven, made of a polyester monofilament yarn of low moisture regain to avoid sagging under conditions of high relative humidity.

$$I = \frac{WVTR}{WVTR_{ref}} \times 100(\%) \quad (17)$$

In Fig. 4, there are highlighted three distinct zones for the mass transfer. In Zone I there is a diffusion of water



FIG. 3: Dish method test for determination of the fabric water-vapor permeability

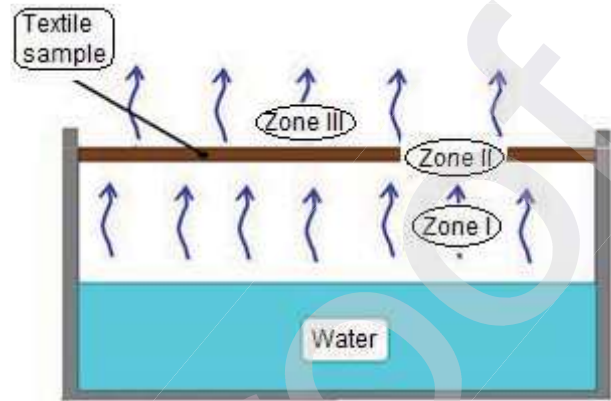


FIG. 4: Scheme of the dish method test

vapor through air layer, in Zone II there is a diffusion of water vapor through the fabric, and in Zone III, which is a boundary air layer on the surface of the fabric, there is a free convective mass transfer. The mass flux of the water vapor, Φ_{m2} ($\text{kg}/\text{m}^2 \cdot \text{s}$) at steady state is the same for all these zones:

$$\text{Zone I } \Phi_{m2} = \frac{D_{\text{air},20}}{L_{\text{air}}} \cdot \frac{p_{\text{sat},20} - p_1}{R_{\text{H}_2\text{O}}T_{20}} \quad (18)$$

$$\text{Zone II } \Phi_{m2} = \frac{D_{f,20}}{L_f} \cdot \frac{p_1 - p_2}{R_{\text{H}_2\text{O}}T_{20}} \quad (19)$$

$$\text{Zone I II } \Phi_{m2} = h_m \cdot \frac{p_2 - p_{v,65}}{R_{\text{H}_2\text{O}}T_{20}} \quad (20)$$

where $D_{\text{air},20}$ is the diffusion coefficient of water vapor through the air at 20°C (m^2/s), L_{air} is the thickness of the air gap between the water and sample (m), $p_{\text{sat},20}$ is the saturation water-vapor partial pressure at 20°C (Pa), T_{20} is the temperature in Kelvin corresponding to 20°C, $R_{\text{H}_2\text{O}}$ is the universal constant of water vapor ($\text{J}/\text{kg} \cdot \text{K}$), p_1 is the partial pressure of the water vapor at the lower surface of the textile sample (Pa), $D_{f,20}$ is the diffusion coefficient of water vapor through the fabric at 20°C (m^2/s), L_f is the fabric thickness (m), p_2 is the partial pressure of the water vapor at the upper surface of the textile sample (Pa), h_m is the mass convection coefficient (m/s), and $p_{v,65}$ is the partial pressure of the water vapor at 20°C and 65% RH (Pa).

Similar to Eq. (14), for a textile material with porosity ε and tortuosity τ , the effective diffusivity of the water vapor through the fabric is defined as:

$$D_{f,20} = D_{\text{air},20} \cdot \frac{\varepsilon}{\tau} \quad (21)$$

From Eqs. (18)–(21) it follows that

$$\frac{L_f \cdot \tau}{\varepsilon} = D_{\text{air},20} \left[\frac{p_{\text{sat}20} - p_{v,65}}{R_{\text{H}_2\text{O}} T_{20}} \cdot \frac{1}{\Phi_{m_2}} - \left(\frac{L_{\text{air}}}{D_{\text{air},20}} + \frac{1}{h_m} \right) \right] \quad (22)$$

Taking into account that

$$p_{\text{sat},20} - p_{v,65} = p_{\text{sat},20} (1 - \Phi_{65}) \quad (23)$$

where Φ_{65} is the relative humidity of 65%, from Eqs. (15) and (22) it follows that

$$\Phi_{m_2} = \frac{\frac{p_{\text{sat},20} (1 - \Phi_{65})}{R_{\text{H}_2\text{O}} T_{20}}}{\frac{D_{\text{air},35}}{D_{\text{air},20}} \cdot \frac{\lambda_{\text{H}_2\text{O}}}{R_{\text{H}_2\text{O}} T_{35}} \cdot R_{\text{etf}} + \frac{L_{\text{air}}}{D_{\text{air},20}} + \frac{1}{h_m}} \quad (24)$$

where the mass flux of the water vapor is in $[\text{kg}/\text{m}^2 \cdot \text{s}]$.

Finding the mass transfer coefficient h_m presents a more difficult problem. Mass convection (or *convective mass transfer*) is the mass transfer mechanism between a surface and a moving fluid that involves both *mass diffusion* and *bulk fluid motion*. Fluid motion enhances mass transfer considerably (Çengel, 2011).

In mass convection, we define a *concentration boundary layer* in an analogous manner to the thermal boundary layer in heat transfer by convection, and define new dimensionless numbers that are counterparts of the Nusselt (Nu) and Prandtl (Pr) numbers in heat transfer.

The Prandtl number is replaced by Schmidt number (Sc), and the Nusselt number is replaced by Sherwood number (Sh):

$$\text{Sc} = \frac{\nu}{D_{a,b}} \quad (25)$$

where ν is kinematic viscosity (m^2/s), $D_{a,b}$ is diffusivity of “a” element in “b” element (m^2/s).

$$\text{Sh} = h_m \frac{L_{ch}}{D_{a,b}} \quad (26)$$

where L_{ch} is the geometrical characteristic of the surface (m), h_m is the mass transfer coefficient (m/s).

Thus,

$$h_m = \text{Sh} \cdot \frac{D_{\text{air},20}}{L_{ch}} \quad (27)$$

Under the low mass flux conditions, the mass convection coefficients h_m can be determined by choosing the appropriate Nusselt number relation for the given geometry and analogous boundary conditions, replacing the Nusselt number by the Sherwood number and the Prandtl number by the Schmidt number. Table 1 gives the analogy between convective heat transfer and convective mass transfer (Çengel, 2011).

The rotation of the device provided by the standard BS 7209/1990 leads to a tangential velocity of 0.005 m/s that can be neglected in terms of forced convection. This rotation has a decisive role in avoiding humid air stratification

TABLE 1: The analogy between convective heat transfer and convective mass transfer

Convective heat transfer	Convective mass transfer
1. Forced convection over flat plate a. Laminar flow $\text{Nu} = 0.664 \cdot \text{Re}^{0.5} \cdot \text{Pr}^{1/3}$ $\text{Re} < 5 \times 10^5$; $\text{Pr} > 0.6$	$\text{Sh} = 0.664 \cdot \text{Re}^{0.5} \cdot \text{Sc}^{1/3}$ $\text{Sc} > 0.5$
2. Forced convection over flat plate b. Turbulent flow $\text{Nu} = 0.037 \cdot \text{Re}^{0.8} \cdot \text{Pr}^{1/3}$ $5 \times 10^5 < \text{Re} < 10^7$; $\text{Pr} > 0.6$	$\text{Sh} = 0.037 \cdot \text{Re}^{0.8} \cdot \text{Sc}^{1/3}$ $\text{Sc} > 0.5$
3. Natural convection over surfaces c. Upper surface of a horizontal plate $\text{Nu} = 0.54 (\text{Gr} \cdot \text{Pr})^{1/4}$ $10^4 < \text{Gr} \cdot \text{Pr} < 10^7$	$\text{Sh} = 0.54 (\text{Gr} \cdot \text{Sc})^{1/4}$ $10^4 < \text{Gr} \cdot \text{Sc} < 10^7$
4. Natural convection over surfaces d. Upper surface of a horizontal plate $\text{Nu} = 0.15 (\text{Gr} \cdot \text{Pr})^{1/3}$ $10^7 < \text{Gr} \cdot \text{Pr} < 10^{11}$	$\text{Sh} = 0.15 (\text{Gr} \cdot \text{Sc})^{1/3}$ $10^7 < \text{Gr} \cdot \text{Sc} < 10^{11}$

where Re is the Reynolds number, and Gr is the Grashof number.

in the space between the water surface and the textile sample. If the climatic chamber in which the device is placed is large enough, we can consider that at the textile sample surface there is a free convection mass transfer.

In order to choose the right formula we should calculate the Grashof and Schmidt numbers (Çengel, 2011):

$$\text{Gr} = g \cdot \frac{\Delta \rho_v}{\rho} \cdot \frac{L_{ch}^3}{\nu_{20}^2} \quad (28)$$

where ρ_v is the partial density of water vapor and ρ is the air density (kg/m^3), ν_{20} is the kinematic viscosity at 20°C (m^2/s), and g is the gravitational acceleration (m/s^2).

$$\text{Sc} = \frac{\nu_{20}}{D_{air,20}} \quad (29)$$

The kinematic viscosity can be calculated as

$$\nu = \frac{\mu}{\rho} \quad (30)$$

where μ is the dynamic viscosity ($\text{Pa} \cdot \text{s}$).

From Eqs. (28)–(30) it follows that

$$(\text{Gr} \cdot \text{Sc}) = g \cdot \frac{L_{ch}^3}{\mu \cdot D_{air,20}} \cdot \Delta \rho_v \quad (31)$$

or, using the partial pressures,

$$(\text{Gr} \cdot \text{Sc}) = g \cdot \frac{L_{ch}^3}{\mu \cdot D_{air,20}} \cdot \frac{\Delta p_v}{R_{H_2O} T_{20}} \quad (32)$$

We can consider the maximum value for $(\text{Gr} \cdot \text{Sc})$ when Δp_v is maximum.

$$\Delta p_{v,\max} = p_{sat,20}(1 - \phi_{65}) \quad (33)$$

$$10^4 < [(\text{Gr} \cdot \text{Sc})_{\max} = 7.7051 \times 10^4] < 10^7 \quad (34)$$

Thus, from Table 1, Sh can be calculated as

$$\text{Sh} = 0.54 (\text{Gr} \cdot \text{Sc})^{1/4} \quad (35)$$

$$\text{Sh} = 0.54 \left(g \cdot \frac{L_{ch}^3}{\mu \cdot D_{air,20}} \cdot \frac{\Delta p_v}{R_{H_2O} T_{20}} \right)^{1/4} \quad (36)$$

where

$$\Delta p_v = p_2 - p_{v,65} \quad (37)$$

From Eqs. (20) and (27) it results that

$$\Delta p_v = \Phi_{m_2} \cdot \frac{R_{H_2O} T_{20}}{\text{Sh} \cdot D_{air,20} / L_{ch}} \quad (38)$$

By replacing Δp_v from Eq. (38) to Eq. (36), Sherwood number (Sh) can be calculated as

$$\text{Sh} = 0.54 \left(g \cdot \Phi_{m_2} \frac{L_{ch}^4}{\mu \cdot D_{air,20}^2} \cdot \frac{1}{\text{Sh}} \right)^{1/4} \quad (39)$$

or,

$$\text{Sh} = \left(g \cdot \frac{(0.54)^4 L_{ch}^4}{\mu \cdot D_{air,20}^2} \right)^{1/5} \cdot (\Phi_{m_2})^{1/5} \quad (40)$$

Equation (40) together with Eqs. (27) and (24) allow the mass flux of the water vapor to be expressed as

$$\Phi_{m_2} = \frac{p_{sat,20}(1 - \phi_{65})}{R_{H_2O} T_{20}} / \left[\frac{D_{air,35}}{D_{air,20}} \cdot \frac{\lambda_{H_2O}}{R_{H_2O} T_{35}} \cdot R_{et} + \frac{L_{air}}{D_{air,20}} + \frac{L_{ch}}{D_{air,20}} \cdot \left(\frac{\mu \cdot D_{air,20}^2}{g \cdot (0.54)^4 L_{ch}^4} \right)^{1/5} \frac{1}{(\Phi_{m_2})^{1/5}} \right] \quad (41)$$

Finally, the water-vapor resistance of the fabric is obtained as

$$R_{et} = \left[\frac{p_{sat,20}(1 - \phi_{65})}{R_{H_2O} T_{20} \cdot \Phi_{m_2}} - \frac{L_{air}}{D_{air,20}} - \frac{L_{ch}}{D_{air,20}} \right] \times \left(\frac{\mu \cdot D_{air,20}^2}{g \cdot (0.54)^4 L_{ch}^4} \right)^{1/5} \frac{1}{(\Phi_{m_2})^{1/5}} / \left[\frac{D_{air,35}}{D_{air,20}} \cdot \frac{\lambda_{H_2O}}{R_{H_2O} T_{35}} \right] \quad (42)$$

This equation makes determining the correlation between the two methods more straightforward.

3. RESULTS AND DISCUSSION

Experimental results from the skin model (R_{et} values), were plotted against the individual values of WVTR obtained for fabrics by the test method BS 7209 (Fig. 5). A general inverse relationship between the results obtained from the two methods can be seen. Figure 5 shows also, by continuous line, the R_{et} values determined by Eq. (42).

When the correlation is represented using the index of WVTR (Fig. 6), a more precise correlation is obtained, all the points lying within 3% of the line except for the hybrid sample. The better correlation is due to the fact that the errors introduced by the slight variation of the ambient atmosphere parameters (temperature and relative humidity) are avoided. A linear correlation can be considered for R_{et} values smaller than $10 \text{ m}^2 \cdot \text{Pa/W}$, and this is in accordance with Gretton et al. (1996) and Gibson (1992).

Figure 7 show the values of index of WVTR, measured and calculated according to Eq. (42) as well as the difference between the measured and calculated values for all the tested fabrics.

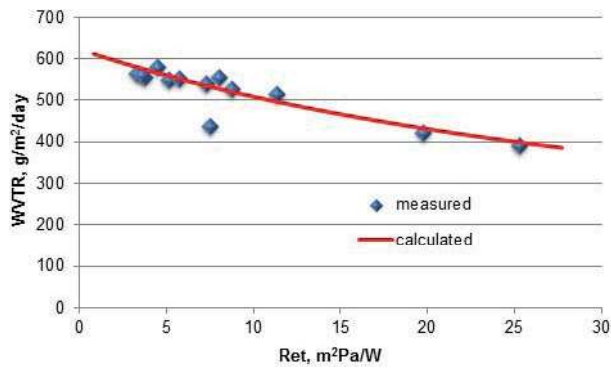


FIG. 5: Correlation between evaporative resistance (R_{et}) from the sweating guarded hot plate test and water-vapor transmission rate (WVTR) from dish method

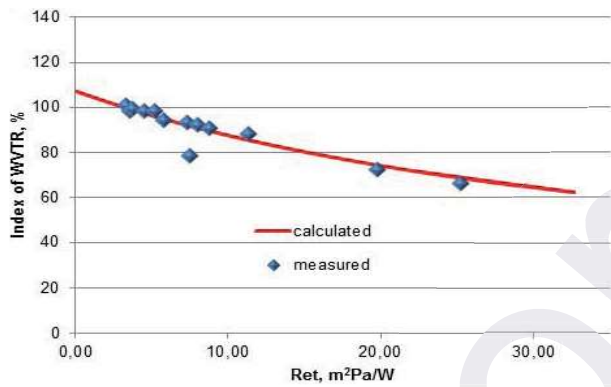


FIG. 6: Correlation between evaporative resistance (R_{et}) from the sweating guarded hot plate test and the index of WVTR from the dish method

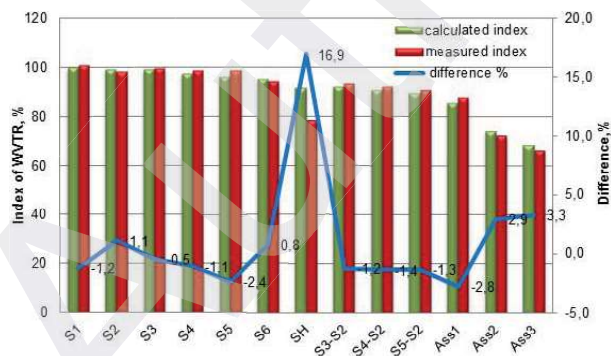


FIG. 7: The difference between the index of WVTR measured according the standard BS 7209 and calculated by Eq. (42)

The smallest differences were registered for all monolayers (woven and knitted fabrics). These fabrics are air permeable fabrics that transmit water vapor through the pores within their structure and this transmission obeys Fick’s law of diffusion. The diffusion coefficient does not vary with changes in water-vapor concentration or with changes in temperature and a good correlation is obtained. The difference between the measured and calculated index of WVTR is less than 2.4%. Similar differences show bilayer fabrics are combinations of these monolayers (S3-S2, S4-S2, and S5-S2) and the three-layer fabric (Ass1) that does not contains a membrane.

The highest difference was registered for the hybrid sample (HS) consisting of nonwoven aramid laminated with a PTFE membrane to which a thin hydrophilic coating had been applied. The difference is 16.9%, the calculated value being higher than the measured one due to the hydrophilic component. Through this sample the water vapor is transmitted by both Fickian and non-Fickian diffusion. The test conditions in the guarded sweating hot plate test result in a much higher equilibrium water content in the hydrophilic polymer layer, which changes the polymer permeability, thereby greatly increasing the water-vapor transport rate through the membrane (Lomax, 1990).

The water-vapor resistance of multilayer clothing systems containing a hybrid membrane (Ass2 and Ass3) was also altered by the changes in water-vapor concentration. However, if the hydrophilic polymer layer is incorporated as an inner layer and it is further away from the skin, a smaller influence is registered. Anyway, for the four-layer assembly (Ass2 and Ass3) comprising this hybrid sample between aramid layers, the correlation was better and the difference was only 3.3% and 2.9%, respectively.

According to Eq. (42) one can easily determine R_{et} based on the Φ_{m2} value measured by the evaporative cup method, or using the numerical methods (bisection method, tangent method, etc.). Φ_{m2} may be determined knowing R_{et} from the skin model, with a sufficiently small error.

However, this requires deep analysis of the errors that may occur due to variations of different experimental conditions, i.e., humidity and temperature, for the two standards.

To assess the size of these influences we calculated relative variation of the water-vapor resistance ($\Delta R_{et}\%$) for each case.

Figures 8–11 present the variations of R_{et} (calculated values) depending on errors approximation of the temperature and relative humidity at which mass flow is mea-

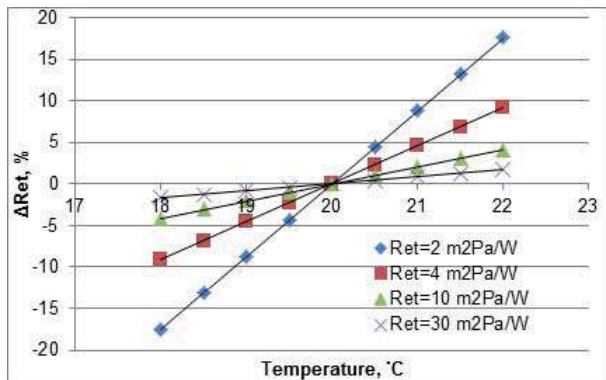


FIG. 8: Effect of temperature on the water-vapor resistance variation calculated from the mass flux

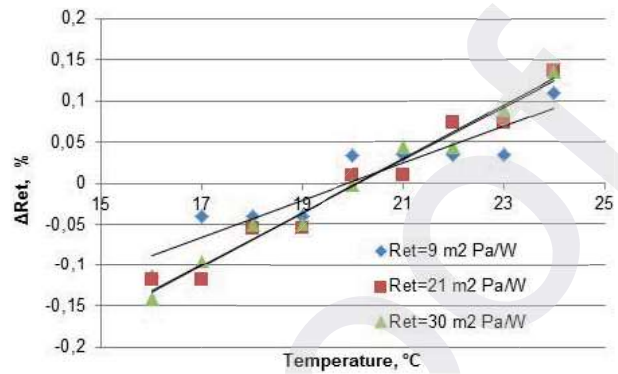


FIG. 11: Effect of temperature on the water-vapor resistance variation calculated from the index of WVTR

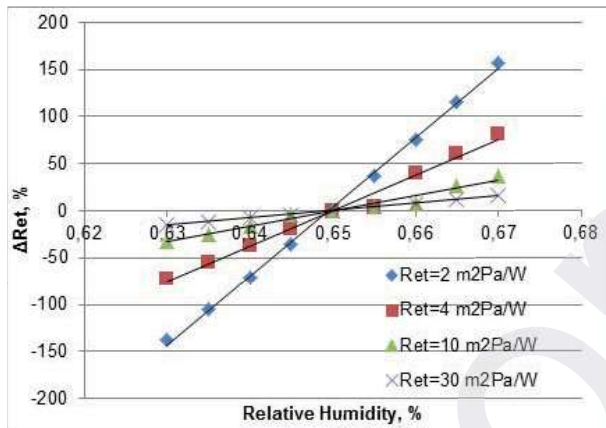


FIG. 9: Effect of relative humidity on the water-vapor resistance variation calculated from the mass flux

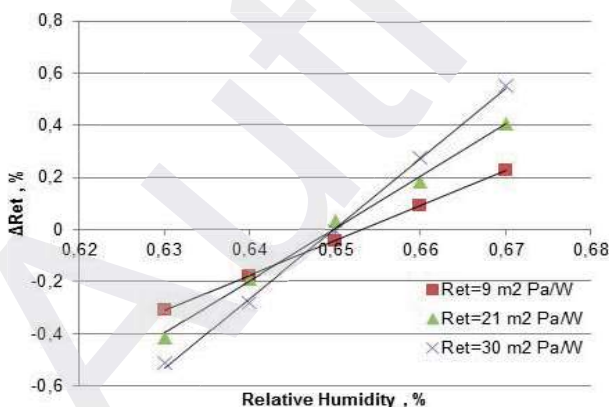


FIG. 10: Effect of relative humidity on the water-vapor resistance variation calculated from the index of WVTR

sured according to the BS 7209 standard. In Figs. 8 and 9 we used mass flow rate to calculate R_{et} , while in Figs. 9 and 10 we used water-vapor permeability index.

Thus, ISO 11092 accepts variations of temperature $35 \pm 0.1^\circ\text{C}$ and of relative humidity $40 \pm 3\%$. Based on these conditions, acceptable variations of R_{et} are obtained. Using the bisection method (or interval halving method) and Eq. (42) we found out the variation of the mass flux as follows: $\Delta\Phi_{m_2} = 0.067\%$ for lower values of R_{et} ($\cong 2 \text{ m}^2 \cdot \text{Pa/W}$) and $\Delta\Phi_{m_2} = 0.057\%$ for higher values of R_{et} ($\cong 30 \text{ m}^2 \cdot \text{Pa/W}$). In conclusion, Φ_{m_2} (and consequently WVTR) can be calculated with good accuracy using Eq. (42) from the R_{et} determined from the skin model.

On the other hand, the standard BS 7209 accepts the temperature variations of $20 \pm 2^\circ\text{C}$ and relative humidity variation of $65 \pm 2\%$. These variations lead to variations of WVTR and consequently of mass flow variations. Using the same Eq. (42) we determined the variation of water-vapor resistance (ΔR_{et}) and the results are shown in Figs. 8 and 9. The largest variations occur for small values of R_{et} and are due to the moisture variation. For $R_{et} = 2 \text{ m}^2 \cdot \text{Pa/W}$, the variation of water-vapor resistance ΔR_{et} have a range of $\pm 150\%$ due to the $\pm 2\%$ moisture variation and $\Delta R_{et} = \pm 18\%$ due to the $\pm 2^\circ\text{C}$ temperature variation. These large variations make this transformation unusable.

In order to reduce these errors we can use the index of WVTR, as defined by Eq. (17). The relationship between R_{et} and the index value can be calculated by the same numerical method (bisection method) using Eqs. (42) and (17). The influence of the humidity and temperature variations is summarized in Figs. 10 and 11. Again, the largest

variation occurs due to the moisture variation, but for $R_{et} = 30 \text{ m}^2 \cdot \text{Pa}/\text{W}$ the variation is $\pm 0.5\%$ and for $R_{et} = 9 \text{ m}^2 \cdot \text{Pa}/\text{W}$ it ranges between -0.24% and $+0.22\%$.

Variations due to temperature are below 0.1 % and can be neglected.

In conclusion, one can determine R_{et} , with a good accuracy, indirectly, using the index of water-vapor transmission rate and Eq. (42) through a simple numerical method.

4. CONCLUSIONS

Air permeable fabrics that follow Fick's law, hybrid membrane containing microporous and hydrophilic components, and multilayer systems consisting of combinations of these were investigated on their breathability using two methods: sweating guarded hot plate and evaporative dish method.

A mathematical correlation was established between the resistance to evaporated heat loss determined by the sweating guarded hot plate (ISO 11092) and water-vapor transmission rate of fabrics measured using the evaporative dish method (according to the standard BS 7209). An equation has been derived allowing R_{et} values to be calculated from the evaporative dish method. On the other hand, through a simple numerical method (bisection method), the water-vapor transmission rate of the fabrics can be determined with good accuracy, using the resistance to evaporated heat loss from the skin model.

Both the experimental and theoretical results indicate an inverse relationship between the results obtained by the two methods.

A good correlation between the two methods was obtained for air permeable fabrics. For narrow intervals of $R_{et} (< 10 \text{ m}^2 \cdot \text{Pa}/\text{W})$, a linear correlation can be considered for these fabrics, and that is consistent with results obtained by other authors.

The hybrid membrane shows no correlation between the sweating guarded hot plate data and the water-vapor transmission rate of the evaporative dish method. On the contrary, there is a good correlation of the multilayer fabrics comprising this hybrid material as an inner layer, i.e., placed further from the skin.

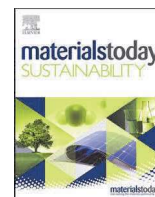
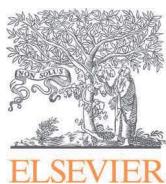
Other researchers have established a correlation between the different methods by plotting the trend line, from the experimental results. We have obtained an equation, theoretically demonstrated, that reflects the correlation between the two methods of determining the water-vapor permeability of textiles.

ACKNOWLEDGMENTS

The authors gratefully acknowledge the region Nord-Pas-de-Calais and the European Regional Development Fund for their financial support.

REFERENCES

- Arabuli, S., Vlasenko, V., Havelka, A., and Kus, Z., Analysis of modern methods for measuring vapor permeability properties of textiles, In *Proc. of 7th International Conference-TEXSCI 2010*, September 6–8, Liberec, Czech Republic, 2010.
- BS 7209-1990, Water vapor permeable apparel fabrics, British Standards Institutions, 1990.
- Çengel, Y. A., *Heat and Mass Transfer: A Practical Approach*, 4th ed., Boston: McGraw-Hill, 2011.
- Chitphiromsri, P. and Kuznetsov, A. V., Modeling heat and moisture transport in firefighter protective clothing during flash fire exposure, *Heat Mass Transfer*, vol. 4, pp. 206–215, 2004.
- Gibson, P. W., Comparison of sweating guarded hot plate and upright cup methods of measuring water vapor permeability, Technical report NATICK/TR-92-046, Massachusetts, 1992.
- Gibson, P. W., Factors influencing steady-state heat and water vapor transfer measurements for clothing materials, *Text. Res. J.*, vol. 63, pp. 749–764, 1993.
- Gretton, J. C., Brook, D. B., Dyson, H. M., and Harlock, S. C., A correlation between test methods used to measure moisture vapour transmission through fabrics, *J. Ind. Text.*, vol. 25, pp. 301–310, 1996.
- Huang, J. and Qian, X., Comparison of test methods for measuring water vapor permeability of fabrics, *Text. Res. J.*, vol. 78, pp. 342–352, 2008.
- ISO 11092:1993, Textiles—Physiological effects—Measurement of thermal and water-vapour resistance under steady-state conditions (sweating guarded-hotplate test). ISO: Geneva, Switzerland, 1993.
- Lomax, G. R., Hydrophilic polyurethane coatings, *J. Ind. Text.*, vol. 20, pp. 88–107, 1990.
- Lomax, G. R., Breathable polyurethane membranes for textiles and related industries, *J. Mater. Chem.*, vol. 17, no. 27, pp. 2755–2784, 2007.
- McCullough, E. A., Kwon, M., and Shim, H., A comparison of standard methods for measuring water vapour permeability of fabrics, *Meas. Sci. Technol.*, vol. 14, pp. 1402–1408, 2003.
- Onofrei, E., The properties of knitted fabrics for bio-functional textiles, presented at Symposium: Technical textile present and future, Iasi, Romania, October 22–23, 2009, published in The Scientific Bulletin of the “Gh. Asachi” Technical University of Iasi, Tom LV (LIX), Fasc. 4, pp. 89–96, 2009.



Synthesis of ultra-stretchable thermoelectric nanofibrous membrane based on wet-electrospun Polyurethane/MWCNTs composites

Teodor Cezar Codau^{a,b}, Elena Codau^{b,*}

^a University of Minho, Fibrenamics – Institute for Innovation in Fiber-based Materials and Composites, Campus de Azurém, 4800-058, Guimarães, Portugal

^b Technical University “Gheorghe Asachi” of Iasi, Industrial Design and Business Management Faculty, 29 Professor Dimitrie Mangeron Blvd., 700050, Iasi, Romania

ARTICLE INFO

Keywords:

Wet-electrospinning
Thermoelectric
Nanofibers
Polyurethane
Carbon nanotubes

ABSTRACT

Electrospinning is a versatile method used to create nanofiber membranes with surface-to-volume ratios much higher than those achievable with other film fabrication methods. This technique allows the control of nanofiber morphology, including diameter, shape, and orientation. Such nanostructuring can enhance the thermoelectric performance of composite materials due to quantum confinement and filtering effects. However, the thermoelectric efficiency of a typical electrospun composite is limited due to the insulating nature of the polymer matrix. Therefore, many researchers have combined electrospinning with other techniques or post-treatments to accomplish higher thermoelectric performance. In this study, a new strategy to prepare a stretchable thermoelectric nanofibrous membrane is proposed. The ternary composite of Thermoplastic Polyurethane (TPU)/Multi Wall Carbon Nanotubes (MWCNTs)/Poly(3,4-ethylenedioxythiophene)polystyrene sulfonate (PEDOT: PSS) is obtained by electrospinning of TPU/MWCNTs solution in coagulation bath of PEDOT: PSS water dispersion. The nonsolvent-induced phase separation (NISP) phenomenon, and consequently, the formation of CNTs/PEDOT: PSS/CNTs electrically-conductive chains, were controlled by tuning the concentrations from binary solvents. The optimal value of the Power Factor, $4.28 \mu\text{W m}^{-1} \text{K}^{-2}$, was obtained for 0.12% MWCNTs and a 1:4 ratio of Tetrahydrofuran (THF) to N, N-Dimethylformamide (DMF) in the binary solvent. The sample exhibits a high value of electrical conductivity of 85 S m^{-1} and shows a strain range of 190 %. This study demonstrates the significant potential of the wet-spinning method for producing wearable and sustainable thermoelectric devices, offering an alternative to conventional devices that raise concerns regarding resource scarcity and environmental impact.

1. Introduction

The challenge of harvesting the energy required to meet global demands is one of the most pressing issues we face today. Scientists are actively exploring new materials and technologies for renewable and clean energy resources. Thermoelectric (TE) materials are among those that have garnered great attention in recent years due to their promising applications in waste heat harvesting, flexible electronics, soft robotics, and the Internet of Things. The conventional use of rare elements, such as bismuth and telluride, in TE materials raises concerns about resource scarcity and environmental impact. Consequently, there is an urgent need to investigate alternative materials that can replace traditional composites, ensuring both environmental sustainability and enhanced TE performance. Nowadays, considerable advancements have been achieved in the field of organic TE materials, driven by their distinct

advantages such as affordability, superior mechanical flexibility, lightweight, and inherently low thermal conductivity [1]. Even though the figure of merit (ZT) values of organic materials still lag behind their inorganic counterparts, various techniques, such as doping, nanostructuring, adding fillers, or post-treatments, have been demonstrated as effective approaches to realize enhancements in TE performance [2, 3].

Recently, special attention has been paid to thermoelectric composites based on conjugated/conductive polymers and CNTs, particularly within the realm of thermoelectric sensors. However, the reports have highlighted the low stretchability of these composites, limiting their practical utility [4]. Consequently, various strategies have been employed to enhance the mechanical properties of organic thermoelectric devices.

Electrospinning is a cost-effective method for the preparation of

* Corresponding author.

E-mail addresses: cezarcodau@yahoo.com (T.C. Codau), elena.codau@academic.tuiasi.ro (E. Codau).

<https://doi.org/10.1016/j.mtsust.2024.100831>

Received 28 February 2024; Received in revised form 26 April 2024; Accepted 15 May 2024

Available online 16 May 2024

2589-2347/© 2024 The Authors. Published by Elsevier Ltd. This is an open access article under the CC BY-NC license (<http://creativecommons.org/licenses/by-nc/4.0/>).

flexible and stretchable nanofibrous films with a relatively high production rate [5]. Although electrospinning has been known for quite some time, interest in the method has increased particularly in recent years due to the high demand for air filters, given the increasingly polluted air and recent pandemic threats [6]. Moreover, the functionalization of these nanofibrous materials by the integration of active nanoparticles such as zinc oxide (ZnO) has led to remarkable results regarding the inhibition of SARS-CoV-2 virus growth [7]. Shao et al. [8] fabricated an electrospun membrane with an air filtration efficiency of 99.83 % for 0.3 μm NaCl particles, while the bacteriostatic rates against *Escherichia coli* and *Staphylococcus aureus* were 99.5 % and 98.9 %, respectively.

As thermoelectric materials, electrospun membranes should offer a significant advantage in terms of flexibility and stretchability, as well as enhanced electrical properties due to the quantum confinement effect [9]. However, the conditions required for the electrospinning process (e.g., viscosity of precursor solution) limit the efficiency of the TE phenomenon. Li et al. [10] utilized electrospinning technology and n-type conjugated polymer (N2200) to fabricate a flexible nanofibrous membrane exhibiting a conductivity of $7.06 \times 10^{-4} \text{ S cm}^{-1}$ and a power factor of $0.0085 \mu\text{W m}^{-1} \text{ K}^{-2}$. Similar results were obtained by Mombini et al. [11] for electrospun nanofiber membranes based on polyvinyl alcohol (PVA), chitosan (CS), and CNTs. The maximum conductivity value obtained for their membrane was $4.1 \times 10^{-5} \text{ S cm}^{-1}$. Evaldz et al. [12] reported a conductivity of 3 S cm^{-1} and a power factor of $0.1 \mu\text{W m}^{-1} \text{ K}^{-2}$ for a film based on PEDOT: PSS. From the examples presented, it can be observed that the electrical properties of membranes obtained through the typical electrospinning process are significantly lower compared to the values reported from other preparation methods (e.g., spin coating, drop casting, knife coating, etc.) [9]. Therefore, many researchers have combined electrospinning with other techniques or post-treatments in order to accomplish higher thermoelectric performance. Jin et al. [13] immersed the nanospun membrane of PEDOT: PSS/PVA in different concentrations of silver ammonia solution ($\text{Ag}(\text{NH}_3)_2\text{OH}$) resulting in the increase of power factor up to $1.2 \mu\text{W m}^{-1} \text{ K}^{-2}$ at room temperature. He et al. [4] fabricated ultra-stretchable PEDOT: PSS/CNT composite films via electrospinning, vacuum filtration, and hot pressing. The highest power factor of $1.9 \mu\text{W m}^{-1} \text{ K}^{-2}$ was achieved in the composite films with a weight ratio of 7:3 between PEDOT: PSS and CNTs. A strategy that has yielded good results both electrically and mechanically is coating flexible scaffolds with conductive polymers or CNTs [14]. By alternating electrospinning and spraying techniques, He et al. [15] achieved a CNTs/polyvinyl pyrrolidone (PVP)/polyurethane (PU) composite membrane with high stretchability (approximately 250 %) while the Seebeck coefficient and power factor at room temperature reached $51 \mu\text{V K}^{-1}$ and $5.14 \mu\text{W m}^{-1} \text{ K}^{-2}$, respectively.

First described by Yang et al. [16] in 2005 and patented five years later, wet electrospinning quickly found utility in medical applications (e.g., cardiac tissue, cartilage, hepatic tissue, wound dressings, skin, etc.), water purification, air filtration or energy (e.g., Solar cells, Li-Batteries, Fuel Cells, Hydrogen storage, etc.) [17].

Nonetheless, the thermoelectric applications of wet-electrospun nanofibrous membranes have been seldom explored [18]. By combining electrospinning and self-assembly strategies, He et al. [19] fabricated an ultra-stretchable nano-wire that exhibited a maximum Seebeck coefficient of $44 \mu\text{V K}^{-1}$. Shaker et al. [20] realized a flexible strain gauge sensor based on wet electrospinning of TPU/PEDOT: PSS, which can elastically withstand a strain of up to 40 % and exhibits a unique electrical conductivity of 0.08 S cm^{-1} .

In this study, wet-electrospinning was employed to produce a stretchable thermoelectric nanofibrous membrane based on TPU/MWCNTs/PEDOT: PSS. The nonsolvent-induced phase separation (NISP) phenomenon, and consequently, the formation of CNTs/PEDOT: PSS/CNTs electrically-conductive chains, were controlled by tuning the concentrations of binary solvents.

Carbon nanotubes (CNTs) are often used in composite materials to enhance their conductive properties, but their use in electrospinning solutions comes with some challenges. Van der Waals forces and the high aspect ratio of CNTs often lead to their agglomeration, resulting in uneven and poorly conductive composite. Gao et al. [21] showed that the uniform dispersion of CNTs in PU/polyethersulfone (PES) composite constructs electrically conductive networks with a low percolation threshold, resulting in significantly high electrical conductivity of 2.8 S m^{-1} at a relatively low CNTs concentration of 0.85 vol %. Chen et al. [22] evidenced an improved electrical conductivity by up to two orders of magnitude in epoxy composite materials when CNTs are functionalized.

By combining CNTs and the conductive polymer PEDOT: PSS, interfacial layers can be created that act as filtering barriers for phonons and low-level electrons [9]. This filtering effect is very important because, in addition to their excellent electrical conductivity, CNTs also exhibit high thermal conductivity, which can have a significantly negative impact on the efficiency of the TE phenomenon [23]. PEDOT: PSS is a mixture of two ionomers, PEDOT and a polyelectrolyte, PSS, and this combination offers a unique synergy that enhances the overall conductivity and stability of the material. Among conductive polymers, PEDOT: PSS is considered to have the best thermoelectric properties [24]. Concurrently, TPU is an elastomer composed of alternating hard and soft segments linked by covalent bonds. The physical cross-links from pseudo-crystalline areas contribute to the high elasticity of TPU, while the soft chains impart elongation characteristics to the polymer [25].

The substantial improvement in mechanical properties achieved by incorporating the elastomers (TPU) into TE ternary composite is accompanied by drawbacks in terms of electrical properties. To address this issue, electrospinning was combined with nonsolvent-induced phase separation (NISP) as a strategy to construct interconnected conductive chains of CNTs/PEDOT: PSS/CNTs within a polymeric elastomeric scaffold of TPU to obtain efficient thermoelectric elastic membranes.

2. Experimental section

2.1. Materials

Thermoplastic polyurethane (Elastollan® C95, $M_w = 107,010 \text{ g/mol}$) was purchased from BASF Co., Ltd, Germany. Poly(3,4-ethylene dioxithiophene) poly(styrene sulfonate) (PEDOT: PSS), the conductive grade with 3–4 % solid content dispersed in distilled water, was obtained from Sigma-Aldrich Co. Multi-wall carbon nanotubes (MWCNTs) NC7000™, with an average diameter of 9.5 nm and an average length of 1.5 μm , produced via the Catalytic Chemical Vapor Deposition (CCVD) process, were purchased from Nanocyl S.A. (Sambreville, Belgium). N, N-Dimethylformamide (DMF) with a purity of $\geq 95\%$, Sulfuric Acid (H_2SO_4) molecular weight: 98.07 g/mol, Nitric Acid (HNO_3) molecular weight: 63.01 g/mol, and Tetrahydrofuran (THF) were supplied by Fisher Chemical. All chemicals were of analytical grade and employed as received.

2.2. Methods

2.2.1. TPU/MWCNTs electrospinning solution preparation

The first step in preparing the electrospinning solution involves the acid treatment of MWCNTs, aiming to introduce polar functional groups, such as carboxyl (-COOH) and hydroxyl (-OH), enhancing compatibility with polymers and polar solvents. Initially, 1 g of MWCNTs were dispersed in a mixture of 100 ml concentrated sulfuric acid and nitric acid, with a volume ratio of 1:3. Subsequently, the mixture was sonicated (53 kHz frequency) for 4.5 h at 40°C , followed by dilution with distilled water and vacuum filtration through a $0.45 \mu\text{m}$ polytetrafluoroethylene (PTFE) membrane [26]. The functionalized multiwall

carbon nanotubes (f-MWCNTs) underwent multiple washing and vacuum filtration steps to eliminate any residual acid traces until the solution reached a pH of approximately 7. Finally, the f-MWCNTs were dried in an oven at 103 °C for 24 h.

After functionalization, the required weight fractions of f-MWCNTs were initially dispersed in 10 ml of a DMF/THF mixture with varying (v/v) ratios. To ensure uniform dispersion, the solution underwent a 2-h ultrasonication treatment, followed by an additional 2 h of magnetic stirring. Subsequently, the weighed TPU was gradually added to the solutions, achieving a 10 % concentration. This was followed by stirring for 2 h at a temperature of 40 °C, and a 30-min sonication step was performed to remove any air bubbles present in the solution. The electrospinning solutions thus obtained contain 10 % TPU, in which the volumetric ratio of THF to DMF varied between 10 % and 40 % (v/v), with a concentration of f-MWCNTs ranging from 0.04 % to 0.16 %.

2.2.2. Wet electrospinning of TPU/MWCNTs solution

Electrospun TPU/MWCNT nanofibers were produced by utilizing the NANON-1B electrospinning system from MECC CO., LTD. (JAPAN). During the electrospinning process, the ambient temperature fluctuated between 20 °C and 22 °C, while the humidity ranged from 40 % to 45 %. Fig. 1 illustrates the electrospinning setup employed in this study. The prepared TPU/MWCNT solutions were introduced into a 10 ml plastic syringe equipped with a 19-gauge stainless-steel needle. A constant flow rate was maintained by the syringe pump of the system through the needle. The high voltage was applied between the needle and the collector, which was connected to the ground. Initially, the TPU/MWCNT nanofibers were deposited on aluminum foil to optimize the electrospinning parameters.

Subsequently, the nanofibers were accumulated in a glass container positioned over the collector, which contains an aqueous dispersion of PEDOT: PSS, serving as a coagulation bath. The TPU/MWCNTs nanofibers were instantaneously saturated by the conductive polymer solution, resulting in a porous TPU/MWCNTs/PEDOT: PSS solidified membrane through the nonsolvent-induced phase separation process (NIPS). The nanoporous membranes, thus obtained, were maintained in the coagulation bath for an additional 180 min, followed by washing and vacuum drying at 70 °C for 48 h.

2.2.3. Characterization and thermoelectrical performance

The microstructures of nanofibrous materials were characterized using a Leica DMRXE optical microscope (Leica Microsystems) with Leica QWin Plus software and a scanning electron microscope (SEM) JEOL JSM-6010V (JEOL Benelux). X-ray diffraction (XRD) measurements were conducted with LabX XRD-6100 (Shimadzu, Japan), and Fourier transform infrared (FTIR) analysis was performed using the IRPrestige-21 spectrophotometer (Shimadzu Europe GmbH, Duisburg,

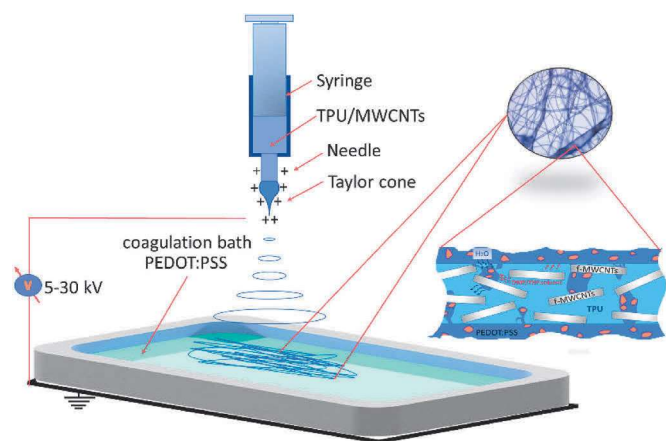


Fig. 1. A schematic setup of the wet electrospinning technique.

Germany). The electrical conductivity, σ , was measured by the Two-Point Probe (2-point) technique with a Keithley 6487 Picoammeter/Voltage Source, and the thickness of the samples was determined using a step profiler, Amboise XP-200.

To assess the Seebeck coefficient, the setup depicted in Fig. 2 was employed. A heating element (flat resistance) and a cooling system were used to create a temperature gradient across the sample material, which was monitored by K-type thermocouples. For recording and analyzing electric power generated, as well as temperature gradient measurement, a data acquisition DAQ NI 9214 (National Instruments), along with LabVIEW software, was employed.

The mechanical properties were examined using an Instron 5969 dual-column testing system according to ISO 37:2017. Tensile stress-strain tests were performed at 20 °C and 65 % RH. A minimum of five samples (10 mm × 20 mm) were tested for each membrane type, and the average value was considered. A traverse speed of 10 mm/min was employed, and Young's modulus was determined by calculating the slope of the linear section of the stress-strain curve.

3. Results and discussions

3.1. Mechanism of fibrous membrane formation

The TPU/MWCNTs/PEDOT: PSS hybrid porous membrane was prepared using electrospinning and nonsolvent-induced phase separation method (NISP). The proposed mechanism of the membrane-formation process is illustrated in Fig. 3.

In the first stage, rapid evaporation of the solvent takes place, especially THF which has a lower boiling point than DMF [27], forming slight craters on the surface of the nanofibers. The second stage is characterized by a slow exchange of solvents/non-solvents and finger-like micropores formation. The slow diffusion process is attributed to the lower affinity of THF for water compared to DMF [28]. In stage 3, all residual solvents are evaporated, defining the porous structure, followed by the final stage in which the membrane is washed and dried.

Due to the uniform dispersion of f-MWCNTs, many of these pores reach carbon nanotube ends, and the carboxylic groups may not only form hydrogen bonds with the sulfonate groups from PEDOT: PSS but also generate a conjugated structure between the f-MWCNTs and PEDOT: PSS, facilitating the movement of charge carriers [29].

Zhang et al. [28] analyzed the formation of micropores in TPU films using a binary solvent. They found that the average micropore sizes can be controlled by altering the THF concentration, reaching several hundred nanometers when using the cast-on glass mold method, and subsequently transferring it into the water coagulation bath. In the case of the electrospinning method, the TPU/MWCNTs composite nanofibers contain less binary solvent when deposited in the aqueous coagulation

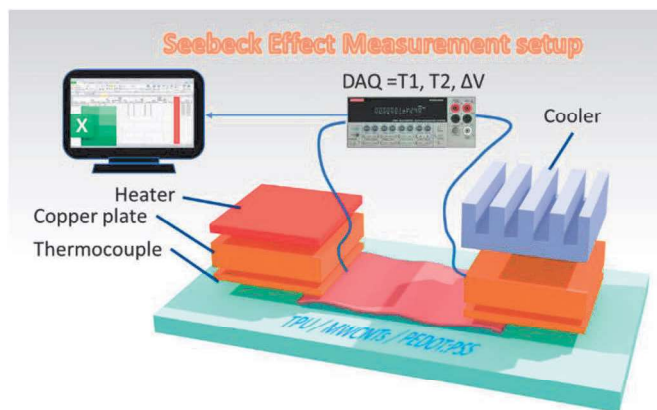


Fig. 2. Seebeck coefficient measuring setup.

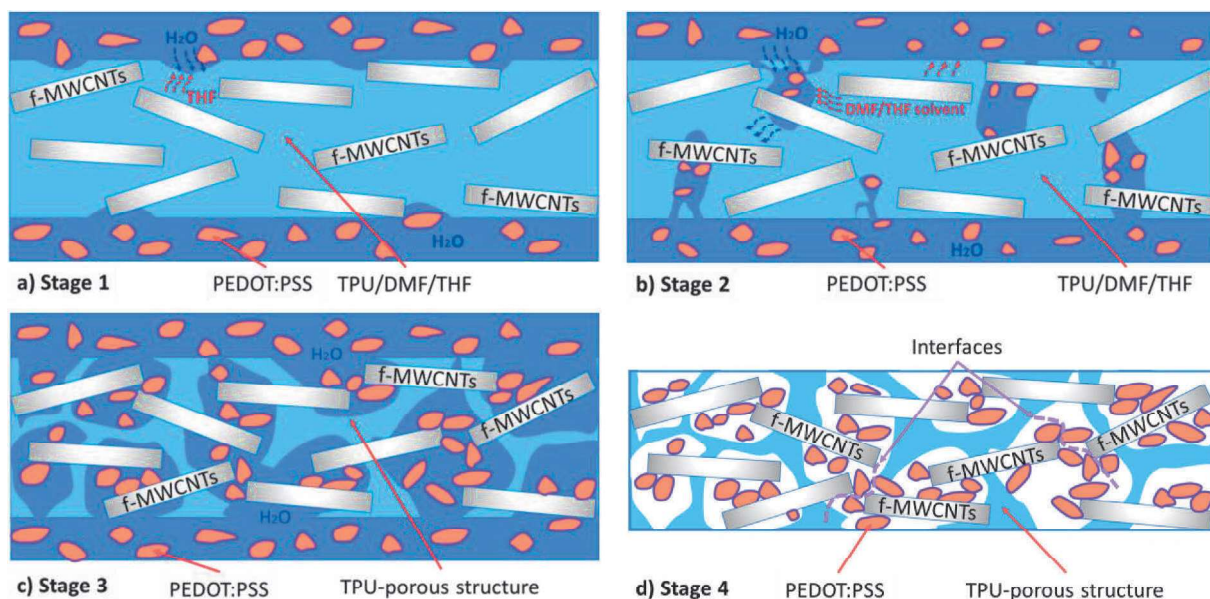


Fig. 3. Schematic representation of the formation mechanism of hybrid nanofiber mats based on solvent/nonsolvent-induced phase separation.

bath, and as a result, the micropores will also decrease in size. However, when their size exceeds a few tens of nanometers, the PEDOT: PSS particles, which typically have sizes between 12 nm and 19 nm [30], penetrate inside the micropores, creating filtering interfaces between the carbon nanotube chains.

3.2. Hybrid film characterization

3.2.1. Characteristics and morphology of hybrid nanofiber mats

The morphology analysis of the TPU/MWCNTs/PEDOT: PSS hybrid nanofiber film is presented in Fig. 4.

The initial microscopic examination of dry electrospun nanofibers, as shown in Fig. 4 a), revealed agglomerated MWCNTs forming small clusters and bundles. Physical methods, such as mechanical stirring or

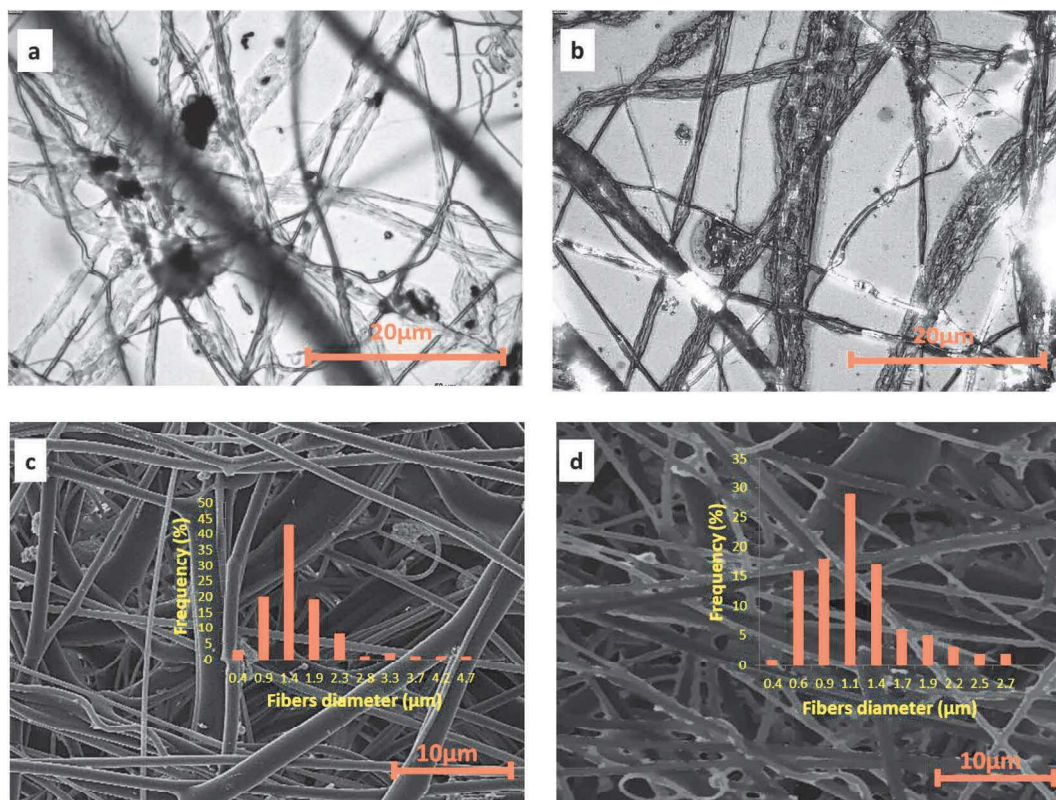


Fig. 4. Morphological analysis of hybrid nanofiber mats: micrographs (200x optical) of dry electrospun films of a) TPU/MWCNTs and b) TPU/f-MWCNTs, respectively, and SEM images and fiber diameter distribution for c) dry electrospun TPU/f-MWCNTs and d) wet electrospun TPU/f-MWCNTs in a coagulation water solution of PEDOT: PSS.

sonication [31,32], employed to disperse pristine MWCNTs in the binary solvent, did not yield satisfactory results, even though the electrospinning process started immediately after solution preparation. The slow nanospinning process facilitates phase separation, even though the Van der Waals forces are weak, and the electrospinning solution has a high viscosity. The uniform dispersion of MWCNTs in the TPU matrix is a crucial factor for the charge carriers' behavior. Therefore, the functionalization of MWCNTs was deemed necessary. Fig. 4 b) presents a microscopic image of the TPU/f-MWCNTs nanofiber mat. The alignment of f-MWCNTs along the fiber axis is evident, with no signs of particle aggregation, highlighting the effectiveness of the functionalization process. Comparable findings regarding electrospun nanofibers of TPU/MWNTs were reported in other studies as well [33].

The SEM images of optimized nanofiber structures are presented in Fig. 4 c) and 4. d), wherein the histograms of diameters were made using Image-J software for 100 randomly selected fibers. The average fiber diameters for both dry and wet electrospun nanofiber mats were 1.38 μm and 1.10 μm , respectively. The dry electrospun TPU/f-MWCNTs samples (Fig. 4 c) reveal a smooth 3D fibrous configuration without the presence of beads, along with a broad distribution of fiber diameters. Moving to wet electrospinning (Fig. 4 d), the TPU/f-MWCNTs nanofiber mat exhibits more uniform fiber diameters and also the absence of beads. However, the borders of the 3D fibers are not as uniform.

Although the fibers reaching the collector have solidified, they still retain a residual amount of solvent. The solvent concentration is higher in fibers with larger diameters, making them more susceptible to the induced phase separation process, which can result in dimensional changes. Consequently, the diameters' distribution becomes more uniform. The uniformity of the nanofibers' diameters reduces stress concentrations in the material to a minimum, thereby enhancing mechanical stability and preventing potential fractures during stretching operations [34]. Moreover, the nanofibers with smaller dimensions exhibit more pronounced quantum-like properties, leading to an improvement in electrical conductivity [35].

To validate the hybridization of the TPU/f-MWCNTs/PEDOT: PSS nanofiber mats via the wet electrospinning process, we investigated structural evolutions arising from covalent bond interactions of the functional groups, using both XRD and FTIR characterization techniques. FTIR spectra of f-MWCNTs, PEDOT: PSS, TPU, and the hybrid membrane TPU/f-MWCNTs/PEDOT: PSS are shown in Fig. 5.

As indicated in previous research [33,36], pristine MWNTs do not show any characteristics in the infrared region. However, following acid treatment, distinctive peaks at 1556 cm^{-1} , 1732 cm^{-1} , 1769 cm^{-1} , and

3446 cm^{-1} are observed. The strong bands at 1733 cm^{-1} and 1769 cm^{-1} are often associated with the carbonyl (C=O) stretching vibrations in MWCNT-COOH [37], confirming the successful oxidation of CNTs. Additionally, the peak at 1555 cm^{-1} is attributed to the carboxylate anion stretch mode [38], and the small peak at 3446 cm^{-1} corresponds to O-H bond [39].

Regarding the FTIR characteristics of PEDOT: PSS, it notes peaks at 2918 cm^{-1} and 2850 cm^{-1} corresponding to the asymmetric and symmetric stretching vibration of C-H bonds in the aliphatic (non-aromatic) hydrocarbon chains of PSS, at 1712 cm^{-1} associated with C=O stretching vibrations indicating carbonyl groups likely from the PSS component, at 1015 cm^{-1} usually attributed to C-O stretching vibrations indicative of ether or ester groups related to PSS, and at 732 cm^{-1} indicating the stretching vibrations of the C-S-C bond, characteristic of the thiophene rings present in PEDOT [40].

The FTIR spectra of TPU exhibit broad peaks at 3330 cm^{-1} indicating N-H stretching vibrations associated with carbamic acid ester, while the peaks at 2955 cm^{-1} and 2872 cm^{-1} are typically attributed to the stretching vibrations of asymmetric and symmetric methylene (CH_2), respectively, in the aliphatic chains. The strong band observed at 1731 cm^{-1} , and 1597 cm^{-1} are usually associated with the stretching vibration of the carbonyl group (C=O) of urethane, while the 1529 cm^{-1} medium peak indicates N-H bending vibrations, potentially from amide groups [41]. Additionally, the peak located at 1070 cm^{-1} suggests the C-O stretching vibrations, which may be attributed to ether linkages in TPU, and the peak at 712 cm^{-1} corresponds to C-H bending vibrations in the aliphatic structure of TPU [42].

From the FTIR spectra of TPU/f-MWCNTs/PEDOT: PSS it can be noted that the hybrid nanofiber membrane exhibits many similar peaks at different intensities as PEDOT: PSS. Nevertheless, the broad absorption band at 3423 cm^{-1} , associated with the stretching vibrations of N-H, present in the spectroscopy data of the dry electrospun TPU membrane is also observed in the FTIR spectra of TPU/MWCNTs/PEDOT: PSS nanofiber mats.

Furthermore, the peaks at 2918 cm^{-1} and 2850 cm^{-1} from PEDOT: PSS spectra, associated with C-H stretching vibrations in the aliphatic hydrocarbon chains of PSS, are slightly shifted and broadened in the hybrid TPU/MWCNTs/PEDOT: PSS. This could be due to a more complex and heterogeneous environment in the hybrid film, involving interactions between TPU and PEDOT: PSS components. Similarly, the peak at 1712 cm^{-1} , attributed to the stretching vibration of C=O bonds in sulfonate groups of PSS, involved in the complex copolymer structure PEDOT: PSS, is shifted to 1724 cm^{-1} in the FTIR spectrum of the TPU/

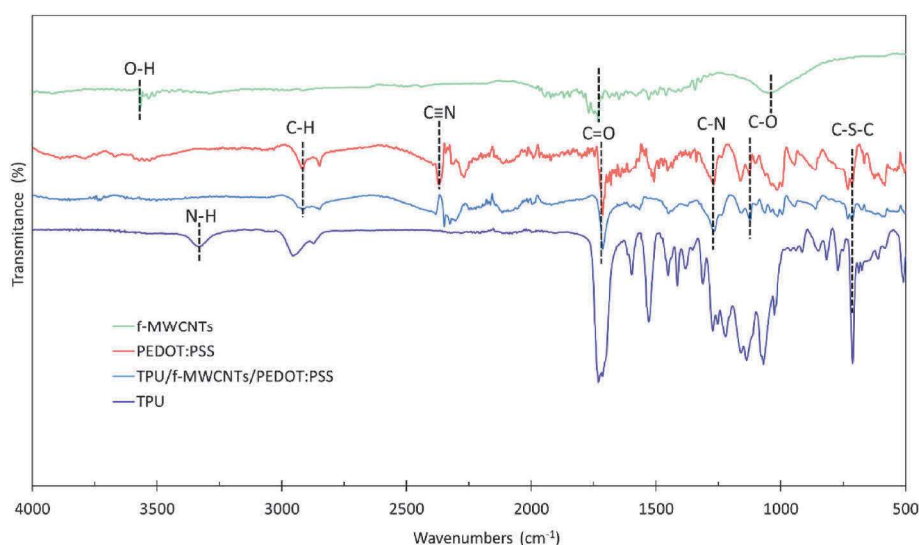


Fig. 5. FTIR spectra of f-MWCNTs, PEDOT: PSS, TPU, and TPU/f-MWCNTs/PEDOT: PSS film.

MWCNTs/PEDOT: PSS membrane. These observations indicate an evident interaction between MWCNTs and the PEDOT: PSS.

To further explore the micro-structure of hybrid nanofiber mats, the XRD pattern of the f-MWCNTs, TPU, TPU/f-MWCNTs, and TPU/f-MWCNTs/PEDOT: PSS were investigated. Phase analysis was conducted using the X-ray diffractometer (XRD) with Cu-K α X radiation with a wavelength of 1.54056 Å, and a scan rate of 0.02°/s. The diffraction was performed at Bragg angles between 10° and 80°, as shown in Fig. 6.

The diffraction pattern of the f-MWCNTs is characterized by two peaks. The high peak $2\theta = 26.07^\circ$, corresponds to the (002) reflection plane of the hexagonal graphite structure and the smaller one $2\theta = 44.65^\circ$ corresponds to (100) graphitic planes [43]. A more in-depth analysis of the XRD characteristic peaks reveals the high crystallinity of the MWCNTs, attributed to the sharp intensity of the (002) peak. The asymmetry in its line shape indicates the presence of distinct crystalline species. Furthermore, it is well known that the functionalization of MWCNTs does not affect the organization of the graphene layers [44]. The inter-atomic spacing value, d-spacing, at a specific 2θ value can be calculated with Bragg's Law. Thus, the d-spacing values for MWCNTs peaks are approximately 3.41 Å and 2.02 Å for $2\theta = 26.07^\circ$ and $2\theta = 44.65^\circ$, respectively.

Polyurethane is generally a semi-crystalline polymer, and for this reason, the XRD pattern of the dry electrospun TPU membrane shows a broad reflection at 2θ of 20.8°, which is produced by the (110) planes of the TPU soft segments [45]. The presence of a regular order within the hard and soft segments interplays with the disordered structure of the amorphous TPU matrix, giving rise to these characteristics. This reflection from small crystallites is obscured by the broad reflection of the amorphous region [46].

By adding f-MWCNTs as a filler in the TPU nanofiber mats, the ordering of TPU is enhanced, revealing two distinct peaks at approximately 20.4° and 25.9°. The weak intensity of the (002) plane of MWCNTs can be explained by the presence of TPU on the surface of CNT, indicating a homogeneous dispersion of f-MWCNTs in the TPU matrix. Moreover, MWCNTs serve as nucleation points, promoting the formation of larger and more organized crystalline structures within the TPU matrix [36].

On the other hand, in the case of the wet electrospun membrane of TPU/f-MWCNTs in a PEDOT: PSS water dispersion, the intensity of the (002) plane of MWCNTs significantly increases. This observation indicates that portions of the MWCNTs are no longer covered by TPU and interact with PEDOT: PSS, which exhibits a peak around the value of 26.0°, associated with the structure of PEDOT macromolecular chains [47,48]. The abundant π -bonds of MWCNTs contribute to a strong π - π connection with the PEDOT chains, which, in turn, have plentiful π bonds. Concurrently, the intensity of the first characteristic peak of the hybrid membrane becomes weak and slightly shifts from 20.4° to 19.8°.

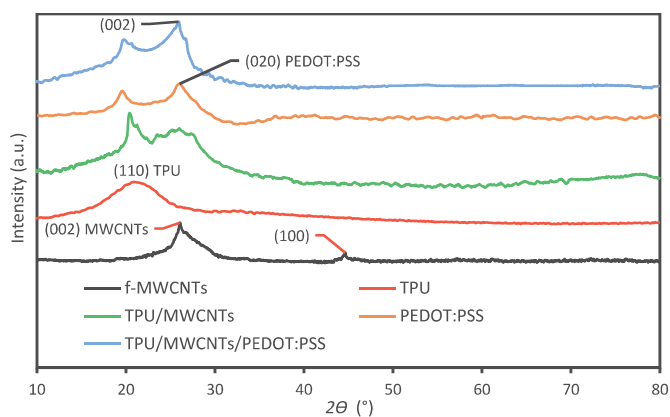


Fig. 6. XRD patterns of f-MWCNTs, TPU, TPU/f-MWCNTs, and TPU/f-MWCNTs/PEDOT: PSS nanofiber mats.

This can be explained by the broad peak of PSS around 19.6°, which can engage in hydrophilic-hydrophilic interactions with the functional groups of f-MWCNTs [48].

3.2.2. Thermoelectrical performance of hybrid film

The impact of THF and f-MWCNTs concentrations on the TE properties of electrospun TPU/f-MWCNTs/PEDOT: PSS hybrid film is presented in Fig. 7.

As shown in Fig. 7 a), the electrical conductivity of the samples shows values ranging from 5.36 S cm⁻¹ to 97.26 S cm⁻¹ when the concentration of f-MWCNTs varies between 0.04 % and 0.16 %, and the ratio of THF to DMF in the binary solvent is 1:4. In recent studies it was observed that loading f-MWCNTs in PU/MWCNTs composites below 0.5 % wt (corresponding to 0.05 % in electrospinning solution), resulted in an electrical conductivity that did not exceed 1.0×10^{-1} S m⁻¹ [49,50]. The increase in electrical conductivity by several orders of magnitude can be attributed to both the aligned conductive chains of f-MWCNTs obtained through wet electrospinning [15] and the PEDOT: PSS conjunctive polymer, which creates a conductive network in the fibrous TPU/f-MWCNTs composite [51]. However, when the concentration of carbon nanotubes exceeds 0.12 %, there are only marginal improvements in electrical conductivity, and it is accompanied by a reduction in the Seebeck coefficient. Therefore, the Power Factor no longer shows significant improvements (Fig. 7 b). It is important to note that electrical conductivity does not exhibit a sharp transition from low to high values around the threshold percolation of MWCNTs, as commonly observed in other research works [33,52].

Fig. 7 c) illustrates the impact of cosolvent (THF) concentration in the electrospinning solution on electrical conductivity and Seebeck coefficient when the concentration of f-MWCNTs is 0.12 %. The electrical conductivity obtained for 10 % (v/v) THF in an electrospinning solution was measured to be 101.4 S cm⁻¹. The higher concentration of THF changes the pore morphologies of the resulting fibrous film due to the non-solvent-induced phase separation mechanism [28], leading to a decrease in the electrical conductivity accompanied by a significant improvement in the Seebeck coefficient. The alterations in TE properties appear to originate from the size and density of the formed micropores. These micropores interrupt the specific chains of MWCNTs.

However, at a concentration of approximately 25 % (v/v) THF, a threshold can be observed. The thermoelectric properties of the nanofibrous membrane come from two sources: MWCNTs, which form conductive chains inside of nanofibers and PEDOT: PSS, which decorates the surface of the nanofibers. At a constant concentration of CNTs, the only condition that changes is the ratio of THF: DMF in the binary solvent, which, according to Zang et al. [28], alters the pore size. Therefore, when the nanopores increase in size, surpassing the average size of PEDOT: PSS (12–19 nm) [30], the conductive polymer penetrates the voids, forming conductive chains of MWCNTs-PEDOT: PSS-MWCNTs. These bonds, attributed to the PEDOT: PSS coating on the surface of the functionalized CNTs, act as interfaces for filtering phonons and low-energy electrons [53], resulting in a more than 2.5-fold increase in the Power Factor. Above 25 % (v/v) of THF in the electrospinning solution, the power factor exhibited by nanofibrous films (Fig. 7 d) begins to decrease. This suggests that the voids are saturated with PEDOT: PSS and the specific chains of MWCNTs continue to break as the size and density of micropores increase.

3.2.3. Mechanical characterization

To investigate the influence of THF concentration on the mechanical properties of the obtained fibrous membranes, when the electrospinning solution contains 0.12 % MWCNTs, tensile strain tests were performed. Fig. 8 a) shows the stress-strain curves for each sample of TPU/MWCNTs/PEDOT: PSS composite, while Fig. 8 b) presents the values of Young's modulus measured at the strain of 5 % inside a linear stress-strain region. The failure strength and break strain of composite samples are shown in Fig. 9.

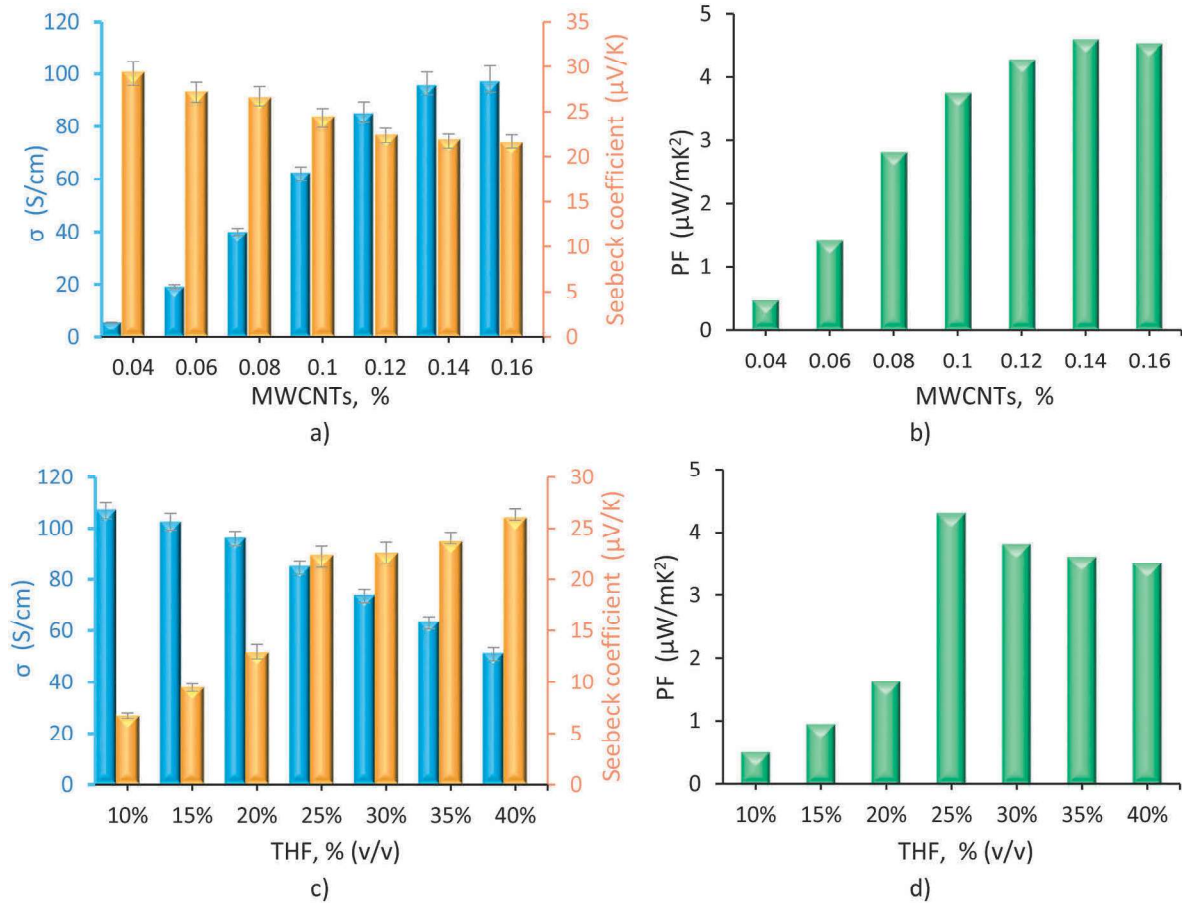


Fig. 7. Thermoelectric properties of the TPU/f-MWCNTs/PEDOT:PSS hybrid nanofiber mats: a) Electrical conductivity and Seebeck coefficient, and b) Power Factor at a TPU concentration of 25 % (v/v) in the electrospinning solution, with f-MWCNTs varying between 0.04 % and 0.16 %; c) Electrical conductivity and Seebeck coefficient, and d) Power Factor at a f-MWCNTs concentration of 0.12 % in the electrospinning solution, with TPU varying between 10 % and 40 % (v/v).

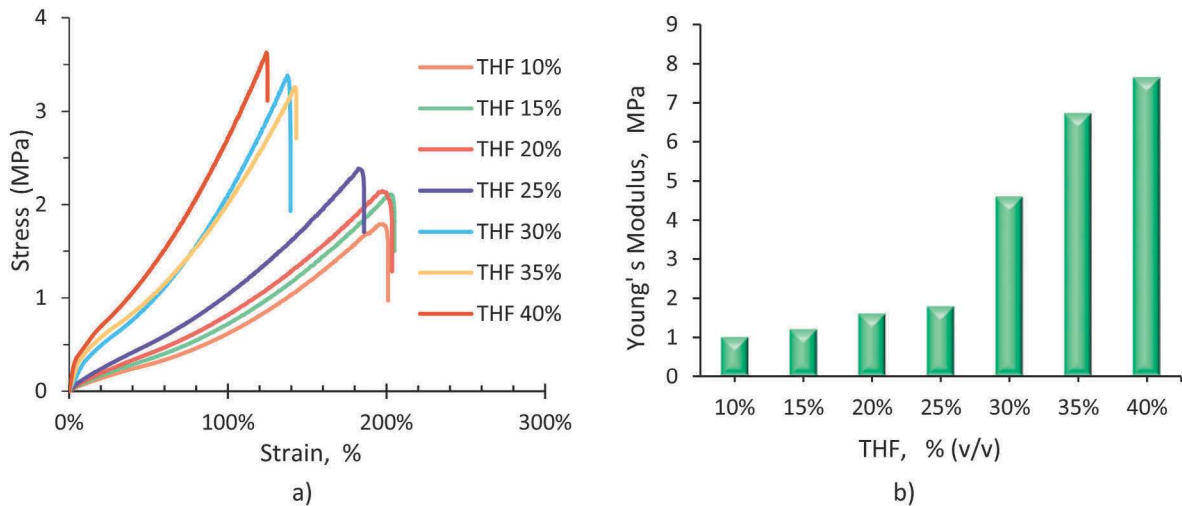


Fig. 8. The influence of THF concentrations on mechanical properties of fabricated composite fibrous membranes (TPU/MWCNTs/PEDOT:PSS): a) stress-strain diagrams and b) Young's modulus.

As can be seen from Figs. 8 and 9, the THF concentrations lower than 25 % (v/v) do not significantly influence the tensile properties of the hybrid film. The failure strength varies between 1.8 MPa and 2.4 MPa, and the strain break ranges from 200 % to 186 %. Young's modulus within the same range concentration has very low values (between 1 MPa and 1.8 MPa) indicating a good stretchability. Shamsi et al. [54]

reported that the dry electrospun TPU showed a failure strength of 45 MPa and Young's modulus of 25 MPa. Therefore, the lower failure strength can be attributed to the presence of carbon nanotubes inside of nanofiber structure, as confirmed by other studies as well [50]. On the other hand, the high elasticity can be explained by the deformation of the micropores resulting from the nonsolvent-induced phase separation

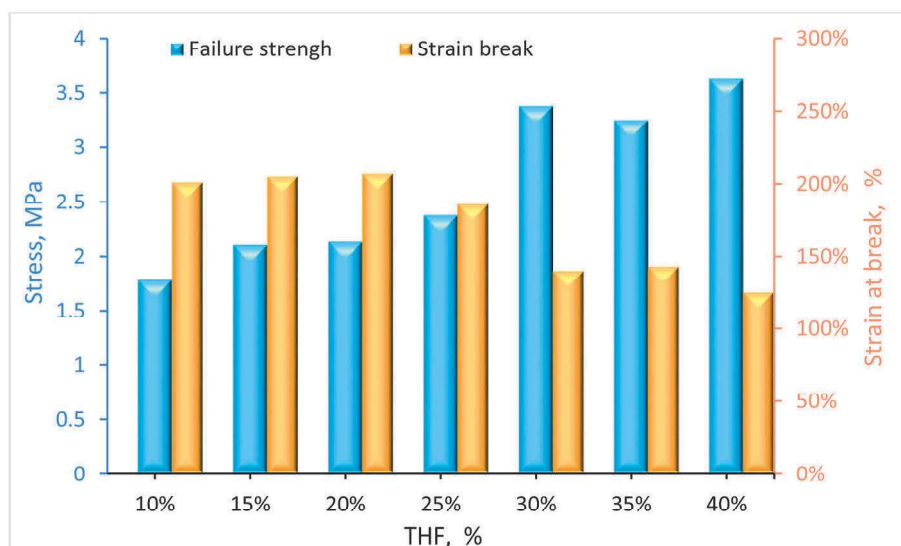


Fig. 9. The influence of THF concentrations on failure strength and break strain of fabricated composite fibrous membranes (TPU/MWCNTs/PEDOT: PSS).

process.

Concomitantly with the increase in THF concentration, the micropores grow in size and are filled with PEDOT: PSS particles, hindering their deformation and leading to higher rigidity. The increase in failure strength may be a result of the new bonds formed between functionalized carbon nanotubes and PEDOT: PSS.

4. Conclusions

Thermoelectric nanocomposites based on conductive polymers and carbon nanotubes as fillers are of high interest due to their applicability in wearable electronics. Through the method described in this paper, elastic nanoporous membranes based on thermoplastic polyurethanes were obtained. By adjusting the ratio of THF in the binary solvent, the morphology of nanoporous membranes can be fine-tuned, allowing for the creation of numerous conductive chains of PEDOT: PSS/MWCNTs while, simultaneously, maintaining the stretchability of the composites. These bonds were facilitated by the functionalization of the carbon nanotubes, the carboxyl group acting as a surfactant to bind the CNTs.

The optimal value of the Power Factor, $4.28 \mu\text{W m}^{-1} \text{K}^{-2}$, combined with the high stretchability of the sample, was obtained for 0.12 % MWCNTs and a 1:4 ratio of THF to DMF in the binary solvent. The sample exhibited a high value of electrical conductivity of 85 S m^{-1} and showed a strain range of 190 %.

The stretchable TPU/MWCNTs/PEDOT: PSS nanocomposite produced by the wet-electrospinning method can be a good candidate for wearable electronic applications such as self-powered sensors, medical devices, or power generators, offering an alternative to conventional devices that raise concerns regarding resource scarcity and environmental impact.

CRediT authorship contribution statement

Teodor Cezar Codau: Investigation, Conceptualization. **Elena Codau:** Writing – original draft, Supervision, Methodology.

Declaration of competing interest

The authors declare that they have no known competing financial interests or personal relationships that could have appeared to influence the work reported in this paper.

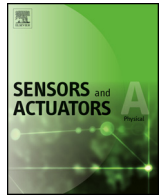
Data availability

No data was used for the research described in the article.

References

- [1] K. Namsheer si, C.S. Rout, Conducting polymers: a comprehensive review on recent advances in synthesis, properties and applications, *RSC Adv.* 11 (10) (2021) 5659–5697.
- [2] Y.H. Kang, S.-J. Ko, M.-H. Lee, Y.K. Lee, B.J. Kim, si S.Y. Cho, Highly efficient and air stable thermoelectric devices of poly(3-hexylthiophene) by dual doping of Au metal precursors, *Nano Energy* 82 (April 2021) 105681.
- [3] T.A. Yemata, A.K.K. Kyaw, Y. Zheng, X. Wang, Q. Zhu, W.S. Chin si J. Xu, Enhanced thermoelectric performance of poly(3,4-ethylenedioxythiophene):poly(4-styrenesulfonate) (PEDOT:PSS) with long-term humidity stability via sequential treatment with trifluoroacetic acid, *Polym. Int.* 69 (November 2019) 84–92.
- [4] X. He, J. Shi, Y. Hao, L. Wang, X. Qin si, J. Yu, PEDOT:PSS/CNT composites based ultra-stretchable thermoelectrics and their application as strain sensors, *Compos. Commun.* 27 (October 2021) 100822.
- [5] Z. Shao, H. Chen, Q. Wang, G. Kang, X. Wang, W. Li, Y. Liu si G. Zheng, High-performance multifunctional electrospun fibrous air filter for personal protection: a review, *Separ. Purif. Technol.* 302 (December 2022) 122175.
- [6] Z. Shao, G. Kang, J. Xie, R. Shen, H. Li, Z. Zeng, J. Jiang, X. Wang, W. Li, S. Guo, Y. Liu si G. Zheng, Electrospun mutualism-inspired CA/CMA/PHMB ultrafine bimodal nanofibrous membrane for high-performance, antibacterial, and mosquito-repellent air filtration, *Separ. Purif. Technol.* 327 (December 2023) 124920.
- [7] T. Ferreira, A.C. Vale, A.C. Pinto, R.V. Costa, V. Pais, D. Sousa, F. Gomes, G. Pinto, J.G. Dias, I.P. Moreira, C. Mota, J. Bessa, J.C. Antunes, M. Henriques, F. Cunha si R. Fangueiro, Comparison of zinc oxide nanoparticle integration into non-woven fabrics using different functionalisation methods for prospective application as active facemasks, *Polymers* 15 (August 2023) 3499.
- [8] Z. Shao, Y. Chen, J. Jiang, Y. Xiao, G. Kang, X. Wang, W. Li si G. Zheng, Multistage-split ultrafine fluffy nanofibrous membrane for high-efficiency antibacterial air filtration, *ACS Appl. Mater. Interfaces* 14 (April 2022) 18989–19001.
- [9] T.C. Codau, J.C. Antunes, F. Cunha, E. Codau, si R. Fangueiro, Polymer-based thermoelectric fibers and composites: individual and combined approaches towards enhanced efficiency, *Mater. Today Commun.* 38 (March 2024) 107682.
- [10] J. Li, C. Dong, J. Hu, J. Liu si Y. Liu, Self-standing and flexible thermoelectric nanofiber mat of an n-type conjugated polymer, *ACS Appl. Electron. Mater.* 3 (August 2021) 3641–3647.
- [11] S. Mombini, J. Mohammadnejad, B. Bakhshandeh, A. Narmani, J. Nourmohammadi, S. Vahdat si S. Zirak, Chitosan-PVA-CNT nanofibers as electrically conductive scaffolds for cardiovascular tissue engineering, *Int. J. Biol. Macromol.* 140 (November 2019) 278–287.
- [12] E. Ewaldz, J.M. Rinehart, M. Miller si B. Brettmann, Processability of thermoelectric ultrafine fibers via electrospinning for wearable electronics, *ACS Omega* 8 (August 2023) 30239–30246.
- [13] S. Jin, T. Sun, Y. Fan, L. Wang, M. Zhu, J. Yang si W. Jiang, Synthesis of freestanding PEDOT:PSS/PVA@Ag NPs nanofiber film for high-performance flexible thermoelectric generator, *Polymer* 167 (March 2019) 102–108.
- [14] X. He, B. Li, J. Cai, H. Zhang, C. Li, X. Li, J. Yu, L. Wang si X. Qin, A waterproof, environment-friendly, multifunctional, and stretchable thermoelectric fabric for continuous self-powered personal health signal collection at high humidity, *SusMat* 3 (September 2023) 709–720.

- [15] X. He, J. Shi, Y. Hao, M. He, J. Cai, X. Qin, L. Wang și J. Yu, Highly stretchable, durable, and breathable thermoelectric fabrics for human body energy harvesting and sensing, *Carbon Energy* 4 (April 2022) 621–632.
- [16] W. Yang, H. Yu, M. Zhu, H. Bai, și Y. Chen, Poly(m-Phenylene isophthalamide) ultrafine fibers from an ionic liquid solution by dry-jet-wet-electrospinning, *J. Macromol. Sci., Part B* 45 (August 2006) 573–579.
- [17] A. Barhoum, K. Pal, H. Rahier, H. Uludag, I.S. Kim, și M. Bechelany, Nanofibers as new-generation materials: from spinning and nano-spinning fabrication techniques to emerging applications, *Appl. Mater. Today* 17 (December 2019) 1–35.
- [18] M.L. Mejía Suaza, Y. Hurtado Henao, și M.E. Moncada Acevedo, Wet electrospinning and its applications: a review, *Tecnológicas* 25 (June 2022) e2223.
- [19] X. He, J. Gu, Y. Hao, M. Zheng, L. Wang, J. Yu și X. Qin, Continuous manufacture of stretchable and integratable thermoelectric nanofiber yarn for human body energy harvesting and self-powered motion detection, *Chem. Eng. J.* 450 (December 2022) 137937.
- [20] A. Shaker, A.H. Hassanin, N.M. Shaalan, M.A. Hassan, și A.A. El-Moneim, Micropatterned flexible strain gauge sensor based on wet electrospun polyurethane/PEDOT: PSS nanofibers, *Smart Mater. Struct.* 28 (June 2019) 075029.
- [21] J. Gao, H. Wang, X. Huang, M. Hu, H. Xue și R.K.Y. Li, Electrically conductive polymer nanofiber composite with an ultralow percolation threshold for chemical vapour sensing, *Compos. Sci. Technol.* 161 (June 2018) 135–142.
- [22] J. Chen și J. Han, Effect of hydroxylated carbon nanotubes on the thermal and electrical properties of derived epoxy composite materials, *Results Phys.* 18 (September 2020) 103246.
- [23] J. Li, A.B. Huckleby, și M. Zhang, Polymer-based thermoelectric materials: a review of power factor improving strategies, *Journal of Materiomics* 8 (January 2022) 204–220.
- [24] G. Prunet, F. Pawula, G. Fleury, E. Cloutet, A.J. Robinson, G. Hadziioannou și A. Pakdel, A review on conductive polymers and their hybrids for flexible and wearable thermoelectric applications, *Materials Today Physics* 18 (May 2021) 100402.
- [25] Z. Li, Y. Sun, B. Zhou, Y. Feng, C. Liu și C. Shen, Flexible thermoplastic polyurethane/MXene foams for compressible electromagnetic interference shielding, *Materials Today Physics* 32 (March 2023) 101017.
- [26] L.Y. Jun, N.M. Mubarak, L.S. Yon, C.H. Bing, M. Khalid și E.C. Abdullah, Comparative study of acid functionalization of carbon nanotube via ultrasonic and reflux mechanism, *J. Environ. Chem. Eng.* 6 (October 2018) 5889–5896.
- [27] T.Y. Chee, A.R. Mohd Yusoff, F. Abdullah, W.M. Asyraf Wan Mahmood, M.J. Fathi Jasni, N.A. Nizam Nik Malek, N.A. Buang, și M. Govarathanan, Fabrication, characterization and application of electrospun polysulfone membrane for phosphate ion removal in real samples, *Chemosphere* 303 (September 2022) 135228.
- [28] C. Zhang, P. Lyu, L. Xia, Y. Wang, C. Li, X. Xiang, F. Dai, W. Xu, X. Liu și B. Deng, Regulation of pore morphologies of PU films and thereof water vapor permeability by varying tetrahydrofuran concentration in binary solvent, *Polym. Test.* 69 (August 2018) 32–38.
- [29] D. Wang, C. Lu, J. Zhao, S. Han, M. Wu și W. Chen, High energy conversion efficiency conducting polymer actuators based on PEDOT:PSS/MWCNTs composite electrode, *RSC Adv.* 7 (2017) 31264–31271.
- [30] K. Jain, A.Y. Mehandzhiyski, I. Zozoulenko și L. Wågberg, PEDOT:PSS nanoparticles in aqueous media: a comparative experimental and molecular dynamics study of particle size, morphology and z-potential, *J. Colloid Interface Sci.* 584 (February 2021) 57–66.
- [31] K. Nasouri, A.M. Shoushtari, A. Kafrou, H. Bahrambeygi și A. Rabbi, Single-wall carbon nanotubes dispersion behavior and its effects on the morphological and mechanical properties of the electrospun nanofibers, *Polym. Compos.* 33 (September 2012) 1951–1959.
- [32] F.N.A.M. Sabri, M.R. Zakaria și H.M. Akil, Dispersion and stability of multiwalled carbon nanotubes (MWCNTs) in different solvents, în *AIP Conference Proceedings* 2267 (September 2020) 020043.
- [33] F. Pouladzadeh, A.A. Katbab, N. Haghighipour și E. Kashi, Carbon nanotube loaded electrospun scaffolds based on thermoplastic urethane (TPU) with enhanced proliferation and neural differentiation of rat mesenchymal stem cells: the role of state of electrical conductivity, *Eur. Polym. J.* 105 (August 2018) 286–296.
- [34] S. Gu, Q. Wu, J. Ren și G.J. Vancso, Mechanical properties of a single electrospun fiber and its structures, *Macromol. Rapid Commun.* 26 (April 2005) 716–720.
- [35] J.-H. He, Y.-Q. Wan, și L. Xu, Nano-effects, quantum-like properties in electrospun nanofibers, *Chaos, Solit. Fractals* 33 (July 2007) 26–37.
- [36] S. Kumar, T.K. Gupta și K.M. Varadarajan, Strong, stretchable and ultrasensitive MWCNT/TPU nanocomposites for piezoresistive strain sensing, *Compos. B Eng.* 177 (November 2019) 107285.
- [37] M. Hassani, A. Tahghighi, M. Rohani, M. Hekmati, M. Ahmadian și H. Ahmadvand, Robust antibacterial activity of functionalized carbon nanotube-levofloxacin conjugate based on in vitro and in vivo studies, *Sci. Rep.* 12 (June 2022).
- [38] T.L.d.A. Montanheiro, F.H. Cristóvan, J.P.B. Machado, D.B. Tada, N. Durán și A. P. Lemes, Effect of MWCNT functionalization on thermal and electrical properties of PHBV/MWCNT nanocomposites, *J. Mater. Res.* 30 (November 2014) 55–65.
- [39] V.B. Sarode, R.D. Patil și G.E. Chaudhari, Characterization of functionalized multi-walled carbon nanotubes, *Mater. Today: Proc.* (July 2023), <https://doi.org/10.1016/j.matpr.2023.06.288>. Available online.
- [40] J. Ram, R.G. Singh, F. Singh, V. Kumar, V. Chauhan, R. Gupta, U. Kumar, B. C. Yadav, și R. Kumar, Development of WO₃-PEDOT: PSS hybrid nanocomposites based devices for liquefied petroleum gas (LPG) sensor, *J. Mater. Sci. Mater. Electron.* 30 (June 2019) 13593–13603.
- [41] L. Tong, X.-X. Wang, X.-X. He, G.-D. Nie, J. Zhang, B. Zhang, W.-Z. Guo, și Y.-Z. Long, Electrically conductive TPU nanofibrous composite with high stretchability for flexible strain sensor, *Nanoscale Res. Lett.* 13 (March 2018).
- [42] A. Shaker, A.T. Khedewy, M.A. Hassan, și M.A. A. El-Baky, Thermo-mechanical characterization of electrospun polyurethane/carbon-nanotubes nanofibers: a comparative study, *Sci. Rep.* 13 (October 2023).
- [43] P.C. Nagajothi, L. Veeranjanya Reddy, K.C. Devarayapalli, S.V. Prabhakar Vattikuti, Y.J. Wee și J. Shim, Environmentally friendly synthesis: photocatalytic dye degradation and bacteria inactivation using Ag/f-MWCNTs composite, *J. Cluster Sci.* 32 (June 2020) 711–718.
- [44] X. He, X. Xu, G. Bo, și Y. Yan, Studies on the effects of different multiwalled carbon nanotube functionalization techniques on the properties of bio-based hybrid non-isocyanate polyurethane, *RSC Adv.* 10 (2020) 2180–2190.
- [45] J. Muñoz-Chilito, J.A. Lara-Ramos, L. Marín, F. Machuca-Martínez, J.P. Correa-Aguirre, M.A. Hidalgo-Salazar, S. García-Navarro, L. Roca-Blay, L.A. Rodríguez, F. Mosquera-Vargas și J.E. Diosa, Morphological electrical and hardness characterization of carbon nanotube-reinforced thermoplastic polyurethane (TPU) nanocomposite plates, *Molecules* 28 (April 2023) 3598.
- [46] H. Liu, J. Gao, W. Huang, K. Dai, G. Zheng, C. Liu, C. Shen, X. Yan, J. Guo și Z. Guo, Electrically conductive strain sensing polyurethane nanocomposites with synergistic carbon nanotubes and graphene fillers, *Nanoscale* 8 (2016) 12977–12989.
- [47] J. Zhao, D. Tan și G. Chen, A strategy to improve the thermoelectric performance of conducting polymer nanostructures, *J. Mater. Chem. C* 5 (2017) 47–53.
- [48] F.-P. Du, N.-N. Cao, Y.-F. Zhang, P. Fu, Y.-G. Wu, Z.-D. Lin, R. Shi, A. Amini și C. Cheng, PEDOT:PSS/graphene quantum dots films with enhanced thermoelectric properties via strong interfacial interaction and phase separation, *Sci. Rep.* 8 (April 2018).
- [49] S. Mojtaba Alizadeh Darbandi, M. Nouri și J. Mokhtari, Electrospun nanostructures based on polyurethane/MWCNTs for strain sensing applications, *Fibers Polym.* 13 (November 2012) 1126–1131.
- [50] Z. Eivazi Zadeh, A. Solouk, M. Shafieian și M. Haghbin Nazarpak, Electrospun polyurethane/carbon nanotube composites with different amounts of carbon nanotubes and almost the same fiber diameter for biomedical applications, *Mater. Sci. Eng. C* 118 (January 2021) 111403.
- [51] Y. Ding, W. Xu, W. Wang, H. Fong, și Z. Zhu, Scalable and facile preparation of highly stretchable electrospun PEDOT:PSS@PU fibrous nonwovens toward wearable conductive textile applications, *ACS Appl. Mater. Interfaces* 9 (August 2017) 30014–30023.
- [52] P. Zhang, B.-b. Wang, Q.-j. Xia, și J. Zou, Study on the effect of tailoring the segmented PU molecules on electrically conductive properties and percolation threshold of PU/MWCNTs nanocomposites, *Synth. Met.* 261 (March 2020) 116300.
- [53] Y.-S. Jun, B.G. Hyun, M. Hamidinejad, S. Habibpour, A. Yu, și C.B. Park, Maintaining electrical conductivity of microcellular MWCNT/TPU composites after deformation, *Compos. B Eng.* 223 (October 2021) 109113.
- [54] R. Shamsi, M. Koosha și M. Mahyari, Improving the mechanical, thermal and electrical properties of polyurethane-graphene oxide nanocomposites synthesized by in-situ polymerization of ester-based polyol with hexamethylene diisocyanate, *J. Polym. Res.* 23 (December 2016).



Embedded textile heat flow sensor characterization and application



Teodor-Cezar Codau^a, Elena Onofrei^{b,c,*}, Gauthier Bedek^a, Daniel Dupont^a, Cedric Cochrane^b

^a Université Catholique de Lille, HEI, GEMTEX, France

^b Université Lille Nord de France, ENSAIT, GEMTEX, Roubaix F-59056, France

^c Technical University "Gheorghe Asachi" of Iasi, Iasi 700050, Romania

ARTICLE INFO

Article history:

Received 3 June 2015

Received in revised form

30 September 2015

Accepted 2 October 2015

Available online 20 October 2015

Keywords:

Textile sensor

Heat flow

Moisture transfer

Intelligent textiles

ABSTRACT

Measuring heat flow can be useful in determining the amount of heat exchanged between the human body and the environment in order to improve the comfort, efficiency and sometimes, the safety of the wearer. Scientists use passive heat flow sensors to measure body heat exchanges with the environment. In recent years, several such sensors have been developed and concerns about their proper calibration have been expressed. Moreover, the existing heat flow sensors are impermeable and prevent evaporation which gives inaccurate results when the evaporation phenomenon is present. We developed a flexible heat flow sensor which is permeable to water vapor. This sensor takes into account the evaporation phenomenon and allows a better measurement of the energy during the heat exchange. This paper describes the textile heat flow sensor realization, calibration and possible applications.

© 2015 Elsevier B.V. All rights reserved.

1. Introduction

By controlling heat passing through a clothing system it is possible to protect the body against overheating as well as against undercooling. Moreover, measuring heat flow can be useful in determining the amount of heat exchanged between the human body and the environment in order to improve the comfort and efficiency of the wearer. Heat flow is monitored by using heat flow sensors. Heat flow sensors measure the voltage caused by heat flow passing across a thermal resistance using thermocouples. Thermocouples are based on the thermoelectric effect discovered by Seebeck in 1821. In a closed circuit formed of two different metals a voltage flows if the two junctions are at different temperatures. The generated voltage depends on the thermocouple used and the temperature difference between the two junctions. The generated voltage is proportional to the heat flow which passes through its surface. The response is linear and the linearity coefficient is supplied by the manufacturer, i.e. sensitivity in $\mu\text{V}/(\text{W}/\text{m}^2)$. When the heat flow is positive, heat goes out of the body, the subject removes the metabolic heat over-production to avoid internal temperature increase. When the heat flow is negative, heat enters in the body. The subject gets heat from the environment and his core temperature increases [1].

Scientists use passive heat flow meters to measure body heat exchanges with the environment. In recent years, several such sensors have been developed and concerns about their proper calibration have been expressed. The sensors respond differently to the calibration setups and therefore, one overall calibration model is not valid. Therefore, a proper calibration corresponding to the intended purpose of use is required [2,3]. It is also important to report details of the calibration procedure. As the heat flow from the human surface is typically very small, factors influencing the sensor reading, such as thermal resistance, weight, or flexibility of the carrier material have to be considered. It is recommended to use a thin, light sensor with good thermal conductance for human subject studies. However, it is also needed to evaluate these sensors in transient conditions, tested under steady-state conditions are not all the time relevant [2]. A sensor generally refers to a device that converts a physical measure into a signal that is read by an instrument. All sensors have similar fundamental properties defined by sensitivity, range, accuracy, precision, and the need to be calibrated against known reference standards. Another important property is the interaction between sensor and the measured phenomenon [3].

Commercially available heat flow sensors are impermeable and prevent evaporation which gives inaccurate results when the evaporation phenomenon is present [4]. On the other hand, the sensor is a new thermal resistance layer added to the thermodynamic system and consequently changes the heat flow in the measured area.

We developed a new flexible heat flow sensor which is permeable to water vapor. This sensor takes into account the evaporation phenomenon and allows a better measurement of the energy

* Corresponding author at: Technical University "Gheorghe Asachi" of Iasi, Romania.

E-mail addresses: elena.onofrei@hei.fr, eonofrei@yahoo.com (E. Onofrei).

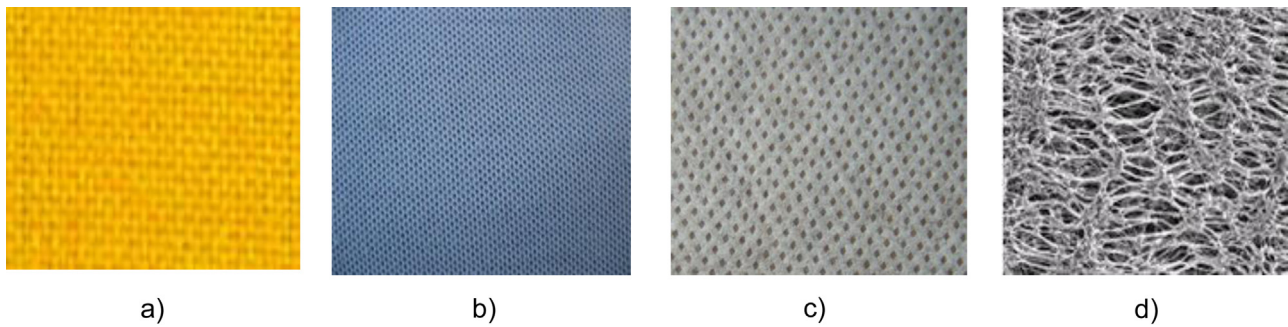


Fig. 1. Examples of fabrics.

(a) woven fabric; (b) knitted fabric; (c) non-woven fabric; (d) PTFE membrane.

during the heat exchange. This paper describes the textile heat flow sensor realization, calibration and applications.

2. Realization of the textile flow sensor

Textile fabrics are flat porous materials which are produced by different textile manufacturing techniques using different fibrous forms of input material (or structural elements), and consequently having different porous structures:

- Woven fabrics are made by interlacing vertical warp and horizontal weft yarns at right angles to each other (Fig. 1a);
- Knitted fabrics are made by interlacing yarn loops (Fig. 1b);
- Non-woven fabrics are produced from staple fibers or filaments by different web-forming, bonding and finishing techniques (Fig. 1c);
- Membranes which are thin, soft materials made from a polymer, that contains a lot of pores with diameter smaller than the water molecule and larger than water vapor molecules; the membranes are often laminated to the fabric to provide properties such as strength, water-proofing or wind-proofing to enhance the performance of the fabrics (Fig. 1d).

The textile heat flow sensor will be integrated into a firefighter jacket to perform the monitoring of the human–environment interface, through monitoring the heat flow. Therefore, the textile substrates used are parts of the overall fire protection assembly. Protective clothing systems consisting of three aramid-based layers (outer shell, thermal barrier and moisture barrier) are typical for firefighters. In firefighting, underwear with the role to provide an additional layer of material between the hazard and the person's skin is used [5].

Six sensors with a surface of $5 \times 5 \text{ cm}^2$ were produced on a textile substrate according to Table 1.

The physical properties (thickness, surface weight, bulk density) and the thermo-physical properties (water-vapor resistance and thermal resistance) of the fabrics were measured and are displayed in the Table 1. Thickness was measured under the pressure of $1 \pm 0.01 \text{ kPa}$, according to the standard ISO 5084:1996. Density was calculated from the values of fabric monolayer thickness and surface weight (which was determined using an analytical balance). The average of ten measurements was calculated. Measurements of thermal (R_{ct}) and water-vapour resistance (R_{et}) of fabrics were conducted on the sweating guarded hotplate according to the standard ISO 11092:1993. Specific environment testing conditions prescribed by this standard were met using a climatic chamber [5].

To manufacture the textile heat flow sensors the following procedure was followed:

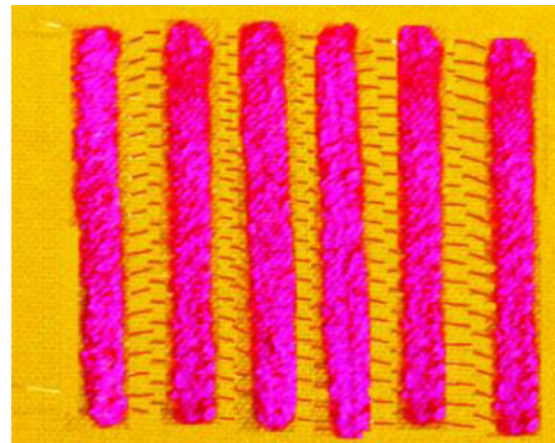


Fig. 2. Treatment with polymer.

- Insertion of a constantan wire (from Omega[®]: SPCC-005 127 μm diameter) within the textile structure with a float of 5 mm. The sensors having as textile substrate the knitted and the nonwoven fabrics were produced by inserting manually the wire into the structure. For the sensors with the woven fabric substrate, the constantan wire was inserted during the weaving process. The weaving process was performed on a weaving machine Patronic, 24 shafts, with Selectron-MAS-Control.
- Local treatment with polymer (resin) in order to allow the partial copper deposition. For that, resin was deposited on a zone consisting of two half-segments located on both sides of the textile, to protect from copper deposition, (Fig. 2). The resin is resistant to an electrolytic solution.
- Electrochemical deposition of copper on the constantan wire (Fig. 3). The thermo-electrical wire was obtained.
- Post-treatment for polymer removal. The textile flow sensor are shown in Fig. 4.

3. Textile heat flow sensor characterization

All sensors have similar fundamental properties defined by sensitivity, range, accuracy, precision, and the need to be calibrated against known reference standards. These basic properties are important when we design, calibrate, use, and model output data for the purpose of objective physical activity monitoring [3].

Researchers raised concerns regarding the development of a sensor with accurate calibration. Danielsson [6], Ducharme and Frim [7], noted that the calibration technique used greatly affects both the calibration value and the measurement obtained on humans. In addition, Ducharme et al. [8] reported a mean difference of 20 % when comparing the sensitivity delivered by the manufacturer with the authors' own recalibration measurements. In

Table 1
Physical and thermo-physical properties of the carrier material (fabrics) for textile heat flow sensor

Sensor	Textile substrate of sensor	Surface weight, g/m ²	Thickness, mm	Density, kg/m ³	Thermal resistance R_{ct} m ² K/W	Water-vapour resistance R_{et} m ² Pa/W
S_{UW}	Underwear Functionalized polyamide base knitted–piqué	283	1.19	238	0.0281	4.08
S_{Th1}	Thermal liner 100% aramid non-woven	49	0.38	129	0.015	1.99
S_{Th2}	Thermal liner 100% aramid non-woven	49	0.38	129	0.015	1.99
S_{OS}	Outer shell woven aramid base	242	0.50	484	0.0129	5.76
S_{K1}	Woven aramid Kevlar®	222	0.67	331	0.0135	4.93
S_{K2}	Woven aramid Kevlar®	222	0.67	331	0.0135	4.93

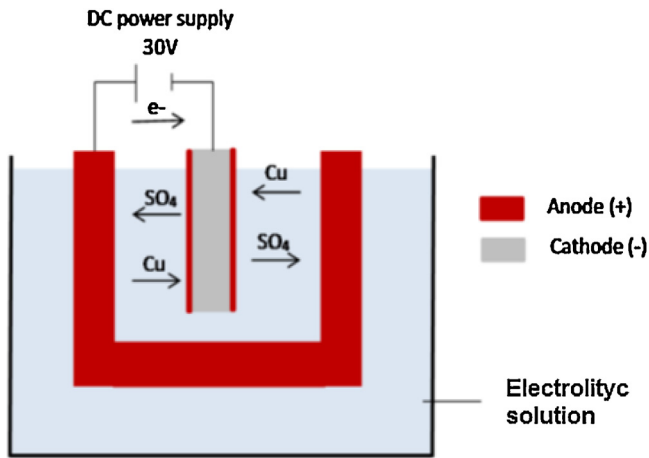


Fig. 3. Electrochemical deposition of copper on a constantan wire.

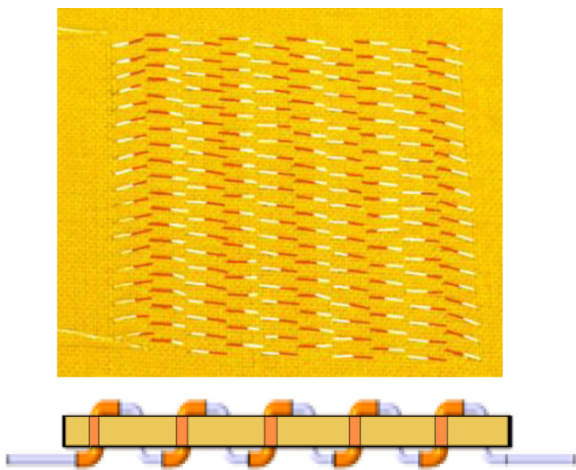


Fig. 4. Textile flow sensor.

addition, Perl et al. [9] recommended calibrating heat flow sensors before use, hence correcting inappropriate calibration factors.

3.1. Sensitivity

The standard protocol used by most manufacturers of sensors for determining the sensor sensitivity is shown in Fig. 5 (Protocol.1).

The following elements are involved in this protocol:

- Isolation material with very low thermal conductivity ($\lambda = 0.03$ W/mK), polystyrene plate having dimensions 100×100 mm² and thickness of 50 mm.
- Electrical resistance of 21.24Ω , 50×50 mm² surface and 0.2 mm thickness.

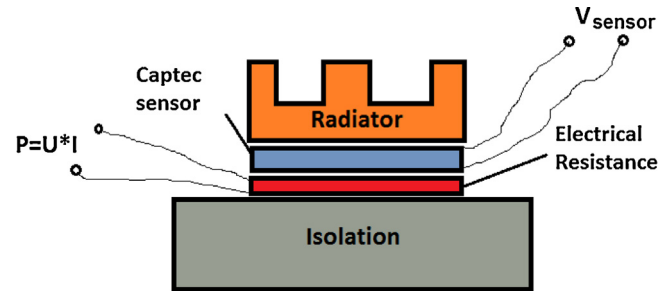


Fig. 5. Protocol.1.

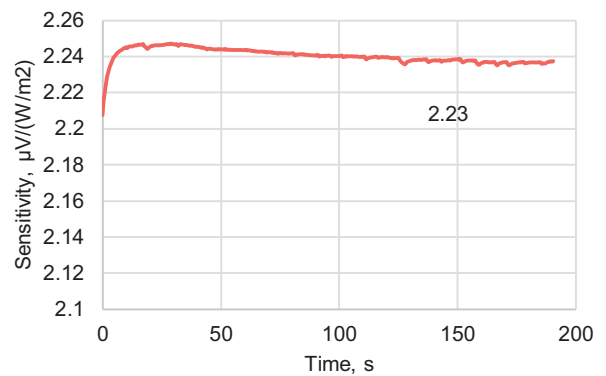


Fig. 6. Sensitivity of Captec.2.26.

- Radiator made of copper with high power thermal dissipation.
- Data acquisition system Keithley 2700.
- PC for data recording.
- DC power supply that provides voltage between 0 and 30V.

According to Protocol.1 an electrical resistance supplies a constant power. Due to the high capacity of heat dissipation of radiator we can consider that the whole energy goes through the sensor and the sensitivity is defined by formula (1):

$$S = \frac{V}{(U \times I)/A} \quad (1)$$

S —sensitivity, $\mu V/(W/m^2)$; V —voltage, (μV); U —voltage at the terminals of resistance, (V); I —current intensity through the resistance, (A); A —surface of heat dissipation, (m²). Using this protocol we tested the sensitivity of three heat flow meters provided by Captec® Company, with characteristics shown in Table 2. The results are displayed in the Figs. 6–8.

Differences smaller than 1% are registered between the measured sensitivity and the sensitivity provided by the Captec Company®. Thus, the results are in good agreement with the sensitivity supplied by the manufacturer and this protocol is appropriate for Captec® sensor characterization. Furthermore, we will use these sensors as standard reference.

Table 2
Technical parameters and properties of the Captec® heat flow sensors [2,10].

Parameter	Captec_2.26	Captec_9.17	Captec_23.3
Thickness (mm)	0.4	0.4	0.4
Shape and dimension (mm)	Rectangle 20 × 20	Rectangle 50 × 50	Rectangle 50 × 50
Bending properties	Flexible	Flexible	Rigid
Material carrier	Copper foil	Copper foil	Copper foil
Nominal sensitivity ($\mu\text{V}/\text{Wm}^{-2}$)	2.26	9.17	23.32
Thermal resistance ($\text{m}^2\text{K}/\text{W}$)	0.004	0.004	0.006
Temperature range ($^{\circ}\text{C}$)	−180 up to +200	−180 up to +200	−180 up to +200
Input range (kW/m^2)	−500/+500	−500/+500	−500/+500
Thermal conductivity material carrier (at 20°C) (W/mK)	0.067	0.067	0.067

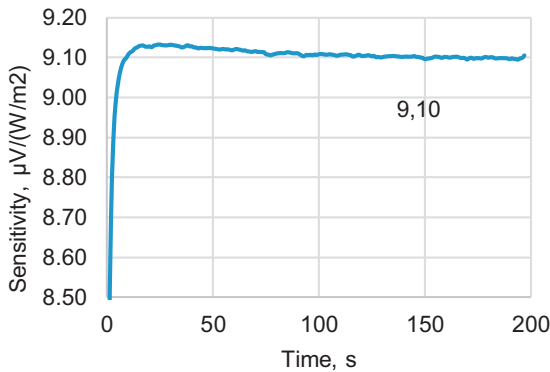


Fig. 7. Sensitivity of Captec_9.17.

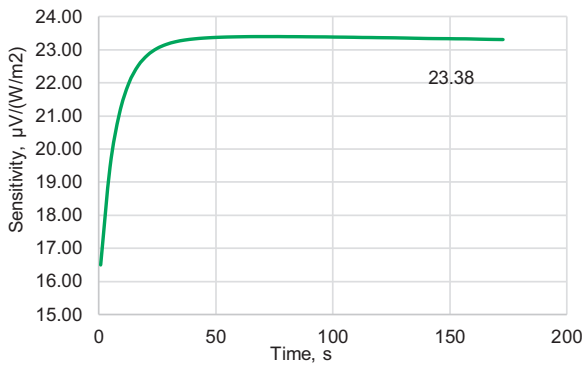


Fig. 8. Sensitivity of Captec_23.3.

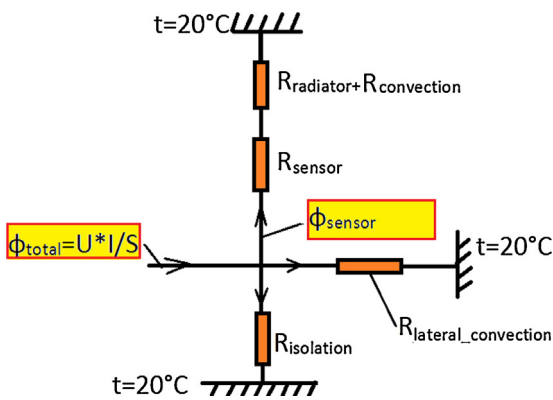


Fig. 9. Electrical diagram.

In order to analyze the possibility of using this protocol for textile sensor calibration we achieved a corresponding electrical diagram, considering a planar power source (Fig. 9).

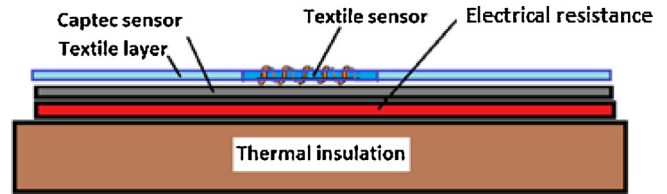


Fig. 10. Protocol.2—for single textile layer.

The equation of heat flow is:

$$\Phi_{\text{total}} = \Phi_{\text{sensor}} + \Phi_{\text{lateral}} + \Phi_{\text{isolation}} \quad (2)$$

where: Φ_{total} —total power supplied by the heat source on surface A, that is constant; Φ_{sensor} —heat flow through the sensor; $\Phi_{\text{isolation}}$ —heat flow through the isolation; Φ_{lateral} —heat flow lost by lateral convection of the sensor.

Using the thermal resistances, Eq. (2) becomes:

$$\Phi_{\text{total}} = \frac{\Delta T}{R_{\text{sensor}} + R_{\text{convection}} + R_{\text{radiator}}} + \frac{\Delta T}{R_{\text{lateral_convection}}} + \frac{\Delta T}{R_{\text{isolation}}} \quad (3)$$

ΔT —difference between electrical resistance temperature and ambient temperature.

The balance of heat flow into a system depends of thermal resistance for each component.

- The Captec® sensor has a low thermal resistance R_{sensor} ($0.006 \text{ m}^2\text{K}/\text{W}$). Also, $R_{\text{convection}} + R_{\text{radiator}}$ are very small due to the surface of heat dissipation and thermal properties of the radiator. For a source temperature of about 35°C , the resistance ($R_{\text{convection}} + R_{\text{radiator}}$) is approximately $0.018 \text{ m}^2\text{K}/\text{W}$. All of this leads to a high value of the first term of Eq. (2) (Φ_{sensor}) compared to the third term, $\Phi_{\text{isolation}}$ ($R_{\text{isolation}}$ is $1.0 \text{ m}^2\text{K}/\text{W}$).
- Taking into account the real conditions of the intended purpose of use, for the textile heat flow sensor calibration it is not appropriate to use a radiator. Without a radiator $R_{\text{convection}}$ increases greatly. $R_{\text{convection}}$ was measured for a source temperature of 35°C , and a value of $0.17 \text{ m}^2\text{K}/\text{W}$ was obtained. Taking into account that $R_{\text{sensor}} = 0.015 \text{ m}^2\text{K}/\text{W}$, the first term (Φ_{sensor}) is comparable with the last term ($\Phi_{\text{isolation}}$) of Eq. (2).

In this situation, it is necessary to know more precisely the heat flow passing through the sensor and the heat flow going through the isolation. On the other hand, in order to reduce the lateral energy loss, the textile sensor should be much smaller than the surface of the tested textile.

Based on these remarks we propose two protocols to measure the textile sensor sensitivity, depending on the intended purpose of use: the first one for the use of the sensor embedded in a single external layer (Fig. 10) and the second one for the sensor integrated into a multilayer textile assembly, as an interior layer (Fig. 11).

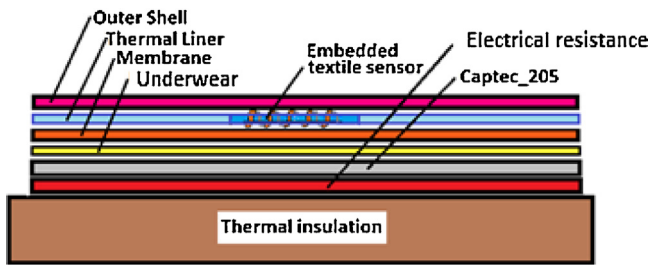


Fig. 11. Protocol_3—for multilayer textile assembly.

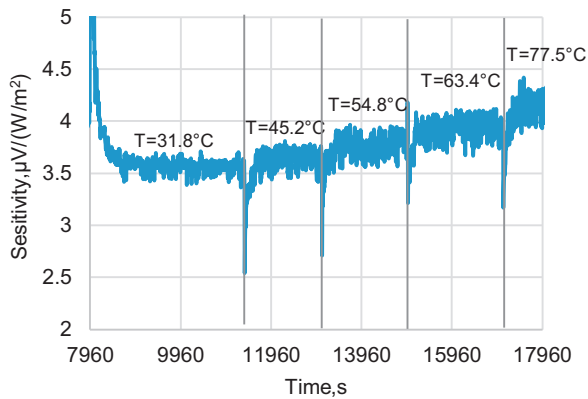


Fig. 12. Sensitivity of S_{O5} sensor for different temperatures.

These protocols involve the following elements:

- Isolation material with very low thermal conductivity ($\lambda = 0.03 \text{ W/mK}$).
- Polystyrene plate having an area of $200 \times 200 \text{ mm}^2$ and a thickness of 50 mm.
- Electrical resistance, 5.9Ω , $200 \times 200 \text{ mm}^2$.
- Captec[®] sensor having a sensitivity of $205 \mu\text{V}/(\text{W}/\text{m}^2)$.
- Data acquisition system Keithley 2700.
- PC for data recording.
- DC power supply that provides voltage between 0 and 30 V.

Thus we can consider that the power supplied by the electrical resistance will be dissipated in two directions: one through the isolator and the second through the textile layers. The heat flow passing through the textile layers can be considered constant and equal to the heat flow measured by Captec.205. The lateral energy losses are very low because it is relative to the surface of dissipation. In these conditions the sensitivity can be calculated with (4)

$$S = \frac{V}{\Phi_{\text{Captec.205}}} \quad (4)$$

S —sensitivity of the textile sensor, ($\mu\text{V}/(\text{W}/\text{m}^2)$); V —voltage supplied by textile sensor, (μV); $\Phi_{\text{Captec.205}}$ —heat flow measured by Captec[®] sensor, (W/m^2).

3.2. The influence of temperature on the textile heat flow sensor sensitivity

The Seebeck effect depends on the temperature of the junctions and the relation is a complex function when the temperature has a large variation [11]. Using the Protocol.3 the sensitivity variation with temperature was established for the textile sensor S_{O5} for a temperature variation between 30°C and 80°C (Figs. 12 and 13).

For that temperature interval a linear correlation can be considered between the heat flow textile sensor sensitivity and the

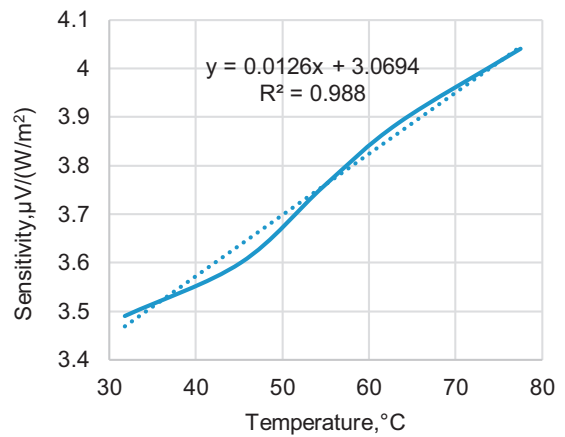


Fig. 13. Sensitivity variation with the temperature.

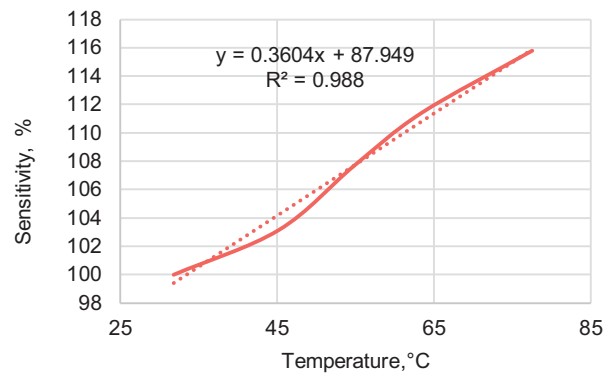


Fig. 14. Percentage variation of sensitivity with the temperature.

temperature variation. The sensitivity variation is $0.36\%/1^\circ\text{C}$. For every 10°C change in temperature the textile sensor sensitivity varies by 3.6% (Fig. 14). These results are consistent with those obtained by Machut [11]. For applications where temperature varies significantly a compensation of the sensitivity with temperature is required. The compensation could be natural (using a variable resistance) or electronic (an additional temperature sensor is necessary to provide a temperature reading from which the correction of sensitivity can be calculated).

3.3. The influence of humidity on the textile heat flow sensor sensitivity

To determine the influence of moisture on the sensor sensitivity Protocol 2 was used and the textile sensor S_{UW} . The fabric containing the sensor was wetted and the electrical resistance was powered at 12 V. To determine the moisture content we used a balance Mettler Toledo. The sensitivity according to the moisture content was calculated with Eq. (4) and the results are shown in Fig. 15.

The sensitivity variation depending on the moisture content can be determined starting from Seebeck coefficient:

$$N \times \alpha = \frac{V}{\Delta T} \quad (5)$$

where: N —number of junctions; α —Seebeck coefficient for copper-constantan thermocouple, ($\mu\text{V}/\text{K}$); ΔT —the temperature difference between the two junctions (between the two surfaces of the textile fabric), (K); V —the voltage supplied by the sensor, (μV). On the other hand,

$$\Delta T = \Phi \times R_{ct} \quad (6)$$

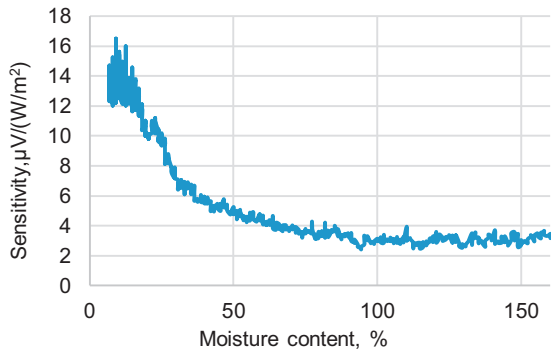


Fig. 15. Sensitivity variation of SUW sensor—measured values.

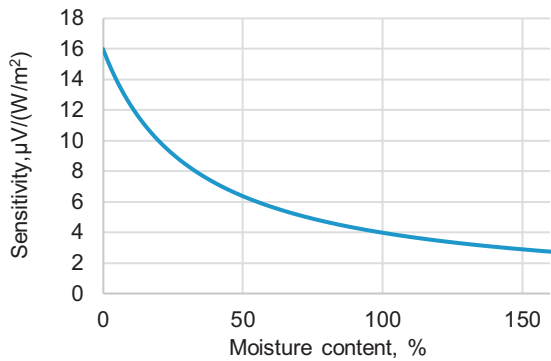


Fig. 16. Sensitivity variation of S_{UW} sensor—calculated values.

$$V = S \times \Phi \quad (7)$$

S —sensitivity, $\mu V/(W/m^2)$; R_{ct} —thermal resistance of the fabric, (m^2K/W) ; Φ —heat flow through the fabric, (W/m^2) .

From (Eqs. (5)–(7)), the textile heat flow meter sensitivity is:

$$S = (N \times \alpha) \times R_{ct} \quad (8)$$

But:

$$R_{ct} = \frac{1}{k_{tot}} \quad (9)$$

where: l —thickness of fabric (m), k_{tot} —thermal conductivity of wetted fabric (W/mK) .

The thermal conductivity of the wet textile k_{tot} is given by the Eq. (10), [12,13]:

$$k_{tot} = k_{fabric} + (k_{liq} - k_{fabric}) \times \frac{\rho_{fabric}}{\rho_{liq}} \times \frac{m_{liq}}{m_{fabric}} \quad (10)$$

k_{fabric} —thermal conductivity of conditioned fabric (W/mK) , k_{liq} —thermal conductivity of liquid water (W/mK) , ρ_{fabric} —density of the conditioned fabric (kg/m^3) , ρ_{liq} —density of the liquid water (kg/m^3) , m_{liq} —moisture content (kg), m_{fabric} —fabric mass in conditioned state (kg).

From Eqs. (7)–(10) follows that:

$$S = (N \times \alpha) \times \frac{1}{k_{fabric} + (k_{liq} - k_{fabric}) \times \rho_{fabric} / \rho_{liq} \times m_{liq} / m_{fabric}} \quad (11)$$

The sensitivity according to the moisture content was calculated with Eq. (11) and the results are shown in Fig. 16. There is a good correlation between the measured and the theoretical results and the humidity has an important influence on the sensitivity of the textile heat flow sensor.

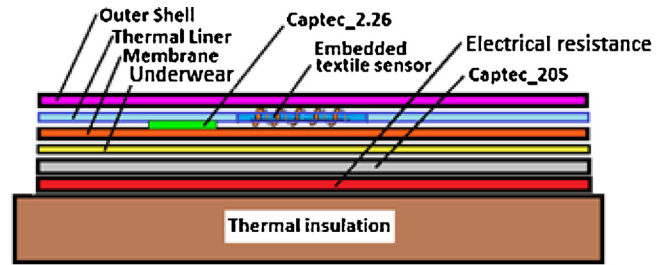


Fig. 17. Measuring device for heat flow through the multilayer system.

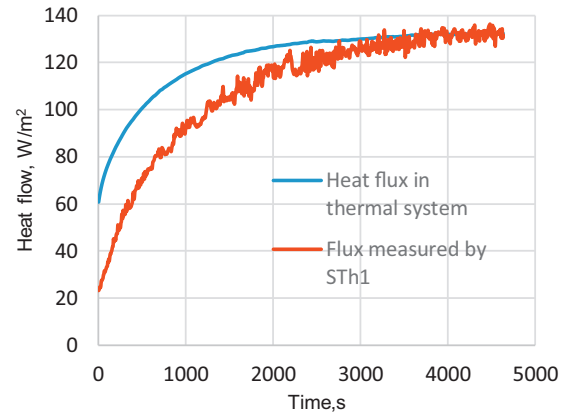


Fig. 18. Heat flow measured by S_{Th1} sensor.

4. Applications of embedded textile heat flow sensor

4.1. Measuring the energy exchanged between human body and the environment in dry state

Oliveira [14] proposed to use commercially available sensors to measure the heat flow in firefighter clothing. Even if, in the last time, this sensor has registered a significant increase in accuracy, the errors due to the interaction between sensor and measuring phenomenon cannot be avoided. These errors depend on the total thermal resistance of the system, temperature and heat flow. In the following experiment (Fig. 17) we used a Captec® sensor (Captec.2.26) and an embedded textile sensor S_{Th1} to measure the heat flow through a multilayer textile system, firefighter clothing assembly (Protocol 3). Power is supplied by an electrical resistance and it is calibrated by a large Captec® sensor (Captec.205), $200 \times 200 \text{ mm}^2$. The Captec.2.26 sensor is very small ($20 \times 20 \text{ mm}^2$) thus the impact of its own thermal resistance is reduced.

The heat flow measured by S_{Th1} and Captec.2.26 are shown in Figs. 18 and 19. The total heat flow passing through the textile layers is given by Captec.205. As we can see the heat flow measured by the textile sensor in steady-state conditions is close to the real value (given by Captec.205) while the heat flow measured by Captec.2.26 shows an error of 14.39%. Thus, the Captec® sensor substantially alters the measured heat flow value, due to the local thermal properties changes introduced into the system.

4.2. Measuring the energy exchanged between human body and the environment in wet state

To measure the heat flow through a textile system in wet conditions we used the same experiment described in Fig. 17, but the whole system was placed on the electronic balance. After a few minutes for thermal stabilization (steady-state was reached) a certain amount of water was injected into the first layer (underwear). The

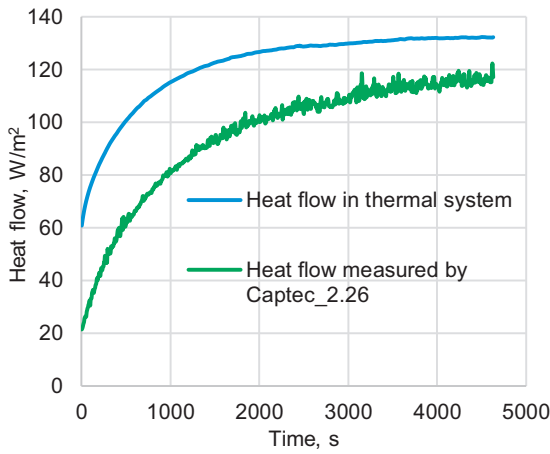


Fig. 19. Heat flow measured by Captec.2.26.

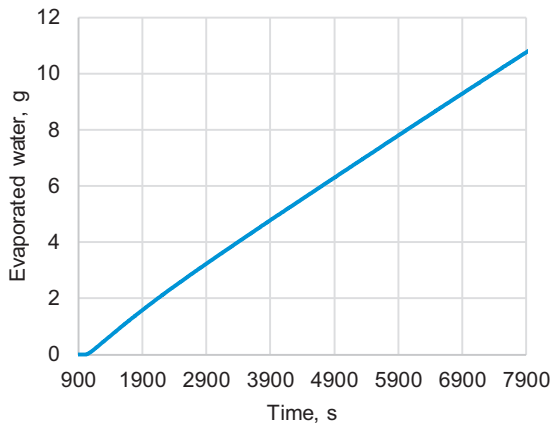


Fig. 20. Evaporated water.

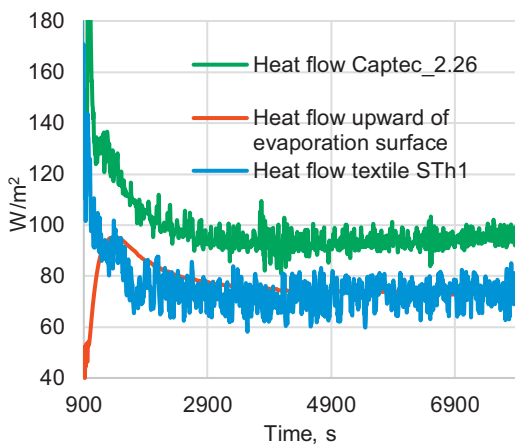


Fig. 21. Heat flow variation.

mass of evaporated water is shown in Fig. 20. For the linear section, the evaporation rate is about 0.0015 g/s that corresponds to the heat flow of evaporation $\Phi_{\text{evap}} = 84.63 \text{ W/m}^2$, calculated according to [15]. Thus, through the textile layers placed above the evaporation surface the heat flow Φ is:

$$\Phi = \Phi_{\text{Captec.205}} - \Phi_{\text{evap}} \quad (12)$$

The measured heat flow variations are shown in Fig. 21: with red line the heat flow through the system, Φ measured by Captec.205,

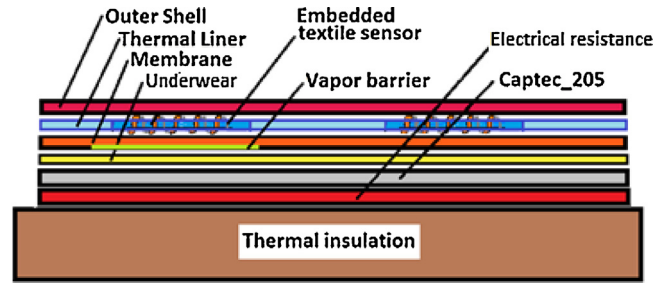


Fig. 22. Measuring device for the evaporation rate.

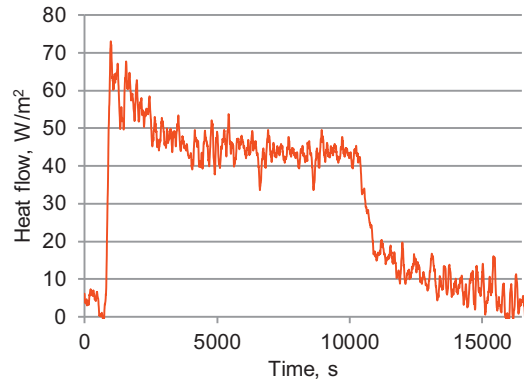


Fig. 23. Evaporation heat flow.

with the green line the heat flow measured by Captec.2.26 and with the blue line the heat flow measured by the textile sensor S_{Th1} .

The heat flow measured by Captec.2.26 sensor is with 23 W/m^2 higher than the real value of heat flow through the textile layers, i.e. an error of about 27%. This error is due to the fact that under the Captec® sensor evaporation does not occur, because it is impermeable to water vapor. The heat flow measured by the textile sensor is very close to the heat flow passing through the system.

The ambient temperature was 20°C and the heater surface 37°C .

4.3. Measuring the evaporation rate

The textile flow sensors can be used to measure evaporation rate (Fig. 22), which is defined as the amount of water evaporated from a unit surface area per unit of time. From energy point of view it is an energy that is consumed by the phenomenon of evaporation. In a firefighting clothing system the evaporation phenomenon presents a particular importance, because it changes the time of exposure to heat sources at which the critical temperature is achieved.

To demonstrate this, Protocol.3 was used and the whole system was placed on an electronic balance. Two embedded sensor S_{Th1} , S_{Th2} with sensitivity determined according to the same protocol were used. The membrane surface was treated with a synthetic resin, only on the area of first sensor, to create a vapor barrier. The ambient temperature was 20°C and the heater surface 37°C at steady-state. When the steady-state was reached a certain quantity of water at 37°C was injected into the first textile layer (underwear). The difference of heat flow measured by the two sensors is displayed in Fig. 23.

Due to the slow process of evaporation and capillarity phenomenon we can always consider a uniform distribution of water

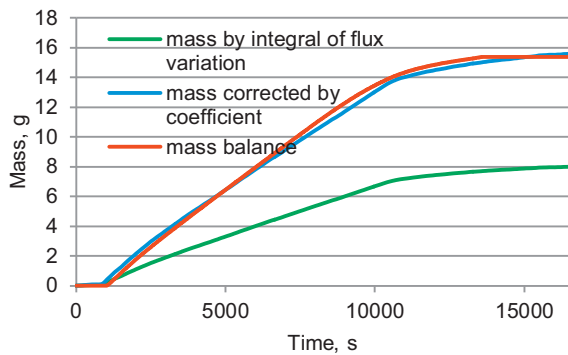


Fig. 24. Mass of evaporated water.

in the textile layer. With this hypothesis the mass of evaporated water can be calculated from Eq. (13):

$$m(t) = \frac{A}{\lambda} \times \int_0^t d\Phi(t) \quad (13)$$

where: $d\Phi(t)$ —heat flow difference between the two textile sensors, (W/m^2), (Fig. 23); A —surface of evaporation, (m^2); λ —latent heat of evaporation of water at $37^\circ C$, (kJ/kg).

The evaporated mass calculated from Eq. (13) is displayed in a green line in Fig. 24 and represents the total amount of water evaporated in time. The ratio between mass variation and time variation gives the rate of evaporation for the entire surface. For the linear region of the graphic the evaporation rate is relatively constant and it is given by the line slope. In the same figure, the red line shows the mass of evaporated water measured with the electronic balance. The difference between the two values of evaporation rate, can be explained by the heat transfer inside every textile layer, from the areas with higher temperature to the areas with lower temperature. This transfer is more intense in wet layer where the thermal conductivity is higher. Applying a correction factor (1.92), the two curves almost overlap, indicating a good correlation.

The textile flow sensors can perform the monitoring of moisture transfer between human body and the environment with a good accuracy. The correction coefficient depends on the specific properties of each system.

5. Conclusions

A textile heat flow sensor that is flexible and permeable to water vapor was developed. The sensor takes into account the evaporation phenomenon and allows a better measurement of the energy during heat exchange. This paper describes the textile heat flow sensor realization, calibration and some possible applications.

A proper calibration corresponding to the intended purpose of use is required for the textile heat flow sensor.

The textile flow sensor sensitivity depends on temperature. For applications with a large variation in temperature, compensation of the sensitivity with temperature is required.

The textile heat flow sensor sensitivity has a significant and complex variation with the moisture content. For that reason this sensor is recommended for applications where it is isolated from the liquid water by a membrane permeable to water vapor.

The textile heat flow sensor integrated into a firefighter jacket could be used for the monitoring of human-environment interface, through monitoring the heat flow and the evaporated heat losses. Similarly, it could be integrated into a garment for sport to assess the local energy expenditure of the wearer. Further experiments are planned to be made on a thermal manikin to confirm this.

Acknowledgements

The authors gratefully acknowledge the region Nord-Pas-de-Calais and the European Regional Development Fund for their financial support.

References

- [1] A. Oliveira, C. Gehin, G. Delhomme, A. Dittmar, E. McAdams, Thermal parameters measurement on fire fighter during intense fire exposition, in: 31st Annual International Conference of the IEEE EMBS Minneapolis, Minnesota, USA, September 2–6, 2009.
- [2] R. Niedermann, A. Psikuta, R.M. Rossi, Heat flux measurements for use in physiological and clothing research, *Int. J. Biometeorol.* 58 (2014) 1069–1075, <http://dx.doi.org/10.1007/s00484-013-0697-0>.
- [3] K.Y. Chen, K.F. Janz, W. Zhu, R.J. Brychta, Re-defining the roles of sensors in objective physical activity monitoring, *Med. Sci. Sports Exerc.* 44 (2012) S13–S23, <http://dx.doi.org/10.1249/MSS.0b013e3182399bc8>.
- [4] D. Dupont, P. Godth, D. Lecklercq, Design of textile heat flowmeter combining evaporation phenomena, *TRJ* 76 (10) (2006) 772–776.
- [5] E. Onofrei, T.C. Codau, S. Petrusic, G. Bedek, D. Dupont, D. Soulat, Analysis of moisture evaporation from underwear designed for fire-fighters, *Autex Res. J.* (2014), <http://dx.doi.org/10.2478/aut-2014-0015>.
- [6] U. Danielsson, Convective heat transfer measured directly with a heat flux sensor, *J. Appl. Physiol.* 68 (1990) 1275–1281.
- [7] M.B. Ducharme, J. Frim, *Methodology for Calibration and Use of Heat Flux Transducers*, Institute of Environmental Medicine, Ontario, 1991.
- [8] M.B. Ducharme, J. Frim, P. Tikuisis, Errors in heat–flux measurements due to the thermal resistance of heat–flux disks, *J. Appl. Physiol.* 69 (1990) 776–784.
- [9] T. Perl, A. Brauer, W. Weyland, U. Braun, Application of heat flux transducers to determine perioperative heat exchange, *Thermochim. Acta* 422 (2004) 35–40.
- [10] www.captec.fr/.
- [11] C. Machut, Contribution a l'etude de thermocouples plaques. Application à l'autocompensation en temperature de nouveaux capteurs, in: PhD. Thesis, Université Lille 1: Sciences et Technologies, France, 1997.
- [12] C. Keiser, Steam burns. Moisture management in firefighter protective clothing, in: PhD Thesis, Swiss Federal Institute of Technology Zurich, Swiss, 2007.
- [13] E. Onofrei, T.C. Codau, S. Petrusic, G. Bedek, D. Dupont, D. Soulat, Simulation and modeling of heat and mass transfer through fabrics exposed at low-level thermal radiation, in: 7th International Textile, Clothing & Design Conference—Magic World of Textiles, 5–8 October 2014, Dubrovnik, Croatia, 2015, pp. 418–423.
- [14] A. Oliveira, Conception et développement de capteurs et vêtements intelligents pour le suivi et la protection des pompiers: mesures thermiques non-invasives ambulatoires, PhD. Thesis, L'Institut National des Sciences Appliquées de Lyon, France, 2011.
- [15] P. Godth, D. Dupont, D. Lecklercq, Direct measurement of the latent heat of evaporation by flowmetric method, *IEEE Trans. Instrum. Meas.* 50 (6) (2005) 2364–2369.

Biographies



Teodor-Cezar Codau graduated in 1986 the Informatics High School of Iasi, Romania, with the thesis “The Numerical Methods for Linear Equations and Matrices”. In 1992, he graduated from Technical University “Gh. Asachi” Iasi, Romania as a specialist of building machines with the thesis “Honing Process Simulation for Special Tools-Machine”. From 2009 to 2011, he was research engineer at CT2M—Mechanical Engineering Department, Minho University, Portugal. Since 2012 he is research engineer at GEMTEX (HEI/ENSAIT), Lille, France, where he studied the heat and moisture transfers in textiles and contributed to the design of innovative smart textile by flow-metric method to control thermal and mass transfers.



Elena Onofrei is Lecturer (since 1992 to present) at the Technical University “Gh. Asachi” Iasi, Romania, Textile Leather and Industrial Management Faculty. In 2003 she obtained the PhD degree in “Industrial Engineering” in Romania. From 2008 to 2011 she was Post-Doc Researcher at University of Minho, Centre for Textile Science and Technology, Portugal and from 2012 to 2015 Post-Doc Researcher at GEMTEX Laboratories (HEI/ENSAIT), Lille, France. Her competences: Textile comfort properties, modeling and simulation of heat and mass transfer, technical textiles, optimizing technological parameters in spinning process, design and optimizing the woven structures and production of fabrics with special destinations.



Gauthier Bedek is Assistant Professor at Hautes Etudes d'Ingénieur, Lille, France, and member of the GEMTEX Laboratory. He is specialized in characterizing and modelling of thermal and mass transfers. He developed functionalized textile to improve the thermal comfort, in relation with the human physiology. He worked for industrials, R&D laboratories such as Oxylane and Damart. He is a scientific leader of two European research projects, FLUTEX (Improvement of comfort and performances of firefighters by the modelling of PPE's multilayers) and HYDRAX (Design of an innovative smart textile by flow-metric method to detect, characterize, and monitor thermal and mass transfers).



Daniel Dupont was born in Le Cateau-Cambrésis, France, on April 16, 1959. He received a M.Sc. degree in electronic, electrical engineering and automatism in 1982, and an MPhil in 1983 from Lille University, Lille, France. In 1986, he received this PhD degree in automatism for his work on "Control and decision aid: Applied to building numerical control with expert system on line". Since 2005, he has been Professor at the HEI, Lille, France. His current research interest is in instrumentation and modelisation. Since 1999, he has been head research team on systems and microsystems control, Lille, France.



Cedric Cochrane was born in 1979 in France. He received the MS degree in Materials Sciences in 2003 from the University Lille Nord de France. He obtained a PhD degree in Engineering Science in 2007 from the University Lille Nord de France. Between 2007 and 2012 he was researcher at GEMTEX, the laboratory of ENSAIT. He is currently Associate professor at ENSAIT (University Lille Nord de France). His research interest includes smart and multifunctional textiles, flexible sensors and actuators for aeronautic, composite and health. He is reviewer for several international journals in the field of material science and textile technology.

Textile sensor for heat flow measurements

Elena Onofrei^{1,2}, Teodor-Cezar Codau³, Gauthier Bedek³,
Daniel Dupont³ and Cedric Cochrane¹

Textile Research Journal
2017, Vol. 87(2) 165–174
© The Author(s) 2016
Reprints and permissions:
sagepub.co.uk/journalsPermissions.nav
DOI: 10.1177/0040517515627167
trj.sagepub.com



Abstract

This paper describes the concept of creating and testing of a textile heat flow sensor in order to determine the amount of heat exchanged between the human body and its environment. The main advantage of this sensor is the permeability to moisture, which allows taking into account the evaporation phenomenon, contrary to the traditional heat flow sensors. Another property related to this new sensor is its flexibility conferred by the textile substrate, which allows it to be applied on deformable surfaces.

Keywords

heat flow meter, textile sensor, heat transfer, water vapor transfer, smart textiles

The thermal and moisture properties of textiles are significant properties affecting comfort, especially in sportswear and thermal protective clothing, during intense physical activity and/or special environmental conditions (e.g. high temperature and thermal radiation). The requirements of these garments (a high level of protection and minimal physiological burdens) have led to the development of new materials, and the design and engineering of such textiles have become increasingly important.^{1,2} Apart from the studies in garment structure and design for improving the thermal comfort of clothing, efforts are conducted in monitoring of people in several professional high-risk occupations (that require wearing of heavy protective clothing) and athletes (who need to dissipate an increased amount of heat during physical activity).

Measurement of the heat exchanged between the human body and environment throughout the clothing system can be performed with indirect calorimeters or with direct calorimeters. Direct calorimeter systems, based on heat flow meters, fit better into a body-worn device. Heat flow meters, which are easily worn on the skin, work by measuring the small thermal difference that develops when heat flows across an insulator. Measuring the temperature difference and knowing the heat flow resistance of the insulator allows calculation of the heat flow.^{3,4}

Scientists use passive heat flow meters to measure the heat exchanged by the human body with the

environment. These sensors may influence the measurement accuracy due to their own properties. Thus, the error for heat flux measurement can have different sources, including the thermal resistance or the thickness of the sensor.^{5,6} These sensors measure local changes in heat flux and temperature and extrapolate to the level of the whole body. In many cases, the effect of additional layers of clothing and the changes in temperature due to the thermal resistance of the sensor are not taken into account. The errors caused by the thermal resistance of the heat flow meters and changes to convective losses measured are described in the literature.⁶

Some of these sensors are rigid, and by integrating them in clothing, they cause discomfort to the wearer. In addition, the sensors for measuring heat flow are impermeable to water vapor. The importance of the water vapor permeability is apparent from the balance of heat transfer, where evaporation plays an important

¹ENSAIT, GEMTEX, University Lille Nord de France, France

²Faculty of Textiles-Leather and Industrial Management, Technical University “Gheorghe Asachi” of Iasi, Romania

³HEI, GEMTEX, Catholic University of Lille, France

Corresponding author:

Elena Onofrei, PhD, 2 Allée Louise et Victor Champier, BP 30329,
59100 Roubaix Cedex 1, France.

Email: elena.onofrei@hei.fr, elena.codau@ensait.fr, eonofrei@yahoo.com

role. A number of researchers have published studies focused on the measurement of the heat flow using commercially available sensors⁷⁻⁹ or in-house produced sensors.¹⁰ None of these studies mentioned the measurement of evaporative heat flow. In a previous study, we analyzed the moisture evaporation from underwear designed for firefighters, and the important influences of this phenomenon were underlined.¹¹

We developed a textile heat flow sensor that is flexible and permeable to water vapor. This paper describes the concept of creating, testing and integrating of a textile heat flow sensor into firefighter protective clothing, in order to determine the amount of heat passing through the clothing system. This measurement will be useful in determining the amount of heat exchanged between the human body and environment, and will contribute to improving the comfort, efficiency and, sometimes, the safety of the wearer.

Working principle and design consideration

Heat flow sensors measure the temperature difference caused by heat flow passing across a thermal resistance using thermocouples.

Thermocouples are based on the thermoelectric effect discovered by Seebeck in 1821. In a closed circuit formed of two different metals, a voltage flows if the two junctions are at different temperatures (Figure 1). The electric voltage generated V (μV) depends on the metals used and the temperature difference between the two junctions:¹²

$$V = \alpha \cdot \Delta T \quad (1)$$

where α is the Seebeck coefficient ($\mu\text{V}/\text{K}$) and ΔT the temperature difference between the junctions (K).

The Seebeck coefficient is the difference between the thermoelectric potential of the two metals.

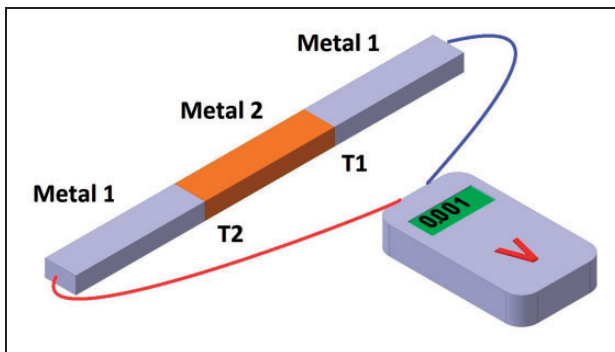


Figure 1. Seebeck effect.

Most heat flow sensors use paired thermocouples to measure the temperature difference, wired in series. The output of the paired thermocouples is directly proportional to the temperature difference and, thus, the heat flow. To increase the sensitivity, a network of thermocouple pairs is typically used, with each thermocouple pair stacked end-to-end like a string of batteries to increase the voltage produced for a given heat flux. This stacked arrangement of thermocouples is commonly referred to as a thermopile.^{3,13}

A heat flow sensor measures the local heat flow density in one direction, Φ . The result is expressed in watts per square meter and the calculation is done according to Equation (2):

$$\Phi = \frac{V}{S} \quad (2)$$

where V is the sensor output (V) and S is the sensitivity ($\text{V}/(\text{W}/\text{m}^2)$), specific for the sensor.

The textile heat flow meter that we have produced consists of a woven textile and a bimetallic wire inserted into it, in order to appear alternatively on both sides of the textile structure. The weaving process was performed on a weaving machine “Patronic” (24 shafts, with Selectron-MAS-Control). The constantan wire (from Omega®: SPCC-005, 127 μm diameter) was inserted into the structure during the weaving process. Insertion was realized between two weft yarns in the form of weft floats with the length covering 10 warp yarns (0.5 cm; Figure 2).

The yarn used in the warp and weft was a para-aramid yarn (Kevlar® from DuPont™) Nm 36/2. The weave is a plain weave with warp density of 22 yarns/cm and weft density of 16 yarns/cm. The surface is 50 \times 50 mm^2 , so 200 thermocouples are present on the whole surface. The weave pattern consists of 6 weft yarns and 20 warp yarns, as presented in Figure 3.

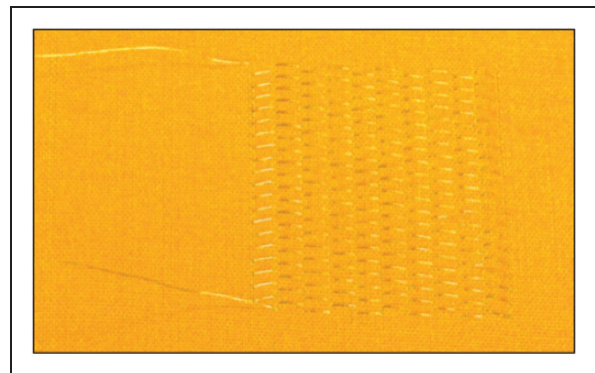


Figure 2. Textile with constantan wire.

The thermocouples were made by electrolytic deposition of copper on the constantan wire. For that, a resin was filed on a zone consisting of two half-segments located on both sides of the textile, to protect from copper deposition (Figure 4). The resin has chemical resistance to the electrolytic solution and was finally

removed by a dissolving solution. The setup used for the electrolytic deposition of the copper on the constantan wire (Figure 5) consisted of a power source (direct current (DC) power supply) and a glass container with a saturated solution of copper sulfate. The inside of the glass container was covered with copper plates (1.5–2 mm thickness) and over these with perforated plates of Plexiglass. The fabric was completely immersed in the electrolytic solution. Constantan wire was the cathode and the copper plate was the anode for the electrochemical reaction. Both were connected to the DC power supply. The obtained textile heat flow sensor is shown in Figure 6. The operational limits in

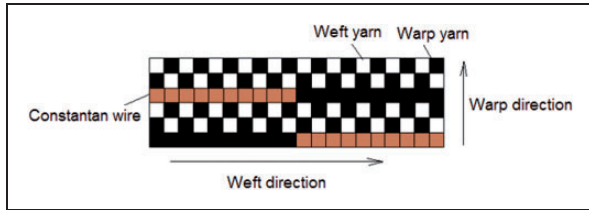


Figure 3. Weave pattern.

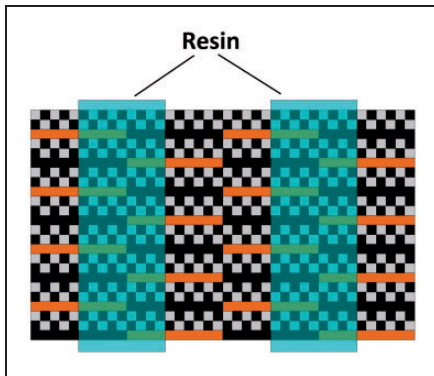


Figure 4. Principle of thermopile production.

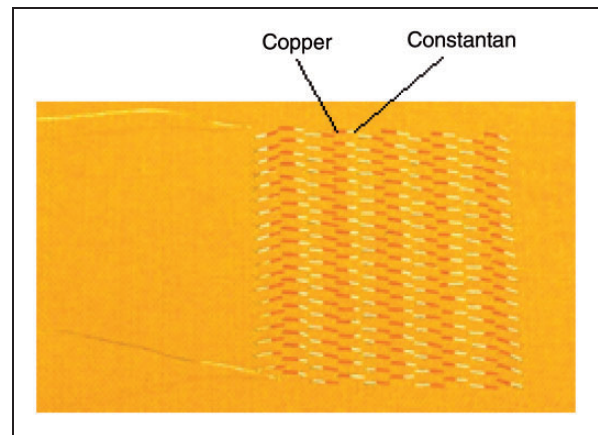


Figure 6. Textile heat flow sensor.

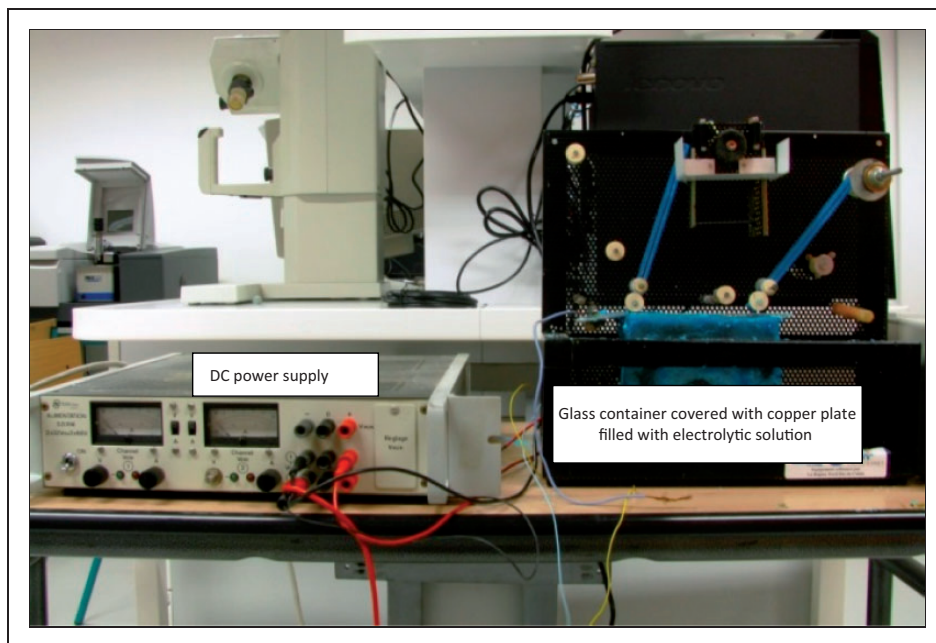


Figure 5. The copper deposition system.

temperature are determined by the Kevlar decomposition temperature, which is 427–482°C.¹⁴

Sensor calibration

Calibration of heat flow sensors is crucial for validating sensor readings. However, due to the complexity of performing controlled measurements, calibration is generally difficult. In recent years, concerns about the proper calibration of sensors have been addressed. The sensors respond differently to the calibration setups and, therefore, one overall calibration model is not valid. Thus, a proper calibration corresponding to the intended purpose of use is required.^{5,15}

Thus, taking into account that the sensor will be used as an internal layer in a multilayer textile system, for calibration it was placed between two textile layers and the protocol shown in Figure 7 was used.

An electrical resistance supplies a constant heat flow. The resistance is placed on a thermal isolation material (polystyrene) with very low thermal conductivity ($\lambda = 0.03 \text{ W/mK}$), a surface area of $200 \times 200 \text{ mm}^2$ and a thickness of 50 mm. The heat flow, supplied by electrical resistance, will be dissipated in two directions: mainly through the textile layers and a smaller part through the isolator. The heat flow passing through the textile layers is measured by a Captec[®] sensor. This sensor was provided by the Captec[®] Company; it has $0.006 \text{ m}^2\text{K/W}$ of thermal resistance, an operating temperature between -180°C and $+200^\circ\text{C}$ and sensitivity of $205 \mu\text{V}/(\text{W/m}^2)$.

The lateral energy loss is small because it is relative to the surface of dissipation, and can be neglected. A Data Acquisition System “Keithley 2700” and a computer are used for data recording. In these conditions, the sensitivity can be calculated with Equation (3):

$$S = \frac{V}{\Phi_{\text{Captec}}} \quad (3)$$

where S is sensitivity ($\mu\text{V}/(\text{W/m}^2)$), V is voltage recorded by the textile sensor (μV) and Φ_{Captec} is the heat flow measured by the Captec[®] sensor (W/m^2).

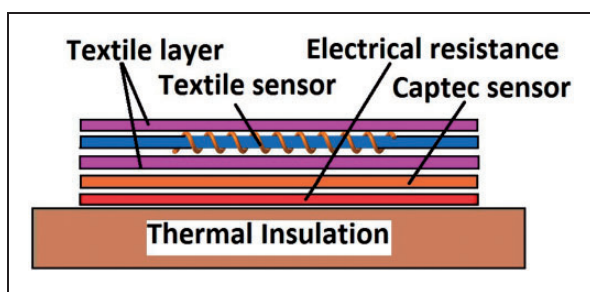


Figure 7. System arrangement for textile heat flow sensor calibration.

Five measurements have been done. The textile heat flow meter sensitivity according to this protocol is $10.13 [\pm 0.07] \mu\text{V}/(\text{W/m}^2)$.

Two factors should be considered when the sensor is calibrated: the sensitivity variation with the temperature and the humidity.

Heat flow sensors are based on the Seebeck effect, which depends on the average temperature of the two junctions. Machut, in his PhD thesis,¹² developed a detailed study on the variation of the thermoelectric effects with the temperature. Our sensor was created to be used in a firefighter clothing system during routine conditions, where the ambient temperature can reach up to $60\text{--}70^\circ\text{C}$. For this temperature variation, the Seebeck coefficient (for the Cu–constantan junction) has a linear variation with the temperature and does not exceed 3%. Thus, no thermal compensation was used. For a smaller error or for applications that involve higher temperature variations, it is necessary to use a linear coefficient of compensation.

The water in the textile layer of the sensor should change its thermal resistance and therefore the sensitivity. However, in our applications, a membrane prevents the transfer of liquid water to the textile sensor. Only water vapors can pass. The textile fabric used as substrate for the textile sensor is aramid based (Kevlar). These fibers can absorb up to 3% of water. In these conditions, the textile sensor sensitivity is sufficiently stable.

Performance

To evaluate the performance of the textile sensor, it was tested using a protective clothing system for firefighters, in comparison with a traditional heat flow meter. Tests were conducted in the dry state and in wet conditions (simulated sweating conditions). Firstly, the textile sensor was used as an additional layer, then it was directly integrated (embedded) into the thermal layer of the clothing system.

Protective clothing systems consisting of three or four aramid-based layers are typical for firefighters. The multilayer firefighter jacket used for analysis (Figure 8) was composed of an outer shell, a thermal barrier and a moisture barrier.

In firefighting, underwear is used to provide additional protection between the hazard (radiant or direct flame contact) and the person’s skin. Cotton is the most commonly used underwear but wool, silk, aramid or other flame-resistant materials are also used.¹⁶ Fabrics made with 100% synthetic fibers or blended with natural fibers are used for underwear for firefighters, due to their resistance to high temperatures and chemical agents and improved ability to remove moisture. This could improve firefighters’ comfort and might increase their efficiency.

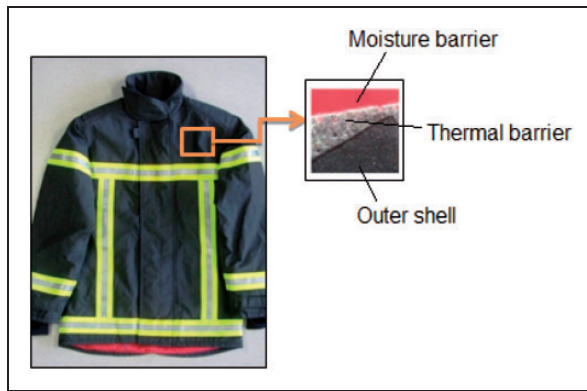


Figure 8. Multilayer firefighter jacket.

In this study, underwear made of functionalized polyamide-based fibers, resistant to high temperatures and chemical agents, and with good moisture management capacity, was used.

The textile heat flow sensor can be used within a multilayer fabric system in two ways:

- A. adding the textile sensor to the multilayer system, as a new additional layer;
- B. inserting the copper–constantan wire in a textile layer that already exists in the system (embedded textile sensor).

The textile sensor as an additional layer: test in the dry state

Experimental details. This test was conducted according to the standard procedure used to measure the conductive heat flow.¹⁷ The textile heat flow sensor had been placed under the outer layer of the jacket. Experiments were carried out using a thermostatic bath “Julabo F12-ED” (Refrigerated/Heating Circulator) to keep the temperature of the calorimeter constant (35°C) and to more accurately simulate the actual process of using protective equipment. A Captec® sensor, Captec_1 100 × 100 mm², was placed upon the calorimeter to measure the total heat flow. A second Captec® sensor, Captec 50 × 50 mm², was placed under the outer shell, for comparison. A type-J thermocouple was used to measure the temperature between the outer shell and thermal liner. The ambient temperature ($T_{ambient}$) was constant during the experiments at 22°C. A Data Acquisition System “Keithley 2700” and a computer were used for data recording. The textile heat flow sensor sensitivity was considered to be $S = 10.13 \mu V / (W/m^2)$, as determined according to the protocol of calibration previously described.

The system arrangement is shown in Figure 9.

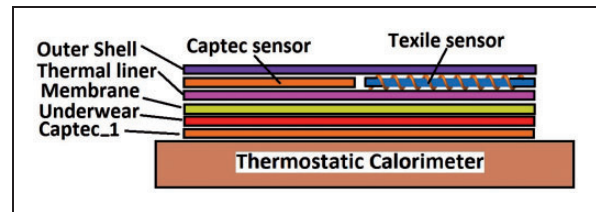


Figure 9. System arrangement for the textile sensor test.

Results and discussion. The measurements were repeated three times and similar results were obtained.

The temperature variations recorded by the thermocouple (T_{int}) and the thermostatic calorimeter (T_{TB}) are shown in Figure 10.

Heat flow variations recorded by the Captec (Flux_Captec), the Captec_1 (Total heat flux) and the textile heat flow sensor (Flux_Textile-sensor) are shown in Figure 11.

The difference between the flows measured by the Captec sensor and by the textile sensor was 12 W/m² and this is attributed to the different thermal resistance of the two sensors. The thermal resistance of the Captec sensor is 0.006 m²K/W (value from the manufacturer) and the thermal resistance of the textile sensor is 0.0135 m²K/W (measured with the sweating guarded hotplate, in compliance with the standard ISO 11092).

Both sensors (the Captec sensor as well as the textile sensor) were added as an extra layer and, consequently, they changed both the temperature gradient and heat flow through each. Thus, they altered the results.

A difference of 17 W/m² (20%) was registered between the flux measured by the textile sensor and the total heat flux. In the dry state, the Captec sensor measures more precisely the heat flux; the difference was around 6%. The error of measurement depends mainly on the ratio of the thermal resistance of the sensor and the total thermal resistance of the system. Thus, it is necessary to use sensors with a thermal resistance as small as possible, in order to minimize the effect.

However, the textile sensor has the advantage of being flexible, and therefore more easily integrated into the textile structure than the Captec® sensor.

In addition, it is permeable to water vapor and may take into account the evaporation process, as can be seen from the following experiment.

The textile sensor as an additional layer: test in the wet state

Experimental details. The same multilayer system comprising an outer shell, thermal liner, moisture barrier and underwear was used, but the underwear (below the membrane) was wet with a certain amount of

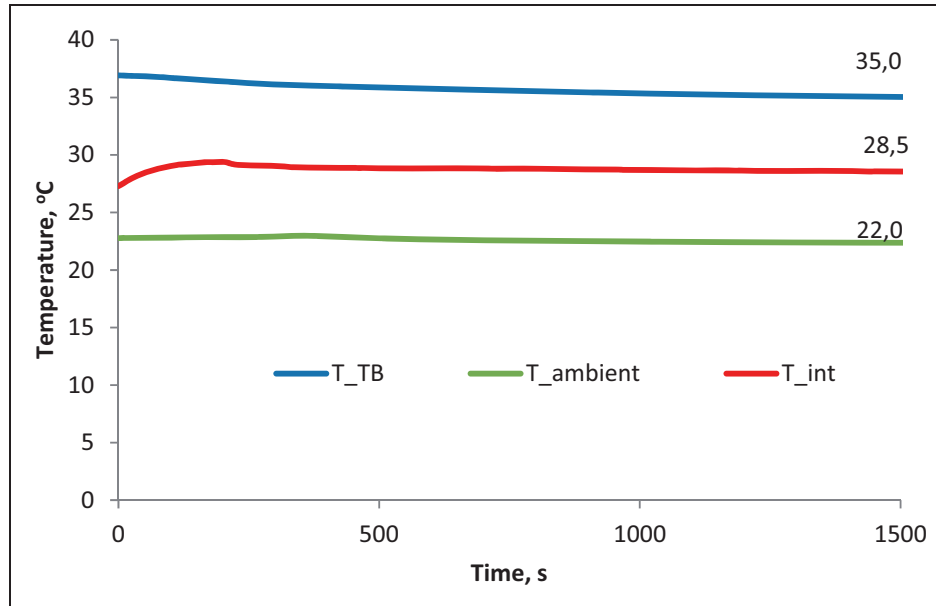


Figure 10. The temperature variation.

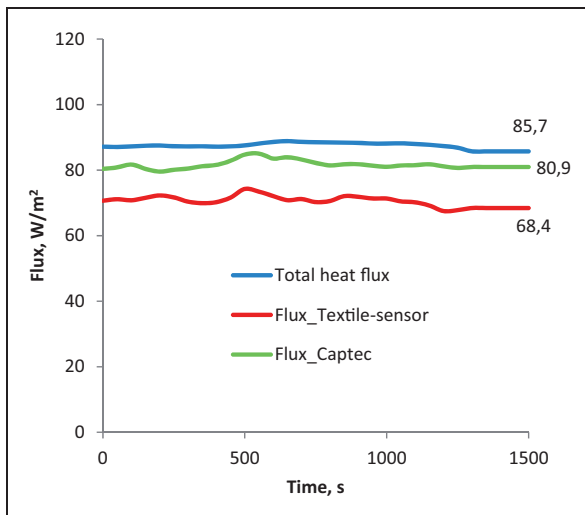


Figure 11. The heat flow variation.

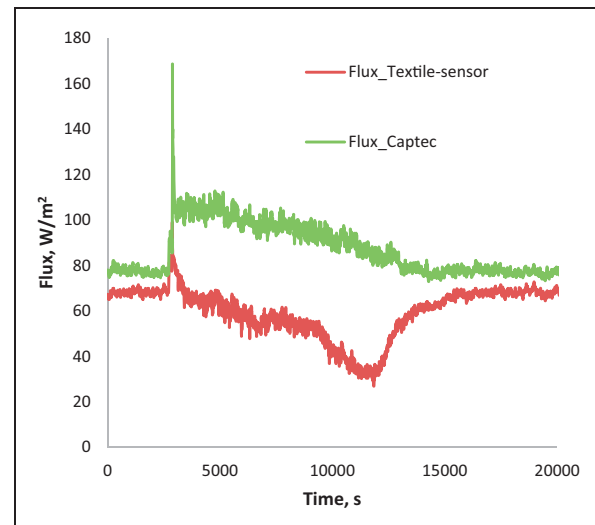


Figure 12. The heat flow variation during the wet test.

water. Using a syringe, 2.3 g of water was inserted within the underwear layer, at the moment of 2880 s, in order to simulate perspiration. The temperature of the inserted water was the same as the temperature of the thermal calorimeter, 35°C.

Results and discussion. The measurements were repeated three times and similar results were obtained. The heat flow variations indicated by the two sensors (*Captec* and *Textile sensor*) are displayed in Figure 12 and their difference in Figure 13.

Again, in the dry state (the first part of the graph), the difference between the measured heat flows by the two sensors was due to their different thermal

resistances ($\sim 12 \text{ W/m}^2$). When water was introduced into the system and began to evaporate, the difference was higher ($\sim 45 \text{ W/m}^2$, see Figure 13). It cumulated the effect caused by the impermeability of the *Captec*[®] sensor to water vapors.

The *Captec*[®] sensor prevents evaporation of water in the layers below it, and the mass transfer. The *Captec*[®] sensor registers only the flux variations caused by increased thermal conductivity in the underwear. Thus, we can see an increase in the heat flow measured by the *Captec*[®] sensor, as long as water was present in the system.

The textile sensor is permeable to water vapor and allows evaporation and mass transfer. The flow measured by the textile sensor varies due to both the

evaporation phenomenon as well as due to the thermal conductivity variation of the system (due to the water presence in the system). During the water evaporation, the energy was consumed (endothermic process) and the heat flow decreased. The effect of evaporation exceeded the effect of increased thermal conductivity.

In conclusion, the textile heat flow sensor responds to water vapor evaporation, in contrast to the traditional heat flow sensors. The membrane prevents the transfer of liquid water to the upper layers and only water vapors can pass.

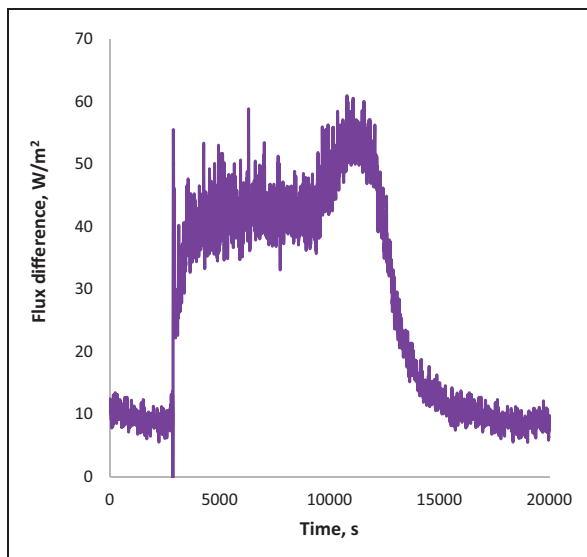


Figure 13. Heat flow difference between the measured heat flows by the Captec[®] sensor and the textile sensor.

The effect of an additional layer on the heat flux measurement

Experimental details. Any additional textile layer introduced into the system contributes with its own resistance and with the resistance of a new air gap between textile layers, and consequently changes the measured heat flow compared with the actual heat flow passing through the system. To compute, with a good accuracy, the effect of an additional layer on the heat flux passing through the multilayer system, the arrangements shown in Figure 14 have been used. Experiments were carried out using a thermostatic bath “Julabo F12-ED” (Refrigerated/Heating Circulator) to keep the temperature of the calorimeter constant (35°C).

A Captec[®] sensor was used to measure the total heat flow. In the first experiment the flux passing through a firefighter clothing system composed of four layers (outer shell, thermal liner, membrane and underwear) was measured (Figure 14(a)). In the second experiment, a textile sensor was added to the initial system (Figure 14(b)) and in the third experiment, the textile sensor was made directly in the thermal liner layer (Figure 14(c)). The textile heat flow sensor sensitivity was $S = 11.7 \mu V/(W/m^2)$, as determined according to the described calibration protocol.

Results and discussion. Heat flow variations recorded by the Captec[®] sensor and corresponding to the situations described in Figure 14 are shown in Figure 15. For the transient response of the sensor, a sudden jump was registered, because the textile clothing system, initially at ambient temperature (22°C), was put onto the pre-heated

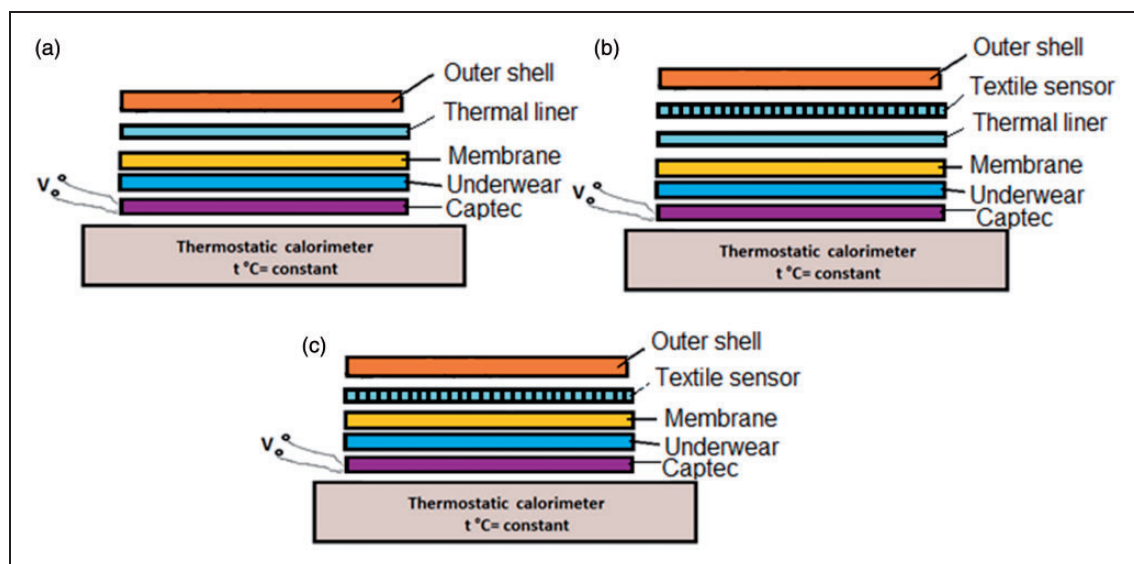


Figure 14. The system arrangement to compute the effect of an additional layer on the heat flux measurement: (a) firefighter clothing system; (b) firefighter clothing system + textile sensor; (c) firefighter clothing system with the textile sensor in the thermal layer.

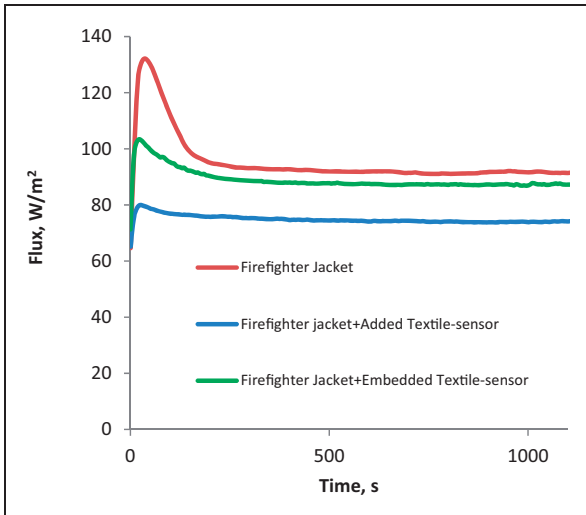


Figure 15. The influence of an additional layer on the heat flow measurement. (Color online only.)

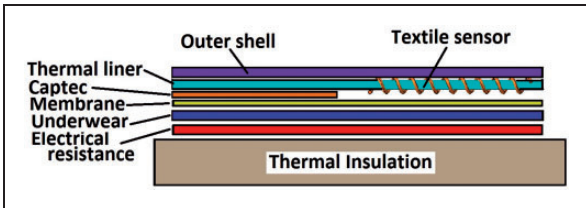


Figure 16. System arrangement for the textile sensor test.

calorimeter. At steady state, a difference of 18% is registered between the heat flows crossing the firefighter clothing system (red line) and the heat flow crossing the firefighter clothing system + added textile sensor (blue line). Compensation coefficients can be used in order to eliminate these differences if there is no change of the thermal convection coefficient, h_c . However, by changing the thermal resistance of the whole system, the heat flow and the surface temperature of the outer shell will be changed automatically and hence the convection coefficient, h_c . In other words, compensation coefficients depend directly on the source temperature and thermal resistance of the system, as well as the ambient temperature. In these circumstances, it becomes difficult to estimate the ratio between the heat flow that passes through the sensor zone and the zone without a sensor. By inserting the copper–constantan wire into an already existing textile layer of the system, for the $50 \times 50 \text{ mm}^2$ textile sensor, the difference between the heat flows crossing the firefighter clothing system (red line) and the heat flow crossing the firefighter clothing system + embedded textile sensor (green line) is only 3–4%.

Textile sensor embedded in a textile layer already existing in the system

Thus, in order to measure the heat flow with a textile heat flow sensor, it is recommended to use the method of inserting a constantan–copper wire within an

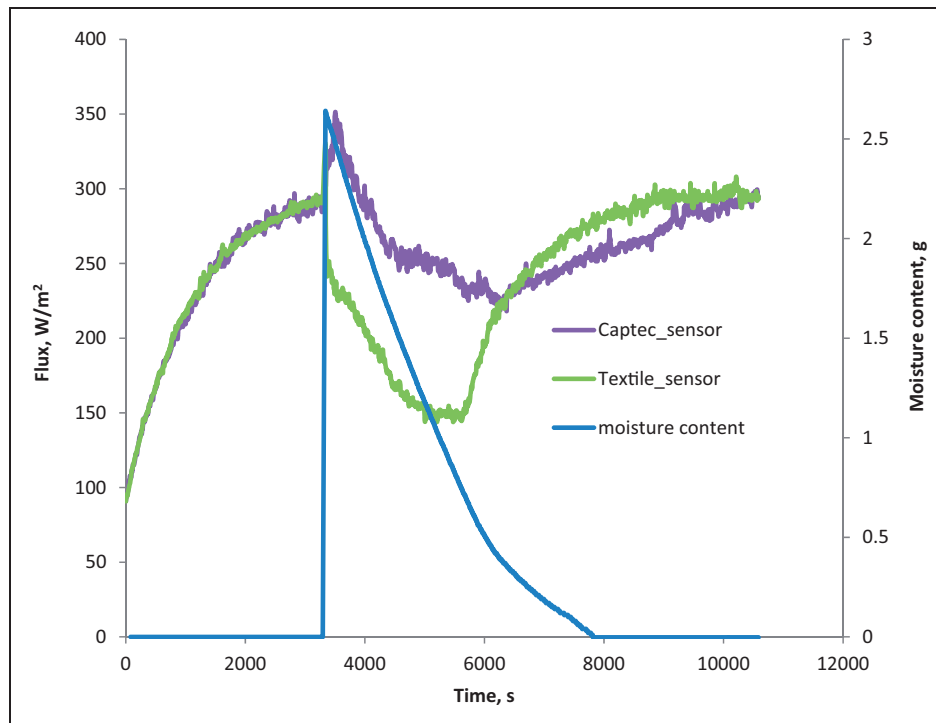


Figure 17. The heat flow measured by the Captec[®] sensor and the textile sensors.

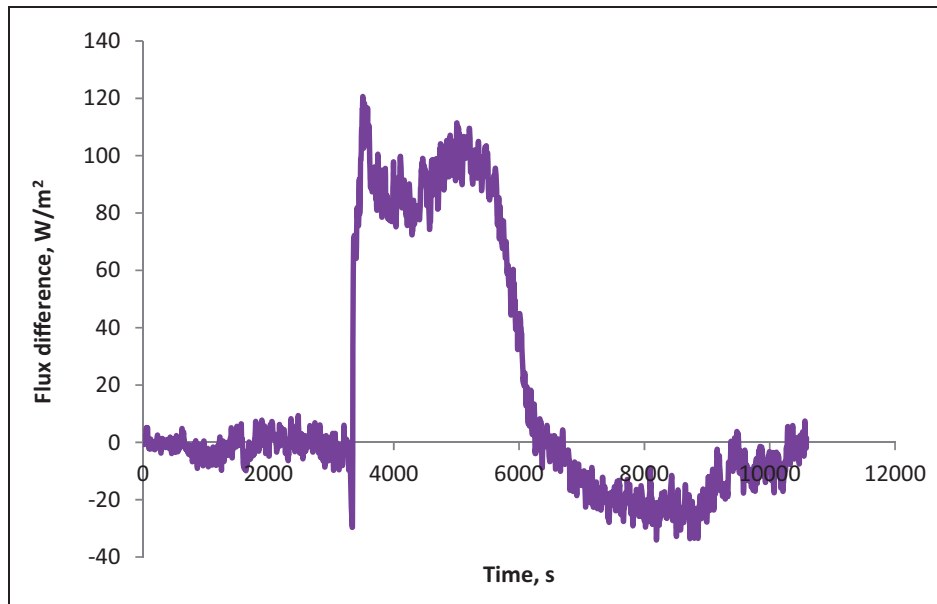


Figure 18. The difference between the heat flows measured by the impermeable sensor and by the textile sensor.

existing textile layer of the multilayer system (see the test described in the section). If this is not possible, it is recommended for the textile heat flow sensor to use a textile substrate identical with the already existing layer of the multilayer system and to place the textile sensor within this layer by making a cutout. In this way, the additional resistance (thermal resistance as well as water vapor resistance) introduced into the system will be minimal.

Experimental details. This experiment was conducted according to the settings from Figure 16, with the textile sensor embedded in the thermal liner (the textile layer already existing in the multilayer system). The sensitivity of this sensor is $11.7 \mu\text{V}/(\text{W}/\text{m}^2)$. For a heat flow of $300 \text{ W}/\text{m}^2$, the temperature in thermal liner, at steady state, was 75°C . For this experiment, an electrical resistance was used as the heat power source and the whole system was placed on a balance (Mettler Toledo) in order to register the mass variation. The amount of water introduced in the underwear layer was 2.64 g.

Results and discussion. The heat flows measured by the Captec[®] sensor and by the textile sensor are shown in Figure 17. The water content variation is also represented in Figure 17.

In this case, there is no significant difference between the heat flow measured by the Captec[®] sensor and the heat flow measured by the textile sensor during the dry experiment, that is, from 0 to 3340 s. The difference between the two heat flows measured by the impermeable sensor and by the textile sensor, respectively,

during water evaporation is about $90 \text{ W}/\text{m}^2$. After complete water evaporation, initial conditions are achieved and the difference between the two measured heat flows no longer appears, as one can see in Figure 18. The area under this graph is directly proportional to the energy absorbed during evaporation. This area is the starting point in evaluating the mass transfer using the textile sensors. This topic will be further developed taking into account all the parameters involved.

Conclusion

For some applications, such as the characterization of the energy assessment in thermal protective clothing, sportswear, etc., it is essential to take into account the phenomenon of water evaporation.

We developed a flexible textile heat flow sensor that is permeable to water vapor, in contrast to the traditional heat flow sensors.

A proper calibration corresponding to the intended purpose of use is required for the textile heat flow sensor.

The textile heat flow sensor, integrated into the firefighter protective clothing, can measure the amount of heat passing through the clothing system, taking into account the evaporation phenomena. This measurement will be useful in monitoring the human–environment interface.

Declaration of conflicting interests

The authors declared no potential conflicts of interest with respect to the research, authorship and/or publication of this article.

Funding

The authors disclosed receipt of the following financial support for the research, authorship, and/or publication of this article: This work was supported by the region Nord-Pas-de-Calais and the European Regional Development Fund.

References

1. Onofrei E, Rocha AM and Catarino A. Investigating the effect of moisture on the thermal comfort properties of functional elastic fabrics. *J Ind Text* 2012; 42: 34–51.
2. Onofrei E. Identification of the most significant factors influencing thermal comfort using principal component analysis and selection of the fabric according to the apparel end-use. *Ind Textila* 2011; 63: 91–96.
3. Szuminsky N, Dykstra J and Melanson E. Measurement of energy expenditure by body-worn heat-flow sensors. In: Sazonov E and Neuman M (eds) *Wearable sensors, fundamentals, implementation and applications*. Elsevier Inc., Imprint: Academic Press, 2014, pp.131–152.
4. Godts P, Dupont D and Leclercq D. Direct measurement of the evaporation latent heat by flow metric method. *IEEE Trans Instrum Meas* 2005; 54: 2364–2369.
5. Niedermann R, Psikuta A and Rossi RM. Heat flux measurements for use in physiological and clothing research. *Int J Biometeorol* 2014; 58: 1069–1075.
6. Frim J and Ducharme MB. Heat flux transducer measurement error: a simplified view. *J Appl Physiol* 1993; 74: 2040–2044.
7. Layton RP, Mints WH Jr, Annis JF, et al. Calorimetry with heat flux transducers: comparison with a suit calorimeter. *J Appl Physiol Respir Environ Exer Physiol* 1983; 54: 1361–1367.
8. English MJ, Farmer C and Scott WA. Heat loss in exposed volunteers. *J Trauma* 1990; 30: 422–425.
9. Mandal S and Song G. Thermal sensors for performance evaluation of protective clothing against heat and fire: a review. *Text Res J* 2015; 85: 101–112.
10. Danielsson U. Convective heat transfer measured directly with a heat flux sensor. *J Appl Physiol* 1990; 68: 1275–1281.
11. Onofrei E, Codau TC, Petrusic S, et al. Analysis of moisture evaporation from underwear designed for fire-fighters. *AUTEX Res J* 2014; 15: 35–47.
12. Machut C. *Contribution a l'etude de thermocouples plaques. Application à l'autocompensation en température de nouveaux capteurs*. PhD Thesis, Université Lille 1: Sciences et Technologies, France, 1997.
13. Dupont D, Godts P and Leclercq D. Design of textile heat flowmeter combining evaporation phenomena. *Text Res J* 2006; 76: 772–776.
14. Dupont. <http://www.dupont.com> (accessed 27 May 2013).
15. Chen K, Janz K, Zhu W, et al. Re-defining the roles of sensors in objective physical activity monitoring. *Med Sci Sport Exer* 2012; 44: S13–S23.
16. Petrilli T and Ackerman M. Tests of undergarments exposed to fire. Fire tech tips, <http://www.fs.fed.us/t-d/pubs/pdfpubs/pdf08512348/pdf08512348dpi72.pdf> (2008, accessed 30 May 2013).
17. Oliveira A. *Conception et développement de capteurs et vêtements intelligents pour le suivi et la protection des pompiers: mesures thermiques non-invasives ambulatoires*. PhD Thesis, L'Institut National des Sciences Appliquées de Lyon, France, 2012.